Spin Injection, Transport, and Modulation in III-V Semiconductors

by

Hyun Kum

A dissertation submitted in partial fulfillment
of the requirements for the degree of
Doctor of Philosophy
(Electrical Engineering)
in The University of Michigan
2012

Doctoral Committee:

Professor Pallab K. Bhattacharya, Chair
Associate Professor Çagliyan Kurdak
Associate Professor Wei Lu
Assistant Professor Zhaohui Zhong

To my Parents and PKB

ACKNOWLEDGEMENTS

First and foremost, I sincerely thank my parents for their constant support and encouragement. I'd like to extend my sincere gratitude to my advisor Prof. Pallab Bhattacharya for his encouragement, support, and guidance throughout my graduate study. This thesis would not have been possible without him. He has taught me beyond what is expected of a graduate student advisor and will remain a constant source of inspiration. I have never seen a fully tenured professor work so hard in my life. It has truly been an honor to work with him. I am grateful to my committee members, Prof. Wei Lu, Prof. Çagliyan Kurdak, and Prof. Zhaohui Zhong, for devoting their time to review this dissertation and providing valuable suggestions and comments to improve the quality of this work.

I would like to acknowledge my collaborators who contributed to this thesis. I express special thanks to Prof. Supriyo Datta and his student Abu Zainuddin at Purdue University for their insights and contributions to the InAs spin modulator and the mesa size dependent magnetoresistance enhancement studies. My gratitude is extended to Fatih Doğan and Prof. Aurelien Manchon at the King Abdullah University of Science and Technology, Thuwal, Saudi Arabia, for their analysis in spin relaxation mechanisms in GaN.

My mentors contributed tremendously to my understanding and experimental techniques. I would like to express my gratitude to Dr. Debashish Basu and Prof.

Dipankar Saha for their guidance in all things related to my spintronics work. I would also like to thank all my past and current research group members, Prof. Wei Guo, Dr. Guan Huang, Dr. Meng Zhang, Dr. Junseok Heo, Dr. Chi-Sen Lee, Ayan Das, Animesh Banerjee, Sishir Bhowmick, Shafat Jahangir, Saniya Deshpande, Thomas Frost, Allan Xiao, and Marc Jankowski for their support and assistance.

I greatly appreciate all the Lurie Nanofabrication Facility staff for their constant support in and out of the cleanroom, especially Matthew Oonk, Edward Tang, Greg Allion, and Dennis Schweiger for their expertise in thin film deposition, lithography techniques, and lab management. I am also grateful to the DCO department for their excellent support and assistance.

I thank Lisa Vogel, Melanie Caughey, Denise Oscar, Laura Jarels, Frances Doman, Deb Swartz, Karen Liska, and Beth Stalnaker for excellent administrative support throughout my graduate career. I wish to acknowledge the University of Michigan Rackham Graduate School for providing partial fellowships to support my education, the Office of Naval Research (ONR), and the National Science Foundation (NSF) for funding this research.

TABLE OF CONTENTS

CHAPTER

LIST OF FIGURES

Figure

LIST OF TABLES

Table

LIST OF APPENDICES

Appendix

Chapter I

Introduction and Overview of Spintronics

1.1 Motivation

Conventional CMOS (complementary metal oxide semiconductor) devices used in every electronic gadget today utilize the charge of electrons (or holes) to perform logic operations or act as a digital memory device. In these devices, a gate electrode is used to control the flow of charge in the active region to ultimately modulate the output resistance of the device. The advancement of CMOS is primarily focused on miniaturization, roughly doubling the number of transistors in a single die every two years. This trend has continued since the realization of the first integrated circuit in 1958 (named Moore’s law after the Intel co-founder Gordon E. Moore), and is not expected to stop anytime in the near future. As shown below in Fig. 1.1, leading semiconductor corporations have been able to keep Moore’s law strong by improving lithographic techniques and creating smaller and smaller transistors. However, in spite of the tremendous enhancement in lithography and innovations in device engineering, conventional CMOS devices will eventually reach a physical limit where further miniaturization of the device will be fundamentally impossible. A paradigm shift in hardware and software architecture, from single core to multiple processing, is also expected to keep improving processing speed, but it is evident that architectural

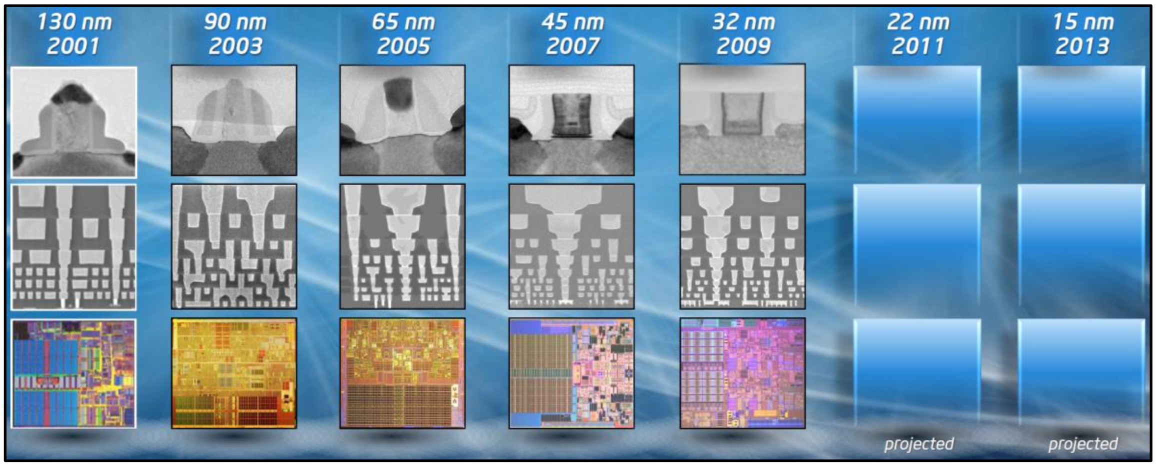

Figure 1.1 Intel's scaling roadmap, showing the evolution of feature size of transistors in 2 year cycles. Moore's law is projected to continue past year 2013 [source: Intel].

improvements alone will not be able to keep the advancement of processing speed and power at a rate we have been able to keep up for the past few decades.

The international technology roadmap of semiconductor (ITRS) has identified several alternate technologies that have the potential to replace current CMOS technology. Spintronics, in particular, is a promising candidate due to the ease of integration with current technology. Spintronics is an emerging discipline which aims to revolutionize the field of information technology by utilizing the inherent quantum spin information present in a charged particle. In its most basic form, spintronics aims to inject/detect, transport, and control/manipulate spin polarized carriers inside a non-magnetic medium such a semiconductor, insulator, or metal. Preliminary theoretical calculations predict that optimized spintronic devices will be faster, consume less power, and have a higher integration density than conventional charged based devices we use today.

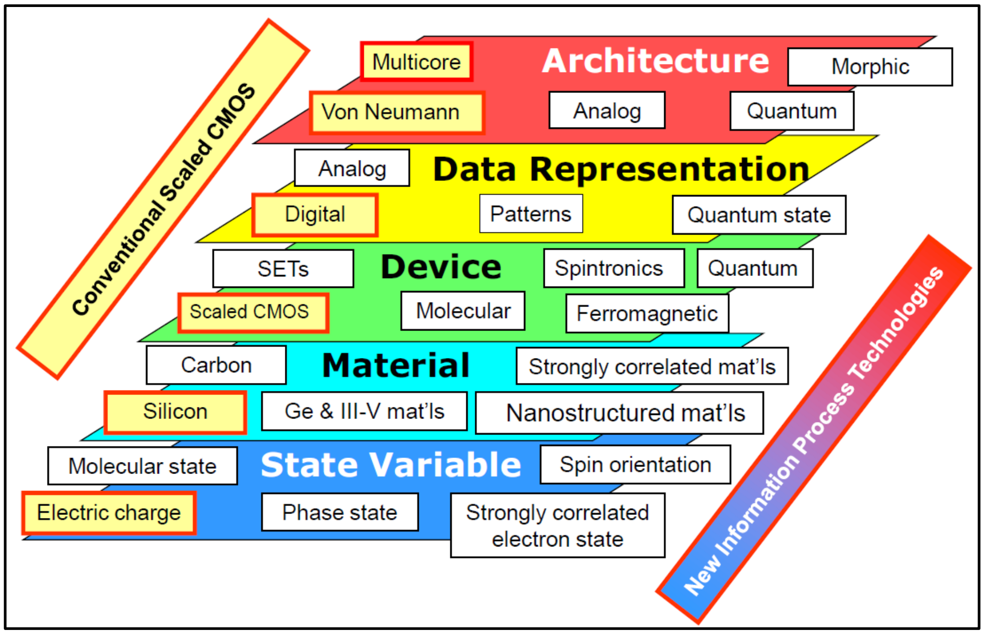

Figure 1.2 ITRS (International Technology Roadmap for Semiconductors) representation of current technologies and new technologies. Spintronics is applicable in the "state variable" and "device" level, and is still categorized as emergent technology [source: ITRS].

1.2 Spintronics Overview

Spin was first observed by Otto Stern and Walther Gerlach (experimentally) in 1922 with experiments on the deflection of atoms subject to a non-uniform magnetic field, now appropriately named the Stern-Gerlach experiment [1]. The experimental setup is shown in Fig. 1.3. A couple important facts were concluded from this experiment (not thoroughly understood at the time of experiment): (1) the unpaired outer electrons had an intrinsic angular momentum equal to $\hbar/2$, (2) the electrons deflected in *quantized* amounts by the non-uniform magnetic field, meaning spin could only take two discrete values of *up* or *down* in any arbitrary orientation θ. However, a complete theoretical understanding of the experimental result was lacking until 1925, when George Uhlenbeck and Samuel Goudsmit, here at the University of Michigan, proposed an explanation for the Stern-Gerlach experiment [2]. They postulated the existence of an intrinsic angular momentum property present in electrons, called *spin*. This intrinsic angular momentum, which has no classical analogue and is purely quantum mechanical, gives rise to a magnetic moment in the electron that interacts with external magnetic fields.

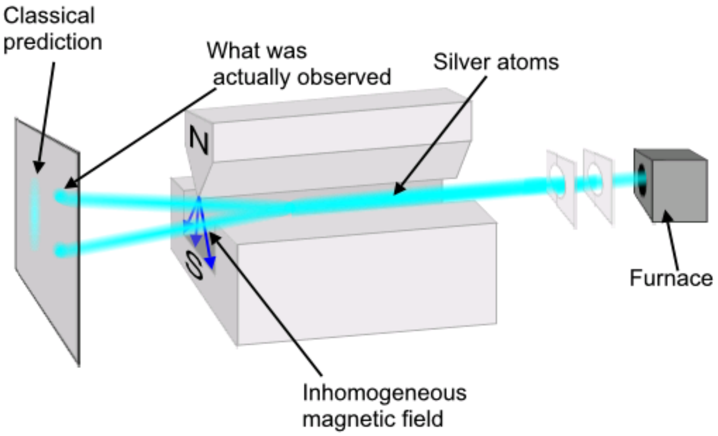

Figure 1.3 Schematic illustration of the Stern-Gerlach experiment setup. [43]

This postulate was later put into equation by Dirac, who later showed that spin arises naturally in a relativistic formulation of the quantum theory (a relativistic generalization of the Schrödinger equation called the *Dirac equation*). The postulate states that the spin of a particle should have an associated magnetic moment

$$\vec{\mu}_s = \frac{g\mu_B}{\hbar}\vec{S} \qquad \textbf{(1.1)}$$

where ***S*** is the spin operator and $g\mu_B / \hbar$ is the spin gyromagnetic ratio (g ≈ 2 in most semiconductor systems).

Such a discovery on the intrinsic quantum variable, spin, has led to the concept of spintronics, where the spin state of electrons are utilized to enhance the functionalities of existing technologies and to create new type of devices. Spintronics is a relatively broad area, which includes spin-based electrical devices (both metal and semiconductor based), optoelectronic devices (spin-LEDs and lasers), and magnetoelectronics (utilization of magnetic properties of materials) (Fig. 1.4). In the following sections, a brief overview of the various categories of spintronic devices will be given. A more detailed explanation will be given in relevant chapters of this thesis.

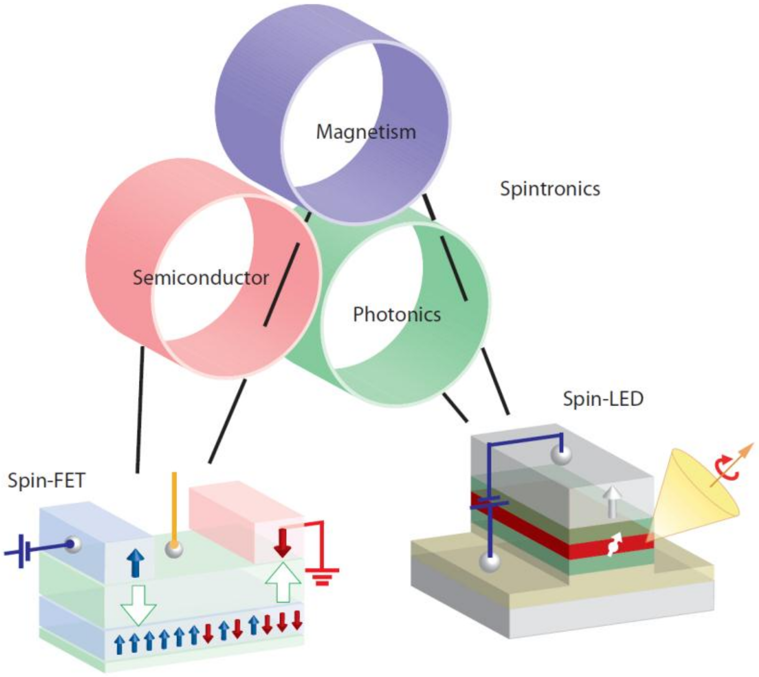

Figure 1.4 Shows two dominant spintronics devices actively being researched. Spin-based electrical and opto-electronic devices promise better device performance than conventional charge-based devices (adapted from [3]).

1.2.1 Metal based magnetic multilayers (GMR devices)

Metal-based spintronics (Nobel Prize in physics awarded in 2007 to Albert Fert and Peter Grünberg for their discovery of giant magnetoresistance (GMR) devices) is probably the most successful yet and the technology is already being widely used in memory applications (hard disk drives). GMR refers to the resistance of two terminal devices consisting of alternating layers of non-magnetic and ferromagnetic films. The effect is manifested as a significant electrical resistance change depending on the relative magnetization direction of the adjacent ferromagnetic layers. The resistance is high when the ferromagnetic layers are in antiparallel configuration (magnetization direction opposite) and low for parallel configuration (magnetization direction same). It was first discovered in 1988 in Fe/Cr/Fe trilayers by Peter Grünberg and independently in Fe/Cr multilayers by Albert Fert a few days later.

Magnetoresistance (MR) is usually defined in three ways: (1) optimistic, (2) pessimistic, and (3) normalized magnetoresistance. The most widely used definition of MR is the optimistic case, where MR is defined as $\Delta R = R_{\uparrow\downarrow} - R_{\uparrow\uparrow} / R_{\uparrow\uparrow}$. The value for the optimistic definition is unbounded, and so far the value has reached up to a few thousand % (colossal magnetoresistance). The pessimistic MR is defined as $\Delta R = R_{\uparrow\downarrow} - R_{\uparrow\uparrow} / R_{\uparrow\downarrow}$, where the value cannot exceed 100%. Finally, the normalized MR is defined as $\Delta R = (R_{\uparrow\downarrow} - R_{\uparrow\uparrow}) / (R_{\uparrow\downarrow} + R_{\uparrow\uparrow})$. The magnetoresistance is a figure of merit for spin valves, where a bigger MR means better signal-to-noise ratio (S/N) and, therefore, more sensitive devices.

The basic physics behind GMR devices is discussed here. Although it is presented in the context of GMR, the general physics and model is universal for most electric spin-based devices (i.e. spin valves). There are two geometries one can associate with GMR devices: (1) CPP, where the current flow is perpendicular to the multilayer and (2) CIP, where current flow is parallel to the multilayer. CPP geometry is easier to treat theoretically, but harder to implement experimentally.

Consider a trilayer structure with a non-magnetic layer in between two ferromagnets, as shown above in Fig. 1.5. We assume that electron spin is conserved over distances greater than the entire thickness of the trilayer (we define the average distance

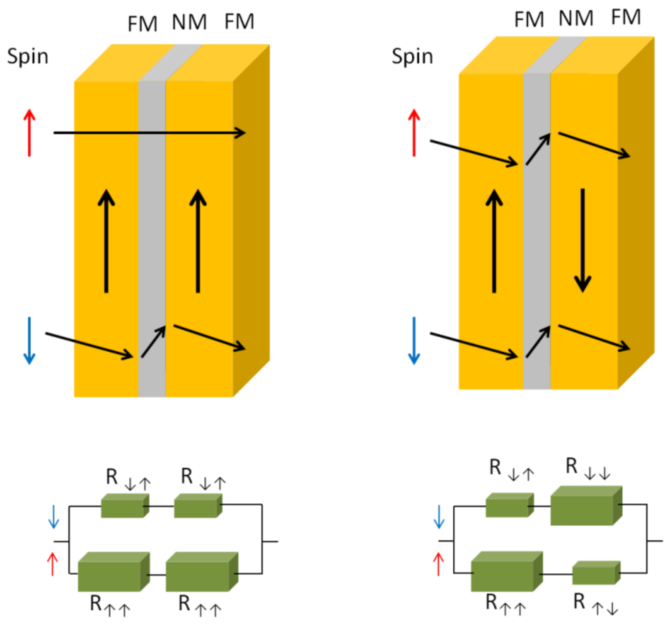

Figure 1.5 Schematic illustration of a GMR spin valve and its associated resistance state in the parallel (left) and anti-parallel (right) configuration. The blue layers with arrows are ferromagnets, while the orange layer is non-magnetic.

---

an electrons travels before losing its spin information as the spin diffusion length, λ_{sf}. We can then separate the current paths for spin up electrons and spin down electrons. Since the spin up and spin down current paths are independent (conserved), they can be modeled as two wires connected in parallel. Electrons with spin parallel and antiparallel to the magnetization of the ferromagnetic layer are scattered at different rates when they arrive at the nonmagnet/ferromagnet interface (NM/FM), a so called spin-dependent scattering. This spin scattering is due to the difference in the density-of-states (DOS) of the ferromagnetic layers for spin up and spin down electrons, as illustrated in Fig. 1.6.

It is evident that the current flow is restricted for the anti-parallel configuration due to the second ferromagnet (FM2) not having enough states to accommodate the majority spin down electrons. Thus, the injected spin down electrons either accumulates in the non-magnetic layer, or for a tunneling magnetoresistance structure (discussed in next section), the tunneling probability reduces significantly.

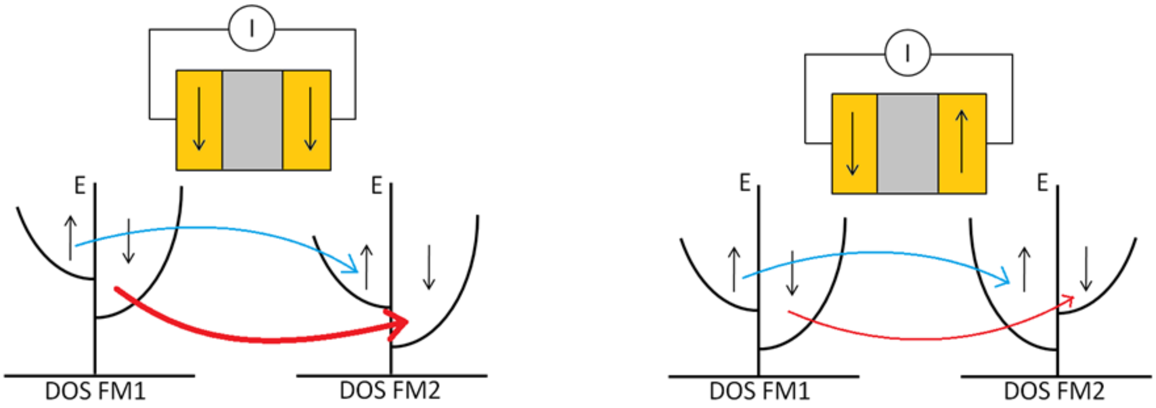

Figure 1.6 Density-of-states difference for parallel (left) and antiparallel (right) configuration of the two ferromagnetic layers.

1.2.2 Tunneling magnetoresistance (TMR)

Tunneling magnetoresistance (TMR) is a subset of giant magnetoresistance, where a very thin layer of *insulator* (instead of a metal) is sandwiched between two ferromagnets, typically no more than a couple of nanometers. The insulator must be thin enough for electrons to tunnel from one ferromagnet to another. TMR response is typically larger than GMR responses, and is used more dominantly in today's technology. The first study of spin polarized tunneling was reported by Tedrow and Mersevey on Al/Al_2O_3/Fe tunnel junctions [4] and later by Julliere on Fe/Ge/Co junctions [5]. Typically, the magnetoresistance of TMR and GMR structures decrease with increasing temperature due to spin-magnon scattering, which reduces the overall polarization of the ferromagnets. The physics behind TMR devices is identical to the physics behind GMR devices explained previously.

1.2.3 Spin torque transfer devices

First reported by Berger [6] and Slonczewski [7] independently in the late 1970s and 1980s, the spin torque effect allows one to switch the magnetization direction of a ferromagnet by injecting a high spin-polarized current into the ferromagnet. If a spin polarized current, $\boldsymbol{I_s}$, is injected into a soft ferromagnet (a ferromagnet with very small coercivity value), it induces a torque $\boldsymbol{T} = \boldsymbol{m} \times \boldsymbol{I_s} \times \boldsymbol{m}$ on the magnetic orientation of the ferromagnet, where $\boldsymbol{m}$ is the magnetization orientation of the ferromagnetic layers. For a strong enough net torque from the spin polarized current, it becomes energetically favorable for magnetic domains in the ferromagnet to rearrange itself.

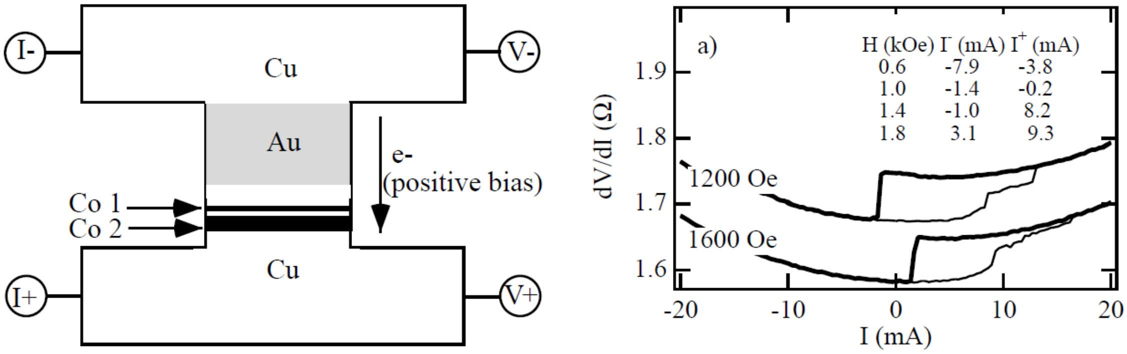

Figure 1.7 (left) Schematic of a spin torque pillar device with Co layers separated by a Cu layer. At positive bias, electrons flow from the thin to the thick Co layer. (right) Change in conductance (dV/dI) as the thin Co layer reverses its magnetization orientation either parallel (high conductivity) or antiparallel (low conductivity) to the thick Co layer from the spin torque effect [159].

Slonczewski predicted that the spin transfer torque could induce two qualitatively different types of magnetic behaviors: (1) switching of magnetic orientation of the ferromagnetic and (2) dynamical state in which the magnetization undergoes steady-state precession. The first behavior has relevance in magnetic memory applications (such as an STT-RAM), whereas the second behavior has direct relevance to gigahertz oscillator applications. It is much more efficient to switch a magnet with the spin torque effect that it is to switch it with an electromagnet, at least with the technology we have today.

STT-RAM (spin torque transfer random access memory) is a spin-based all electrical non-volatile memory that has a potential to compete with existing memory technology and is currently being actively researched and even commercialized. The main attraction of a STT-RAM is that it exhibits the characteristics of a “universal memory” with fast read/write performance of SRAM and non-volatility of Flash with excellent write selectivity, scalability, and a relatively simple architecture that can be readily integrated with current CMOS technology. However, one of the main drawbacks of spin torque devices is that it requires a large current bias for switching action to take place. One of the first experimental demonstrations of the spin torque effect required a current of 45 A across a device with a size on the scale of millimeters. With improvements in lithography and ease of fabrication in the nanometer scale, the current requirement has gone down to a few milliamps.

1.2.4 Spin-LEDs and Lasers

Spin-LEDs were first demonstrated in 1999 simultaneously by two groups, Fiederling *et al.* [8] and Ohno *et al.* [9], using spin injection from II-VI magnetic semiconductor BeZnMnSe in an electrically-pumped GaAs/AlGaAs heterostructure under the Faraday (magnetic field out-of-plane to the sample surface) configuration and (Ga,Mn)As for hole spin injection into an InGaAs quantum well (QW) heterostructure from a remanent state (magnetic field in-plane to the sample surface), respectively. Fiederling was able to achieve a spin polarization of 89% and Ohno was able to achieve a spin polarization of ~1%.

The first unambiguous demonstration of quantum well (QW) and quantum dot (QD) spin lasers was made by Holub *et al.* and Basu *et al.* at the University of Michigan in $Al_{0.2}Ga_{0.8}As$ multiple-QWs and InAs QD VCSEL (vertical cavity surface emitting laser) structures [10, 11]. A threshold current reduction of 11% and a degree of circular polarization of 23% at 50 K was reported for the QW spin laser. A threshold current reduction of 14% and a degree of circular polarization of 8% was observed in the QD spin laser at 200 K. More recently, Saha *et al.* from the same group was able to achieve nearly 55% output circular polarization at 230 K in a InAs QD spin laser using pulsed current bias [12].

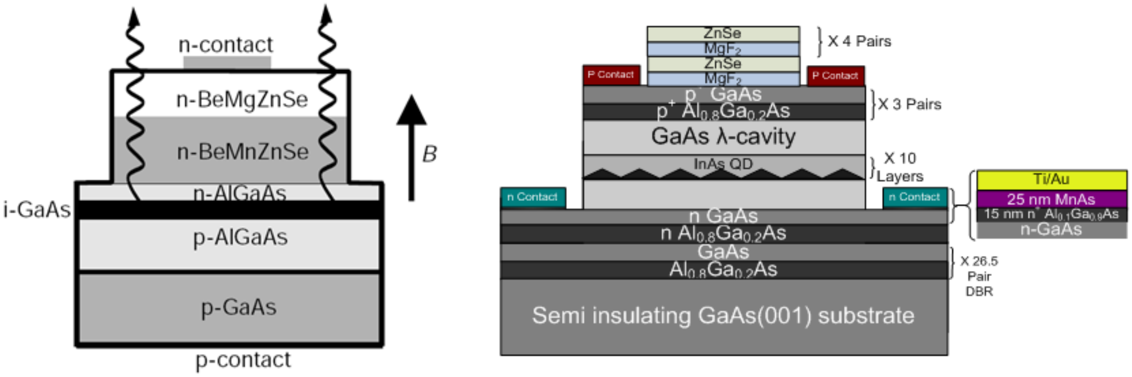

Figure 1.8 Schematic illustration of the heterostructure for a (left) spin-LED and (right) spin-laser. Both devices operate in the Faraday geometry, where the magnetic field is parallel to the direction of photon emission.

Spin-LEDs and lasers are, for the most part, very similar to conventional LEDs or lasers. The only difference is that in spin-based optoelectronic devices, spin-polarized electrons (or holes) are injected into the active region via a ferromagnetic contact. These polarized carriers recombine radiatively with unpolarized holes (or electrons) following the optical selection rule to emit left- or right-circularly polarized light. Due to the direct relation between spin recombination and the output polarization of photons, spin-based optoelectronic devices allow straightforward detection of spin injection efficiency and polarization inside the semiconductor active region.

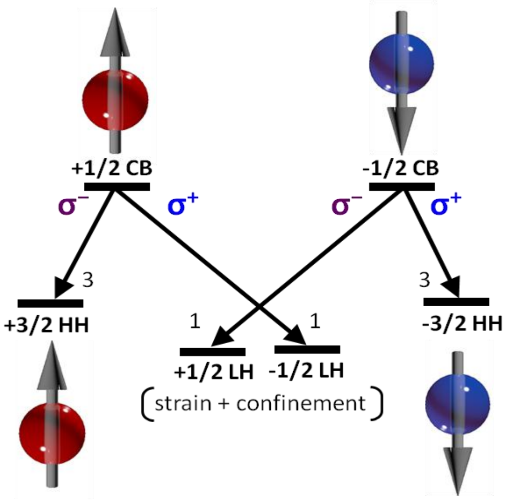

Figure 1.9 Allowed radiative interband transitions and corresponding optical polarization for a quantum well in which epitaxial strain and quantum confinement has lifted the heavy- and light-hole band degeneracy.

In a spin-laser, experimentally demonstrated only in the VCSEL configuration thus far, the spin of recombining e-h (electron-hole) pairs will determine the polarization of the spin-laser emission. It is, in principle, possible to manipulate the spin orientation of the active region carriers without changing the carrier density. Therefore, spin-lasers hold the ability to independently modulate the optical polarization and intensity of their emission. This property can be utilized for applications such as reconfigurable optical interconnects, ultrafast optical switches, chiroptical spectroscopy, cryptography, and telecommunications with enhanced bandwidth.

1.2.5 Semiconductor based lateral spin devices

Lateral spin based devices are generally divided into two categories: a two-terminal spin valve and a three-terminal "spin modulator" (also known as the Datta-Das transistor). Two-terminal spin valves behave similar to GMR or TMR devices, in which

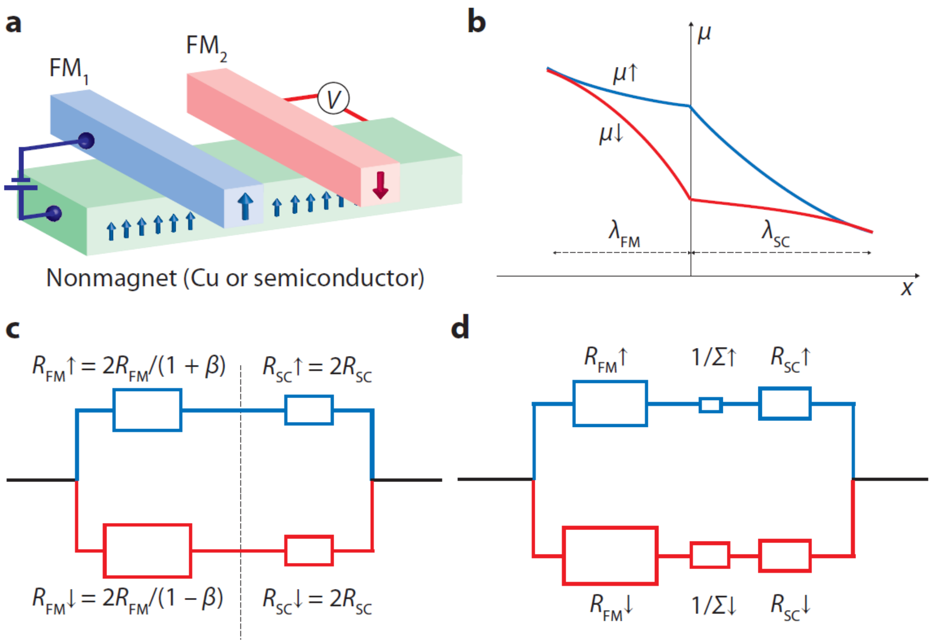

Figure 1.10 (a) Schematic of a simple two-terminal lateral spin valve. FM_1 and FM_2 act as spin injector and detector. (b) Spin splitting at the interface between the FM and SC. (c) Two-channel model without a tunnel barrier between the FM/SC interface. (d) Two-channel mode with a tunnel barrier between the FM/SC interface (adapted from [3]).

---

the resistance between the two ferromagnetic contacts becomes high when the two FMs are aligned in the antiparallel configuration and low when the two FMs are in parallel configuration. Although experimentally observing this spin-dependent resistance switching is relatively easy in all metal-based spin valves, observing such response is not trivial in semiconductor-based materials due to the conductivity mismatch between the metallic ferromagnet and the semiconductor. The conductivity mismatch problem has prevented experimental observation of spin injection into semiconductors for over a decade since the inception of the idea of utilizing spin for practical device applications.

There are several ways to circumvent this issue. The first method, proposed by Rashba [25], is to insert a thin spin-dependent tunnel barrier between the ferromagnet and the semiconductor (or a Schottky barrier). The second method is to use a dilute magnetic semiconductor (DMS) ferromagnet, which has a similar order of conductivity to most semiconductors, for spin injection. Both methods have been employed with great success to achieve spin injection into semiconductors at high temperatures.

1.2.5.1 Spin valves

The injection of spin polarized carriers from a ferromagnet into a non-magnetic medium was first proposed by Aronov [13] and experimentally demonstrated by Johnson and Silsbee [14] in a metallic channel. It was not until 2005 that the first semiconductor based spin valves were experimentally demonstrated [15, 16] in a GaAs channel device.

In this thesis, two types of semiconductor spin valves are addressed. One is in the lateral geometry, where the spin injection and transport directions are orthogonal to each other. Another type is in the vertical geometry, where the spin injection and transport directions are parallel to each other.

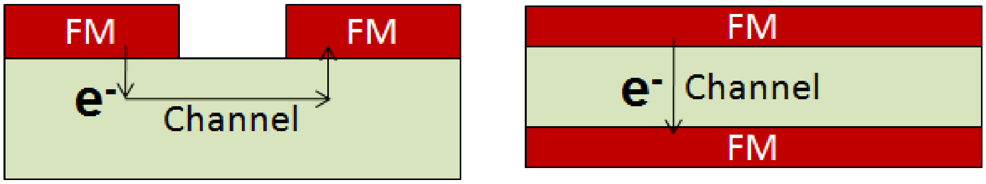

Figure 1.11 Schematic illustration of a (left) lateral spin valve and (right) vertical spin valve geometry.

A spin valve can be thought of as a diode-like device, where the resistance is high when the two ferromagnets are in antiparallel configuration, and the resistance is low when the two ferromagnetic are in parallel configuration. The lateral spin valve (LSV) is based on planar technologies commonly used for conventional microelectronics; therefore, it can be easily integrated without a drastic change in processing methods. LSVs ultimately have the objective of demonstrating all-electrical spin injection and detection, with the possibility of implementing a third gate electrode for electrical spin manipulation purposes. The physics behind the operating principle of a semiconductor spin valve can be best explained by invoking the density of states (DOS) of ferromagnetic semiconductors (refer to Fig. 1.6). However, instead of a reduced tunneling probability from the injecting ferromagnet to the detector, the spin polarized carriers get accumulated in the semiconducting channel as there are no available states for the minority carriers in the detecting ferromagnet.

A vertical spin valve (VSV) has similar properties of a LSV, but show much higher magnetoresistance response due to the fact that the channel length can be precisely controlled and can be made extremely thin using epitaxial growth techniques, thereby allowing more spin-polarized electrons get detected before the spin dephases. However, manipulating spin in this vertical geometry is more difficult to achieve, as it is a non-trivial task to fabricate an all-around gate electrode around the thin channel layer. A more detailed discussion will be given in the relevant chapters.

1.2.5.2 Spin FETs

Spin-based logic devices (spin transistors) are generally viewed as impractical due to its super low operating temperature and response. Several spin-based logic devices have been proposed, with the electronic analogue of the electro-optic modulator, also known as the Datta-Das transistor [17], being the most recognized and sought after. However, a rather convincing experimental realization of the device pointed towards the non-practicality of the concept. Regardless, it provides a benchmark and platform for future spin-based logic devices to improve upon, and verification of the feasibility of the idea of systematically controlling an ensemble of spin using spin-orbit coupling effects.

Spin-transistors are classified as (by ITRS) “Non-Conventional Charge-based Extended CMOS Devices”. In other words, they exhibit transistor-like behavior with the functionalities of a spintronic device. The defining features of spin-based logic devices are variable current or voltage drivability controlled by the magnetization configuration of the ferromagnetic contacts with respect to the spin orientation of the majority carriers and non-volatile information storage using the magnetoresistance and spin torque effects. These features are inaccessible to conventional CMOS circuits and are very desirable functionalities for energy efficient, high-performance circuit architectures.

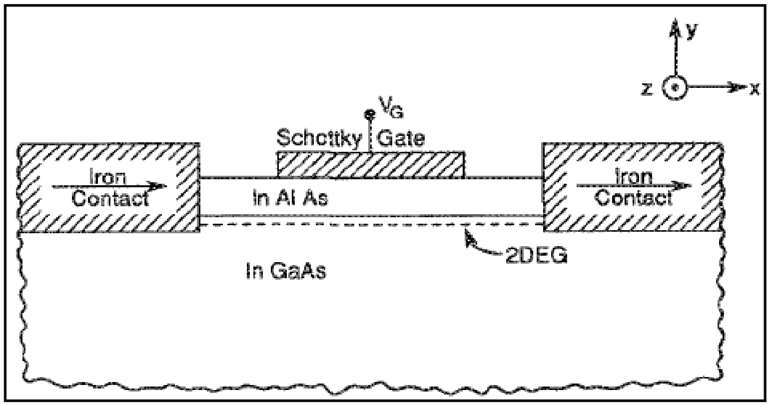

Figure 1.12 Schematic of the original spintronic analog of the electro-optic modulator (“Datta-Das transistor”) proposed by Datta and Das in 1990. [17]

The original idea behind a spin-FET was to utilize the Rashba spin-orbit coupling (SOC) effects to precess the spin of electrons in the channel, thereby eliminating the need of an externally applied magnetic field to switch the magnetization of the ferromagnetic contacts (proposed by Datta and Das in 1990). Recently, experimental demonstration of Datta–Das spin-FET was reported by Koo *et al.* [18] and Kum *et al.* [19] in an InAs 2DEG (2-dimensional electron gas) channel in the non-local and local configurations, respectively. Oscillatory spin signals, in the form of voltage, controlled by a gate bias were observed at low temperatures (~77 K). The oscillatory output behavior implies spin precession of spin-polarized carriers in the channel. However, the origin of the observed spin signals is still controversial [20].

Another potential spin-logic device is the magnetic bipolar transistor (MBT) proposed by Fabian and Zutic [21]. This type of device is a conventional bipolar junction transistor with added spin and offers the possibility of controlling current amplification by spin. To maximize the gain in a conventional BJT, one needs to minimize the relative contribution of holes in the emitter current or inhibit the e-h (electron-hole) recombination in the base region. MBTs allow spin control of the gain by realizing this condition [22].

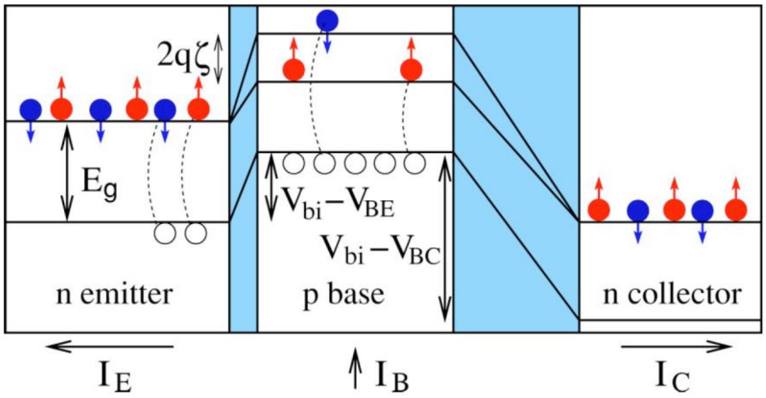

Figure 1.13 Schematics of the (band energy diagram) magnetic *npn* transistor in the amplification mode. The *b-e* junction is forward biased with $V_{be} > 0$, lowering the barrier and reducing the depletion layer width. The *b-c* junction is reverse biased with $V_{bc} < 0$, raising the barrier and increasing the depletion layer width. The current amplification $\beta = I_C/I_B$ can be controlled by the spin polarization in the base as well as by the nonequilibrium spin in the emitter. [21]

Other exotic methods for realizing spin-MOSFETS have been proposed, such as a pseudo-spin-MOSFET. It is a circuit for replicating the functions of spin-MOSFETs using an ordinary MOSFET and a MTJ that is connected to the MOSFET with a negative feedback configuration. It is predicated that the pseudo-spin-MOSFET can accurately reproduce the spin-transistor behaviors such as variable current drivability. No experimental demonstration of such a circuit has been report yet.

1.3 Thesis Outline

The central theme of this thesis is about spin injection, transport and detection in III-V semiconductor materials, with a secondary focus on manipulation of magnetoresistance via an externally applied voltage in the absence of magnetic field. Several III-V materials were investigated, including GaAs, InP, and GaN. Efforts on realizing high-temperature spintronic devices with magnetoresistance control and amplification functionalities are described.

In chapter 2, an in-depth overview of the spin injection, detection, and manipulation mechanism is discussed. Measuring the spin response is a non-trivial task, and one must be extremely careful to rule out spurious effects and charge effects to claim that the observed magnetoresistance response is due to spin injection into the channel only. Therefore, careful control measurements and experimental setup is needed to prove that the observed effect is truly due to spin accumulation and transport.

In chapter 3, an overview of the epitaxial growth of MnAs ferromagnet films is described, along with morphology and hysteresis characterization data. MnAs is a rather robust ferromagnet that can be epitaxially grown with clean interfaces on GaAs, InP, and even GaN. It is possible to grow device quality GaAs on top of MnAs, leading to the realization of a fully epitaxial vertical spin valve. MnAs is also attractive due to its high Curie temperature (~315 K) and magnetization (50%). One drawback is that it reacts to most solvents, bases, acids, and even DI-water.

In chapter 4, spin injection, transport, and control/amplification of magnetoresistance in GaAs based lateral and vertical spin valves are discussed. Characterization of spin transport properties of high-temperature, sub-micron channel spin valves fabricated using the focus-ion-beam (FIB) technique is presented. A two-terminal vertical spin valve and a three-terminal spin amplifier based on MnAs/GaAs/MnAs heterostructure is realized and characterized. The temperature dependent magnetoresistance response is analyzed by considering spin-wave excitation, spin independent tunneling, and spin relaxation in the degenerately doped GaAs channel. A prototype memory cell is achieved using the three-terminal vertical spin amplifier. The topic of confined geometry effect on spin relaxation is lightly touched upon.

In chapter 5, spin precession experiments using the Rashba spin-orbit coupling effect in an InAs 2-dimensional electron gas channel grown on top of an InP substrate is discussed. An in-depth review of the various spin-orbit coupling effects present in III-V zincblende materials is given as well.

In chapter 6, spin injection, transport, and precession measurements in molecular beam epitaxy (MBE) grown defect-free GaN nanowire is presented. Careful material characterizations using transmission electron microscopy (TEM) and diffraction patterns indicate that defects commonly associated with GaN grown on mismatched substrates, such as dislocations, stacking faults, and twins. Four-terminal non-local and hanle effect measurements verify spin injection into the nanowire without doubt.

Finally, chapter 7 provides a summary of this thesis and suggestions for potential future work.

Chapter II

Electrically Injected Spin-Polarized Devices: Relaxation Mechanisms, Materials, Measurement Techniques, and Characterization

2.1 Introduction

The magnetoresistance response of electrical spintronic devices is directly proportional to the amount of spin polarized electrons reaching the detecting electrode. This, in turn, is directly related to the spin relaxation mechanism present in various semiconducting materials. It is crucial to understand which spin relaxation mechanism is dominant for each system to engineer devices with sufficiently large spin-dependent output signal. The ability for a nonequilibrium spin current to survive a relatively long distance within a semiconducting material (compared to metals) enables spintronics to be a viable technology to extend today's microelectronic and optoelectronic devices. Semiconductor materials in particular have gathered much interest as a promising spintronic platform for several reasons. First, the spin lifetime inside a semiconductor is much longer than in a metal. Second, a third gate electrode can easily adjust the potential variation in the semiconductor, allowing electrical control of spin. Third, versatility in doping and device structure allows monolithic integration of semiconductor-based spin devices with conventional charge-based CMOS devices.

Spin-based phenomena must be measured carefully to ensure spurious effects are eliminated. These spurious effects tend to resemble the true spin signal and must be filtered out before claiming that the observed response is truly due to spin injection and detection in the channel. These issues pertain only to electrical measurements. Opto-electrical measurement techniques such as time-resolved Faraday/Kerr rotation and measurement of output circularly-polarized photons from spin-LEDs can provide a more accurate material properties related to spin. However, an all-electrical measurement technique may be more appropriate and establish a better platform to work on for practical electrical spintronic devices.

In this chapter, a description of highly relevant spin relaxation mechanisms will be discussed, along with several important semiconducting materials. Then, several electrical spin measurement techniques will be described. These measurement techniques have become a standard for experimentalists working in the field of spintronics as a way to conclusively verify spin injection into the channel.

2.2 Spin Relaxation Mechanisms

Spin polarized carriers do not retain their initial spin once injected into a semiconductor material. After a certain amount of time, known as the spin lifetime (τ_{sf}), the spin flips and we can no longer claim to know the polarization of the carriers, inevitably leading to spin equilibrium in the system. From Einstein's relation, one can derive the spin diffusion length as:

$$\lambda_{sf}^{N} = \sqrt{\frac{k_B T \tau_{sf}}{2nq^2 \rho_N}} \qquad \textbf{(2.1)}$$

where k_B is boltzmann's constant, T is temperature, τ_{sf} is spin lifetime, n is the doping of the semiconductor, q is electric charge, and ρ_N is the conductivity of the semiconductor. The factor of 2 comes in the dominator due to the fact that we consider spin-up and spin-down electrons separately [23]. The spin lifetime and diffusion length is viewed as a figure of merit, gauging the potential of a material for spintronics applications. The spin lifetime can range from pico-seconds to nano-seconds, depending on the semiconducting material and temperature. There are four main spin relaxation mechanisms that are relevant for spins injected into semiconducting materials. In this context, it is only relevant to discuss the dephasing of spin polarized *electrons*, since holes dephase much quicker (due to the intermixing of the heavy hole and light hole states in the valence band) and are rarely studied, nor useful.

The relative strength of each spin relaxation mechanism can differ from semiconductor to semiconductor and may also change depending on temperature. It may also depend on the quality of the material or the doping level. Therefore, it is critical that the dominant spin relaxation mechanism be known before designing spintronic devices. There is a distinct difference in the spin relaxation mechanism between metallic and insulating materials. In the metallic case, electrons are itinerant as they mostly populate the conduction band, leading to *conduction spin relaxation mechanisms* to be dominant. These mechanisms are dominant in heavily doped materials or at high temperatures. For materials in the insulating regime, electrons are localized mostly near their donor sites. For such a system, *localized spin relaxation mechanisms* become more important. These mechanisms are mostly present in low doped materials or at low temperatures. This thesis is mostly concerned about conduction spin relaxation mechanisms. The physical origin of each relaxation mechanism is described in the following sections.

2.2.1 Elliot-Yafet spin relaxation

The Elliot-Yafet (EY) spin relaxation is one of the conduction spin relaxation mechanisms, where the electron spin relaxes via ordinary momentum scattering to phonons or impurities in lattice ions that induce spin-orbit coupling in the electron wave function. The spin-orbit potential is given as

$$V_{SO} = \frac{\hbar}{4m^2c^2} \nabla V_{SC} \times \hat{p} \cdot \hat{\sigma} \tag{2.2}$$

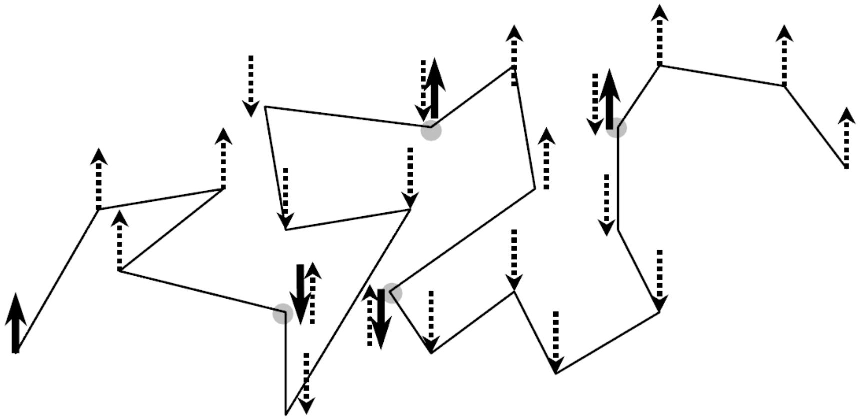

Figure 2.1 Illustration of the Elliot-Yafet spin relaxation mechanism. The spin lifetime is directly proportional to the frequency of momentum scattering rate.

---

where V_{sc} is the scalar (spin independent) periodic lattice potential, m is the free-electron mass, $\hat{p} \equiv -i\hbar\nabla$ is the linear momentum operator, $\hat{\sigma}$ are the Pauli matrices (a mixture of Pauli spin-up and spin-down states), and c is the speed of light. The spin-flip scattering due to the spin-orbit potential causes spin relaxation of conduction electrons. The spin-orbit coupling itself does not cause spin relaxation. It is with the combination of momentum scattering that the spin-up and spin-down states couple and lead to spin relaxation. It is worth noting that the spin-orbit strength increases as the impurity mass increases; the spin orbit strength increases as Z^2, where Z is the atomic number of the impurity. Momentum scattering is typically caused by phonons at high temperatures and impurities at low temperatures. Another possible spin flip mechanism involves phonons in a periodic lattice. The lattice-ion-induced spin-orbit interaction is modified by phonons and can directly couple the Pauli spin-up and spin-down states, leading to spin relaxation. This process is also directly related to the mass of the host ions (same Z^2 dependence). Therefore, Si, with a lower Z, has less SOC than, say, germanium who's Z is higher and thus have larger SOC. A schematic illustration of this mechanism is shown in Fig. 2.1 [24].

The EY mechanism is present in almost all semiconductors, whether they have center inversion symmetry or not. However, it is most prominent in centrosymmetric semiconductors such as Si and Ge. The EY spin relaxation rate for electrons with energy E_k is directly proportional to the electron momentum scattering rate:

$$\frac{1}{\tau_s^{EY}}(E) = A\left(\frac{E_k}{E_g}\right)^2\left(\frac{\Delta_{SO}}{E_g+\Delta_{SO}}\right)^2\frac{1}{\tau_p(E)} \qquad \textbf{(2.3)}$$

where A is a dimensionless constant, Δ is the spin-orbit splitting of the valence band, E_g is the bandgap of the semiconductor, and τ_p is the electron momentum scattering rate. Therefore, one can conclude that the EY mechanism is dominant in small bandgap semiconductors with large electron momentum scattering rate.

2.2.2 D'yakonov-Perel' spin relaxation

The D'yakonov-Perel' spin relaxation mechanism can be qualitatively thought of as the opposite of EY relaxation mechanism. It is dominant in semiconductors lacking center of symmetry (*e.g.* zincblende structures) such as GaAs and GaN. Unlike the EY mechanism where spin relaxes during momentum scattering events, DP mechanism causes spin to relax *between* momentum scattering events. An illustration of this mechanism is shown below in Fig. 2.2.

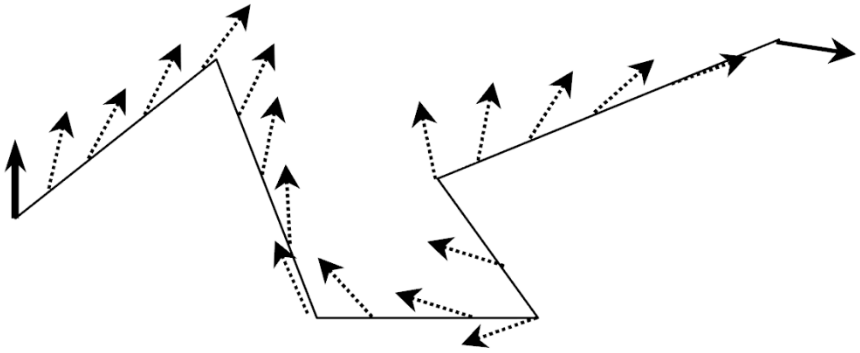

Figure 2.2 Illustration of the D'yakonov-Perel' spin relaxation mechanism. The spin precesses due to the presence of a crystal field, which manifests as an effective magnetic field for the conduction electrons. The spin relxation rate is inversely proportional to the momentum scattering rate.

The DP mechanism can be explained from the point of view of individual spin-polarized electrons precessing around a fluctuating magnetic field induced by the structural inversion asymmetry (SIA). As the electrons are moving in a "random-walk" fashion, the spin rotates about the intrinsic magnetic field at a particular angle. A change in momentum of the spin-polarized electron changes the direction and magnitude of the effective magnetic field, leading to a change in precession angle. Therefore, the faster the momentum relaxation, the slower the spin dephasing since the electron barely gets time to precess enough to cause a "flip" in its spin state. The DP relaxation rate can be expressed as:

$$\frac{1}{\tau_s^{DP}}(E) = Q\alpha^2\left(\frac{E_k^3}{\hbar^2 E_g}\right)\tau_p(E) \quad \textbf{(2.4)}$$

where Q (in the order of 1) and α^2 (dimensionless) are constants related to the strength of the SOC effect. From eq. 2.4, we can conclude that the DP mechanism becomes more important for large bandgap semiconductors and at higher temperatures.

It is important to note and point out that the major difference between EY and DP mechanism is their dependence on the electron momentum scattering rate τ_p. A faster momentum scattering rate increases the effectiveness of EY relaxation mechanism while suppressing the DP mechanism. Even within the same system, knowing the dependence of τ_p to the spin relaxation rate can be helpful in engineering spin-devices with higher performance. For example, quantum confinement generally leads to a decrease in momentum scattering rate compared to bulk, which indicate that the DP relaxation can be more severe in structures with a quantum well active region. And since DP relaxation is also more dominant at high temperatures, it is advantageous to use bulk active regions with structural inversion asymmetry if one is to design a high-temperature spintronic device with long spin lifetimes. This effect is also observed experimentally and presented in chapter 6 of this thesis. Since the DP mechanism is originated from inversion asymmetry of the material structure, this discussion does not apply to diamond structured semiconductors such as Si or Ge.

2.2.3 Bir-Aronov-Pikus spin relaxation

The Bir-Aronov-Pikus (BAP) spin relaxation mechanism is present in materials with high concentration of holes. It is caused by the electron-hole exchange interaction in systems with high overlap between electron and hole wavefunctions. The exchange interaction between electrons and holes is dictated by the Hamiltonian given by

$$H = A\vec{S} \cdot \vec{J}\delta(\vec{r}) \qquad \textbf{(2.5)}$$

where A is proportional to the exchange integral between the conduction and valence states, $\boldsymbol{J}$ is the angular momentum operator for holes, $\boldsymbol{S}$ is the electron-spin operator, and $\boldsymbol{r}$ is the relative position of electron and holes.

The spin scattering rate due to the BAP mechanism ($1/\tau_s^{BAP}$) is proportional to N_a (hole doping concentration) for nondegenerate holes, proportional to $N_a^{1/3}$ for degenerate holes, and weakly dependent in between. The BAP, DP, and EY mechanism all coexist in a heavily p-doped material lacking inversion symmetry. Fortunately, the relative contribution of each mechanism can be distinguished by their unique density and temperature dependences. BAP is most likely dominating in heavily p-doped materials at low temperatures, whereas the DP mechanism becomes more important at high temperatures, regardless of the doping level due to its increased importance for large electron energies.

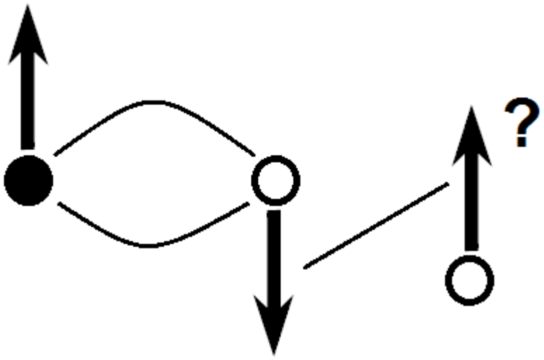

Figure 2.3 Illustration of the Bir-Aronov-Pikus spin relaxation mechanism. The electrons exchange spins with holes (circles), which then lose its spin very fast due to the Elliot-Yafet spin relaxation mechanism.

2.2.4 Hyperfine interactions

Hyperfine magnetic interactions between the magnetic moments of the electrons and the nuclei can become an important mechanism ensemble spin dephasing and single-spin decoherence of localized electrons in confined structures, such as quantum dots

(QDs) or donor bound electrons. In these confined systems, the electron wave function is spread over a region containing many nuclear spins, causing spin dephasing. However, this effect is rather weak to be an effective way of relaxing the spin of free electrons in metals or bulk semiconductors, and is generally never the dominating spin relaxation mechanism.

2.3 Conductivity mismatch problem

The conductivity mismatch problem was one of the major difficulties to overcome to achieve experimental demonstration of spin injection into a semiconductor from a ferromagnetic metal. A general equation to represent the polarization in the semiconductor near the ferromagnet/semiconductor (FM/SC) interface is given as

$$P_{SC} = P\left(\frac{R_{FM}}{R_{SC}}\right)\left(\frac{2}{2(R_{FM}/R_{SC})+(1-P^2)}\right) \tag{2.5}$$

where P and R_{FM} is the polarization and resistivity of the ferromagnet, respectively, and R_{SC} is the resistivity of the semiconductor. One can immediately notice that the factor (R_{FM} / R_{SC}) is extremely small for typical values of metal and semiconductor resistivities ($\sim 10^{-4}$), and therefore, the spin polarization in the semiconductor is nearly non-existent. A solution to overcome this problem was proposed by Rashba [25]. The proposed method involves inserting a tunnel barrier (either a physical oxide barrier or a Schottky barrier) between the semiconductor and ferromagnet.

The influence of inserting a tunnel barrier can be described as follows. In the case of no interface resistance, the Fermi energy splitting due to spin accumulation, $\Delta\mu = \mu_{\uparrow} - \mu_{\downarrow}$, is identical on both sides of the interface and decreases exponentially with decay lengths equal to the respective spin diffusion lengths in the ferromagnet and semiconductor. The variations in the spin flips in the ferromagnet and the semiconductor are proportional to $1/r_F$ and $1/r_N$, where r_F and r_N are the resistivity of the ferromagnet and semiconductor, respectively. This relation can be obtained by integrating the current polarization equation

$$\frac{\partial(J_+ - J_-)}{\partial z} = \frac{2eN(E_F)\Delta\mu}{\tau_{sf}} \qquad \textbf{(2.6)}$$

and integrating with $\Delta\mu = \Delta\mu_I \exp(z/\lambda_{sf})$ in the semiconductor and ferromagnetic regions with their respective spin diffusion length, λ_{sf}. This means that for $r_F << r_N$, much more spin-flips and depolarization is occurring in the ferromagnet and the current is completely depolarized when it crosses the FM/SC interface. An interface resistance introduces a spin dependent discontinuity of $\Delta\mu$ in the semiconductor, leading to a balanced number of spin flips in the semiconductor and ferromagnet and restoring the spin polarization at the interface and in the semiconductor. So far, oxide based barriers such as Al_2O_3, MgO, and SiO_2 have all been successfully used as tunnel barriers for spin injection, as well as graded doped Schottky-type barrier contacts.

2.4 Overview of Semiconductor Material Structures

Most semiconductor materials that are used in CMOS technology have been investigated to see their applicability towards spintronic devices. In this section, some of these materials will be identified along with their spintronic properties. Although, generally, the material with highest spin diffusion length (or spin lifetime) at higher temperature is desired, some materials have unique properties (such as stronger spin-orbit coupling or easier integration with conventional CMOS technology) that makes it more desirable for certain spin applications.

The most fundamental property that affects the spin relaxation mechanisms of electrons in a certain material is its crystallographic structure. The common structures that are investigated in this thesis are (i) diamond, (ii) zincblende, and (iii) wurtzite hexagonal. Silicon and Germanium are examples of diamond structured materials, GaAs and InP are examples of zincblende type semiconductors, and wurtzite-GaN is an example of a hexagonal structure. More recently, exotic materials such as single-/bi-layer graphene (honeycomb structure) have become a popular venue for spin injection experiments.

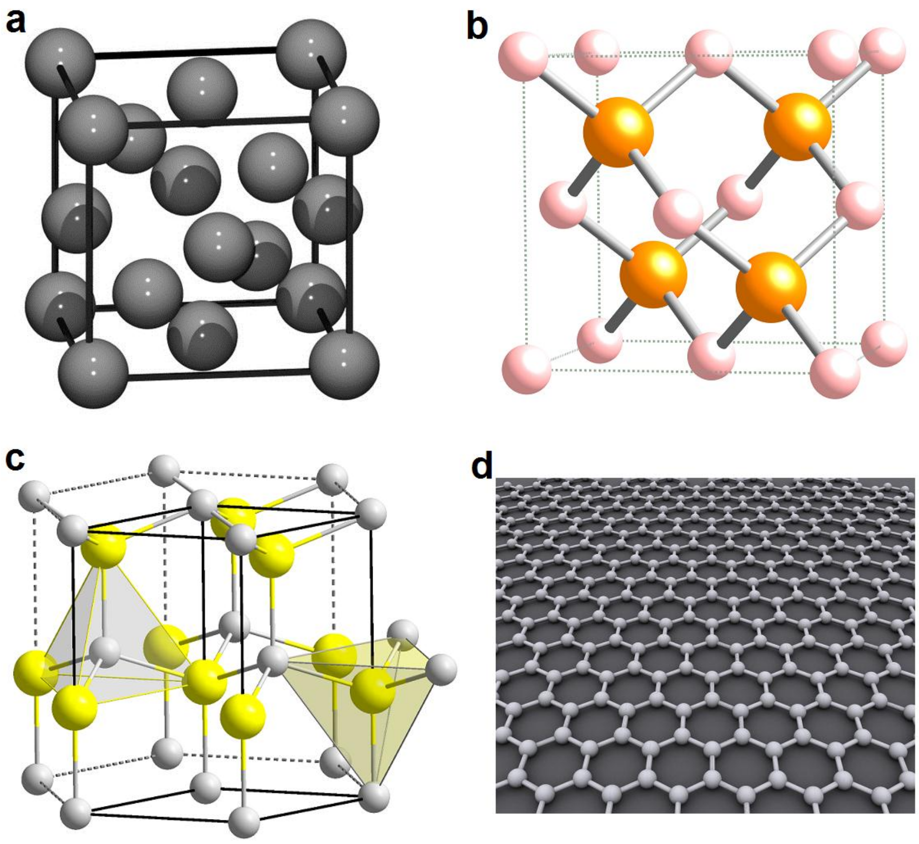

Figure 2.4 Illustration of various semiconductor crystal structures. (a) Diamond (i.e. Si, Ge), (b) zincblende (i.e. GaN, InP), (c) wurtzite hexagonal (i.e. w-GaN), and (d) honeycomb (i.e. single layer graphene) structure. [43]

2.4.1 Silicon (Si)

Silicon is without doubt one of the most important materials in today's semiconductor technology and this era of information technology. It is also one of the more promising materials for two-terminal spintronic applications due to its extremely long spin relaxation time and diffusion length. Because of its diamond crystalline structure, the DP relaxation mechanism is completely absent. However, because of the weak structural inversion asymmetry, it is a difficult material to electrically modulate the spin using spin-orbit coupling effects. Several novel methods [26] have been proposed and experimentally demonstrated, but the overall magnitude of the spin-dependent response is lackluster and nowhere near the level it needs to be for it to become a practical, commercialized device.

Silicon has been subject nearly all electrical and optical spin measurement techniques. It holds one of the longest spin lifetime compared to any other spin material investigated below, with single layer graphene being a close second. At room temperature, a spin lifetime of nearly 1 ns has been reported by Suzuki *et al.*, and nearly 10 ns at 8 K using four-terminal non-local spin valve measurements. Jonker and Jansen *et al.* [27, 28] reported much shorter spin lifetime values (~150 ps at RT) using the three-terminal hanle technique, but argue that the discrepancy is in the way three-terminal Hanle measurements are done, which is shown to give a lower bound of the spin lifetime.

2.4.2 Germanium (Ge)

Germanium has the same crystalline structure as silicon and also shows long spin lifetimes at low temperatures. At the time of writing, crude three-terminal Hanle measurements and two-terminal spin valve measurements have been made at low temperatures to derive the spin lifetime in this material. The most recent report [29] indicates a spin lifetime of ~100 μs at 8 K in a high quality Ge nanowire, but results of high temperature measurements have yet to be published. A conference abstract (APS March Meeting 2012) [30] indicates a room temperature spin lifetime in n-type bulk germanium to vary from 50-123 ps as a function of doping density.

2.4.3 Gallium Arsenide (GaAs)

Gallium arsenide is one of the first semiconductor materials to be subject to spin injection experiments, as well as the first material to conclusively demonstrate that spin injection from a ferromagnetic metal into a semiconductor is indeed possible. The first spin injection into GaAs was experimentally demonstrated by Saha *et al.* [15] in 2006 by two- and four-terminal spin valve measurements, and another experimental result was reported by Lou *et al.* [16] in 2007 with additional Hanle precession measurements.

Due to the presence of both EY and DP spin relaxation mechanism, as well as BAP if p-doped, GaAs has a relatively short spin diffusion length, typically in the range of 10 μm at 10 K and a few nanometers at room temperature. Nevertheless, large magnetoresistance response at room temperature was observed in spin valves in the vertical geometry [31], reiterating the fact that long spin lifetime and diffusion lengths alone are not the sole requirement for practical room temperature spintronic applications.

2.4.4 Indium Phosphide (InP)

Indium phosphide material itself has never been studied extensively in the spintronics community. InP in itself does not have any unique properties that may differentiate this material over other semiconductors. However, the InAs 2-dimensional electron gas (2DEG) that can be epitaxially grown on InP has gathered interest due to its ability to systematically precess an ensemble of spin using Rashba spin-orbit coupling effects. In fact, the first Datta-Das transistor was demonstrated on an InP-based substrate by Koo *et al.* [18] and Kum *et al.* [19] in an InAs 2DEG channel device.

The spin lifetime in an InAs 2DEG channel was found to *increase* with increasing temperature, ranging from 5 ps at 20 K up to 10 ps at 300 K [18]. The momentum scattering time was found to monotonically decrease with increase in temperature, from 0.4 ps at 20 K to 0.1 ps at room temperature. This result is consistent with predictions of the DP relaxation mechanism, and indicates that the EY mechanism is relatively absent in confined 2-dimensional systems. InAs 2DEG channel is, to date, the most promising structures for spin modulation (via electrical bias) applications.

2.4.5 Gallium Nitride

Wide bandgap semiconductor gallium nitride has several advantages over other semiconducting materials that make it a top choice for spintronics. GaN has numerous existing applications in various technology categories, such as optoelectronics, telecommunications, power electronics, and spintronics. It has also been used recently to demonstrate strong coupling and polariton lasing for ultralow threshold lasers [32]. Moreover, GaN doped with Mn (called dilute magnetic semiconductor (DMS)) have shown ferromagnetic behavior beyond room temperature, which can be used to inject spin at high temperatures without the conductivity mismatch problem discussed earlier.

Because of its wide bandgap, GaN has a weak spin-orbit coupling and is mainly dominated by the DP relaxation mechanisms for a wide range of temperatures. Time resolved Faraday and Kerr rotation measurements done by Beschoten *et al.* [33] and Buss *et al.* [34] extracted spin lifetimes of approximately 35-100 ps at room temperature in bulk GaN. However, the measurements were done on epitaxially grown GaN on mismatched substrates, leading to a material with large defect densities (10^8-10^{10} cm^{-2}). In this thesis, the spin lifetime in nearly defect-free GaN nanowire grown on (001) Si is extracted. The spin lifetime is ~150 ps at 300 K and increases non-linearly with decrease in temperature. Early measurements and theoretical analysis indicated that the EY mechanism is entirely absent in GaN materials. To what extent and at what temperature range is still not clear.

2.4.6 Graphene

Graphene is an exotic half-metal or zero-gap wonder material (a single atomic layer of carbon atoms) that has been subject to spin injection experiments only recently. Because of its unique structure and small bandgap, spin-orbit coupling effects are extremely small and most recent reports [35] have placed graphene on par with silicon as a material with one of the highest spin lifetimes of nearly 1.34 ns at 300 K. Reports indicate that spin relaxation in single layer graphene (SLG) is dominated by the EY relaxation mechanism at low temperatures, leading to a linear scaling of the spin lifetime and momentum scattering time. In contrast, bilayer graphene showed the opposite trend, indicating the dominance of DP spin relaxation at low temperatures [36]. Much like its wonderful electrostatic properties, its excellent spin properties make it one of the most important materials for spintronics next to Si and GaN.

2.5 Electrical Spin Injection and Transport Measurements

As mentioned in the introduction of this chapter, care must be taken to measure spin transport phenomena. Magnetoresistance is manifested as a change in the resistance (or voltage) across two terminals at a certain magnetic field range (antiparallel magnetization of the two ferromagnetic electrodes). Unfortunately, this change in voltage as a function of magnetic field can be also a manifestation of several other phenomena, such as Anomalous Hall and anisotropic magnetoresistance (AMR) effects. Several "non-local" measurement setup have been developed to circumvent this problem.

2.5.1 Two-terminal *local* spinvalve

The two-terminal local spin valve is analogous to the metal based spin valves, where spin polarized carriers are injected into a non-magnetic semiconductor from a ferromagnet and detected by a second ferromagnet that is placed within the spin diffusion length associated with the semiconductor material. A typical two-terminal transport measurement setup is shown in Fig. 2.5. Although this measurement outputs the largest change in resistance (e.g. voltage) and is the simplest to set up, it is also highly susceptible to spurious effects, and is no longer accepted as a sole proof of spin injection in the lateral configuration.

Nevertheless, with channel length dependent magnetoresistance data, it is possible to estimate the transverse spin relaxation time using these equations derived by Fert and Jaffres:

$$\Delta R = \frac{2(\beta r_F + \gamma r_b^*)^2}{(r_b^* + r_F) + \frac{r_N}{2}\left[1 + \left(\frac{r_b^*}{r_N}\right)^2\right]\frac{l_N}{\lambda_{sf}^N}} \qquad \textbf{(2.7)}$$

$$R_P = 2(1-\beta^2)r_F + r_N\frac{l_N}{\lambda_{SF}^N} + 2(1-\gamma^2)r_b^* + 2\frac{(\beta-\gamma^2)r_F r_b^* + r_N(\beta^2 r_F + \gamma^2 r_b^*)\tanh\left(\frac{l_N}{2\lambda_{sf}^N}\right)}{(r_F + r_b^*) + r_N\tanh\left(\frac{l_N}{2\lambda_{sf}^N}\right)} \qquad \textbf{(2.8)}$$

where the magnetoresistance is defined as $\Delta R/R_p$. Here, β and γ are the bulk spin polarization and a spin-dependent tunneling parameter, respectively. l_N is the NW channel length, r_F and r_N are the resistivity of the ferromagnet and NW multiplied by λ_{sf}, respectively, and r_b* is the interface resistance of the tunnel barrier contact. Coupled with four-terminal non-local measurements, which can provide conclusive evidence of spin injection, two-terminal measurements can still provide the maximum magnitude of spin response one can expect from a particular material system.

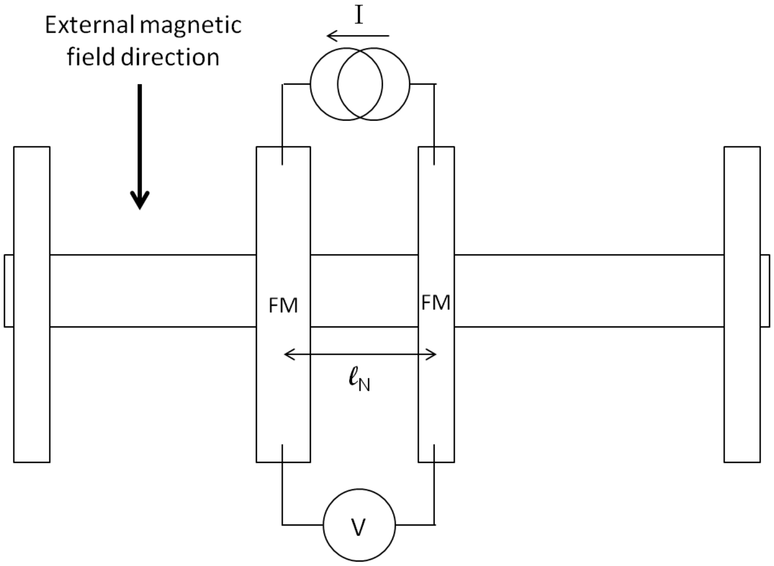

Figure 2.5 Two-terminal "local" measurement scheme on a four-terminal lateral spin valve. Here, l_N is the channel length (center-to-center distance between the two ferromagnets (FM). For a constant current bias across the two FM electrodes, the voltage change is measured as an external magnetic field is swept across the device. The outer two electrodes can either be a FM or non-magnetic ohmic contact.

2.5.2 Four-terminal *non-local* spinvalve

The four-terminal "non-local" spin valve measurement setup separates the charge current path and the pure spin diffusion path, eliminating most of the spurious effects mentioned previously. It consists of two laterally separated ferromagnetic contacts placed on the semiconducting channel, and two outer reference ohmic contacts (either

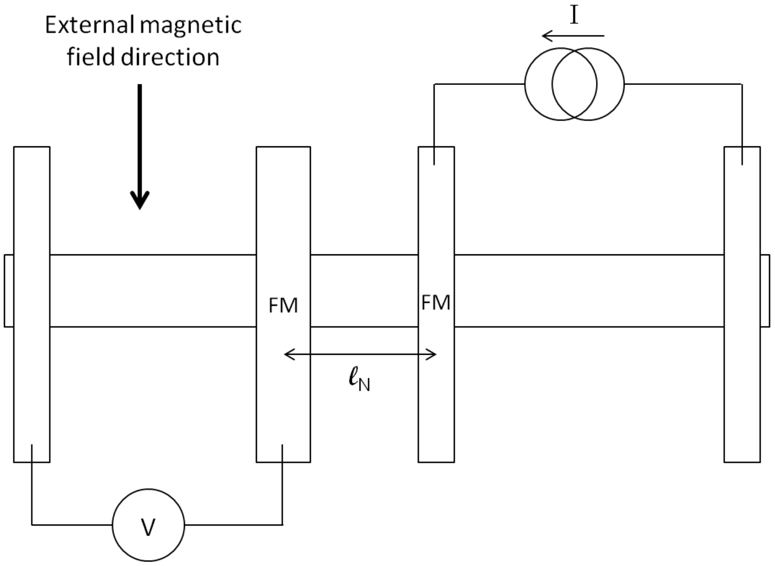

Figure 2.5 Illustration of a four-terminal "non-local" measurement scheme. Current is passed through the outer region of the channel, while a nearby ferromagnetic detector detects the diffused spin accumulation outside of the charge current path.

---

ferromagnetic or non-magnetic). The injection current flows from one of the ferromagnets to its closest outermost reference contact. Thus, a non-equilibrium spin accumulation is induced in the semiconducting channel. The spin accumulation from the injecting FM contact diffuses away from the injection point and relaxes with a characteristics length known as the spin diffusion length. If an adjacent detector ferromagnet is within the spin diffusion length, it will detect the diffused spin electrons outside of the electric current path. The voltage contrast when the injector and detector are in parallel and anti-parallel configuration can be described to be

$$\Delta R = \frac{\Delta V}{I} = \frac{P_1 P_2 \lambda_s \rho}{A} \exp(-L/\lambda_s) \tag{2.9}$$

where P_1 and P_2 are the spin polarization of the current across the interfaces of the injecting ferromagnet/semiconductor and semiconductor/detecting ferromagnet, respectively, I is the electron injection current, ρ is the resistivity of the semiconductor, A

is the cross junction area of the semiconductor, and *L* is the lateral distance between the two ferromagnet electrodes.

2.5.3 Three-terminal Hanle precession measurements

In the three-terminal Hanle precession measurement, spin accumulation and precession under a single ferromagnetic contact is observed. The configuration requires three terminals—two reference contacts (either FM or non-magnetic) and one ferromagnetic contact. The injection of spin polarized carriers into a semiconductor produces a net spin accumulation causing splitting of the spin-dependent electrochemical potential, $\Delta\mu = \mu_{\uparrow}-\mu_{\downarrow}$. This splitting is detected as a voltage $\Delta V_{3T} = \gamma\Delta\mu/2q$, where γ is the tunneling spin polarization of the ferromagnetic tunnel contact. If the spin current is subject to an out-of-plane magnetic field B_z, the spins precess at the Larmor frequency $\omega_L = g\mu_B B_z/\hbar$, resulting in precessional dephasing of the net spin accumulation in the channel, where g is the Lande g-factor, μ_B is the Bohr magneton, and $\hbar$ is the reduced Planck's constant. This precessional dephasing results in a Lorentzian shaped data which can be represented by $V_{3T}(B_z) = \Delta V_{3T}(0) / [1+(\omega_L\tau_s)^2]$, where τ_s is the spin relaxation

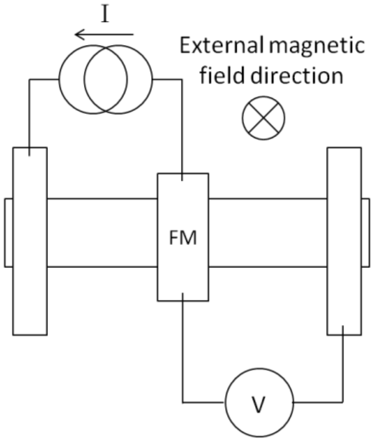

Figure 2.6 Illustration of a three-terminal Hanle measurement scheme. Spin injection and detection is done by a single ferromagnetic contact. The outer two contacts are ohmic reference contacts. The magnetic field is swept orthogonal to the sample surface.

time. An advantage of this measurement technique is that it allows one to focus on and probe the characteristics of the spin system directly underneath the spin injecting contact.

There is, however, a glaring issue that may prevent one from obtaining an accurate spin signal. Since the same injecting electrode is detecting the spin accumulation and precession, the interface quality between the FM/SC becomes significantly important. Tran *et al.* [37] discovered that interface states or defect sites near the FM/SC interface can trap spin polarized electrons, leading to longer spin lifetimes than what the actual value is inside the semiconducting channel and overestimating the spin lifetime value. Therefore, the three-terminal Hanle measurement is not a recommended way of conducting spin-related material characterizations. There are a couple ways to verify that interface states are not affecting the three-terminal signal. First is to vary the doping of the semiconductor and noting the change in spin lifetimes. A higher doping will generally lead to shorter spin lifetimes due to increase in scattering. Another way is to use several tunnel barrier materials. The spin lifetime should remain relatively constant across multiple tunnel barrier materials if interface states are not playing a role.

2.5.4 Four-terminal Hanle precession measurements

The four-terminal Hanle precession measurement is identical to the non-local measurement scheme, except that the magnetic field is applied orthogonal to the sample surface with the ferromagnetic electrodes magnetized either parallel or anti-parallel beforehand. The physics is identical to the three-terminal Hanle measurement, where a perpendicular magnetic field induces a torque ($T = -\mu_B B_z \sin\theta$) and causes spin precession in the channel. The time of travel in a diffusive semiconductor in such a system has broad distribution, which is given by

$$\varphi(t) = \frac{1}{\sqrt{4\pi Dt}} \exp\left(\frac{-L^2}{3Dt}\right) \qquad \textbf{(2.10)}$$

where D is the diffusion constant and L is the distance between the two ferromagnetic electrodes. The resulting measured output voltage for a fixed current bias becomes

$$V(Bz) = \pm I \frac{P^2}{q^2 N(E_F) S} \int_0^\infty \varphi(t) \cos(\omega_L t) \exp\left(-\frac{t}{\tau_{sf}}\right) dt \qquad \textbf{(2.11)}$$

where $N(E_F)$ is the density of states at the Fermi level, τ_{sf} is the spin relaxation time and S is the cross sectional area of the detecting electrode. The (+) and (-) sign corresponds to the parallel and antiparallel magnetization of the injector and detector electrodes, respectively. The polarization value, P, or the spin relaxation time can be accurately determined from eqn. 2.11.

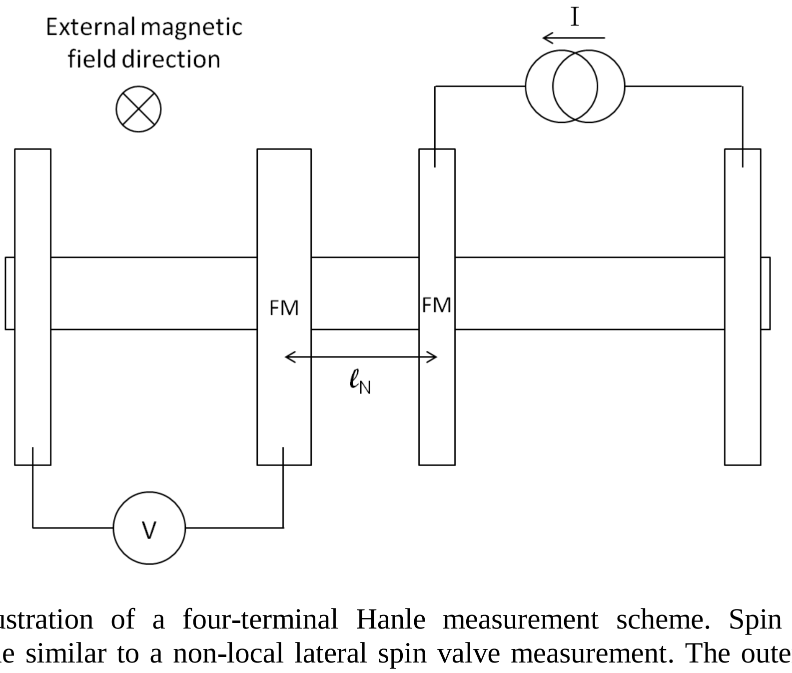

Figure 2.6 Illustration of a four-terminal Hanle measurement scheme. Spin injection and detection is done similar to a non-local lateral spin valve measurement. The outer two contacts are ohmic reference contacts. The magnetic field is swept orthogonal to the sample surface.

At this point, it is instructive to point out that lateral spin valve measurements and Hanle measurements measure two different spin relaxation times.

Spin relaxation time can be split into two components: the longitudinal spin relaxation time (T_1) and the transverse spin dephasing time (T_2). Time T_1 is the time it takes for the longitudinal magnetization of the polarized current to reach equilibrium. It is also equivalently the time of thermal equilibration of the spin population with the lattice. Therefore, generally, energy has to be taken from the spin system to the lattice (usually by phonons). Similarly, an ensemble of transverse electron spins may lose their phase due to spatial and temporal functions of the precession frequency. Time T_2 denotes this dephasing time. In most n-type semiconductors, one can approximate $T_1 \approx T_2$ and, therefore, do not distinguish between the two.

2.6 Summary

In this chapter, an overview of the spin relaxation mechanisms and electrical spin measurements techniques were discussed. An understanding of the physical mechanisms that govern spin relaxation inside various semiconductors is essential for proper design and characterization of these devices. It is shown that two-terminal local spin valve measurements and three-terminal Hanle precession measurements may include spurious effects that are detrimental to extracting the correct spin lifetime values. To date, four-terminal non-local measurements are the best proof of spin injection, transport, and precession in the channel. A more detailed quantitative analysis and overview of spintronics can be found in an excellent review article by Zutic, Fabian, and Sarma [38].

Chapter III

Growth and Characterization of Epitaxial Ferromagnetic MnAs Films

---

3.1 Introduction

The creation and detection of spin polarized current is a basic requirement that any kind of spintronic device must demonstrate. This is typically done by using a ferromagnet, which can either be semiconductors doped with transition metals (such as Mn, also called dilute magnetic semiconductors (DMS)) or ferromagnetic metals. Dilute magnetic semiconductors (DMS) have similar conductivities as their host material, eliminating the need for a spin-dependent tunnel barrier. However, most DMSs have Curie temperatures below room temperature, limiting their applications to cryogenic temperatures. One promising candidate is GaMnN, which has a Curie temperature above 300 K, but it is difficult to grow and nano-sized contacts may not actually be ferromagnetic [39], limiting its use to devices in the micron scale.

Some of the functional attributes and characteristics of a good ferromagnetic film for spintronic applications can be listed as follows [40]. First, it must have a Curie temperature (T_c) well above room temperature up to temperatures typically encountered in modern electronics (~85° C), along with large polarization values (typically greater than 0.5). Second, the material should be compatible with existing device technology such as GaAs, InP, GaN, and Si. Finally, the material should be thermally stable and chemically compatible with any remaining layers in the device.

Simple ferromagnetic metals such as Fe, Ni, or Co can be sputtered or e-beam evaporated for use as spin injectors and detectors, but these must be evaporated as the top-most layer since any epitaxial growth on polycrystalline metal is nearly impossible. Therefore, it is advantageous to develop a ferromagnetic material that can be epitaxially grown, has a Curie temperature above 300 K, and can be integrated monolithically with conventional III-V semiconductor materials such as GaAs. Manganese arsenide (MnAs) is one such material, which was first studied by Heusler [41] in 1904 and its ferromagnetic properties investigated by Hilpert [42] in 1911. MnAs is a ferromagnetic semi-metal with a Curie temperature of approximately 315 K, in which it becomes a paramagnet above this temperature. Nevertheless, this ferromagnetic material is compatible with the most relevant III-V semiconductor materials such as GaAs, GaN, and InP, and can be epitaxially grown with minimal growth related interface defects. This broad compatibility and room temperature Curie temperature, along with the ability to epitaxially grow device quality III-V material *on top* of MnAs makes this material unique and advantageous compared to deposited polycrystalline ferromagnets. In this chapter, a general overview of ferromagnetism is given, followed by a discussion on the growth and characterization of MnAs epitaxially grown on GaAs and InP.

3.2 Ferromagnetism

The defining property of a ferromagnet is that it has a spontaneous magnetic moment which is persistent and occurs in the absence of any externally applied magnetic field. This spontaneous moment can be thought of as an internal interaction which tend to line up the individual magnetic moments parallel to each other, called the exchange field (equivalent to a magnetic field $\mathbf{B}_E$). This field is affected by thermal agitation at elevated temperatures (near the Curie temperature), destroying the spin order. The strength of the exchange field is proportional to the magnetization, **M**, as $\mathbf{B}_E = \lambda\mathbf{M}$, where λ is a temperature independent constant called the mean-field constant. A localized spin in a material can only “sense” the magnetization of its closest neighbors. The Curie temperature, T_c, can be derived from the magnetization equation and the Curie law, leading to the Curie-Weiss law $\chi = C / (T - T_c)$, where C is the Curie constant, χ is the magnetic susceptibility of the ferromagnet, and $T_c = C\lambda$. The Curie constant can be found from the paramagnetic susceptibility $\chi_p = C/T$. The Curie-Weiss law predicts a singularity at $T = T_c$, which qualitatively implies spontaneous magnetization of the material below T_c.

The concept of exchange field can represent the quantum mechanism exchange interaction between the spin polarized electrons in a ferromagnetic material. The energy interaction of atoms i,j with electron spins $\mathbf{S}_i$, $\mathbf{S}_j$, under quantum theory, contains the term $U = -2JS_i \cdot S_j$, where ***J*** is the exchange integral proportional to the charge distribution overlap of atoms i and j. The charge distribution is directly related to the spin orientation of the outermost shell, which is governed by the Pauli exclusion principle. This, in turn, governs the electrostatic energy of a system, which depends on the relative orientation of the spins (either parallel states or antiparallel states). The difference in their energy between these two states is the exchange energy, which can be simply approximated as $-2\boldsymbol{J}\mathbf{s}_i\mathbf{s}_j$. From this simplified analysis, it is reasonable to argue that ferromagnetism can only occur with materials with a partially filled valence shell or materials with equivalent properties.

Ferromagnets have a strong spontaneous saturation magnetization, but the magnetic moment of a virgin ferromagnet may be much less than the saturation magnetization until an external field is applied. Ferromagnetic materials are typically sectioned into small regions called domains, which are regions with long range spin ordering but the orientation of the spin may be different from domain to domain. A ferromagnet may have no microscopic net magnetization if the sum of the domain strength and orientation is zero. This is typically the case for as-grown or as-deposited ferromagnetic films, in which an initial application of an external magnetic field is necessary to set all domains in the same direction and saturation the magnetic moment of the film. The boundaries separating each domain are called the domain wall, and can be visibly identified using measurement techniques such as magnetic force microscopy (MFM).

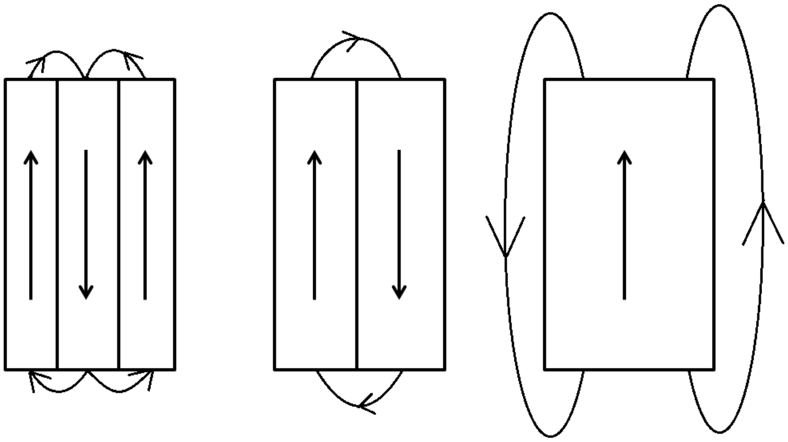

Figure 3.1 Illustration of magnetic domains and associated magnetostatic energy.

The coercivity of a ferromagnet is the magnetic field required to reduce the net magnetic moment to zero. This parameter is important in designing different types of spintronic devices. For example, spin-torque device requires a material with very low coercivity, such as FeCoB (often called a soft ferromagnet), while spin modulation devices may want a material with relatively high coercivity (a hard ferromagnet) so as to not be affected by stray magnetic fields.

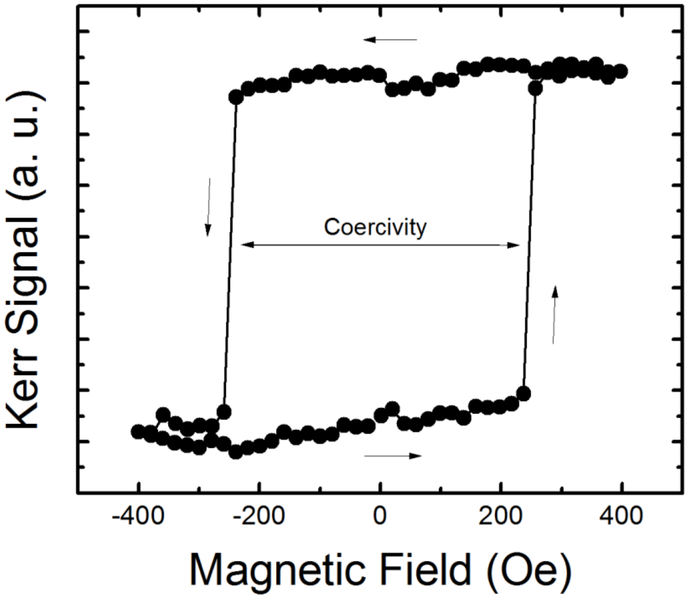

Figure 3.2 Hysteresis characteristics of a 200 nm MnAs film epitaxially grown on (001) GaAs using the magnetic-optical Kerr effect (MOKE) measurement.

3.3 Molecular Beam Epitaxy (MBE)

In this section, a brief description of the molecular beam epitaxy system is given. The MBE is primarily a research tool, allowing epitaxial growth of crystalline structures with atomic scale precision. It is a physical deposition technique, where solid sources in the effusion cells are electrically heated until it evaporates into a "molecular beam", which then impinges on the host substrate and forms epitaxial layers. The parameters that the user can control are the substrate temperature, the temperature of each cell, the substrate rotation speed, and the time to open and close the shutters for each cell. The growth chamber is always kept at ultra high vacuum, typically in the 10^{-10} torr range. This is achieved by using several pumps (ion or cryo pumps) and flowing liquid nitrogen

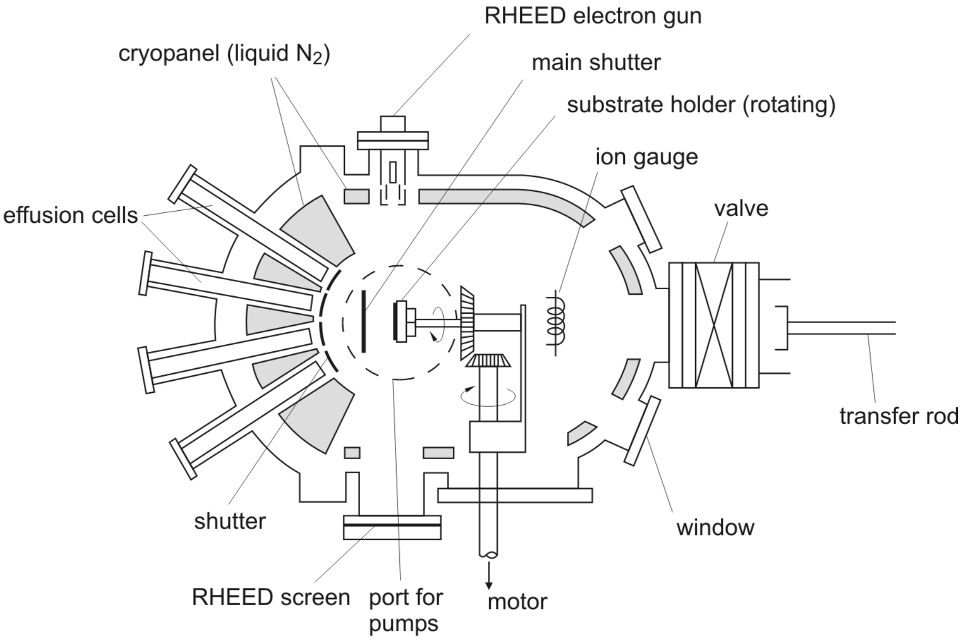

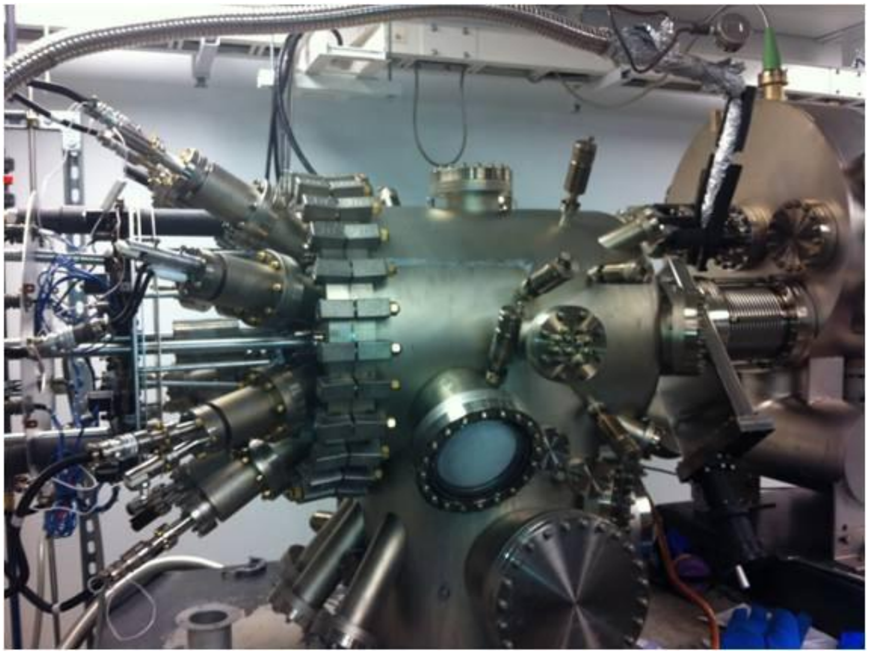

Figure 3.3 (top) Schematic illustration of the growth chamber of a molecular beam epitaxy (MBE) system. Typically, there are two other chambers, the loading chamber and the buffer chamber, which ensures that ultra high vacuum conditions are always present in the growth chamber. [H. Ibach and H. Lueth. *Solid-State Physics*. Springer Verlag, 2003]. (bottom) A Veeco Gen-II MBE tool dedicated for epitaxial growth of magnetic contacts on III-V substrates.

through a cryopanel located near the outer edges of the growth chamber. A low growth chamber pressure leads to a long mean free path of particles, reducing the scattering rate of the growth species and maintaining a pure and homogeneous film. Having a low background pressure also helps in obtaining a more accurate beam flux for calibration purposes. Although the parameter being controlled is temperature, the real meaningful parameter is the beam equivalent pressure, or the vapor pressure of the cells. This parameter is different for every MBE system, and even changes from growth to growth. A diagram of the vapor pressure of a comprehensive list of elements as a function of cell temperature is shown in Fig. 3.6. These diagrams are very important, as it tells which type of effusion cell to use for each element, as well as the optimum temperature range to achieve the desired growth condition. The background growth chamber pressure may also affect this value. Therefore, careful calibration of each cell flux is necessary before every growth. An illustration of various surface processes that may occur during growth is shown in Fig. 3.4.

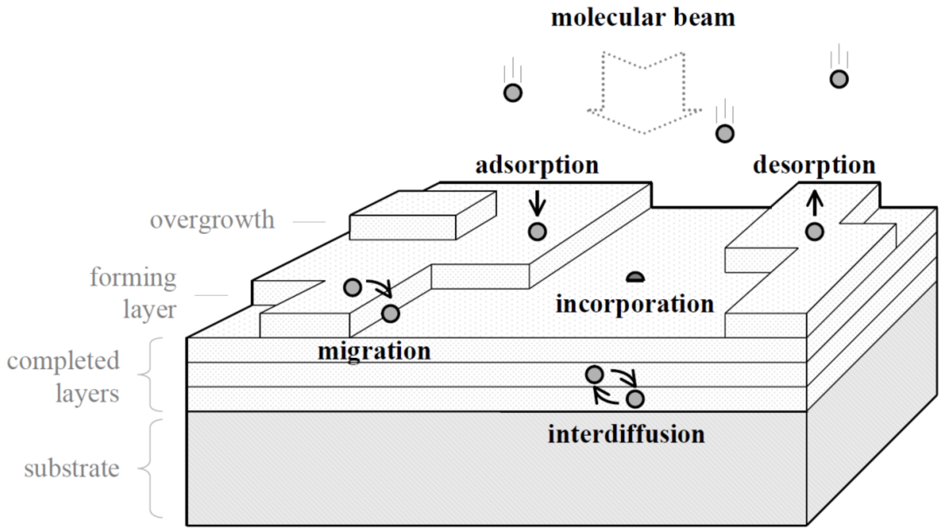

Figure 3.4 Various chemical and physical processes that may occur during an epitaxial growth using MBE [43].

A reflection high-energy electron diffraction (RHEED) is used as an in-situ growth monitoring technique. The RHEED system consists of an electron gun and a photoluminescent detector screen. The electron gun fires electrons with 5-100 keV energy at a grazing angle to the sample surface, providing real-time information about the *surface* morphology. The incident electrons are diffracted by the atoms on the surface of the sample, and depending on the crystallinity of the surface, the electrons constructively interfere, creating a regular pattern on the detector. A streaky pattern indicates crystalline growth, while a spotty or diffused RHEED pattern may indicate formation of islands or defects on the surface.

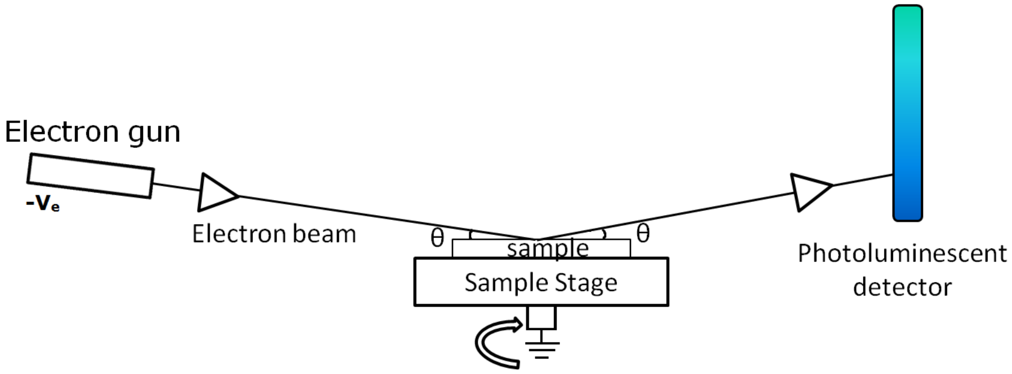

Figure 3.5 Schematic illustration of the reflection high-energy electron diffraction (RHEED) technique. RHEED allows for in-situ monitoring of the

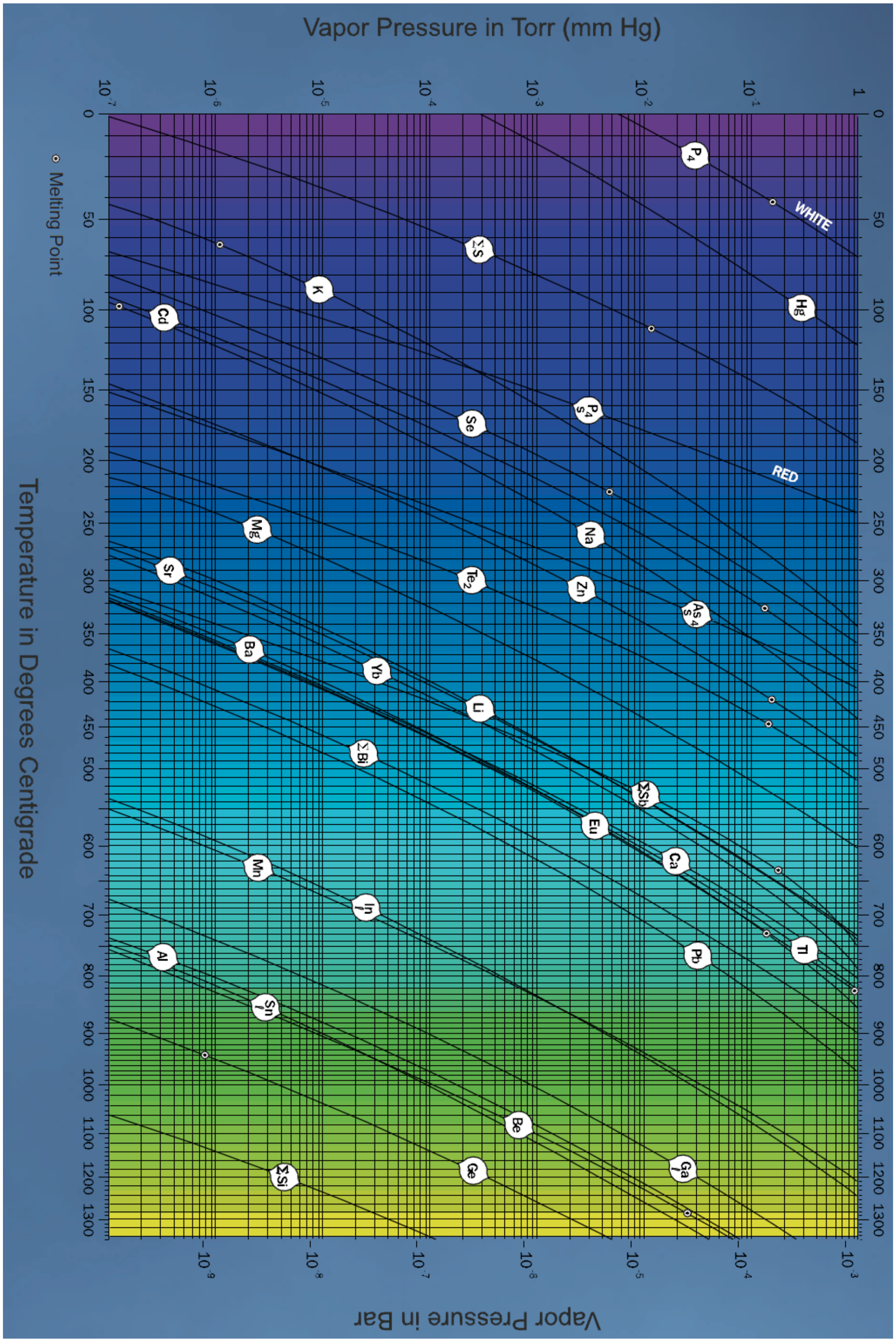
Vapor Pressure in Torr (mm Hg)
Temperature in Degrees Centigrade
Vapor Pressure in Bar
Melting Point
WHITE
RED
P4
Hg
S
K
Cd
P4
Se
Na
Mg
Sr
Te2
Zn
As4
Ba
Yb
Li
Bi
Sb
Eu
Ca
Mn
In
Tl
Pb
Al
Sn
Be
Ge
Ga
Si
0
50
100
150
200
250
300
350
400
450
500
600
700
800
900
1000
1100
1200
1300
1
10⁻¹
10⁻²
10⁻³
10⁻⁴
10⁻⁵
10⁻⁶
10⁻⁷
10⁻³
10⁻⁴
10⁻⁵
10⁻⁶
10⁻⁷
10⁻⁸
10⁻⁹

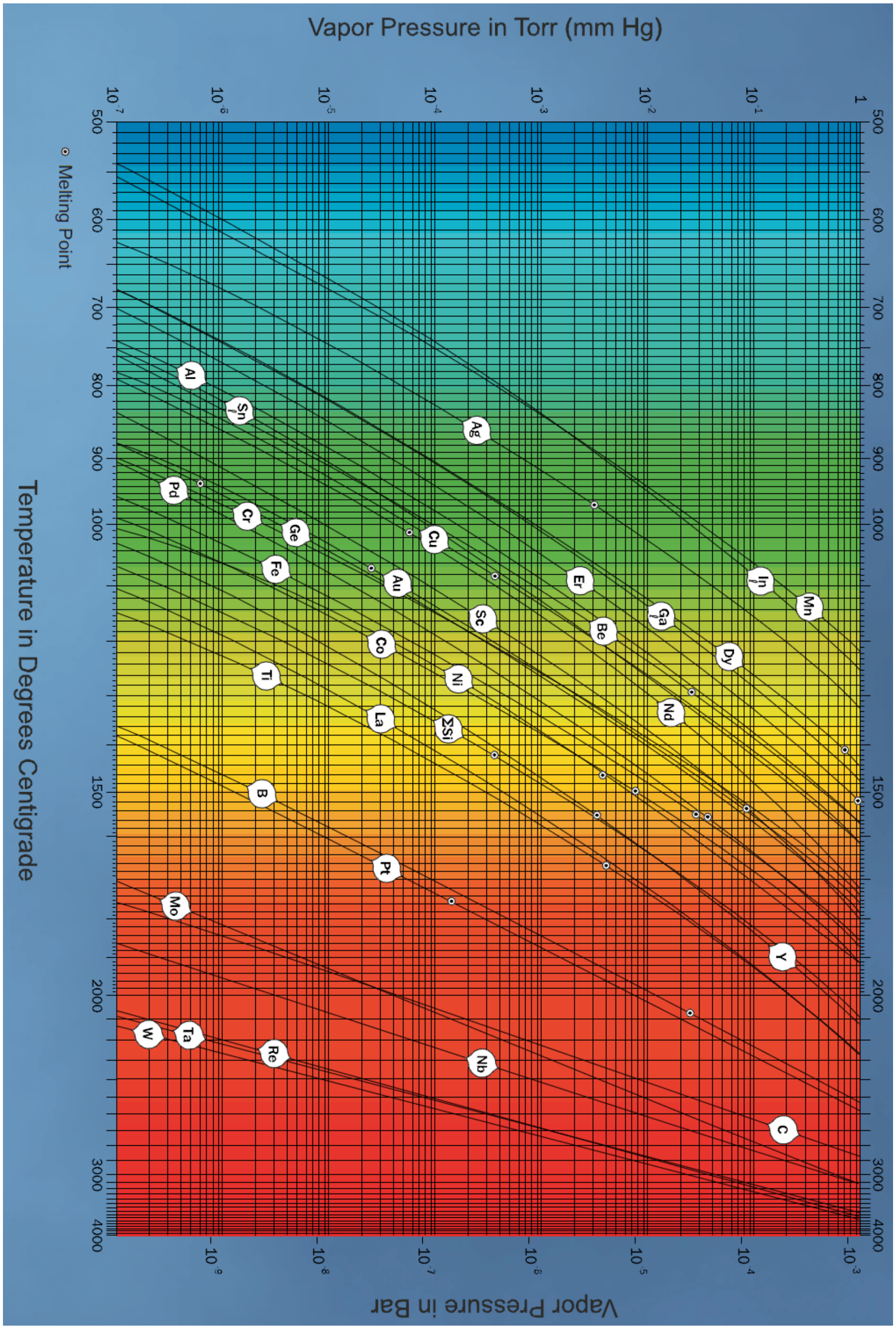

Figure 3.6 Vapor pressure of various elements as a function of element temperature [source: Veeco].

3.4 MnAs Ferromagnetic Films Grown by Low-Temperature Molecular Beam Epitaxy (LT-MBE)

Molecular beam epitaxy (MBE) is an extremely useful technique in material science and for research and development of heterostructures. The ability to grow single crystalline material with nearly atomic scale precision has made MBE one of the most important tools for semiconductor research. Typically, materials of similar lattice constants to the substrate are grown, but materials of completely different crystalline structure and lattice constants can be grown as well if the conditions are well calibrated. For example, the heteroepitaxy of MnAs on (001) GaAs and (001) InP substrate is challenging due to the a geometrical mismatch between these materials. Fig. 3.7 shows the crystalline structure of MnAs, which is hexagonal similar to GaN. However, it has been possible to grow MnAs on most III-V semiconductors such as GaAs, InP, and GaN.

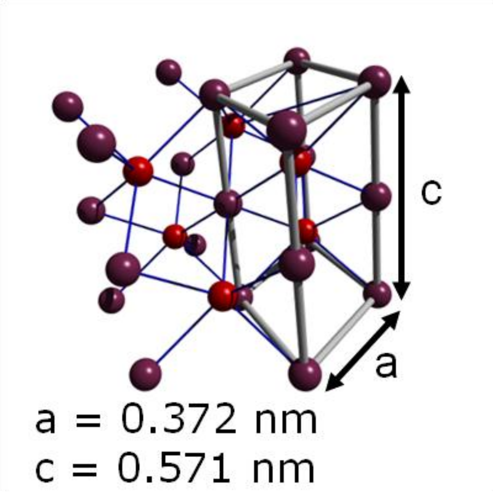

Figure 3.7 Illustration of the crystalline structure of MnAs. The lattice constants are given in the a- and c-axis. Typically, MnAs grows on III-V materials with c-axis parallel to the sample surface.

Most of the GaAs and InP based spintronic device discussed in this thesis uses ferromagnetic MnAs contacts grown by MBE. Therefore, it is appropriate to discuss the growth methods and conditions. Also, Mn atoms can act as acceptors in GaAs, which can enable growth of MnAs/GaAs/MnAs high temperature vertical spin valve as discussed in the following chapter. Interestingly, GaMnAs is also a dilute magnetic semiconductor at low temperature.

3.4.1 Epitaxial growth of MnAs on GaAs, InP, and GaN substrates

The growth of MnAs requires low temperature molecular beam epitaxy (LT-MBE) techniques. Most III-V semiconductors and their alloys are grown at substrate temperatures of ~500-800º C, but growing MnAs at these high temperatures may lead to the segregation of Mn atoms, resulting in Mn-Mn bonds that destroy the ferromagnetic properties of MnAs. To reduce the clustering of Mn atoms, MnAs is typically grown at substrate temperatures of ~200-250º C, and the growth is interrupted every few minutes to allow the Mn atoms to diffuse around the sample surface.

Before any layers are grown, the surface of the host substrate is cleaned in the growth chamber by raising the substrate temperature to its cleaning temperature. By raising the substrate temperature, micro-sized impurities/particles and thin capping layers (capping layers are present in most virgin GaAs wafers) are evaporated. The cleaning temperature is typically 600º C for GaAs, 500º C for InP, and 900º C for GaN. However, since the temperature reading from the thermocouple may be different from the actual substrate temperature, reflection high-energy electron diffraction (RHEED) patterns can be used to find the difference of the actual substrate temperature and the thermocouple reading. A typical RHEED pattern of a clean GaAs surface is shown in Fig. 3.8. It is important to keep the arsenic shutter on (at a beam equivalent pressure, BEP, of 6.6×10^{-6} torr) while cleaning for GaAs samples, as the arsenic will be desorbed above a substrate temperature of 400 º C and you will be left with a gallium rich (or arsenic deficient) surface, which is not desirable for MnAs growth.

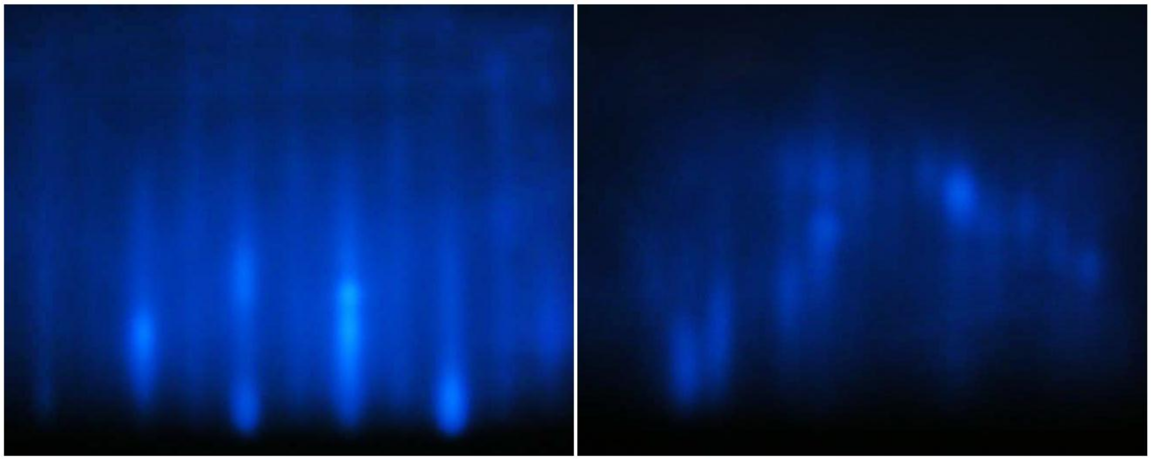

Figure 3.8 RHEED pattern of a clean GaAs surface.

After cleaning, the substrate temperature is reduced to 200º C at a rate of 15 degrees per minute. To prevent the formation of a purely arsenic capping layer, the arsenic shutter is closed when the substrate temperature reaches 400º C. When the substrate temperature is stabilized at 200º C, the arsenic shutter is reopened for 2 minutes to create an arsenic rich surface. This process was shown to improve the uniformity of the MnAs layer. The MnAs layer is grown with a As/Mn BEP ratio of 90-100 (around 295º C arsenic cell temperature and 750º C manganese cell temperature in the MBE system used in this study). This results in a MnAs growth rate of 1 nm per minute. The substrate temperature can be raised to 250º C with a As/Mn BEP ratio of 50 to raise the growth rate to approximately 5 nm/minute. As mentioned previously, the growth is interrupted every 8 minutes for 1 minute to allow the Mn atoms to diffuse around the sample surface to prevent Mn-Mn clustering. This step is unnecessary but ensures a more uniform MnAs film in terms of crystalline integrity. MnAs grows with its c-axis parallel to the substrate surface with a 2:3 coincident lattice with GaAs, as shown in Fig. 3.9.

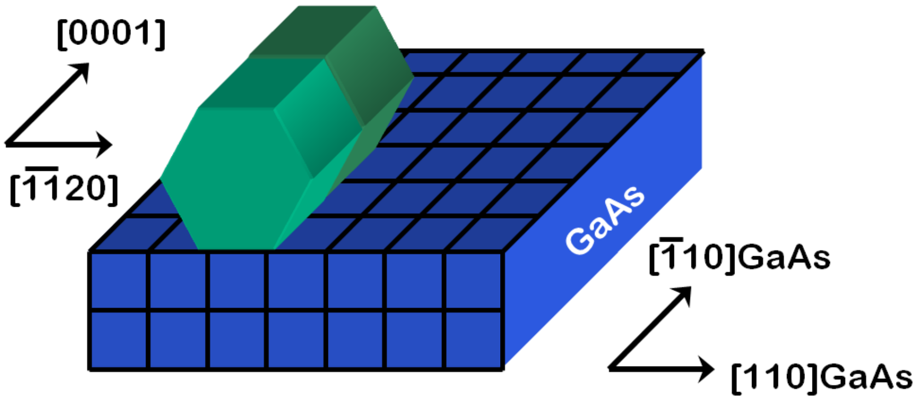

Figure 3.9 Schematic illustration of the growth of MnAs on GaAs. A 2:3 coincidence lattice allows for epitaxial growth.

The RHEED pattern just after the nucleation phase of MnAs is shown in Fig. 3.5. The streaky pattern becomes spotty and diffuses, which indicates a rough sample surface and formation of tiny MnAs droplets. As the growth progresses, these droplets coalesce to form bulk films, in which the RHEED once again becomes streaky with a clear (1x1) reconstruction pattern. A significant amount of Mn-Mn clustering will result in a permanently spotty RHEED pattern until the end of growth, and the surface will be milky and inspection under a microscope will reveal a dense number of dark spots. A micrograph of a MnAs layer with significant Mn segregation and without is shown in Fig. 3.10. Even with Mn segregation, the bulk film may exhibit ferromagnetic behavior, as tiny domains of MnAs will be present. However, devices with micron-sized contacts will not exhibit clear spin signals, or the spin signal will be extremely small compared to using a high quality MnAs layer.

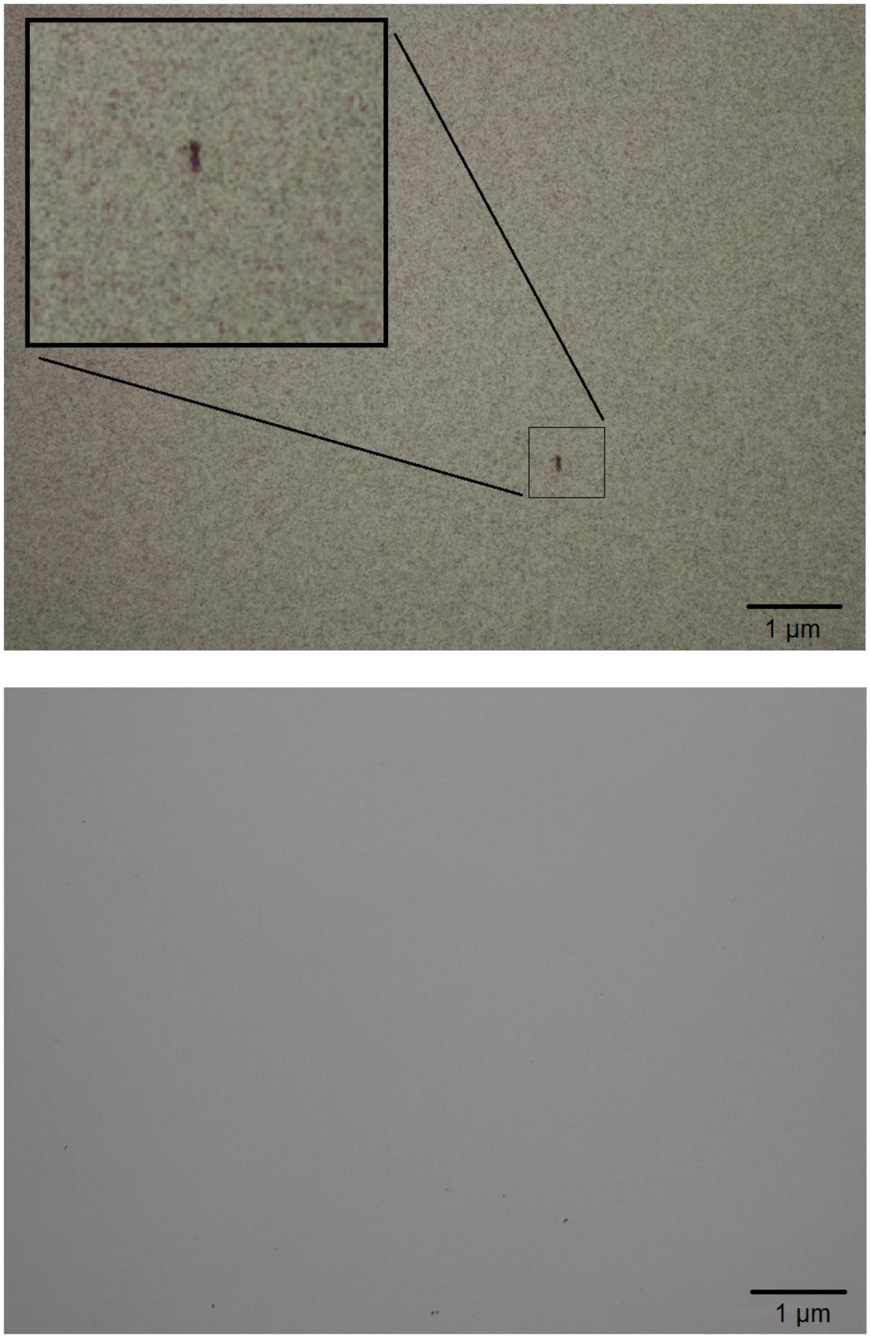

Figure 3.10 Micrograph of MnAs film surface. The top image shows MnAs with significant Mn clustering, which results in dense dark spots and the loss of ferromagnetic properties. The bottom image shows a micrograph image of a featureless MnAs surface resulting from optimized growth conditions.

As a final step, the MnAs film can be annealed at a substrate temperature of 350° C with an arsenic BEP flux of 7×10^{-6} torr to increase the surface smoothness. This step is preferably skipped if the MnAs is the topmost layer of the device, but necessary if other layers are epitaxially grown on top. An atomic force microscopy (AFM) study of MnAs films grown on InP is shown below.

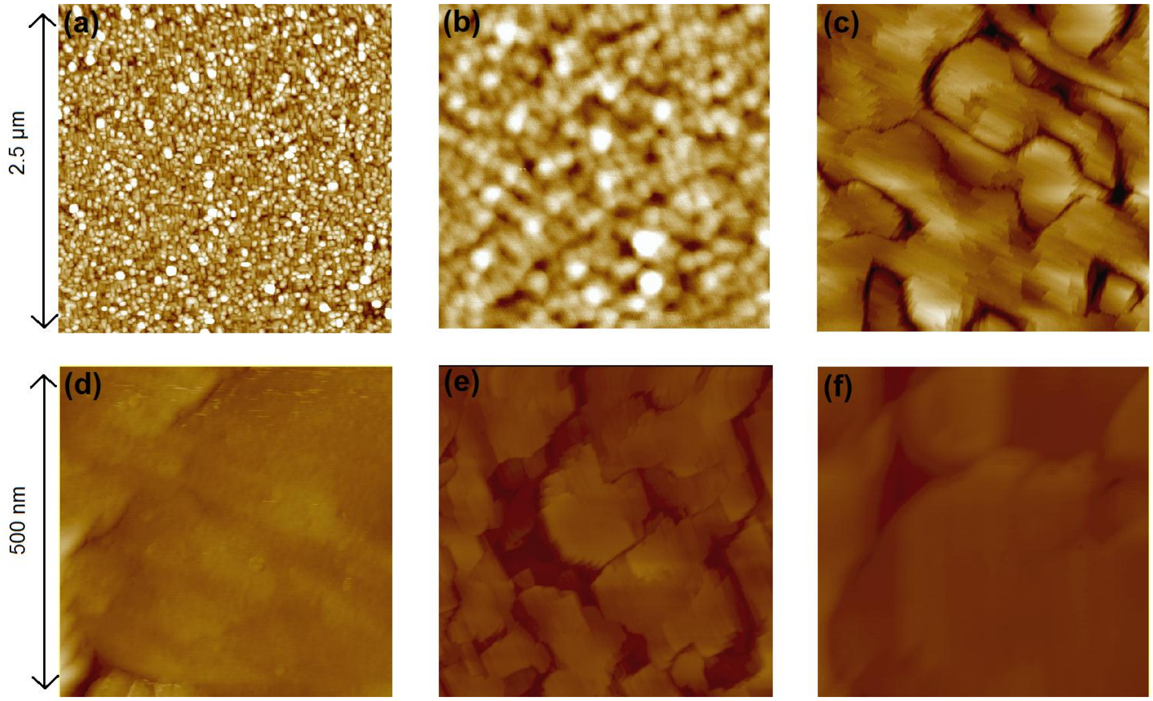

Figure 3.11 Atomic force microscopy (AFM) characteristics of MnAs films grown on InP.

Fig. 3.11(a) shows an AFM image of MnAs in the nucleation phase. As indicated by the RHEED pattern, the AFM shows formation of 3D MnAs islands (indicating Volmer-Weber or Stranski-Krastanov growth modes), which coalesces into a thin film after several monolayers of growth (Fig. 3.11(c)). Figures 3.11(a), (b), and (c) correspond to a scan area of 2.5 μm x 2.5 μm, and (d), (e), and (f) correspond to a scan area of 500 nm x 500 nm. Before annealing, the root mean square (rms) value of the surface roughness is measured to be 19 Å over a lateral distance of 2.5 μm. After annealing, the rms of the surface roughness reduced to 7 Å, which is primarily due to the increase in the in-plane grain size of the MnAs layer with annealing.

The X-ray diffraction (XRD) measurements indicate absolutely no Mn-Mn clustering for films grown at optimal conditions, which can be deduced from Fig. 3.12(a). The zoomed-in (002) GaAs peak is shown in Fig. 3.12(b). MnAs film takes on two phases, depending on the temperature that it is subjected to. Typically, this transition occurs near 40º C. Below this temperature, MnAs stays in the typical hexagonal crystalline structure and is specified as α-MnAs. In this α-phase, MnAs is ferromagnetic. Above this temperature, MnAs undergoes a phase shift and takes on an orthorhombic crystalline structure and is denoted as β-MnAs. MnAs is no longer ferromagnetic in this phase, but paramagnetic. These two phases may coexist in a large temperature range of 20º C - 40º C, which is apparent in fig. 3.12(b). A β-MnAs peak can be observed next to the α-MnAs peak, but with greatly reduced intensity, which indicates that α-MnAs is dominating.

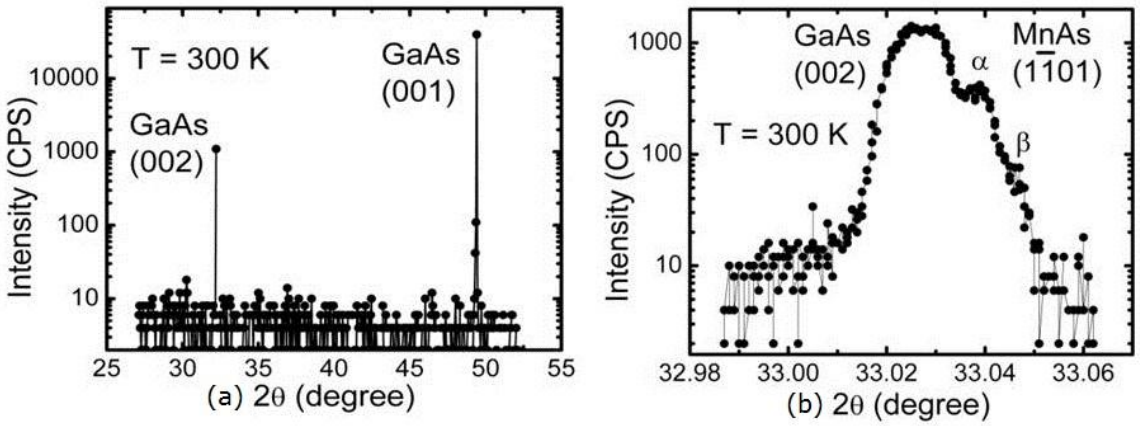

Figure 3.12 (a) A coarse X-ray diffraction (XRD) measurement on a (001) GaAs sample with MnAs grown on top. The absence of Mn-Mn clustering can be observed. (b) XRD showing α-MnAs peak near the (002) GaAs peak.

3.4.2 Magnetic properties of MnAs films

The in-plane magnetic properties of MnAs films have been studied using the superconducting quantum interference (SQUID) and magneto-optical Kerr effect (MOKE) measurement techniques. The domains of a typical MnAs film grown on GaAs observed using the magnetic force microscopy (MFM) by Daweritz et al. is shown in Fig. 3.13. It can be seen that the domain sizes are in the order of a few hundred nanometers.

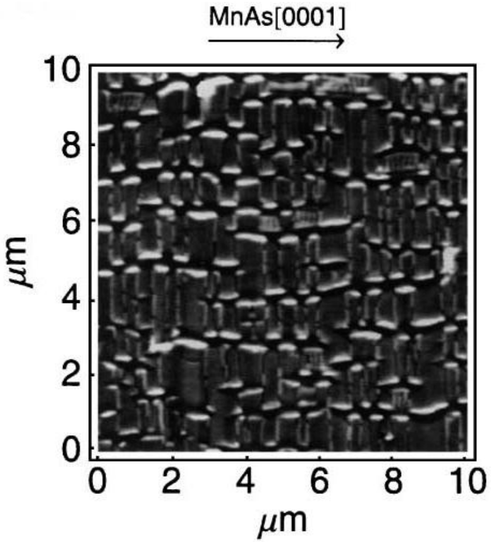

Figure 3.13 Magnetic domains of MnAs on GaAs probed by magnetic force microscopy (MFM) technique. [44].

The SQUID measurements show sharp switching of the magnetization at 10K for a 90 nm thick MnAs film grown on GaAs. The results indicate that the easy axis of magnetization is [-1-120], which is in-plane and parallel to the sample surface. The coercivity is found to be approximately 100 Oe for a 90 nm thick film. Thickness dependent measurements reveal that the coercivity increases with decreasing thickness, up to ~500 Oe for a film thickness of 30 nm. The coercivity of the film also decreases with increasing temperature. As seen in Fig. 3.14(b), the magnetization of the film drops rapidly past its Curie temperature of 315 K. MOKE measurements of MnAs films grown GaN and InP are shown in Fig. 3.14 (c) and (d), measured at T = 300 K. It is worth noting that no matter the host substrate,

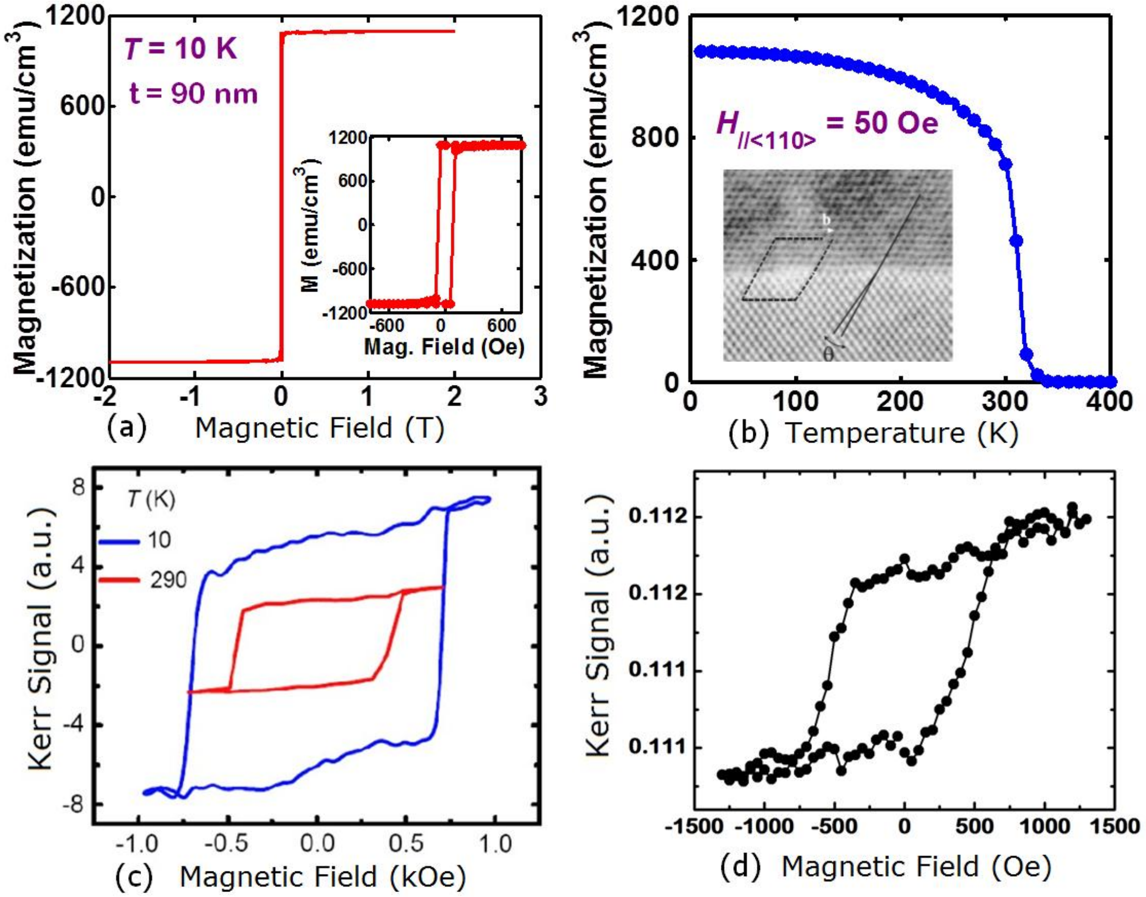

Figure 3.14 (a) Hysteresis characteristics of 90nm thick MnAs grown on GaAs measured by SQUID magnometer; (b) magnetization of the same film as a function of temperature. The inset shows a TEM image of a MnAs/GaAs interface. Hysteresis characteristics of MnAs grown on (c) InP and (d) GaN using MOKE measurement technique.

3.5 Summary

In summary, an overview of MBE and epitaxy of MnAs on III-V materials was presented, along with a brief introduction on ferromagnetism. Ferromagnets are an essential component of any spintronic material, whether it is in the form of a metal or a dilute magnetic semiconductor. The ability to create a spin-polarized current in a purely electrical way offers tremendous potential for multifunctional spin-based logic and memory devices that utilize the spin degree of freedom as well as its charge properties. SQUID and MOKE measurements indicate that the magnetic properties of MnAs films grown on GaAs, InP, and GaN show similar coercivity and Curie temperature, indicating that the final film morphology and phase are identical across these host III-V semiconductors.

Chapter IV

High Temperature Three-Terminal GaAs-based Spintronic Devices

4.1 Introduction

Gallium Arsenide was the first semiconductor material for electrical spin injection experiments from a ferromagnetic metal. The first successful lateral spin-valve device was reported by Saha *et al.* [15] using MnAs as the ferromagnetic spin injector/detector and using a graded-doped Schottky tunnel barrier to overcome the conductivity mismatch problem. Since then, numerous reports on spin injection and transport in GaAs using various ferromagnet and tunnel barrier have been published. However, most experiments are done at cryogenic temperatures (4-77 K), which is not very useful for practical applications. As discussed in chapter 1, the spin lifetime in n-type GaAs is affected by both the DP and EY relaxation mechanism at increasing temperatures, making spin lifetime in GaAs one of the shortest among actively researched semiconductors. Despite this disadvantage, demonstrating high temperature spin valves will show the robustness of spin-related effects and that room temperature devices are possible to design and fabricate. This chapter focuses on high temperature GaAs spin valve devices, both in the lateral and vertical geometry, with a controllable and amplified magnetoresistance response.

4.2 High Temperature Two-Terminal Lateral Spin Valve Using the Focused Ion Beam (FIB) Technique

4.2.1 Introduction

In this short section, the growth, fabrication, and characterization of a simple two-terminal spin valve is described. The main objective of this study was to create a sub-micron channel to increase the operating temperature of two-terminal GaAs-based lateral spin valves with MnAs spin contacts. One of the simplest ways to achieve higher temperature operation is to shorten the channel length. Wet etching process of MnAs, however, makes it difficult to etch channel lengths less than 0.5 μm due to its non-reproducible wet etching properties, resulting in heavy lateral etching and rough edges. Thus, the focus ion beam (FIB) technique is used to etch out a sub-micron sized channel. The operating temperature increased up to 295 K, as opposed to 170 K in previous works [15]. One interesting observation to note is that compared to the broad gradual increase of magnetoresistance in wet etched MnAs spin valves, devices with electrodes created by FIB show very sharp magnetoresistance characteristics.

4.2.2 Heterostructure

The heterostructure of GaAs based spin valve grown by molecular beam epitaxy (MBE) is shown below in Fig. 4.1. The top of the heterostructure is graded doped (n-type with Si dopant) up to 1×10^{19} cm^{-3} to create a tunneling Schottky barrier for spin polarized electrons. The GaAs structure is transported through air and loaded into another MBE specifically tuned to grow MnAs, where the MnAs is grown directly on top of the heterostructure after standard cleaning of the sample surface (cleaning substrate temperature of ~650º C). Refer to chapter 3 for detailed description of the growth of MnAs on III-V materials. The GaAs channel is doped 1×10^{17} cm^{-3} to ensure that spin scattering mechanisms are minimal with respect to the channel conductivity [45]. The advantage of a fully epitaxial structure is that there are minimal interface states and defects, reducing unnecessary spin dephasing or carrier trapping between the ferromagnet/tunnel barrier/semiconductor (FM/TB/SC) interface.

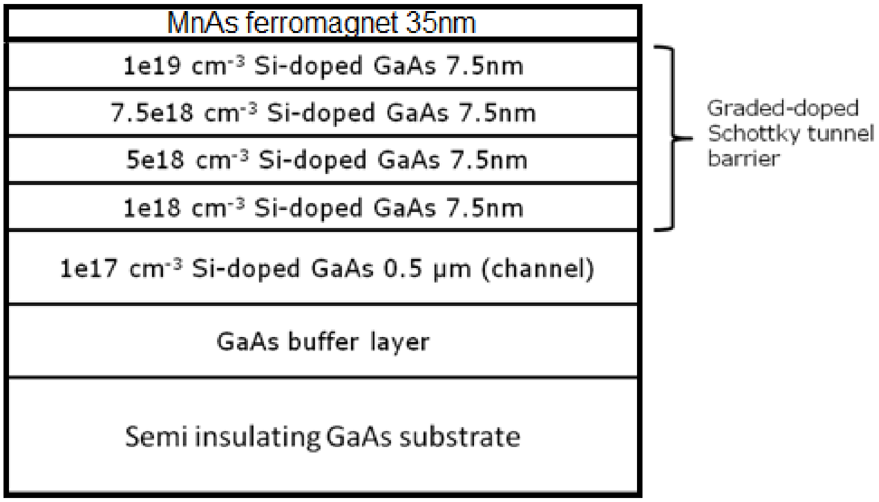

Figure 4.1 Heterostructure used for high temperature GaAs lateral spin valve experiments. The top layer 7.5 nm layers act as a Schottky tunnel barrier for efficient spin injection.

4.2.3 Fabrication details

The fabrication of this device is done by standard optical lithography (5.0x reduction stepper), plasma enhanced chemical vapor deposition (PECVD), and Focused Ion Beam (FIB) technique. The fabrication steps are as follows:

(1) The MnAs contact region is etched by using a solution of 1:1:100 H_3PO_4:H_2O_2:H_2O for approximately 30 seconds. A clear change in color can be observed (from yellowish to dark red/brown). The dark brown hue is actually a residue of arsenic atoms on the surface, which is not conductive and removed on the next step.

(2) The mesa is etched using a solution of 1:1:20 H_3PO_4:H_2O_2:H_2O for approximately 40 seconds. The time is not critical as there is no significant lateral etch that destroys the MnAs contact region.

(3) The sample is transferred into a FIB machine, where the channel is etched. It is critical that the FIB beam is focused and that the sample stage is not moving (sometimes the stage or the sample drifts in position over time). The lower the beam current, the shorter the channel can be made. In this case, a beam current of 30 pA with a beam voltage of 30 V has been used (FEI Nova SEM/FIB machine). The channel for each device is made individually.

(4) Plasma-enhanced chemical vapor deposition (PECVD) is used to deposit approximately 800 nm thick Si_3N_4 passivation layer to protect the devices.

(5) LAM 9400 plasma etch (dry etch) is used to open vias through the Si_3N_4 passivation layer for final metal interconnects. A standard Si_3N_4 etch recipe provided by the LNF staff is used (recipe name: "mnf_oxynit" created in private communication with Brian VanDerElzen).

(6) Before depositing the final metal interconnects, it is good practice to remove the residue photoresist by plasma ashing.

(7) Finally, Ti/Au (30Å/3000Å) metal interconnects are e-beam evaporated. The sample is then loaded onto a chip carrier and wire bonded.

by FIB.

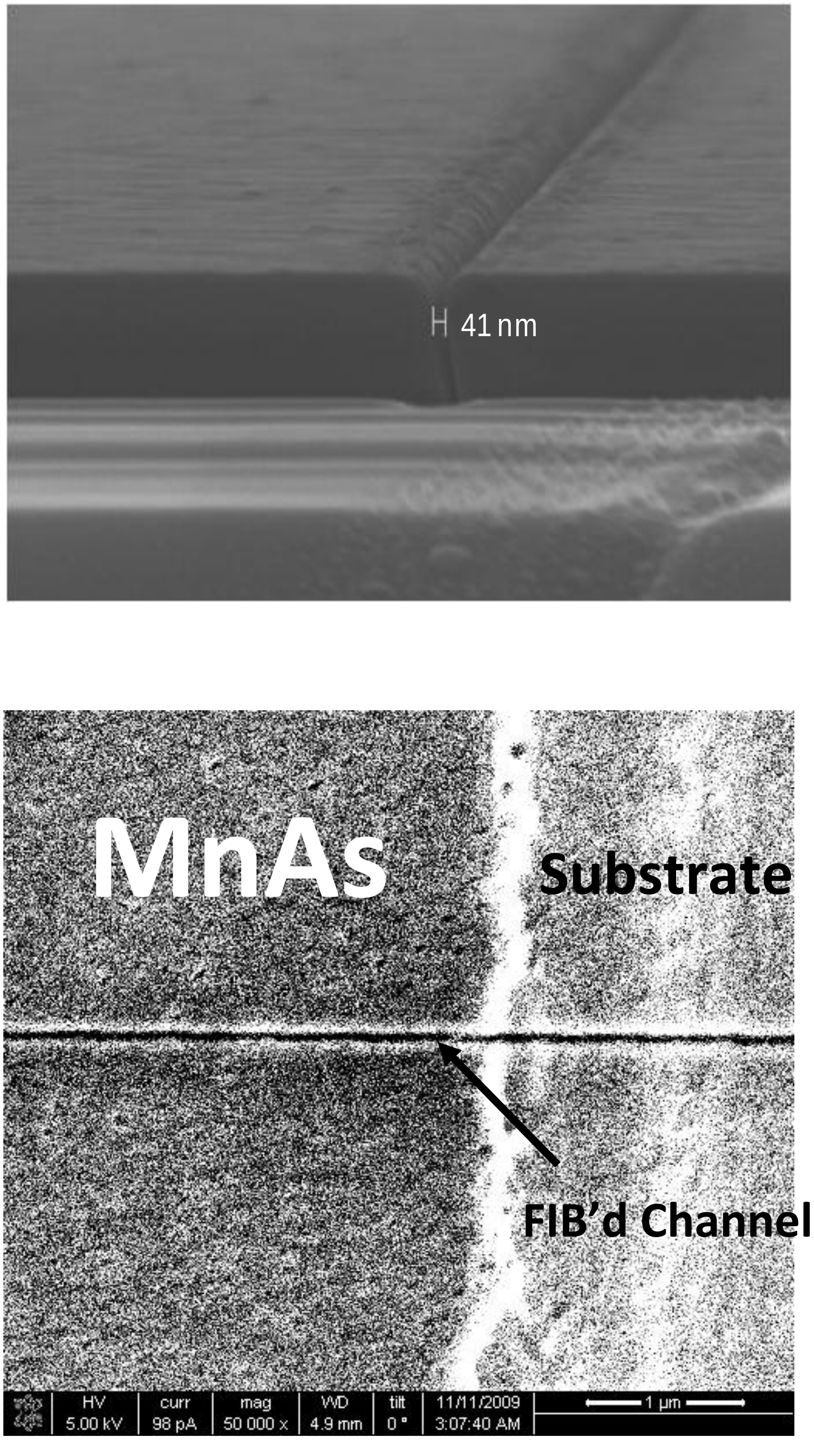

Figure 4.2 (top) Side view SEM image of a 41 nm channel etched by FIB. The beam is slightly slanted due to the slight substrate rotation error. (bottom) Top view SEM image of the FIB’d channel. It is evident that the wet etched MnAs edge is very rough compared to the edge created by FIB.

4.2.4 I-V Characteristics of the MnAs/Tunnel Barrier/GaAs contact

The current-voltage characteristics at room temperature is measured using the Keithley 4200 semiconductor parameter analyzer connected to an Alessi probe station. Low temperature I-V is measured in our cryostat using a Keithley dual source meter. As shown in Fig. 4.3, it is difficult to observe the nonlinear I-V characteristics at room temperature, but is clearly observable at low temperatures. This non-linearity is due to the tunnel nature of carrier transport and is first of three criteria found by Rowell for single step tunneling transport through the FM/TB/SC interface [46].

The tunneling conductance for T = 300 K and T = 20 K is shown in Fig. 4.4. A parabolic dependence of the conductance on voltage can be observed. This is the second Rowell's criteria. The parabolic data can be fit using the Brinkman-Dynes-Rowell model [47], in which the tunneling barrier height and distance can be calculated. The barrier height (*ø*) and tunneling distance (d) is found to be approximately 0.9 eV and 2 nm, respectively.

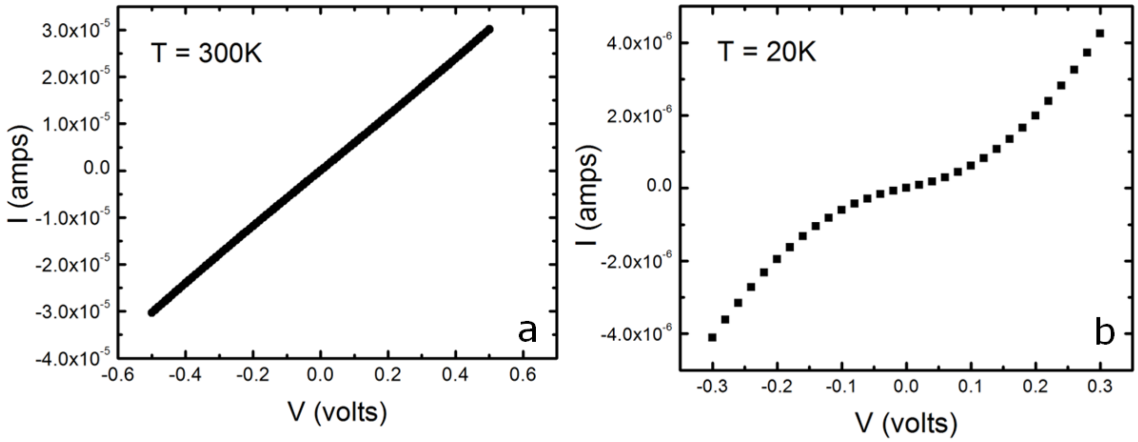

Figure 4.3 I-V characteristics for a simple lateral two-terminal GaAs spin valve at (left) T = 300 K and (right) T = 20 K. The non-linear current as a function of voltage verifies tunneling transport.

Finally, the third and most reliable tunneling criterion is the negligible change in the zero-bias resistance (ZBR) as a function of temperature. For this system, R0(T)/R0(300K) ~ 1.3, conclusively verifying spin injection into the GaAs by single step tunneling.

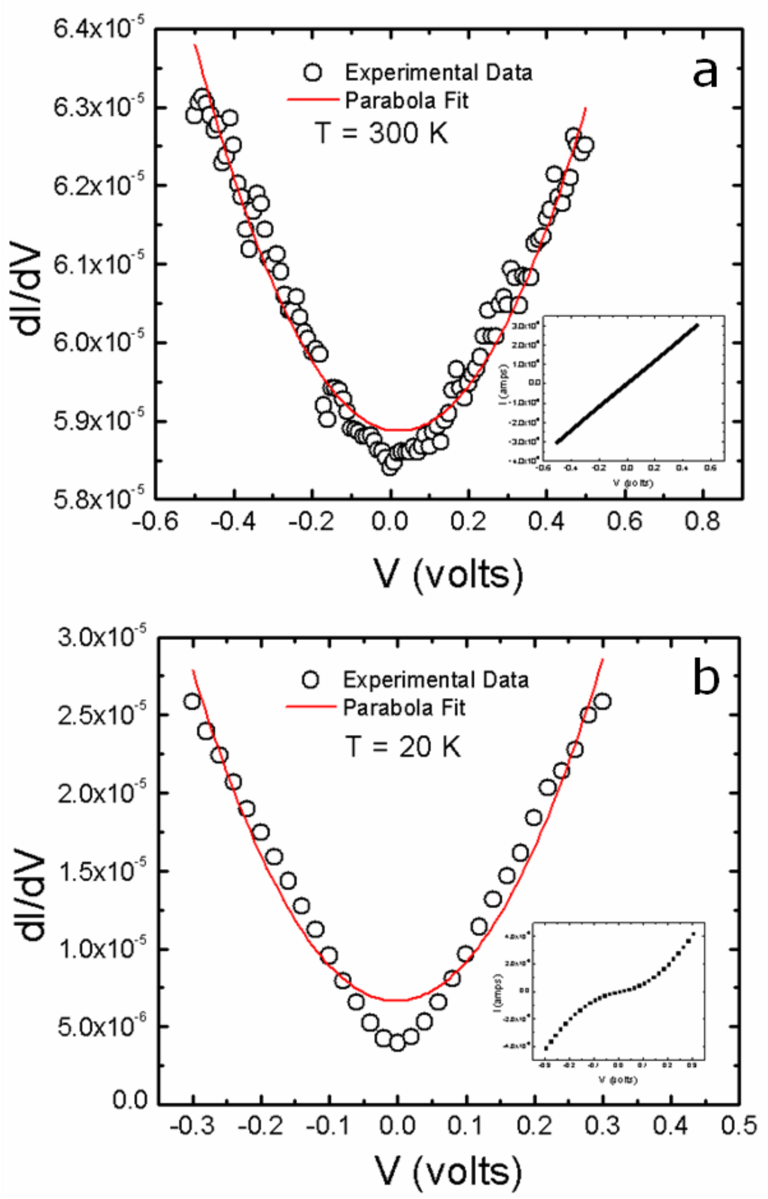

Figure 4.4 Conductance as a function of bias for (top) T = 300 K and (bottom) T = 20 K. Although the nonlinearity in the I-V curve is difficult to observe with the naked eye at high temperatures, the dI/dV plots show a parabolic dependence of conductance vs. voltage bias.

4.2.5 Magnetoresistance characteristics

A host of magnetoresistance data are shown for various temperatures for a device with channel length L_{chan} = 40 nm. A constant dc current of 150 μA is applied between the two ferromagnetic electrodes, and the voltage is measured across the device as an external magnetic field is swept. The figures are plot of the raw data extracted from the measurement setup. The MR show sharp switching characteristics consistent with the coercivity difference between the injector and detector electrodes. A voltage increase of 0.4 mV is measured at 10 K for antiparallel configuration of the two FM electrodes, which corresponds to a magnetoresistance $MR(H) = [R_{AP}(H_{sat})-R_{P}(H)]/R_{P}(H_{sat})$ of ~0.5 %. The MR response persists up to T = 290 K with a value of ~0.04%.

This sharp MR switching characteristics is different from the gradual increase in MR observed by Saha *et al.* [15]. This is primarily due to the fact that the edges of the FIB'd MnAs ferromagnet contacts are much smoother than wet etched MnAs edges. A simulation of the domain switching of the edges of wet etched MnAs show gradual switching, which is absent in FIB'd MnAs.

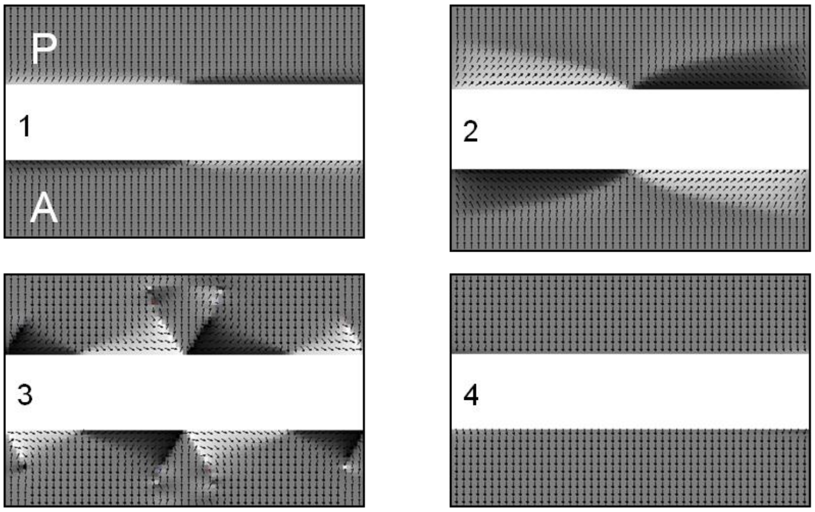

Figure 4.5 Micomagnetic simulation of the domain switching for the edges of a wet etched MnAs film.

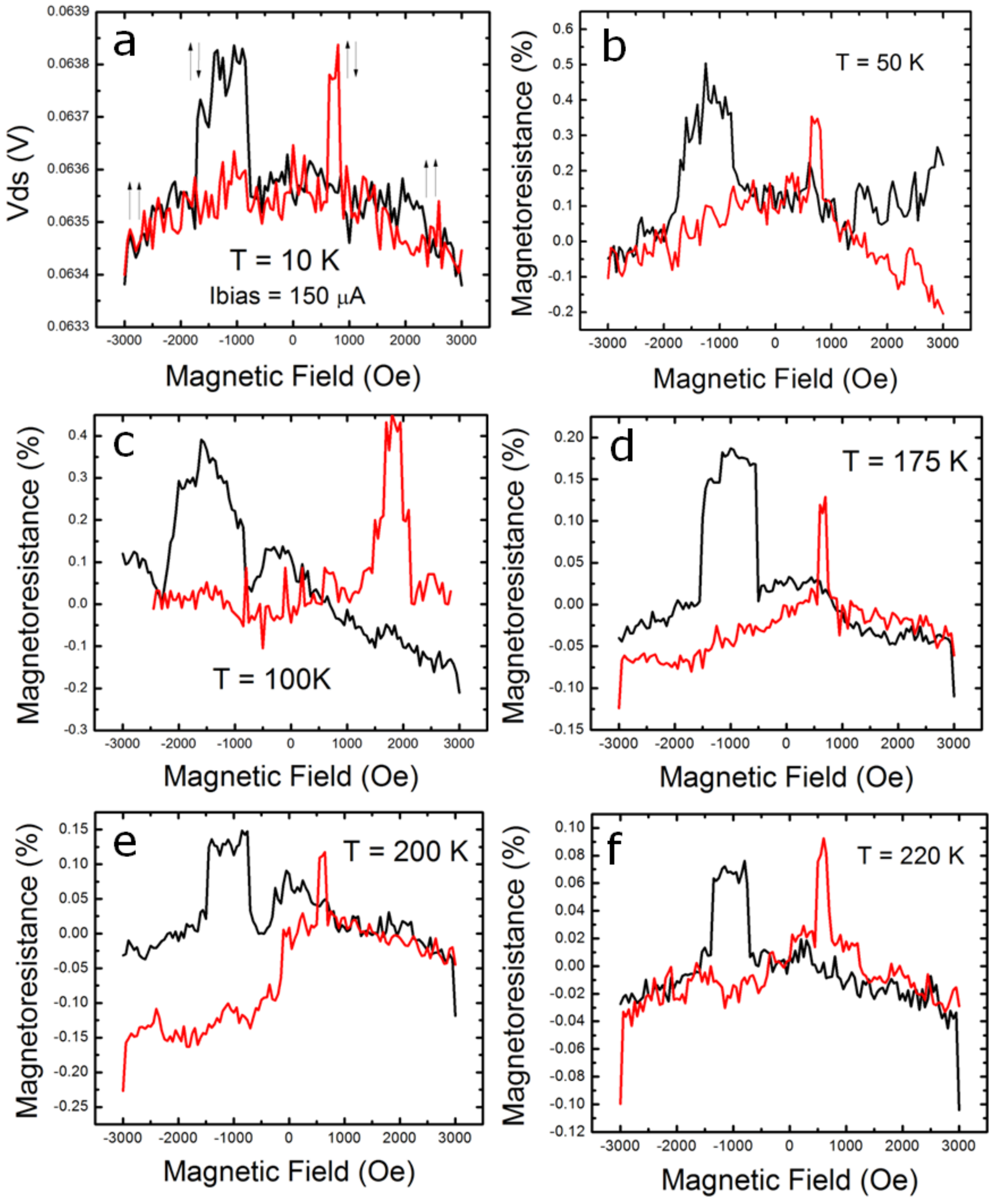

Figure 4.6 Magnetoresistance characteristics of a high temperature lateral spin valve at (a) T = 10 K, (b) T = 50 K, (c) T = 100 K, (d) T = 175 K, (e) T = 200 K, and (f) T = 220K.

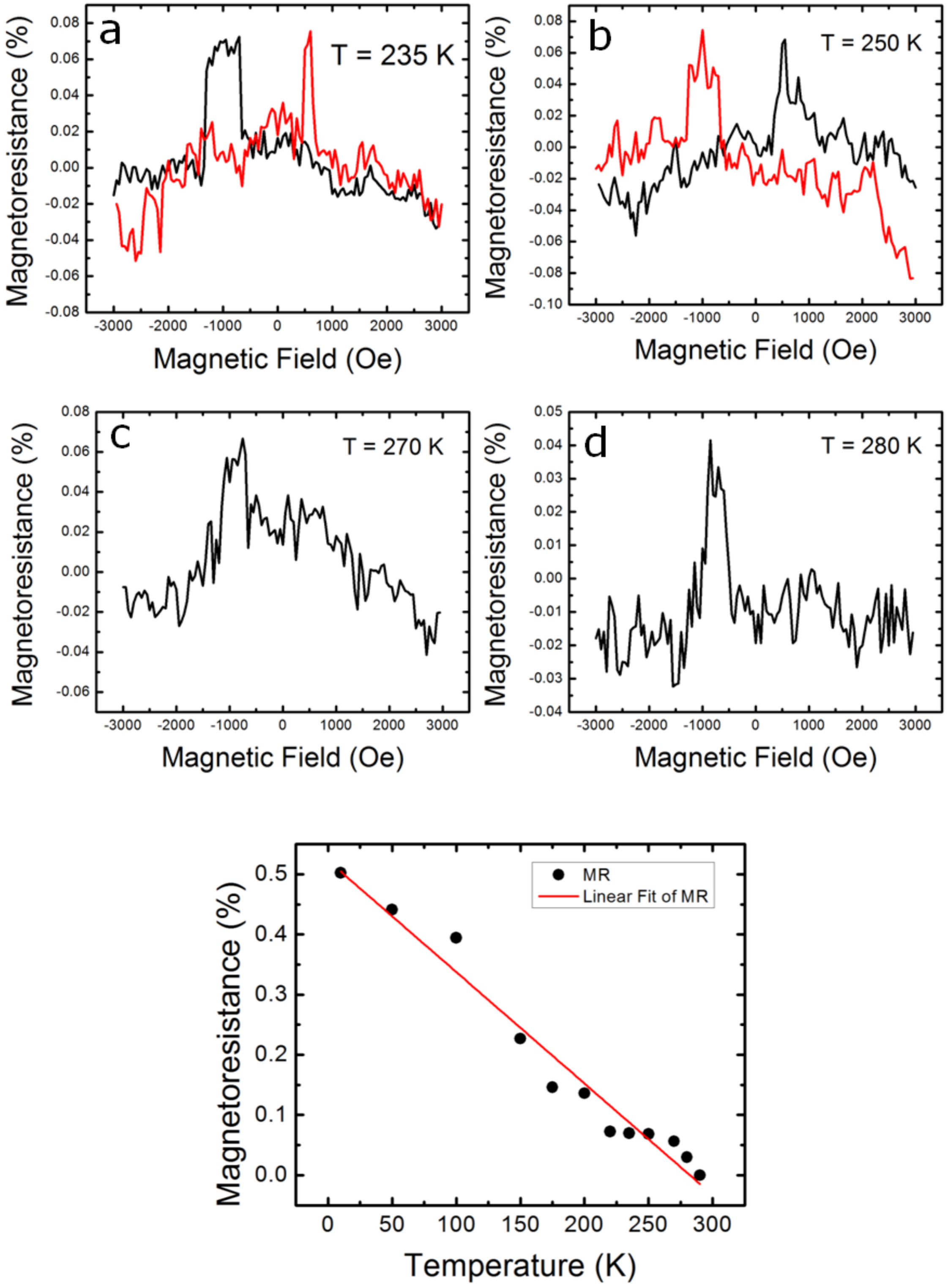

Figure 4.7 Magnetoresistance characteristics of a high temperature lateral spin valve at (a) T = 235 K, (b) T = 250 K, (c) T = 270 K, (d) T = 280 K. (bottom) MR magnitude as a function of temperature.

4.3 MnAs/GaAs/MnAs Vertical Spin Valve

4.3.1 Introduction

Spintronic devices essentially involve the processes of injection, transport, manipulation and detection of spin-polarized carriers. Spin injection, transport and detection in semiconductors are of particular interest because of the relatively long spin coherence length, compared to that in metals, as mentioned in chapter 1. Lateral spin valves with Schottky and insulating tunnel barriers as spin injectors and detectors have been reported, but the operation temperature and the degree of spin-dependent effects are limited by the relatively long channel lengths. While this problem can be partly alleviated by lithographic techniques, a more desirable solution to the problem of spin dephasing is to incorporate spin injection, transport and detection in a vertical heterostructure, where the spin transport length can be precisely controlled to a very small value during epitaxy.

There has been some success with vertical devices incorporating dilute magnetic semiconductors, but the low Curie temperature of these ferromagnetic materials restricts device operation to relatively low temperatures [48]. In this work, we have solved this fundamental problem by using valence band electron tunneling (VBET) in and out of a p-doped semiconductor layer in a vertically stacked heterostructure consisting of ferromagnet and non-magnetic semiconductors. The spin relaxation mechanism in p-doped semiconductors is relatively insensitive to temperature and therefore naturally lends to high temperature operation. Contrary to electron injection in the conduction band and hole injection in the valence band, which pose inherent problems in terms of experimental realization of vertical heterostructures, VBET can be key to the realization of high temperature semiconductor spintronic devices. The spin dependent response in these devices is relatively insensitive to temperature variations and the magnitude of the response can be further enhanced by improving the quality of ferromagnet/semiconductor interface.

4.3.2 Growth and Fabrication

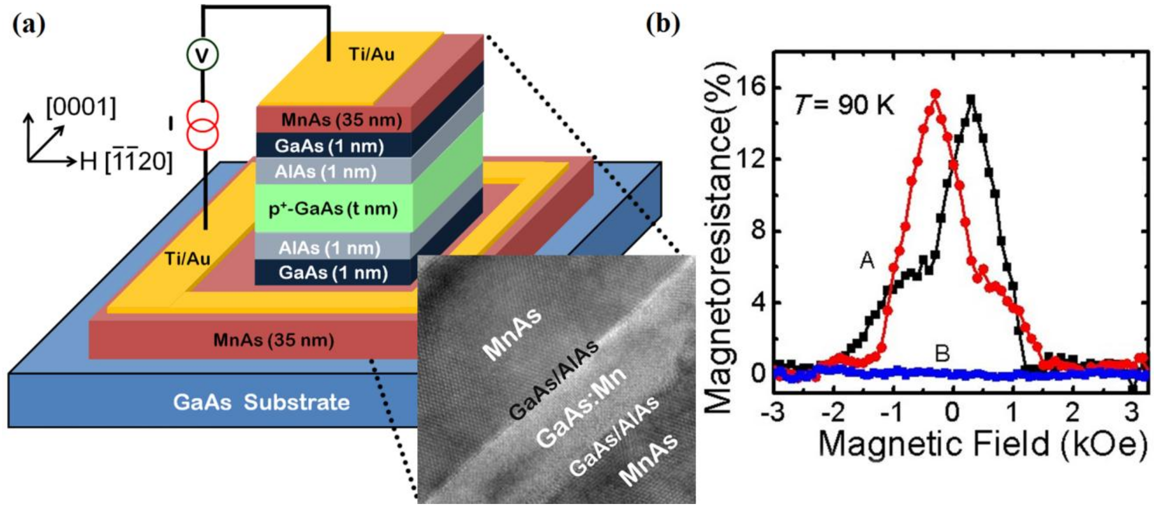

Figure 4.8 (a) Schematic illustration of a MnAs/GaAs/MnAs vertical spin valve. (b) Magnetoresistance characteristics at T = 90 K. The control device with no MnAs spin detector shows no magnetoresistance response.

Figure 4.8(a) shows the device heterostructure. The layers consist of MnAs (35 nm) / GaAs (1 nm) / AlAs (1.5 nm) / p$^+$-GaAs (7 nm, 9x10^{19} cm^{-3} Mn doped) / AlAs (1.5 nm) / GaAs(1 nm) / MnAs (35 nm) on a semi-insulating GaAs (001) substrate. We label this heterostructure as device A. The entire heterostructure was grown at a low substrate temperature of 250 ^{o}C to avoid inter-layer diffusion of Mn atoms and formation of Mn-Mn clusters. The Mn atoms act as p-type acceptors in the GaAs transport layer, and serve a dual purpose: it allows for (1) acceptor doping of the GaAs layer at 250 ^{o}C and (2) growth of device quality GaAs at low temperatures. High resolution transmission electron microscopy (HRTEM) shows abrupt interfaces between each layer (Fig. 4.9). Three control devices were also grown and fabricated. These are labeled B, C, and D.

Table 4.1 Parameters used in designing the various device heterostructures used in our experiment. Full heterostructure consists of substrate/MnAs/GaAs/AlAs/p$^+$-GaAs/AlAs/GaAs/MnAs, while non-full heterostructure consists of substrate/MnAs/GaAs/AlAs/p$^+$-GaAs/AlAs/GaAs/TiAu.

Device	p-GaAs thickness (t)	Mn doping concentration	Full heterostructure
A	7	0.9%	Yes
B	7	0.9%	No
C	7	1.5%	Yes
D	1	0.9%	Yes

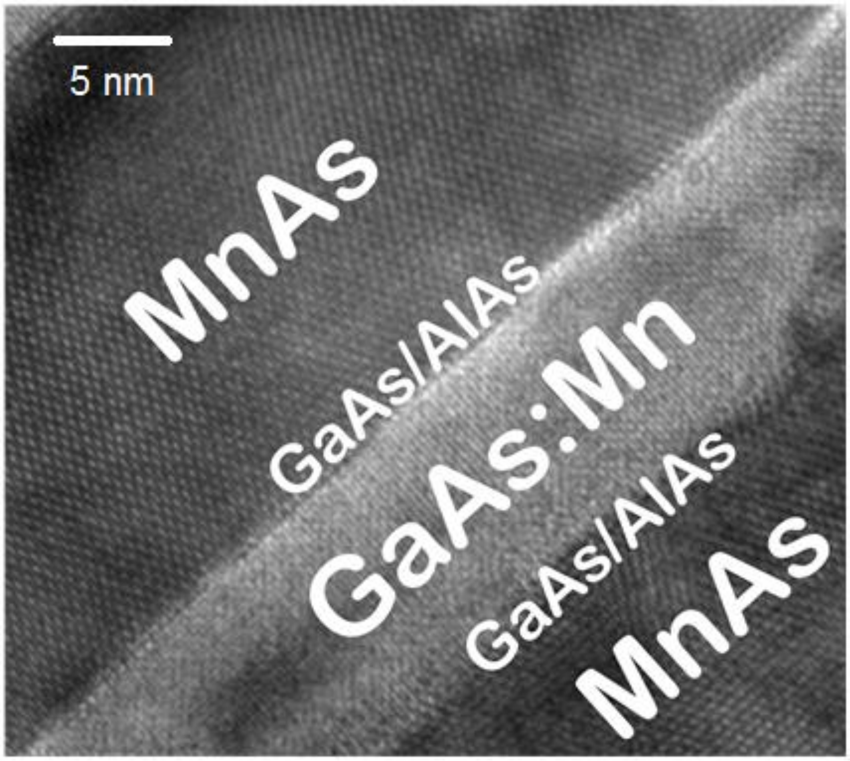

Figure 4.9 High resolution transmission electron microscopy image of the full vertical spin valve heterostructure. The GaAs/AlAs layers are difficult to see due to its contrast being similar to the GaAs:Mn layer.

4.3.3 Magnetoresistance Characterization

Figure 4.8(b) shows the magnetoresistance (MR) of device A and B as a function of magnetic field. The magnetic field is applied in plane along the easy axis of MnAs $[\bar{1}\bar{1}20]$. The two peaks in the magnetoresistance correspond to the anti-parallel alignment of source and drain MnAs pads [49]. The peaks match very well with the coercivity of MnAs pads measured by magneto-optic Kerr effect measurements. No magnetoresistance was observed in control device B where the top MnAs layer was replaced by a non-magnetic Ti/Au contact. It is important to note that the concentration of Mn (0.9%) in the GaAs layer is low and superconducting quantum interference device magnetometry (SQUID) indicates that the Curie temperature is approximately 20 K. Figure 4.10(a) shows the measured peak magnetoresistance of device A as a function of temperature and bias. The magnetoresistance as a function of temperature for devices C and D are shown in Fig. 4.10(b). Although the MR curves look similar throughout the devices (two peaks when the MnAs pads are in anti-parallel alignment), these two devices show much different MR vs. temperature characteristics (Fig. 4.10(b)) compared to the MR vs. temperature characteristics of device A. The measured data can be understood by analyzing the band energy profiles and Fermi levels of the vertical heterostructure.

4.3.4 Band Diagram Analysis

Figures 4.11(a) and (b) show the conduction (E_c) and valence (E_v) band alignment and hole density as a function of position for degenerately ($p = 9 \times 10^{19}$ cm^{-3}) and non-degenerately ($p = 2 \times 10^{19}$ cm^{-3}) doped GaAs under equilibrium ($V_b = 0$), respectively. The band edges were determined by self-consistently solving the Schrodinger and Poisson equations. It can be seen that the Fermi level (E_f) is inside the valence band for

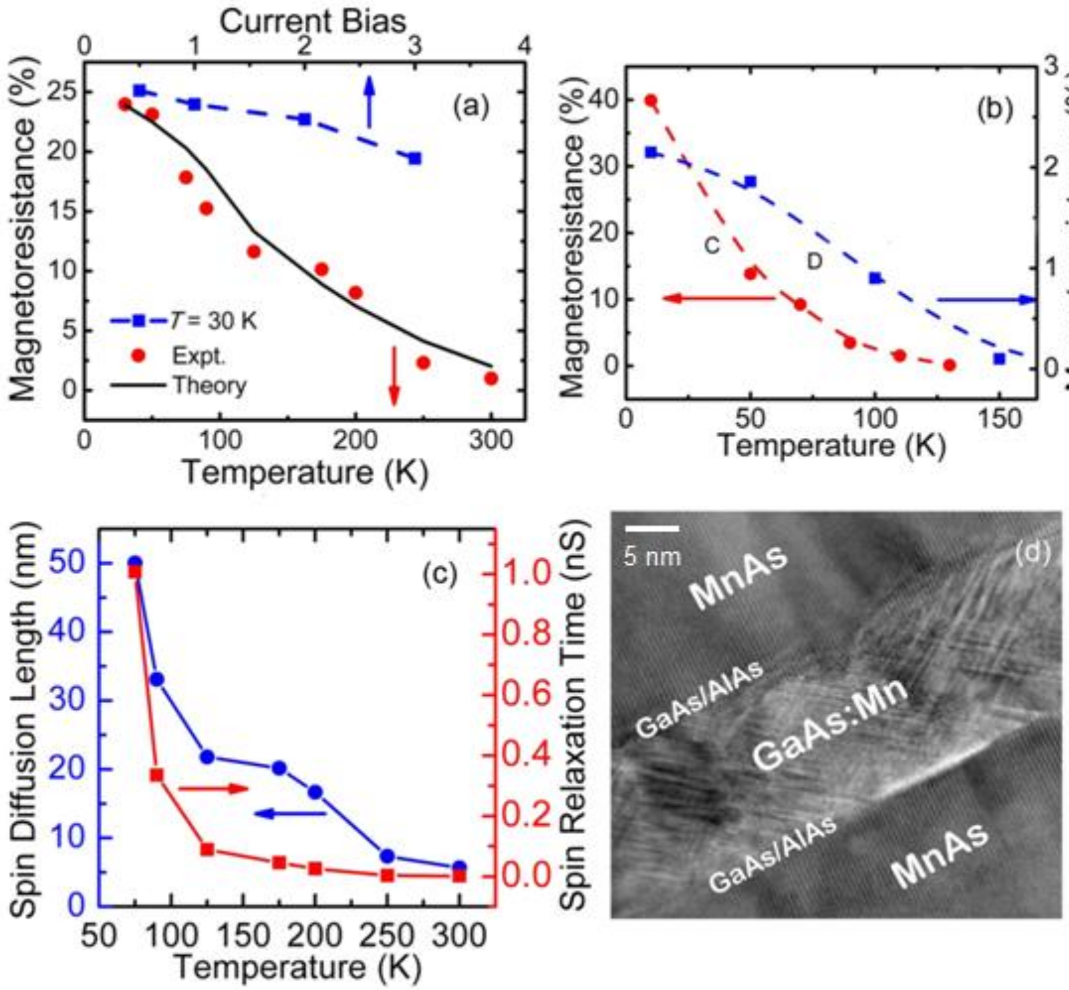

Figure 4.10 (a) measured peak magnetoresistance is shown as a function of temperature and bias. (b) Measured peak magnetoresistance vs. temperature for devices C and D. The dashed lines are guides to the eye. (c) Calculated spin diffusion length and spin relaxation time as a function of temperature. (d) HRTEM image of device C layers.

---

the degenerately doped case, whereas it lies in the bandgap for the non-degenerate case. Under a bias, spin polarized electrons from the Fermi level of the ferromagnet can directly tunnel into the valence band state in the case of degenerately doped GaAs (Fig. 4.11(c)). Since the tunnel barrier is triangular in shape, the tunneling here is similar to Fowler-Nordheim tunneling [50]. There is no such available state for the non-degenerate case and spin injection efficiency decreases dramatically. Figs. 4.11(c) and (d) show band diagrams for applied bias V_b = 1V and 2V, respectively. The change in band bending is

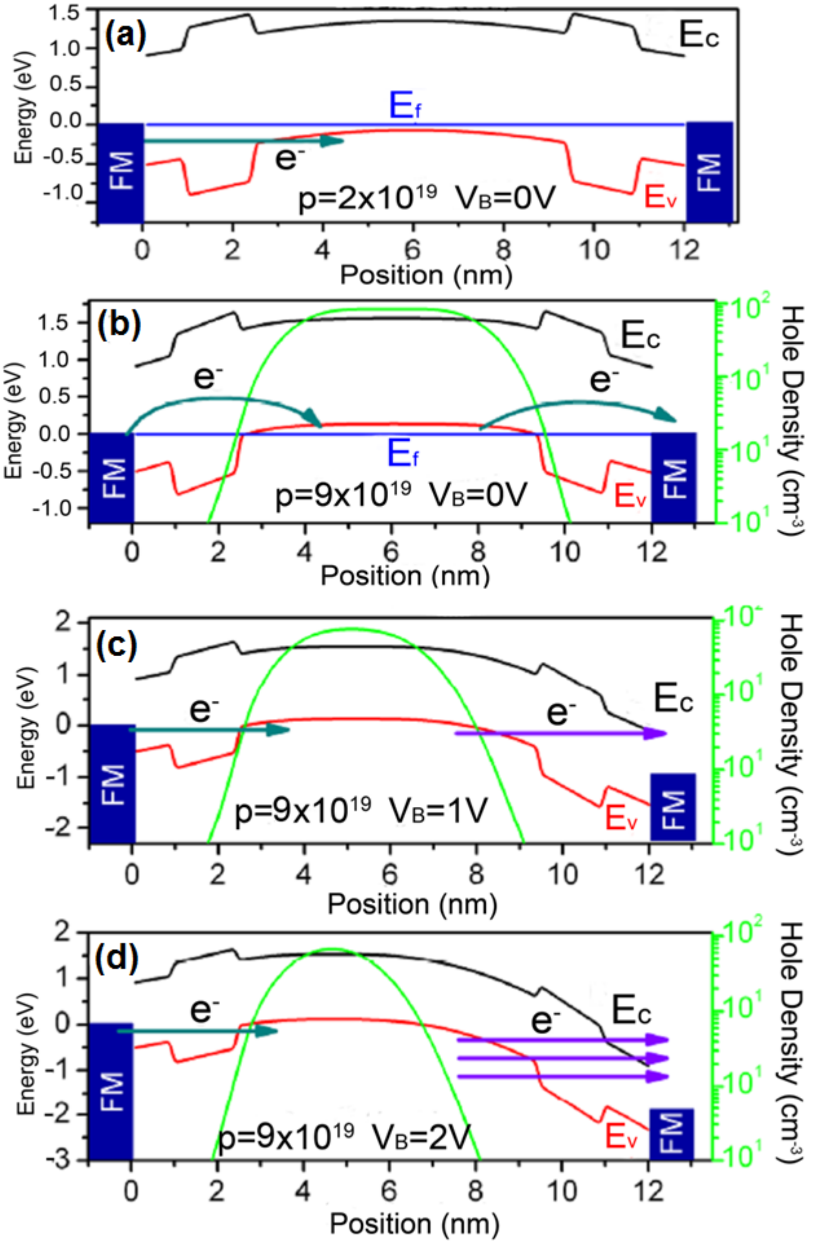

Figure 4.11 Energy band diagrams and electric field profile for different bias conditions and doping concentrations. Band diagrams for (a) p = 9 x 10^{19}cm^{-3} (degenerately doped) and V_B = 0; (b) p = 2 x 10^{19} cm^{-3} (non-degenerately doped) and V_B = 0; (c) p = 9 x 10^{19} cm^{-3} and V_B = 1V (low bias), and (d) p = 9 x 10^{19} cm^{-3} and V_B = 2V (high bias).

mostly restricted to the drain end and there is little change at the source end. The source tunnel barrier thickness and height remain the same and almost all voltage appears across the reverse bias drain terminal. The hole concentration profiles indicate that the drain end depletion width and electric field increases with increasing bias, which leads to the decrease in spin detection efficiency. It may be noted that the electrons tunnel at an energy level which is higher than the Fermi energy at the drain end and the density of states for spin-up and spin-down electrons will change with bias. This effect is also present in tunneling magnetoresistance (TMR) devices [55]. At high enough bias, electrons from the filled valence band states below the Fermi level can tunnel to the empty states of the drain contact (as shown in Fig. 4.11(d)). These unpolarized electrons will not contribute to the spin polarized current. The increasing depletion region width, high electric field, change in ferromagnetic contact polarization and increase in unpolarized current tend to decrease the spin detection efficiency at higher bias values.

The decrease in magnetoresistance with the increase in temperature in device A can be explained by invoking the effects which are commonly associated with vertical devices having single [51] or double tunnel barriers [52]. The effects are (1) decrease in the contact polarization of MnAs with increasing temperature due to spin-wave (SW) excitation; (2) increase in spin independent tunneling (SIT), which does not contribute to magnetoresistance with increasing temperature, and (3) spin-relaxation (SR) in the degenerately doped semiconductor [53]. To determine the degree of contribution from each of these factors and to estimate the spin diffusion length in p^+-doped GaAs, we analyzed the results with the Tsu-Esaki model using Wentzel-Kramers-Brillouin (WKB) approximation for spin injection and detection through tunnel barriers and spin drift-diffusion for spin transport in GaAs [54, 55]. The decrease in effective polarization of MnAs with respect to temperature was determined by SQUID magnetometry. The polarization of MnAs goes to zero at ~320 K and accounts for nearly 50% reduction in magnetoresistance of these devices [56]. To account for the effect of thermally activated spin independent transport we considered a parallel leakage path by hopping conduction in the tunnel barrier. The GaAs/AlAs layer is grown at a much lower temperature and therefore the local defect states can act as hopping sites for electron transport. The temperature (T) dependence of hopping conductance through a series of N localized states is given by [57]:

$$G_{hop} = \sum S_N T^{N-2/N+1}, N = 1,2,... \qquad \textbf{(4.1)}$$

where S_n are determined by the density and nature of localized states. The temperature exponent, $\gamma = N - 2 / (N + 1)$ increases with increasing number of hopping sites and the spin independent hopping conductance goes up. The number of hopping sites is determined to be $N = 2$ from the exponent ($\gamma \approx 1.3$) of temperature dependent current-voltage characteristics of control devices with only one tunnel barrier. A significant degree of spin relaxation occurring in the degenerately p-doped transport layer contributes to a further decrease of magnetoresistance with temperature. Theoretically calculated decrease in magnetoresistance due to the combination of decreasing contact polarization, hopping conductance, and spin-relaxation in the degenerately doped semiconductor layer is plotted in Fig. 4.10(a) and matches well with experimental data. The spin diffusion length (λ) is estimated from the reduction in magnetoresistance from the spin drift-diffusion model. The spin relaxation time ($\tau = \lambda^2 / D$) is determined by using the generalized Einstein relation between diffusion coefficient (D) and mobility (μ) as:

$$\frac{D}{\mu} = \frac{1}{q}\int_0^{\infty} S(E)F(E)dE \Bigg/ \int_0^{\infty} S(E)\frac{\partial F}{\partial E}dE \qquad \mathbf{(4.2)}$$

where S is the density of states, F is the Fermi-Dirac distribution, and q is the electronic charge. Figure 4.10(c) shows the spin relaxation time (τ) and spin diffusion length as a function of temperature. τ decreases very rapidly at low temperature and the long tail indicates that τ is relatively insensitive at higher temperatures. These characteristics can be attributed to the Bir-Aronov-Pikus (BAP) mechanism for spin relaxation which is predominant in p-doped semiconductors, and spin relaxation due to paramagnetic Mn doped GaAs at high temperatures [58, 59]. Therefore, room temperature operation of these devices is not entirely limited by the spin relaxation time in GaAs and spin dependent effects can be increased by improving interface quality and by minimizing the hopping transport.

4.3.5 Control device characteristics

In contrast, the magnetoresistance of devices C and D drops to zero around 150 K. Increase in Mn concentration in device C creates more available states for electrons to tunnel through and leads to a higher magnetoresistance at low temperatures. However, smaller spin diffusion lengths on account of higher Mn doping, together with increased spin independent tunneling (hopping conduction) start dominating at higher temperatures and the magnetoresistance decreases rapidly with increasing temperature (Fig. 4.10(b)). The HRTEM image of this device, shown in Fig. 4.10(d), confirms non-ideal characteristics in terms of Mn clustering and stacking faults, either or both of which could lead to increased hopping conduction. In device D the thin p^+-GaAs layer leads to increased confinement, resulting in a reduced number of available states in the valence band. Thus, spin independent tunneling through defect states dominate, causing a decrease in magnetoresistance measured at low temperatures, as seen in Fig. 4.10(b). The MR values of this device are similar to those reported by Sugahara *et al.* [60] on tunneling magnetoresistance devices. A more complete study of the role of these processes and their dependence on growth parameters is needed.

4.4 Amplification and Control of Magnetoresistance in a Three-Terminal Vertical Spin Valve

4.4.1 Introduction

The overriding goal of the emerging field of spintronics is to develop devices that integrate charge and spin properties of semiconductors to achieve non-volatility, higher processing speeds, higher packing densities, and reduced power consumption [61]. Two fundamental requirements for the realization of successful spintronic devices are the generation and control of spin currents in a non-magnetic semiconductor. The generation of spin currents at room temperature with reasonable polarization by electrical spin injection, using tunnel barriers or Schottky tunnel contacts [62-65] has been quite successful and this has led to the practical realization of devices such as spin light emitting diodes (spin-LEDs) [66], spin lasers [67], and spin valves [68-70]. It is therefore essential to be able to amplify the magnetoresistive effect by controlling the flow of spin polarized carriers in a conventional spin valve. Such control, generally using a third (or gate) terminal, has been proposed [71] by several authors by invoking different physical principles. Some of these include an all-spin logic device with built in memory [72], a multi-terminal fully electrical read/write spin logic device [73], magnetic bipolar junction transistors [74,75], and spin Hall-effect transistors [76]. Of these, at least one, based on the electrical modulation of spin-orbit coupling [77], has been complemented by experiments [78, 79]. Here, we extend on the vertical spin valve discussed above and demonstrate a three-terminal magnetoresistance amplifier.

Higher values of magnetoresistance have been measured at or near room temperature in semiconductor-based tunneling magnetoresistance (TMR) devices [80] and vertical spin valves [81]. This is due to the short tunneling or transport distance in these devices controlled by epitaxial growth. In this work, we developed a new device – a GaAs/MnAs vertical spin valve with a third gate terminal – and produced ~500% modulation of the magnetoresistance at room temperature. The device is produced by a single epitaxial growth step and subsequent processing. The gate terminal effectively shifts the band energy in the GaAs channel and thereby changes spin injection, transport, and detection. The modulation of magnetoresistance has been analyzed by a model based on one-dimensional (1D) spin drift-diffusion and the voltage dependence of tunneling resistance at the tunnel injector contacts. The device can be used as a non-volatile magnetic memory and can be integrated with GaAs based microelectronics circuits [82].

4.4.2 Growth and Fabrication

Fully epitaxial vertical spin valve heterostructures consisting of MnAs (35 nm) / undoped-GaAs (0.5 nm) / undoped-AlAs tunnel barrier (1 nm) / p+-GaAs channel (10 nm, $1\text{x}10^{19}$ Mn-doped) / undoped-AlAs (1 nm) tunnel barrier / undoped-GaAs (0.5 nm) / MnAs (25 nm) were grown by molecular beam epitaxy (MBE) on semi-insulating GaAs (100) substrate. The heterostructure was grown at a substrate temperature of 250 ˚C for the bottom MnAs layer, and 200 ˚C for subsequent layers to avoid interlayer diffusion of Mn atoms and formation of Mn-Mn clusters.

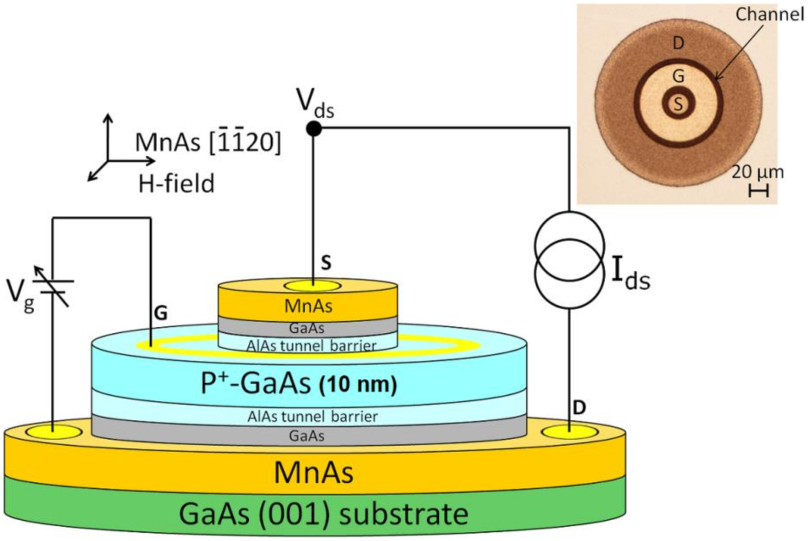

Figure 4.12 Schematic diagram of the device heterostructure and measurement scheme. Inset shows a micrograph of a fabricated device before passivation and metallization. The top MnAs electrode is 15 um in diameter, the channel region is 75 µm in diameter, and the bottom MnAs is 200 um in diameter.

The Mn atoms allow low temperature p-doping of GaAs without affecting the MnAs/GaAs interface, which is otherwise difficult to achieve. The 0.5 nm GaAs layers are grown to provide a smooth surface for growth of successive layers and to prevent interdiffusion between AlAs and MnAs. It may be noted that besides acting as a tunnel barrier for efficient spin injection and detection, the AlAs layers also prevent segregation of Mn atoms at the MnAs/GaAs:Mn interface.

Standard optical lithography was used to fabricate the devices in circular mesas, as shown in Fig. 4.12. Besides the two ferromagnetic type-A MnAs spin injector and detector electrodes, a third “gate” electrode (Ti/Au) was deposited on top of the heavily p-doped GaAs semiconducting channel layer via e-beam assisted evaporation and lift-off. The most critical step in fabricating this device is etching the top MnAs contact and the 1 nm GaAs buffer layer. Since the channel is extremely thin (~7-10 nm) and can easily be destroyed while attempting to create the top MnAs contact. There is no method to consistently fabricate good devices; therefore, multiple wafers were processed with varying etching times. Out of approximately 100 devices, only 2-3 devices showed acceptable I-V characteristics. The coercivity of the topmost MnAs layer is shown in Fig. 4.13.

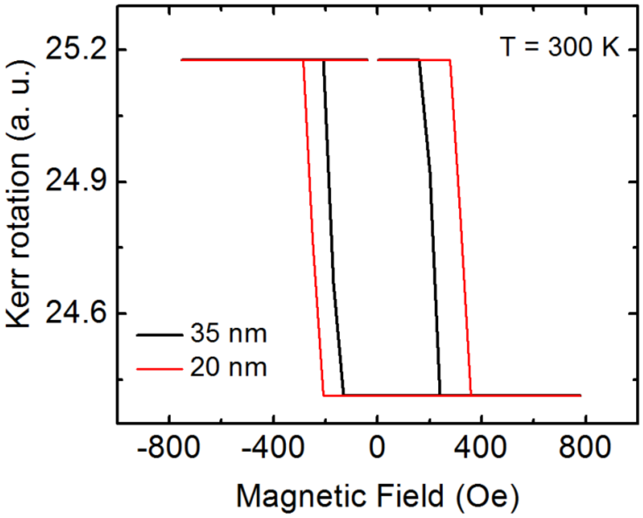

Figure 4.13 Magneto-optic Kerr effect (MOKE) measurement of the top and bottom MnAs ferromagnetic contacts. The hysteresis characteristics indicate good ferromagnetic behavior of both MnAs layers.

4.4.3 Magnetoresistance characteristics

Magnetoresistance (MR) measurements were made with the devices in a closed-loop He cryostat placed between the poles of an electromagnet. The magnetic field is applied in-plane along the easy axis of MnAs $[\bar{1}\bar{1}20]$. Measurements were first made with no bias (gate floating) applied to the gate (third) terminal, the device thereby behaving as a vertical spin valve. The characteristics of such a device [81] and similar two-terminal vertical devices [83] have been described in the previous section, but are described here for completeness. As will be evident later, analysis of the magnetoresistance behavior of such a device helps us to explain the observed characteristics of the three-terminal device.

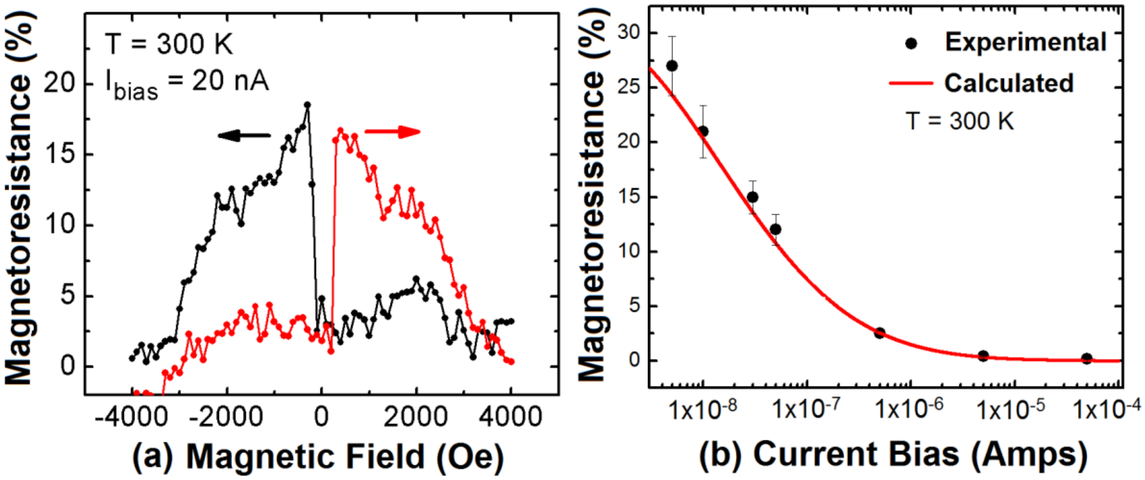

Figure 4.14 (a) Magnetoresistance response at a current bias (I_{ds}) of 20 nA at T = 300 K. The arrows indicate magnetic field sweep direction. (b) Measured and calculated magnetoresistance as a function of current bias at T = 300 K.

A constant dc bias current (I_{ds}) is applied between the two MnAs contact layers (source and drain) and the voltage V_{ds} is measured between the same terminals while varying the applied magnetic field. The magnetoresistance response at a bias current of 20 nA measured at room temperature is shown in Fig. 4.14(a). The magnetoresistance is calculated as MR = $(V_{AP} - V_P) / V_P$, where V_P and V_{AP} are the measured terminal voltage V_{ds} for parallel and anti-parallel alignment of the two MnAs contacts. With optimized device design and epitaxial growth of the ferromagnet-semiconductor heterostructure, we are able to achieve a value of MR $\cong$ 27% which is the largest reported in any semiconductor spin valve at room temperature. The measured variation of MR with bias current is shown in Fig. 4.14(b), where a decrease of MR with increasing bias is observed. The magnetic field difference, ΔH, between the peaks of the magnetoresistance response between positive and negative sweep of the magnetic field at various temperatures was measured. The peaks of the MR curve arise due to the anti-parallel alignment of the top and bottom MnAs layers. It is seen that with increase of temperature from 10 K to 300 K, ΔH decreases from 1600 to 250 Oe, which is related to the decrease in coercivity of the MnAs layers with increasing temperature [84]. No magnetoresistance was observed in control devices with (a) channel thickness much greater than the spin diffusion length and (b) the top MnAs contact replaced by a non-ferromagnetic Ti/Au contact.

4.4.4 Amplification of magnetoresistance

The results of three-terminal measurements, with the application of a gate bias, are described next. With reference to Fig. 4.12, a constant current bias I_{ds} is applied between the two MnAs contacts and a voltage V_g is applied to the gate terminal. The two MnAs contacts are successively set in parallel and anti-parallel magnetization with the application of appropriate magnetic fields (depending on the individual coercivities of the contacts) and in each case $V_{ds} = V_P$ or V_{AP} is measured as the gate bias is varied.

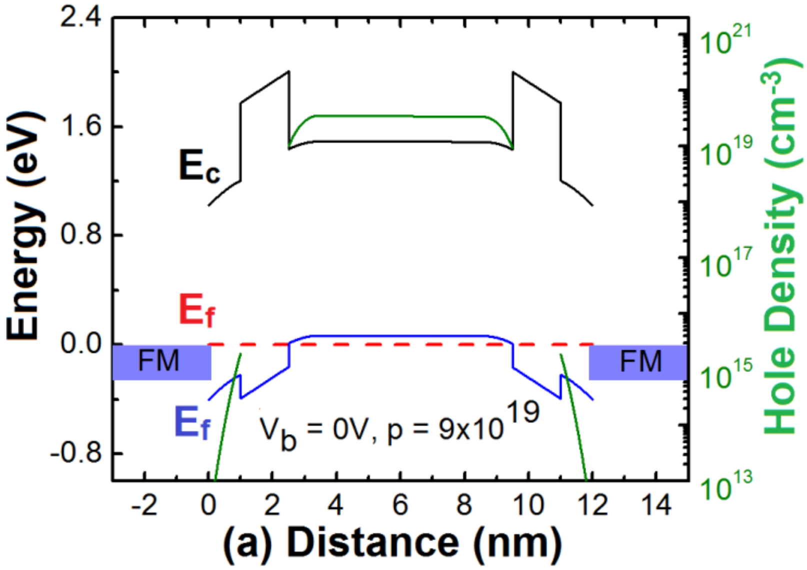

Figure 4.15 Calculated energy band diagram of the vertical spin valve heterostructure. The channel is degenerately p-doped, and the Fermi-level lies within the valence band of the p^+-GaAs channel.

Figures 4.16(a) and (b) depict the measured variation of MR with V_g at room temperature for two values of I_{ds}. The control of magnetoresistance with the gate terminal is evident. Very large values of magnetoresistance are measured in our experiment.

In order to understand the variation of MR with current bias in the two-terminal spin valve and the control of MR with the gate electrode, it is first important to note that the GaAs channel is heavily doped p-type (p ~ $9x10^{19}$ cm^{-3}) with Mn acceptors. The Mn concentration at this doping level is ~0.9%, for which there is no ferromagnetism at room temperature [85] and the Curie temperature is ~20 K [86].

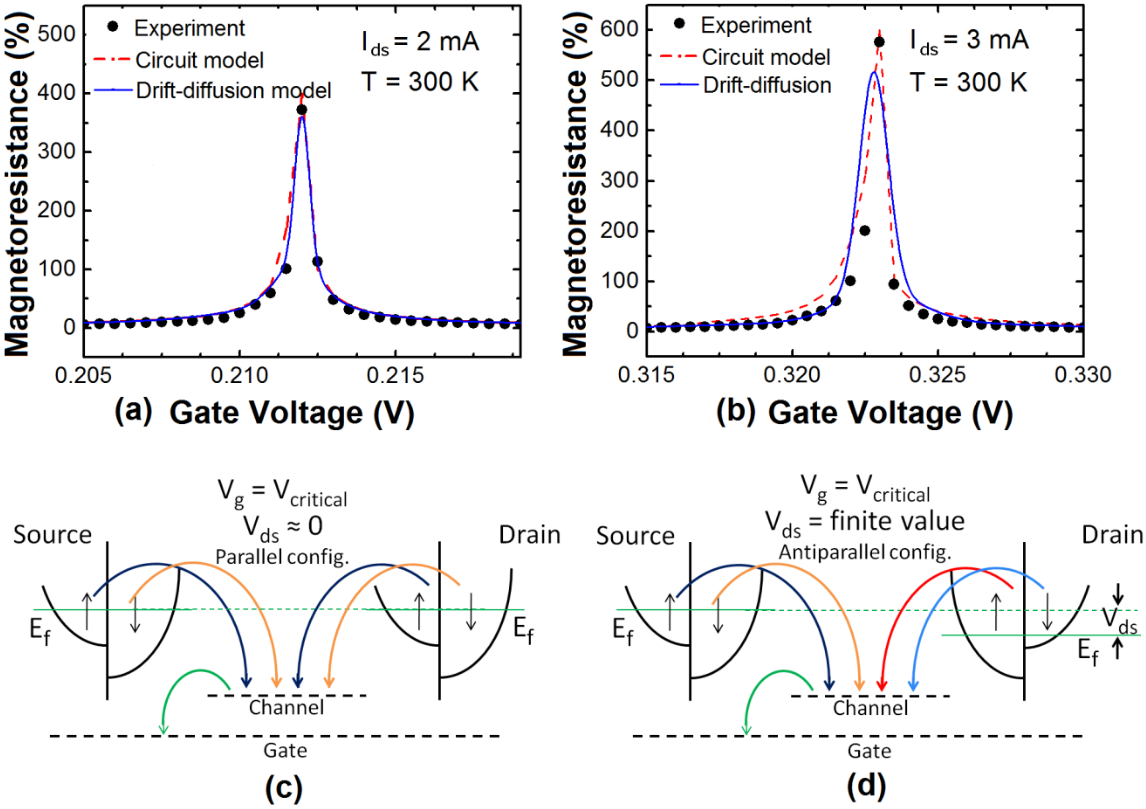

Figure 4.16 Measured and calculated magnetoresistance as a function of gate voltage at T = 300 K at a current bias of (a) 2 mA and (b) 3 mA. The band alignment and current flow when $V_g = V_{critical}$ are shown in (c) and (d) for the parallel and antiparallel MnAs contact alignments, respectively.

The band diagram of the two-terminal heterostructure spin valve with the Schottky tunnel injector contacts, together with the doping profile and the Fermi levels are obtained by a self-consistent solution of the Schrödinger and Poisson equations and are shown in Fig. 4.15 for zero applied bias.

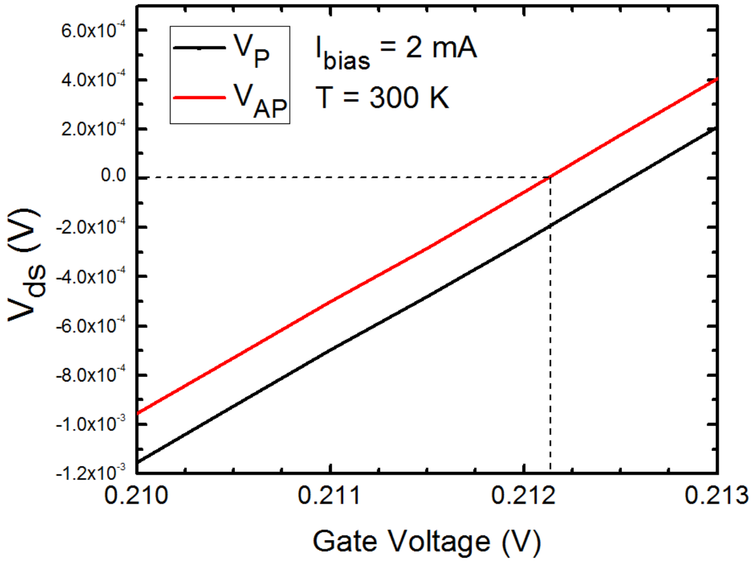

Figure 4.17 Measured parallel and antiparallel (black and red lines, respectively) voltages as a function of applied gate bias. The dotted line shows the region of magnetoresistance amplification.

With an applied current bias, spin polarized electrons injected by the source MnAs/AlAs/GaAs tunnel barrier are transported across empty valence band states at the Fermi energy in the GaAs channel and are collected at the drain ferromagnet-semiconductor Schottky tunnel contact [81]. At the same time, the band bending in the semiconductor changes, mostly at the drain end, accompanied by a change in width and height of the drain Schottky tunnel barrier (see supplementary document). In effect, the interface resistance and spin selectivity of the tunnel contacts are modulated. Additionally, at high values of applied bias, unpolarized electrons from filled valence band states below the Fermi level in GaAs can tunnel into the MnAs contact layer and result in a component of unpolarized current. The bias dependence of magnetoresistance due to the changes in the bands and contacts is analyzed by describing spin transport with the drift-diffusion model of Valet and Fert [87], and Yu and Flatte [88]. Tunneling across the source and drain Schottky barriers is analyzed with the Tsu-Esaki model [89] using the WKB approximation and assuming that there is no spin scattering at the ferromagnet-semiconductor interfaces. The spin diffusion length at room temperature in the p-doped GaAs is obtained from our temperature-dependent measurements reported earlier [81]. Thus, the bias dependence of the tunneling resistance and the MR of the device are obtained. A two-channel model for spin-up and spin-down carriers across the device is described in the supplementary document, together with the relevant equations. Spin injection into a semiconductor material causes the electrochemical potential of spin-up and spin-down electrons to split in the channel. Although the transport direction is vertical in this device, the physics is similar to a lateral spin device, allowing us to model spin transport in this structure using the widely known two-channel spin transport model [90]. The calculated variation of MR with bias in the two-terminal spin valve is shown alongside the measured data in Fig. 4.14(b) and the agreement is very good. Values of the parameters used for the calculations are: $m_e = 0.067m_0$, $N_A = 9x10^{19}cm^{-3}$ for the effective mass and doping density of the p^+-GaAs channel, and $L_{sf} = 5$ nm, $\tau_{sf} = 0 .1$ ns for spin diffusion length and relaxation time at room temperature, respectively. The bias dependent parameters (spin selectivity (γ) and resistance area product (r_b*)) are given in the following section.

4.4.5 Drift-diffusion analysis

Spin injection and detection across the heavily p-doped GaAs channel is modeled by the established spin drift-diffusion model [91-92], given as:

$$\nabla^2(\mu_\uparrow - \mu_\downarrow) + \frac{eE}{k_B T}\cdot\nabla(\mu_\uparrow - \mu_\downarrow) - \frac{(\mu_\uparrow - \mu_\downarrow)}{[L_s]^2} = 0 \tag{4.3}$$

where $\mu_{\uparrow(\downarrow)}$, E, and L_s are electrochemical potential, electric field, and spin flip length, respectively. We assume no spin scattering at the FM/SC interface and current continuity across all interfaces. The majority and minority electrochemical potentials across the FM/SC interface is given as [93]:

$$\begin{gathered}\Delta\mu_\downarrow(z_0) = 2qr_b^*(1+\gamma)J_\downarrow \\ \Delta\mu_\downarrow(z_0) = 2qr_b^*(1+\gamma)J_\downarrow\end{gathered} \tag{4.4}$$

where r_b * is the interface resistance-area product and γ is the spin selectivity. The values of r_b* and γ are dependent on the voltage applied across the device, and are shown in Figures 4.18(a) and (b) for parallel and antiparallel configuration of the ferromagnetic electrodes for a current bias (I_{ds}) of 2 mA, respectively.

The Tsu-Esaki model [89] is used to calculate the tunneling current for both spin-up and spin-down currents, $J_\uparrow$ and $J_\downarrow$. The calculated I-V characteristics for majority and minority bands are then used self-consistently with the majority and minority electrochemical potentials in the spin drift-diffusion model to calculate the total device resistance in the parallel (R_p) and antiparallel (R_{ap}) states of the ferromagnetic injector/detector, where R_p and R_{ap} are defined similar to the two-current model given in [90]. The magnitude of MR is optimistically defined as MR = (R_{ap} –R_p) / R_p.

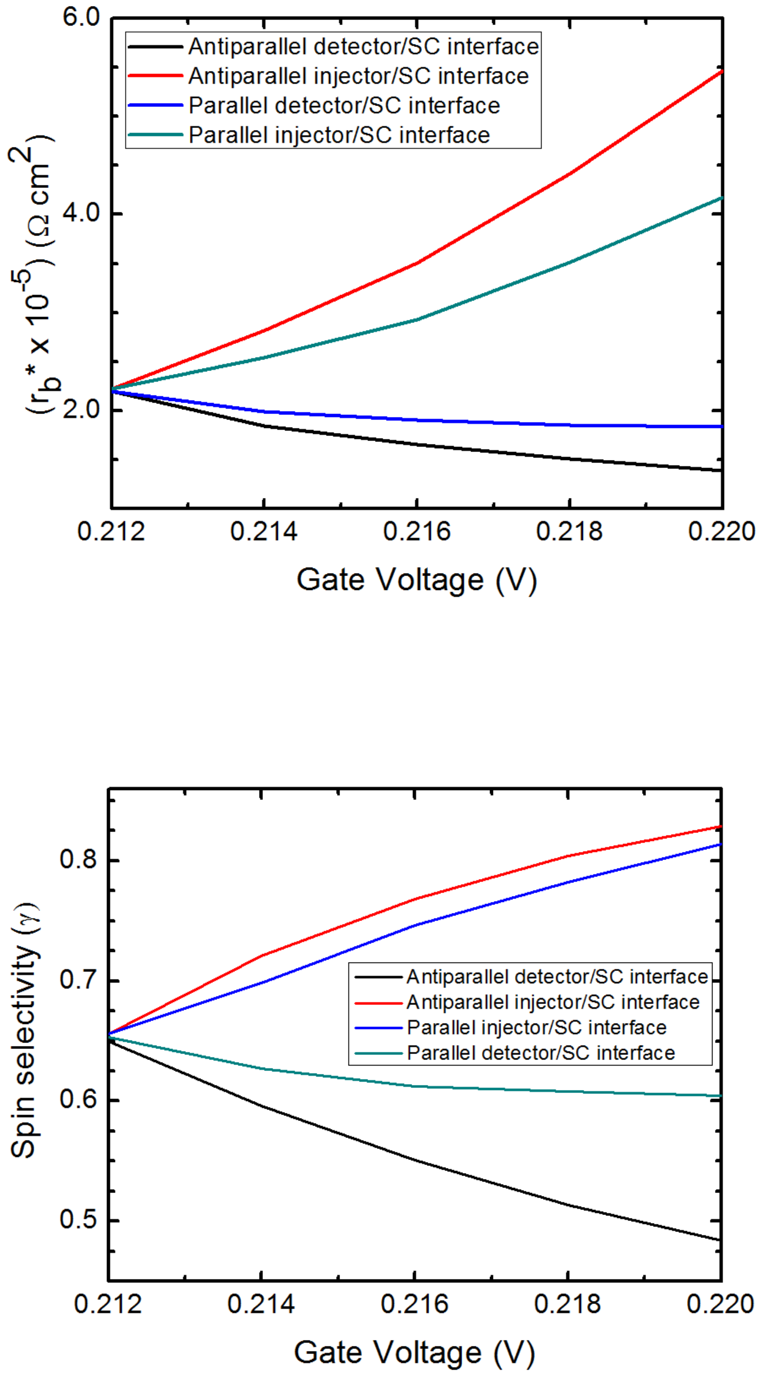

Figure 4.18 Calculated spin-dependent interface resistance-area product (r_b) and the spin selectivity (γ) for various injector/detector configurations.

The band energy profiles of the vertical spin valve are shown in Fig. 4.19 with a bias of 1 V and 2 V, respectively. It can be noted that the band bending is mostly affected at the drain end.

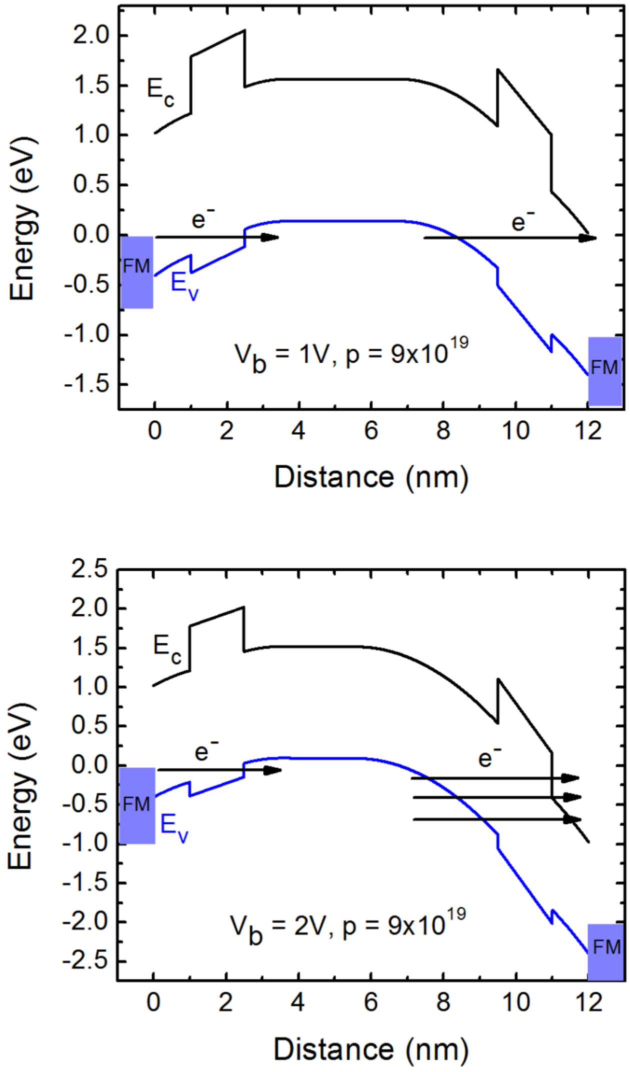

Figure 4.19 The band energy profiles of the vertical spin valve for a source to drain bias of 1 V and 2 V, respectively. It can be noted that the band bending is mostly affected at the drain end, and that increasing unpolarized electrons contribute to the current.

4.4.6 Resistive model analysis

To understand the increase, peaking, and near-symmetrical decrease of the magnetoresistance with gate bias, reference is made to the simple resistive model of the device shown in Fig. 4.20. R_{t1} and R_{t2} are the magnetization and bias dependent interface resistance of the drain and source Schottky tunnel contacts, respectively, R_d is the series resistance of the p-doped GaAs channel, and R_g is the resistance of the gate contact. With no applied gate bias (gate terminal floating), the voltage measured across the device is $V_{ds} = |I_{ds}| (R_{t1} + R_{t2} + R_d)$, where $|I_{ds}|$ is the magnitude of the constant current bias applied across the device. When a gate bias is applied, the bands in GaAs and the tunnel barrier thickness are changed, mostly at the drain contact. A current I_g will flow across R_g and a reduced current $(|I_{ds}|-I_g)$ will flow across R_d and R_{t2} to obey Kirchoff's current law; consequently $V_{ds} = (|I_{ds}|-I_g)(R_{t2}+R_d)+|I_{ds}|R_{t1}$. The current flowing through R_{t1} is always equal to I_{bias} since I_{bias} is an externally applied constant current bias. Similarly, when $I_g = |I_{ds}|$, no current flows across R_{t2} and R_d and $V_{ds} = |I_{ds}|R_{t1}$. With increasing V_g, I_g becomes larger than $|I_{ds}|$ and at a critical value of V_g, the net voltage drop across the source and drain terminal is made zero (voltage drop across R_{t1} is equal to the voltage drop across R_d

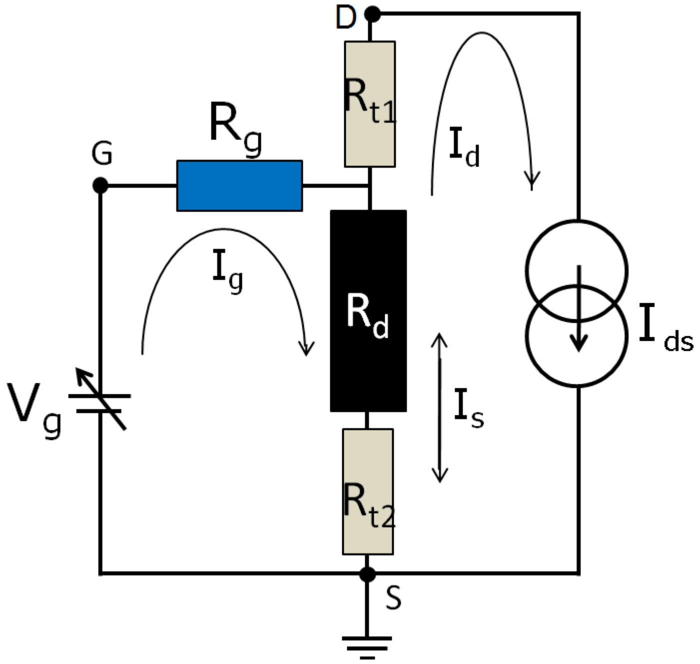

Figure 4.20 Simple circuit model of the three-terminal device.

and R_{t2}, but opposite in sign). At this critical gate voltage, in the parallel magnetization configuration of the two MnAs contacts, $V_{ds} = V_p \approx 0$ and MR becomes very large. At this point there is no net tunneling between the source and drain contacts and the alignment of the bands in the ferromagnets and GaAs together with current flow and Fermi levels, for both parallel and antiparallel alignments, are schematically shown in Figs. 4.16 (c) and (d), respectively. For larger values of V_g, the polarity of V_{ds} is reversed and finite in value (voltage drop across R_{t1} is smaller compared to the voltage drop across R_d and R_{t2}), leading to a sharp decrease of MR. The rise and fall of MR is near symmetric with V_g, as observed experimentally, since the change of V_{ds} with V_g is also near-symmetric around $V_{ds} \cong 0$ (as seen in Fig. 4.17). As I_{bias} is increased, the critical value of V_g, for which MR is a maximum, should also increase since a larger current I_g would be required to offset I_{bias}. This is observed experimentally as seen in Figs. 4.16(a) and (b). The calculated variation of MR with V_g, with respect to the equivalent circuit of Fig. 4.20, is shown by the dashed curves in Figs. 4.16(a) and (b) and is in reasonable agreement with measured data. Also shown by the solid curves in Figs. 4.16(a) and (b) are the calculated MR in accordance with the self-consistent drift-diffusion and tunneling model. The observed variation of MR with V_g is a result of the change in the effective bias applied between the two MnAs Schottky tunnel contacts, which change the band bending in GaAs, the tunnel barrier thickness, and the interface resistance and spin selectivity of the tunnel contacts. In effect, the gate terminal modulates the spin current collected at the drain terminal.

At a critical gate bias, when the two ferromagnetic electrodes are in the parallel configuration, the voltage drop across the device ($V_{ds\text{-}parallel}$) will be near zero (state 0).

When the electrodes are in the anti-parallel direction, the voltage drop ($V_{ds\text{-}antiparallel}$) will be some finite value (state 1). The dual state of this device allows it to be a single bit for a storage element, and the state of this device is determined solely by the relative polarization of the injector/detector ferromagnetic electrodes. Although a magnetic tip would be required for MnAs based devices to switch the device from either parallel or antiparallel state, several ferromagnets exhibit electrical control of magnetism [35] which could be utilized to create an all electrical non-volatile spin memory arrays that are reconfigurable and monolithically integrated with conventional GaAs based microelectronics.

4.5 Mesa Size Dependent Magnetoresistance in a Lateral Semiconductor Spin Valve

Lateral spin valve devices with semiconducting channels have the potential for use in future spin-based information process technology [94]. However spin injection and detection processes are still very inefficient in these devices. For example, in a two terminal local measurement setup the magnetoresistance (MR) values achieved to date are far smaller than the maximum limit of $p^2/(1-p^2)$ [95-97], p being the spin-injection or detection efficiency. In such devices, it has already been discussed that reducing the distance between the injector and detector pad shorter than the spin-diffusion length (λ_s) will reduce spin-relaxation in the current path leading to an increase of MR [98,99]. However this criterion by itself will not achieve the maximum MR. Channel regions outside the current path, which usually remain unetched (see Fig. 4.21), may also act as a source of spin-relaxation and significantly decrease the MR response and forms the subject-matter of this letter. It may be noted that Fert *et al.* [99] and Dery *et al.* [100] have also briefly discussed the influence of extended mesa on MR using spin-diffusion equation. But in this study, we move a step forward to identify, using a simple circuit level description, when such effects play a significant role on MR and verify our results by comparing with preliminary experimental data.

This study serves a three-fold purpose: 1) it introduces a compact circuit-level description of spin transport that is derived from a one dimensional spin-diffusion equation and thus, enables circuit-level insights to assist the optimization of *local two probe lateral* spin-valve devices, 2) it provides an analytical expression for MR, derived from the mentioned circuit model, when the channel length is smaller than spin-diffusion length and identifies the parameters which are responsible for reducing the MR in such a case and describes the conditions under which an extended mesa region beyond the ferromagnetic contacts significantly reduces the MR and finally, 3) it provides preliminary experimental data that seems to support the conclusions. *This work was done in collaboration with Prof. Datta's group in Purdue University. The theory, which is outlined in appendix D for completness of this study, was developed by Abu Naser Zainuddin at Purdue.*

Fig. 4.21(a) and (b) show a side-view of lateral spin-valve with an unetched mesa and completely etched mesa, respectively. Spin transport in such structures are usually described by the spin diffusion equation [101-103] which is valid in the limit where spin-diffusion length is larger than the mean free path [101]. Including an interfacial conductance [104] to account for the ferromagnet-tunnel barrier (FM-TB) the spin-diffusion equation can be written as (V: applied bias),

$$\frac{d^2\mu_x^{+,-}}{dx^2} = (\mu_x^{+,-} - \mu_x^{-,+})/2\lambda_s^2 + 2r_{sc}g_c^{+,-}(\mu_x^{+,-} - V), \text{ under contacts (eq. 1)}$$

$$= (\mu_x^{+,-} - \mu_x^{-,+}) / 2\lambda_s^2 \text{, elsewhere}$$

where $\mu_x^{+,-}$ is the spin-dependent electrochemical potential along the transport direction (x) for majority (+) and minority (-) spins. r_{sc} is the sheet resistance of the semiconducting channel in Ω/m. g_c^+ and g_c^- are the spin dependent interfacial conductances of FM-TB contacts in $m^{-1}\Omega^{-1}$ for '+' and '-' spins, respectively.

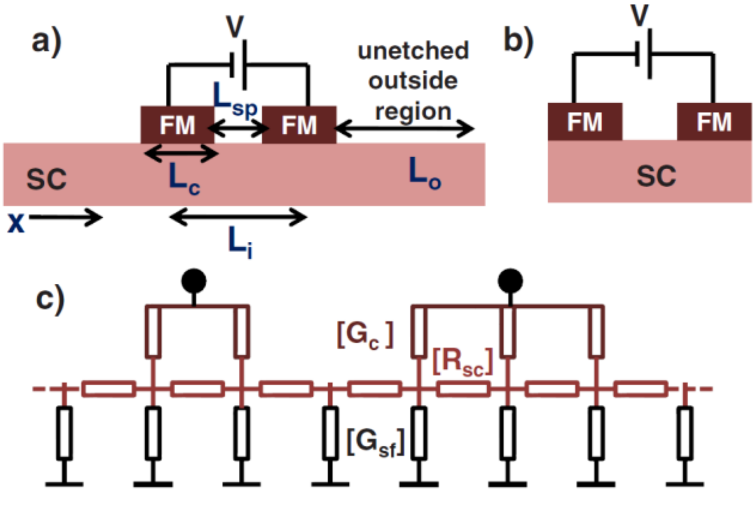

Figure 4.21 Schematic representation of a lateral spin valve with (a) extended regions outside the current path and (b) etched regions outside the current path; (c) A distributed network of spin dependent series and shunt circuit elements representing the structure in (a).

To verify the dependence of MR with unetched regions outside the current path, multiple two-terminal spin valves with varying mesa sizes were fabricated on a semi-insulating GaAs substrate with MnAs as the spin injector/detector [95]. The unetched mesa length, L_o and the channel length (<100 nm) for each of these devices were precisely defined by using the focused-ion-beam (FIB) technique**.** A standard two terminal local MR measurement [95] was performed as a function of unetched mesa length (L_o) for devices with contact length (L_c) of ~1.5 μm. Fig. 4.23(a) shows a top view of a device before and after the mesa etch. Measurements were done at 10 K in a temperature controllable cryostat.

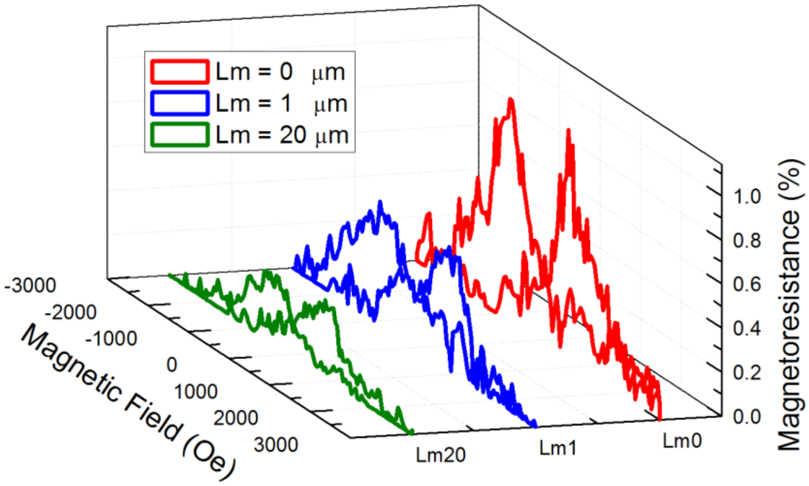

Figure 4.22 Magnetoresistance characteristics as a function of unetched mesa region length. An increase in magnetoresistance is clearly observable as the mesa outside the current path is etched away.

In Fig. 4.23(b) preliminary experimental R_p and R_{ap} data are shown as a function of L_o under fixed I_{bias} = 150µA. Here R_{ap} reduces with L_o whereas R_p stays the almost same. These two trends can be understood from the simple circuit diagrams in Fig. 4.23(c) based on the lumped network described earlier. In the parallel configuration, g_c^+ and g_c^- form a balanced `Wheatstone bridge', leading to a negligible loading effect on $V_{measured}$ due to change in g_s^o with L_o. But the anti-parallel configuration creates significant imbalance in the bridge, which drives a shunt current through both g_s^i and g_s^o. Here, g_s is the spin-relaxation conductance ($m^{-1}\Omega^{-1}$) connecting both spin channels, and is given by $1/(4r_{sc}\lambda_s^2)$. The superscript *i* and *o* indicate inside and outisde the spin current path, respectively. So an increase in g_s^o eventually loads down $V_{measured}$. By calculating the slope of $R_{p(ap)}$ with respect to x^o (as $x^o \propto L_o$) from Equation 2 (appendix D), it is seen that R_{ap} decays faster than R_p with L_o. The experimental data was compared against the two models presented in this article, by solving Equation 1 numerically and

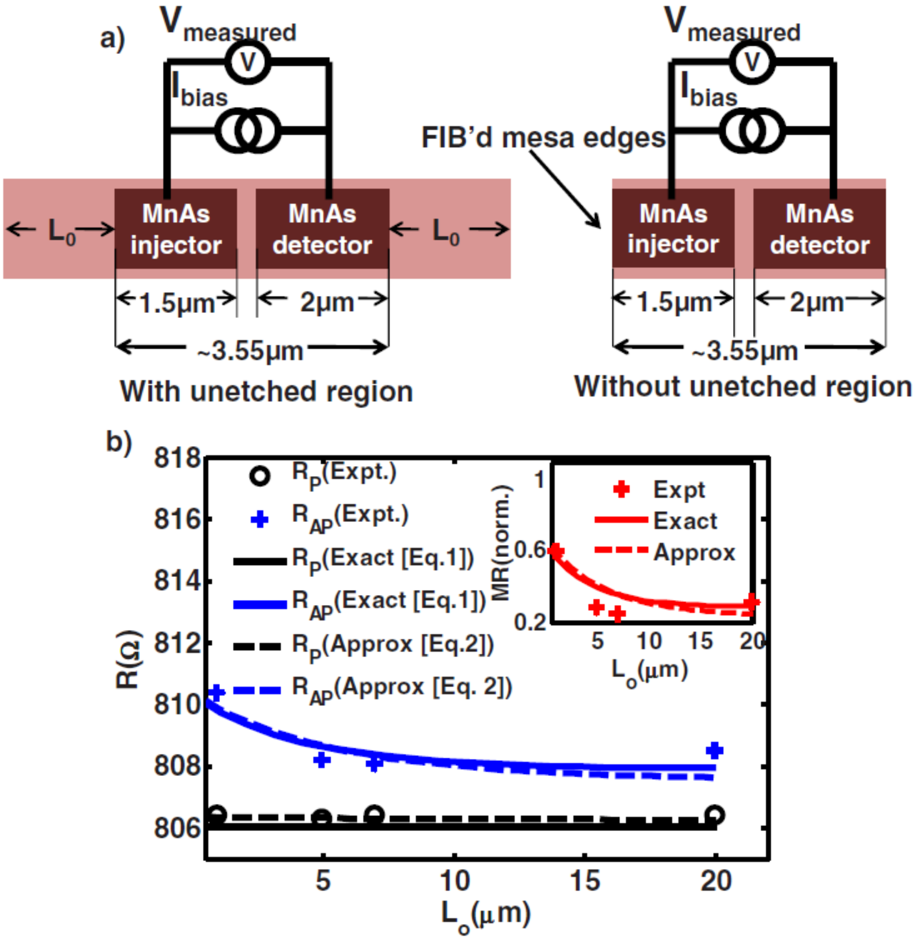

Figure 4.23 Schematic of the measurement setup of a lateral GaAs spin valve with (left) and without (right) unetched mesa regions (L_o) for injector (detector) contact length of L_c=1.5μm (2μm)**,** with an overall center-to-center contact spacing L_i~1.75μm. Measurements were done at 10K. (b) Device resistance at parallel (R_p) and anti-parallel (R_{ap}) configuration (black circles and blue crosses). Inset shows the magnetoresistance response with respect to L_o (red crosses). Experiment is compared against theoretical models (solid and dashed curves).

Equation 2 directly. Model parameters such as carrier density n_s and mobility μ are obtained from Hall measurement data. λ_s is used as 6.5μm which is consistent with the values obtained for bulk-GaAs previously [95, 106]. Contact conductance of $g_c\sim4\times10^{8}\ \mathrm{m}^{-1}\ \Omega^{-1}$ was extracted from R_p data. With these values a reasonable agreement with models to experiment was found for spin-injection efficiency, p of ~9%. We note, although the observed MR is relatively low compared to those in Ref. [95], the improvement due to etching is still clearly noticeable as MR rises from 0.2% to 0.5% after complete etching. However, the MR value is still below its maximum limit. For p ~ 9%, the maximum MR would be $p^2/ (1-p^2)$ ~ 0.8%, whereas we observed only ~ 0.5%. This is mainly due to the spin-relaxation process that is still present inside the current path even though the spin-relaxation process outside the current path is removed by etching, i. e., although $x^o= 0$, we still have $x^i > 0$ in these devices.

In conclusion, a compact model for lateral spin-valve devices with semiconducting channel is provided to assist the optimization of the device performance. The effect of extended channel regions outside the current path is discussed. By deriving a simplified expression for magnetoresistance from a one-dimensional spin-diffusion equation, we show that this unetched region could behave as an additional spin-relaxation source. The effect of MR on such region is demonstrated experimentally, and shows good agreement with the model derived.

4.6 Summary

In summary, we have investigated spin injection, transport, amplification, and detection in a high-temperature GaAs spin valves in the lateral and vertical geometries. It is found that channels created by FIB results in sharp magnetoresistance switching characteristics, contrary to gradual switching characteristics of wet etched channels.

A two- and three-terminal vertical MnAs/GaAs/MnAs vertical spin valve has been demonstrated, which show large magnetoresistance response, ~40%, even at room temperature. A heavily p-doped GaAs channel indicates that spin polarized carriers are transporting through the valence band states created by quantum confinement. With a third terminal placed directly on top of the channel, an amplification of magnetoresistance up to 500% was observed.

The magnetoresistance of lateral semiconductor spin valves as a function of extended mesa regions outside the spin-polarized current path have been investigated. It is observed that the extended regions act as an additional source of spin relaxation, resulting in a lower magnetoresistance response. A 50% increase in MR was experimentally observed when the spin-current was strictly confined within the two MnAs ferromagnetic electrodes.

Chapter V

Electric Field Control of Magnetoresistance in a Lateral InAs Quantum Well Spin Valve

---

5.1 Introduction

While we have recently demonstrated the amplification of magnetoresistance in a 3-terminal spin valve [107], the electrical control of spin transport with a gate-like electrode [108] in a spin valve or lateral magnetoresistance device has proven to be more difficult. This is mainly because of the difficulty in bringing together a channel material with optimal spin-related characteristics with efficient analyzer, polarizer and gate electrodes, as well as engineering a heterostructure with 2D confinement with a strong spin-orbit coupling interaction. This type of device was first proposed by Datta and Das [108], which is credited as the first proposal of semiconductor spintronic device. The central idea was to utilize the Rashba spin-orbit coupling present in a 2-dimensionally confined electron gas to systematically precess an ensemble of spin traveling in the channel at relativistic speeds. This type of device has been the holy grail of spintronics and sought after for nearly two decades.

In the present study we have investigated the modulation of lateral spin transport in an InAs/$In_{0.53}Ga_{0.47}As$ modulation doped heterostructure [109] lattice-matched to InP with a gate electrode. The electrical control of the magnetoresistance in conventional spin valves is unambiguously observed. The modulating gate terminal is intentionally placed *outside* the channel region as opposed to a very recent report in which the gate modulates the non-local spin accumulation [78]. This allows fabrication of devices having nanometer scale channel lengths. Since the spin diffusion length in an InAs quantum well is smaller than in GaAs [110], the small channel length will allow: (a) high-temperature operation and (b) a higher noise margin in terms of modulation of magnetoresistance. These results are compared with those obtained from an identical GaAs channel spin valve, for which no modulation of the magnetoresistance with gate voltage is observed. This confirms that the observed effects in the InAs quantum well spin valves arise from Rashba spin-orbit coupling. A brief introduction to spin-orbit coupling effects is given in the following sections, as it is the primary phenomena driving the operation of this type of device.

5.2 Spin-Orbit Coupling

Spin-orbit coupling (SOC) refers to the quantum mechanical interaction between the motion of the electron and its intrinsic angular momentum, the spin. The origin of this coupling comes from the relativistic nature of electric and magnetic fields. Electric fields are created from charges, while magnetic fields are created from *moving* charges, and, therefore, relative to the coordinate system in which they are observed. The orbital motion of the spin-polarized electrons, in the rest frame of the electron, sees an orbiting proton (charge), which creates an effective magnetic field at the position of the electron. This magnetic field arises due to the motion of the electron (or the motion of the protons in the frame of reference of the electron) and directly interacts with the spin of the electron. This spin-orbit interaction can be induced in a variety of context, which can either be inherently present in a periodic crystalline structure or engineered into a heterostructure.

The effective magnetic field can be expressed as **B** = -(**v** x **E**) / c^2, where **v** is the velocity of the electron, **E** is the surrounding electric field, and c is the speed of light. It is evident that the electrons must be traveling at relativistic velocities (greater than ~10% of speed of light). These velocities can be reached in ballistic channels such as 2-dimensional electron gases present in quantum well structures.

Two types of spin-orbit interactions are relevant in this chapter. One is the Dresselhaus spin-orbit coupling, which arises due to the bulk inversion asymmetry (BIA) typically found in zincblende semiconductors, and the Rashba spin-orbit coupling, which is present in heterostructures with structural inversion asymmetry (SIA), such as quantum well structures with asymmetric barriers at either sides. Spin-orbit interacts are a double edged sword; it allows for control of spin states by applying an electric field, but is the principle cause of spin relaxation. The general Hamiltonian arising due to spin-orbit interactions is expressed as

$$H_{SO} = \frac{\hbar}{4m^{*2}c^2}\sigma \cdot p \times \nabla V_0 \tag{5.1}$$

where σ is the Pauli spin matrix and the rest of the variables takes on their usual meaning.

5.2.1 Dresselhaus spin-orbit coupling

Dresselhaus spin-orbit coupling is present in zincblende structures such as GaAs and InP with lack of inversion center. It is an intrinsic SOC effect due to the arrangement of the constituent atoms comprising the semiconducting material and introduces a

Dresselhaus term (β) in the Hamiltonian. This Hamiltonian is expressed in the form (for a 2-dimensional case)

$$H_D = \beta[\sigma_x k_x - \sigma_y k_y] \tag{5.2}$$

Although the Dresselhaus term is present for nearly all zincblende materials, the magnitude of the effective magnetic field is negligible compared to the effective magnetic field caused by the Rashba spin-orbit coupling interaction.

5.2.2 Rashba spin-orbit coupling

The Rashba spin-orbit term is the dominating effect in 2D quantum well structures, and is what allows control of spin precession in such a system. The Hamiltonian representing this SOC is expressed as

$$H_R = \alpha(\sigma_x k_y - \sigma_y k_x) \tag{5.3}$$

where α is the spin-orbit coupling strength and is a property of the material system involved. Note the direction of the Pauli spin matrix and the momentum vector *k* compared to the Dresselhaus Hamiltonian. The direction of the effective magnetic field created by these Hamiltonians is different.

The strength of the Rashba coefficient (α) can be found by observing the Shubnikov-de Haas (SdH) oscillations at low temperatures in the presence of a large magnetic field. These oscillations in the conductivity of the material are due to the filling of Landau levels created by an intense magnetic field applied normal to the channel surface. The oscillation frequency is directly related to the spin density of states. Two different frequencies are present, one for spin-up and one for spin-down electrons, resulting in a beating pattern. This effect is primarily observable in 2D confined structures.

SdH studies have been carried out in several material structures such as InGaAs/InAlAs and InAs/InGaAs quantum well heterostructures, where one of the first SdH measurements was done by Das *et al*. [111], which showed spin splitting in $In_xGa_{1-x}As$ /$In_{0.52}Al_{0.48}As$ heterostructures as B ~ 0. To date, InAs quantum wells show the strongest Rashba interaction, and is the material system chosen for this study.

The beauty of the Rashba interaction is that since it is directly tied to the structural asymmetry of a particular system, the Rashba strength is tunable if the degree of asymmetry of the structure can be controlled. The tune-ability of the Rashba coefficient in an InAs 2DEG channel via an externally applied gate bias has been reported by Koo et al. [78], which is shown below in Fig. 5.X.

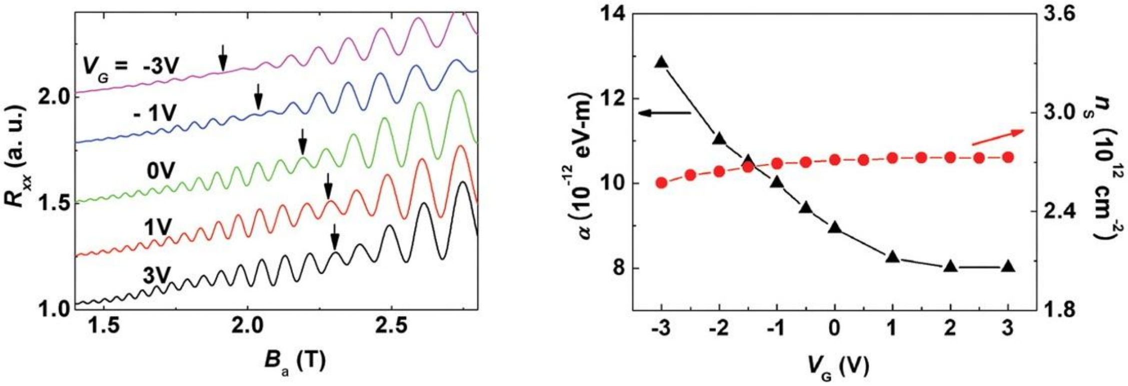

Figure 5.1 (left) Shubnikov-de Hass oscillations observed in an InAs quantum well as a function of applied gate voltage. (right) The Rashba spin-orbit coupling coefficient and the carrier concentration in the 2DEG as a function of applied gate voltage [78].

5.3 Electrical Control of Spin Precession in an InAs Quantum Well

5.3.1 Introduction

In this section, the experimental demonstration of electrical control of spin precession in an InAs 2DEG quantum well structure is described. The results obtained are one of the first demonstrations of spin control in a semiconducting material utilizing the Rashba spin-orbit interaction. A clear sinusoidal modulation of magnetoresistance was observed over several devices and samples. The modulation effect was absent in control devices, indicating that the observed behavior is primarily due to spin-orbit interactions of the spin-polarized electrons in the channel to the applied gate voltage.

5.3.2 Heterostructure design and fabrication

The device heterostructure, grown on semi-insulating (001) InP substrate, is shown in Fig. 5.2, along with the band diagram corresponding to the heterostructure, calculated by solving Poisson and Schrodinger's equation self consistently. Modulation-doped $InAs/In_{0.53}Ga_{0.47}As/In_{0.52}Al_{0.48}As$ heterostructure is chosen as the active channel of the spin valve since the reported modulation of the Rashba coefficient by a gate bias in an $InAs/In_{0.53}Ga_{0.47}As/In_{0.52}Al_{0.48}As$ heterostructure is relatively large [109] compared to that in bulk GaAs. The measured electron mobility and sheet density in the two-dimensional electron gas (2-DEG) formed in the InAs channel are 5500 $cm^2/V\cdot s$ and 6.2×10^{12} cm^{-2}, respectively, at room temperature. The ferromagnetic polarizer and analyzer contacts are realized with 35 nm type-B MnAs grown at 250°C [112] on 30 nm n-doped (graded) $In_{0.52}Al_{0.48}As$ to form Schottky tunnel barriers.

The devices are fabricated by using standard optical lithography, metallization, plasma enhanced chemical vapor deposition (PECVD) and e-beam evaporation techniques. The fabrication steps are as follows. First, MnAs ferromagnetic contacts are wet etched into pads of different aspect ratios [$(L/W)_A=1.5$; $(L/W)_P=6$] with a channel length of 0.6 μm, followed by the definition of a mesa by etching. Then, the insulated gate (100 Å Ti/300 Å Au), situated 0.6 μm from the analyzer, is recessed down as close as possible to the InAs channel for maximum gate action, with a thin layer of 50 nm of Si_3N_4 deposited between the gate and the channel to minimize leakage current during biasing. Fabrication of the gate electrode is extremely critical for an optimum performance of these devices.

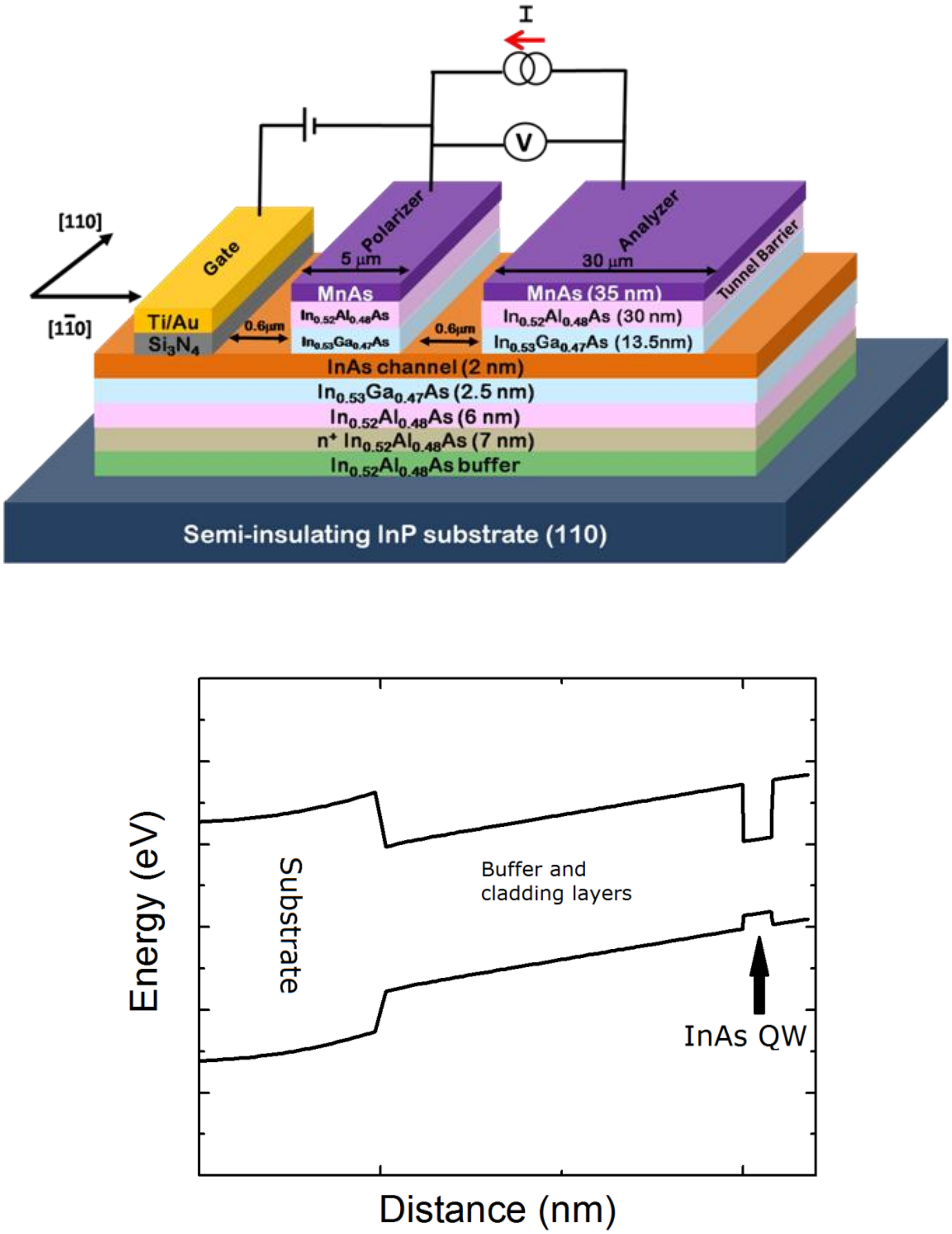

Figure 5.2 (top) Schematic Illustration of the InAs QW spin modulator grown on an InP substrate. (bottom) Corresponding band diagram of the heterostructure shown on top calculated by self consistently solving Poisson and Schrodinger's equation.

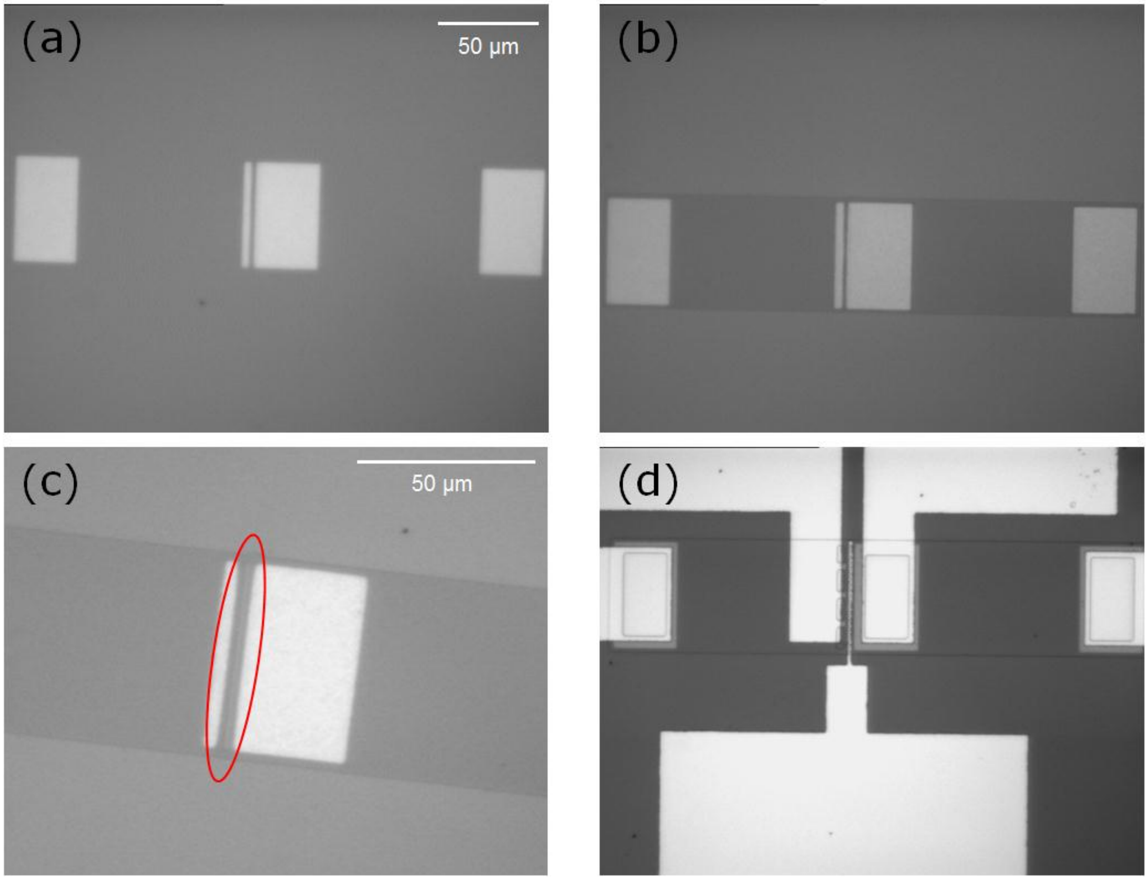

Figure 5.3 Micrograph of the fabrication steps. (a) Creation of the ferromagnetic MnAs electrodes. (b) Definition of the mesa region (difficult to see). (c) Etching of the gate region. (d) Completely fabricated device.

5.3.3 Measurement scheme

An important aspect of our experiment was the orientation of the MnAs and gate contact pads. Type B MnAs films grown on $In_{0.52}Al_{0.48}As$ are found to have an in-plane easy axis along the $[1\bar{1}0]$ crystallographic direction and the magnetization exhibits strong anisotropy between the [110] and $[1\bar{1}0]$ directions [112]. Therefore two sets of devices were fabricated: one with direction of current flow perpendicular to the magnetization direction (device A) and the other with the current flow parallel to the direction of magnetization (device B). The direction of magnetization of the contact pads was along the $[1\bar{1}0]$ direction (easy axis) for both. The different aspect ratios of the analyzer (A) and polarizer (P) contacts result in a difference in their coercivity which is essential for the operation of a spin valve. The schematic of a fabricated device having a non-local gate electrode is shown in Fig. 5.4. Several other control devices were also fabricated. These will be described in the proper context in the following.

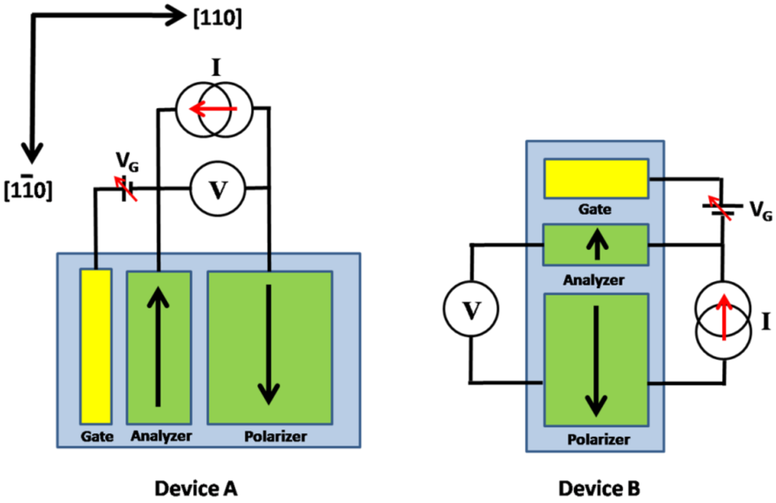

Figure 5.4 Two measurement schemes for (a) device A and (b) device B.

The devices were mounted in a liquid helium cryostat for measurements, with provisions for the application of a magnetic field along the easy axis of the MnAs contacts. Figure 5.5 shows measured magnetoresistance at 10 K as a function of applied magnetic field for device A with zero bias applied to the insulating gate electrode. The device therefore operates as a conventional lateral spin valve and the measured magnetoresistance $MR(H) = [R_{\uparrow\downarrow}(H)-R_{\uparrow\uparrow}(H_{sat})]/R_{\uparrow\uparrow}(H_{sat})$ is a manifestation of the polarizer and analyzer efficiencies changing by different amounts with changing magnetic field, by virtue of their different coercivities.

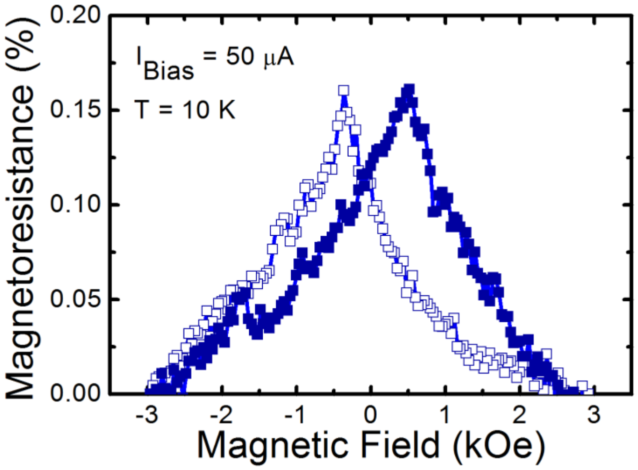

Figure 5.5 Magnetoresistance measured at 10 K in a conventional spin valve setup without gate bias. The channel length of the device is 0.6 μm.

5.3.4 Magnetoresistance characterization

Figure 5.6 shows a variation of peak magnetoresistance versus bias current for the same device at different temperatures. The data indicate an almost negligible decrease of magnetoresistance with applied bias current between the source and drain electrodes. The observed behavior is the result of two competing effects: (1) increased spin dephasing due to Dresselhaus and enhanced Rashba spin-orbit coupling terms at high electron densities, which will lead to a decrease in injected spin polarization [113], and (2) a decrease in the polarizer depletion region width with increasing current bias, which will lead to more efficient tunneling and injection of spin polarized carriers. It can be seen that the strength of the spin-orbit coupling effect is more dominant at low temperatures. In other words, the MR decreases with increasing bias relatively more rapidly at 10 K than 20 K, which is an indication that the spin-orbit interaction is more efficient at lower temperatures, as expected. This is the result of using a Schottky barrier as opposed to using a tunnel barrier (such as oxides). The use of oxide barriers would have led to an even more rapidly decreasing MR with increase in current bias.

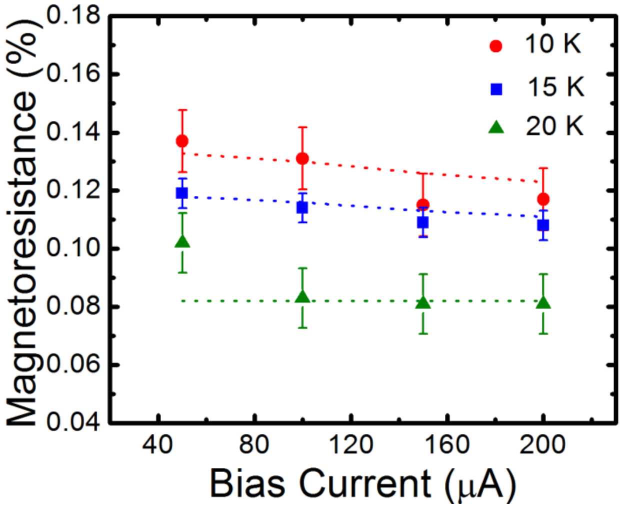

Figure 5.6 Peak Magnetoresistance as a function of current bias applied across the source and drain contacts. Dashed lines are guides to the eye.

Next, the voltage V between the polarizer and analyzer terminals is measured at 10K and 20K for device A as a function of bias applied to the insulated gate, V_G, for both parallel and antiparallel magnetization of the MnAs pads. The measurement is done at a constant injection current of 100 μA and with no externally applied magnetic field. The variation of magnetoresistance with gate bias is shown in Figs. 5.7(c) and (d). The oscillation is a result of the cross-over in the parallel and anti-parallel voltages, shown in Figs. 5.7(a) and (b), which is due to the spin precession of injected carriers. Identical data were recorded with a constant injection current of 150 μA between the polarizer and analyzer. The experiment was repeated with two control devices, in both of which the channel length is 150 μm and in one of them the analyzer is a non-magnetic Ti/Au contact. All other dimensions are maintained the same. For both of these devices, the variation of V with V_G for parallel and antiparallel magnetization of the polarizer and analyzer does not exhibit any cross over. As a consequence no oscillation of the magnetoresistance as a function of gate voltage is observed. These experiments strongly

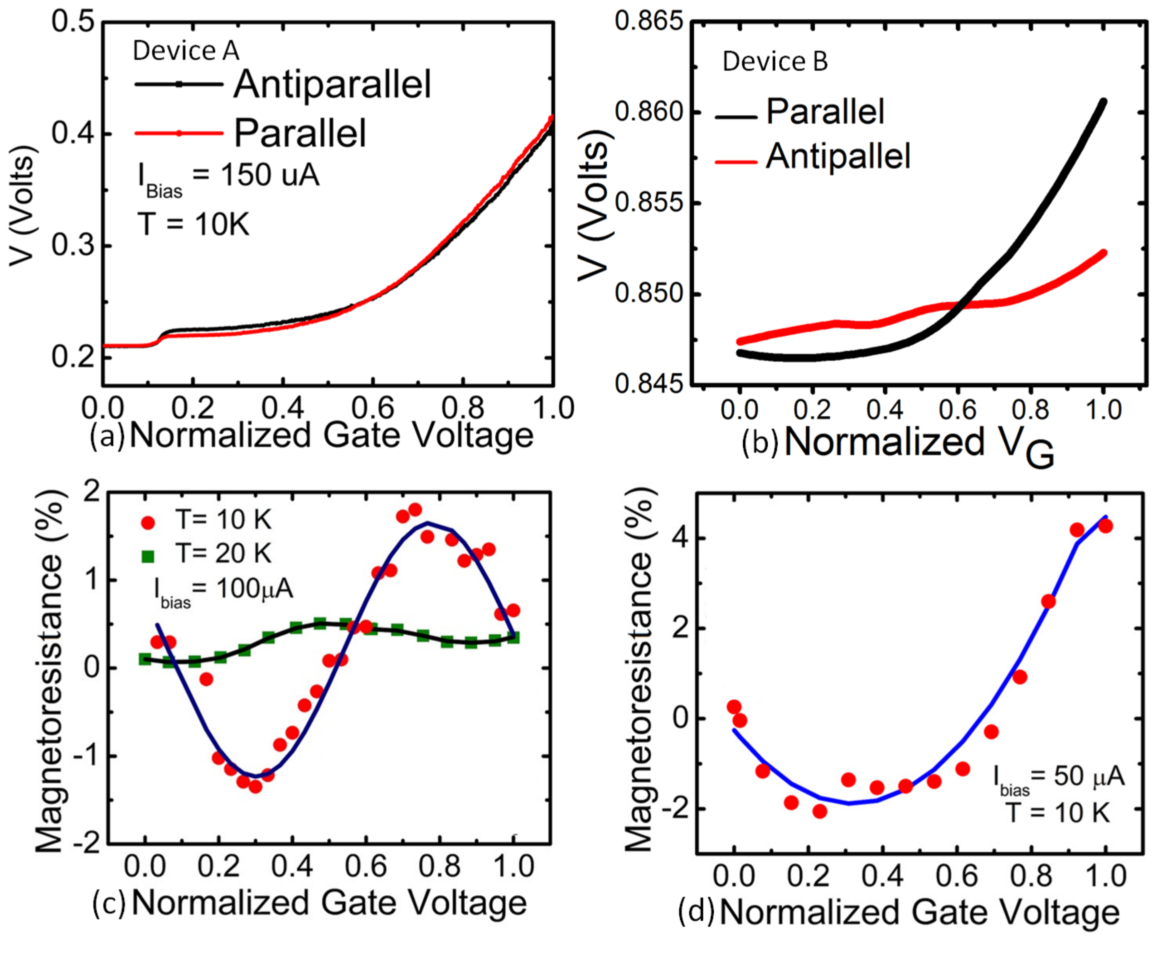

Figure 5.7 Voltage measured across the source and drain for parallel and antiparallel configuration of the source-drain electrodes as a function of gate bias for (a) device A and (b) device B. Modulation of magnetoresistance measured as a function of gate bias for (a) device A and (b) device B.

suggest that the data of Fig. 5.7 are not related to spurious magnetic effects in the contact or channel regions. The oscillation in the magnetoresistance is a manifestation of spin dephasing of the injected electrons and is an indication of the modulation of spin transport by an applied electric field.

The response of device A is not entirely understood in the framework of Rashba spin-orbit coupling. The observed effect is probably operative under the large (5 μm) polarizer contact, rather than in the channel region between the polarizer and analyzer. In this case the variation can be simulated by a function cos(Δθ), where Δθ is not $2m^*\alpha_{so}L/\hbar^2$ [108], but simply $C\alpha_{so}$, where C is a constant dependent on the polarizer characteristics and α_{so} is the spin-orbit coupling constant dependent on the gate bias. The data obtained at 20K show that the effect is reduced.

Measurements were repeated for device B in which the spin current flow is in the same direction as the magnetization of the polarizer and analyzer. In other words they are both along the $[1\bar{1}0]$ crystallographic direction. The measured output voltage (inset) and the magnetoresistance as a function of gate bias are shown in Fig. 5.7(d). In this case a very clear difference and crossing of the output voltage between parallel and antiparallel magnetization directions are observed. Also, the difference becomes very large at higher gate biases. Compared to Fig. 5.7(c), the change in magnetoresistance is a factor of two larger for this device. Therefore, the modulation of spin transport is more significant in this case. Nonetheless, our results are comparable to those for a device with the gate placed in the non-local channel [78].

5.3.5 Control experiments

As control experiments, measurements were made on a GaAs-based spin valve with a gate terminal adjacent to the polarizer and a spin modulator device without a ferromagnetic detector electrode. The geometry is identical to those shown in Fig. 5.2. The channel is formed in a 0.5μm thick layer of Si-doped GaAs with $n = 1\text{x}10^{17}$ cm^{-3}. The Schottky tunnel polarizer and analyzer contacts are formed by a graded heavily

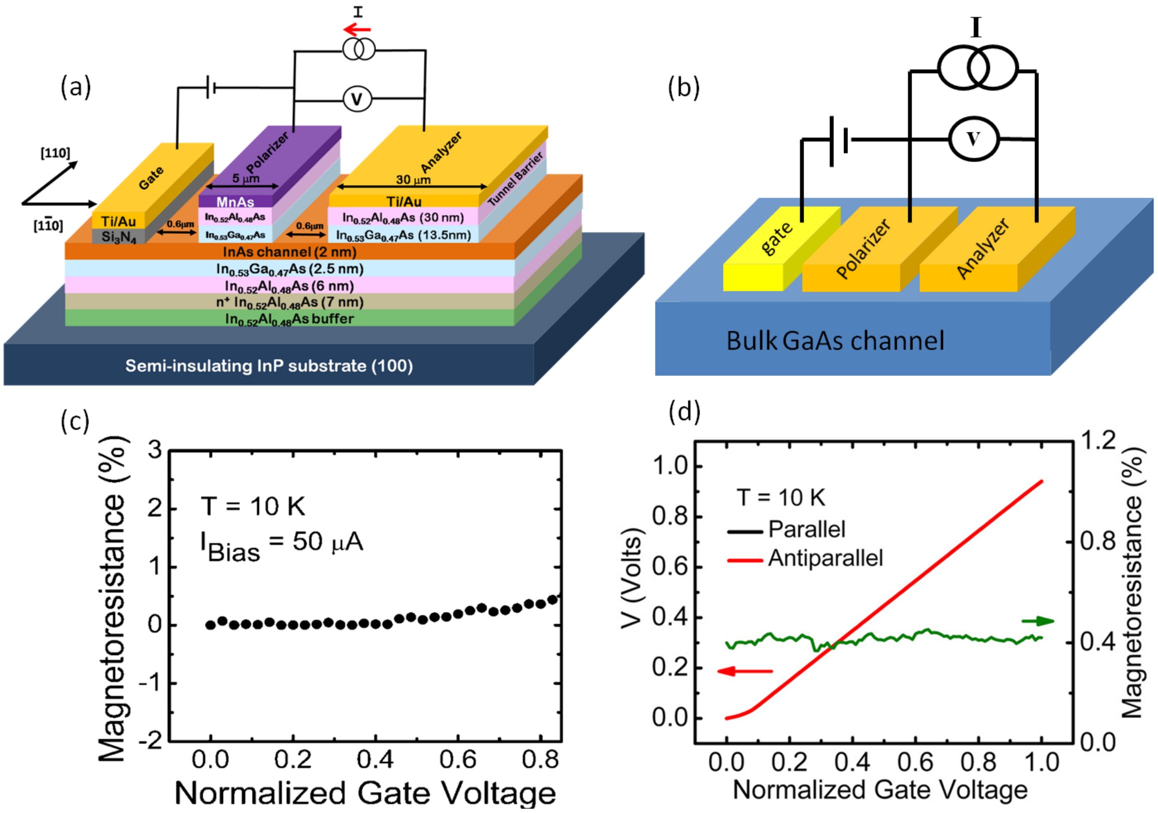

Figure 5.8 Control device (a) without a ferromagnetic detector electrode and (b) bulk GaAs channel. (c) Magnetoresistance change for control device without a FM detector and (d) GaAs bulk channel. Both show no modulation of MR with respect to gate bias.

---

doped 30 nm GaAs layer atop the channel layer and 35 nm MnAs. The direction of magnetization of the polarizer and analyzer is the same as the direction of the spin current. Good spin valve magnetoresistance characteristics are recorded with $V_G = 0$. With an application of gate bias, the magnetoresistance in this device remains constant. This is expected, since spin-orbit coupling is much smaller in GaAs compared to that in InAs. This result also provides additional evidence that the observed effect in the InAs quantum well device B is due to Rashba spin-orbit coupling induced by the gate voltage. The larger effect in device B may be partially due to modulation of spin transport in the channel region also, but it is not possible to ascertain the exact degree of this contribution. It is unlikely that the in-plane anisotropy of spin orbit coupling and spin relaxation time [114,115] play any role in determining the difference in response between device A and B. The fact that the magnetoresistance can be modulated even in a device with large polarizer/analyzer contact dimensions and channel length is very encouraging. By shrinking these dimensions considerably to submicron and nanometer scales, the adjacent gate can easily induce an electric field in the channel region and these devices can be operated at higher temperatures and higher frequencies.

5.4 Summary and Outlook

In summary, we demonstrate the modulation of magnetoresistance of an InAs/$In_{0.53}Ga_{0.47}As$/$In_{0.52}Al_{0.48}As$ lateral spin valve with a gate electrode placed alongside the MnAs polarizer contact and outside the channel. The results indicate that the change in magnetoresistance is caused, in part, by Rashba spin-orbit coupling due to the gate bias. While this demonstration together with the recently reported work [9] are very encouraging, further work is necessary before any claims to practical room-temperature applications can be made. In the words of a reviewer:

> *"...That the paper could measure the effect of electric field control via the spin-orbit interaction is a triumph in experimental physics. The moving of the gate control outside the channel is a masterful stroke… What is the prospect that the Rashba effect can be used for a practical room-temperature device? It seems to me that the beautiful experiment shows the weakness of the premise that the Rashba effect can be used for practical room temperature devices even in the semiconductor with about the largest spin-orbit interaction… I leave it up to the good judgment of the authors and the editor to decide whether to continue the drum beat for the Rashba effect for real-life spintronics or whether it is time for someone to comment on the emperor's clothing."*

Chapter VI

Single GaN Nanowire Spin Valves

6.1 Introduction

Wide bandgap semiconductors such as GaN and their alloys are important for high-power electronics, solid-state lighting, and more recently for studies on strong coupling and polariton lasing [116-119]. GaN crystallizes in the wurtzite or zincblende forms and has inversion asymmetry. It is also characterized by a weak spin-orbit coupling (SOC), which makes it attractive for high temperatures spintronics [120, 121]. It is understood that spin dynamics in GaN is determined by the DP spin relaxation mechanism, wherein the spin state of free carriers is randomized by the effective magnetic field arising from a spin splitting in the conduction band due to the anisotropic SOC. Predictions of long spin lifetimes in GaN have been made from theoretical calculations [122]. Measurements of electron spin lifetimes in bulk wurtzite GaN have been made by TRKR and TRFR spectroscopy and values of the parameter at room temperature ranging from 35 to 100 ps have been derived [123, 124]. However, these measurements have been made almost exclusively on epitaxial GaN grown on mismatched substrates and, therefore, have a large density (10^8-10^{10} cm^{-2}) of threading dislocations and associated defect-impurity complexes. It is quite likely that spin coherence and transport are adversely affected by the presence of a large number of defects. A direct measurement of spin transport characteristics in a device such as a spin valve, with material which is relatively defect-free, is lacking. It has been shown recently by several groups, including ours, that wurtzite GaN nanowires can be grown epitaxially on (001) or (111) silicon substrate with almost a complete absence of extended defects such as dislocations, stacking faults, and twins [125-129]. The nanowires, by virtue of their diameter (50-80 nm) are considered bulk in terms of quantum confinement, but its spatial confinement may suppress spin relaxation, leading to a relatively longer spin lifetime [130-133]. Measurements of fundamental material parameters have been made with such nanowires and they have been incorporated as the active region in the design and fabrication of photon and polariton lasers, light-emitting diodes, and electronic devices [134-137]. The measurement of spin transport parameters in the nanowires would yield the intrinsic values of the parameters in GaN and could serve as a standard for future reference.

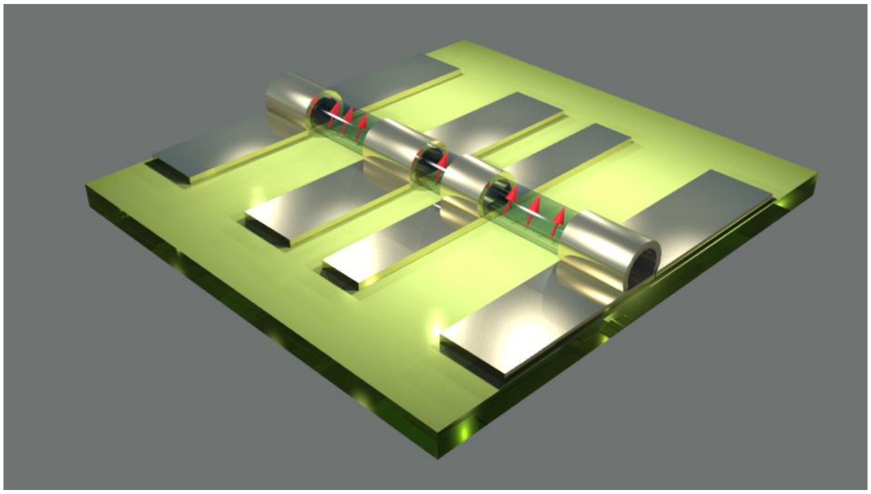

Figure 6.1 Schematic rendering of a four-terminal nanowire spinvalve. Spatial confinement in nanowires may lead to longer spin lifetimes, resulting in higher magnetoresistance response.

Measurements on a device such as a spin valve involve successful spin injection and detection in the semiconductor channel via ferromagnetic contacts. Schottky and oxide tunnel contacts, first proposed by Rashba [138, 139], have been very successful for injecting spin polarized carriers in GaAs-, InP-, and Si-based spintronic devices. An ultra thin tunnel barrier between the ferromagnet and semiconductor provides a large interface resistance with high spin asymmetry—a requirement for efficient spin injection. Ferromagnetic FeCo, together with MgO as the tunnel barrier have demonstrated the highest spin injection efficiency of 32% into GaAs at 300 K [140, 141]. We have used this tunnel contact for the spin injection and detection in the present study.

We report here spin injection, transport, and detection in single wurtzite GaN nanowire (NW) spin valves. Measurements have been made as a function of temperature and transport length in the nanowire in the longitudinal direction between the ferromagnetic contacts. A magnetoresistance (MR) of 10.5% is measured at 300 K. This is the highest MR in a semiconductor-based lateral spin valve. Analysis of the data yields a longitudinal spin relaxation time as high as ~120 ps and a corresponding spin diffusion length of ~300 nm at 300 K. Four-terminal non-local MR and Hanle measurements were performed to confirm spin injection into the nanowires.

6.2 Previous Studies on Spin Transport Properties of Epitaxial GaN

The most relevant studies on spin relaxation properties of GaN have been investigated by Beschoten *et al.* and Buss *et al.* on bulk MOCVD grown wurtzite GaN layers. Beschoten used the optical pump/probe method technique of time-resolved Faraday rotation (TRFR) to systematically investigate spin decoherence with various carrier concentrations. They observed, despite the high density of charged threading dislocations, a relatively long spin lifetime of ~20 ns at T = 5 K which persisted up to room temperature. The Elliot-Yafet relaxation mechanism predicts momentum scattering to play a crucial role in dephasing spin, which should be manifested via local spin-orbit interactions due to the large density of dislocations and defects present in the material. The relation between the density of dislocations and defects and momentum scattering rate can be seen by measuring the carrier mobility, which decreases with increasing number of defects. However, the spin lifetime remained relatively constant over a broad temperature and defect density range. Beschoten argued that this may be due to the fact that the valence-band spin-orbit coupling in wurtzite GaN is ~100 times weaker than in other III-V materials such as GaAs, resulting in a decoupling of momentum- and spin-scattering processes.

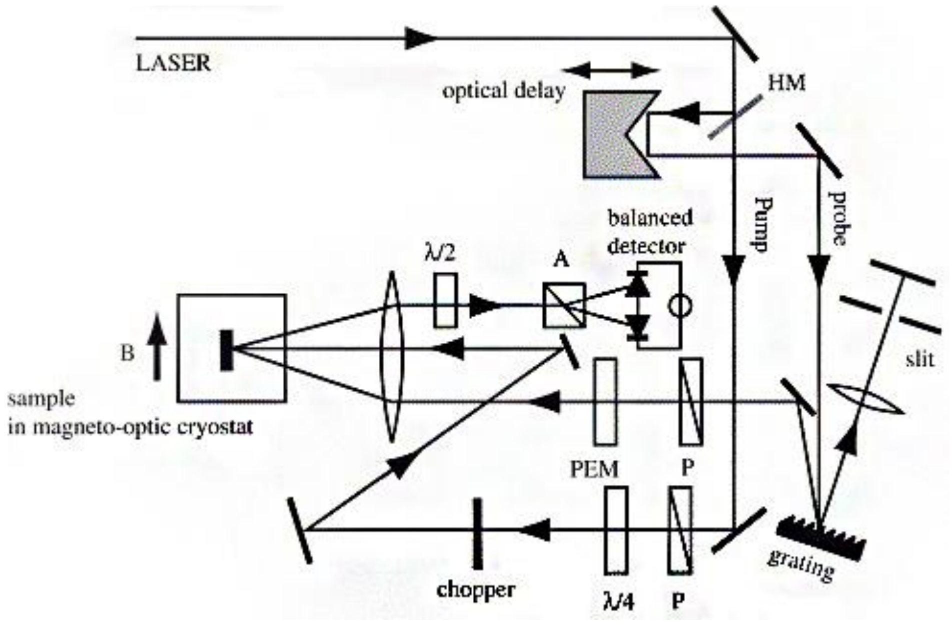

Figure 6.2 Schematic illustration of a typical time-resolved Kerr rotation setup. The Faraday rotation setup measures the laser transmission instead of reflection off the sample surface [142].

Buβ *et al.* conducted similar experiments, this time using time-resolved Kerr rotation (TRKR) measurements. They reported spin lifetime values of ~70-100 ps at room temperature and fitted their experimental results using only the D'yakonov-Perel' relaxation mechanism, considering the Rashba and Dresselhaus spin-orbit coupling interactions. Their theory results in an equation with no fitting parameters, where the spin relaxation rate is given as

$$y_{zz} = \frac{4k_B T m^*}{\hbar^8}\{[\alpha_E \hbar^2 + (b-4)\gamma_e m^* k_B T]^2 + (2b^2+8)\gamma_e^2 m^{*2}(k_B T)^2\}\tau_p \qquad \textbf{(6.1)}$$

where the spin lifetime is then calculated as $\tau_{sf} = 1/y_{zz}$. Here, α_e is the Rashba coefficient (eVÅ), γ_e is the Dresselhaus coefficient (eVÅ^3), and b is a unitless material parameter. It is found that the DP relaxation in GaN is almost completely governed by the Rashba term at any temperature.

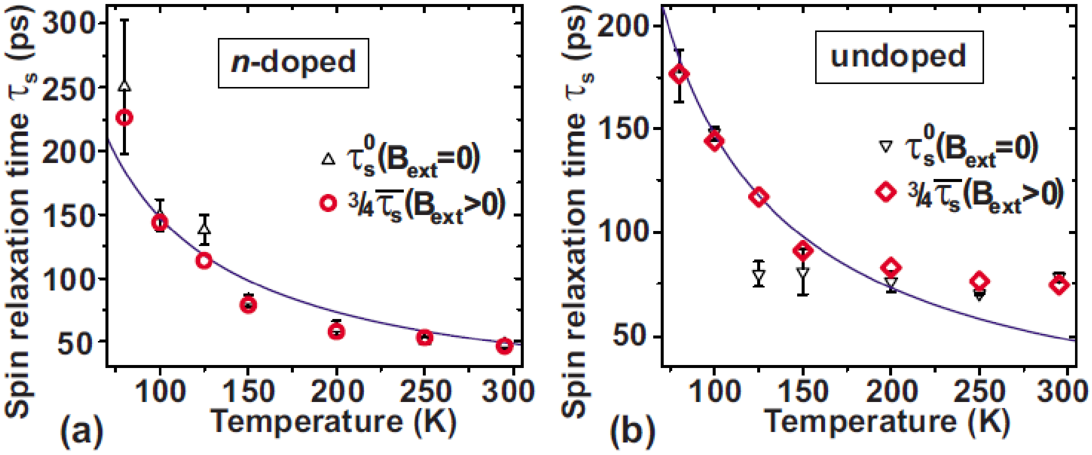

Figure 6.3 Schematic illustration of a typical time-resolved Kerr rotation setup. The Faraday rotation setup measures the laser transmission instead of reflection off the sample surface [124].

TRKR studies on metastable cubic-GaN structure reveal that the symmetry of the lattice may be playing a big role in determining the spin relaxation dynamics in this material. Another recent paper by Buβ *et al.* [143] reported a spin lifetime of nearly 500 ps at room temperature in a MBE grown cubic-GaN material, almost five times longer than the value obtained in wurtzite-GaN. The only difference seemed to be the lattice structure, where the zincblende structure of GaN showed reduced spin splitting compared to its wurtzite counterpart. This conclusion is, in fact, consistent with the conclusion arrived in Beschoten's work.

6.3 Growth of GaN Nanowires free of growth defects on (001) Silicon

Several GaN NW samples were epitaxially grown on (001) Si substrate in a plasma-assisted molecular beam epitaxy (PA-MBE) system, with length and diameter ranging from 2-4μm and 50-80nm, respectively. The general growth steps and conditions are as follows. First, the surface oxide on the Si substrate is removed in a solution of HF-H_2O and annealed in the growth chamber at a temperature of 900 ºC, after which the temperature is lowered to 800 ºC and a few monolayers of Ga are deposited with a Ga flux of 1.5×10^{-7} Torr in the absence of nitrogen. The GaN NW growth is then initiated at the same substrate temperature at a rate of 300 nm/hr under nitrogen-rich conditions. Steady Ga flux and nitrogen flow rate are maintained at 1.5×10^{-7} Torr and 1 sccm, respectively.

A scanning electron microscope (SEM) image of a grown sample and a high-resolution transmission electron microscopy (HR-TEM) of a single nanowire are shown in Figs. 6.4 and 6.5, respectively. The SEM image was taken by cleaving through the middle of the nanowire forests in mounted on a 45º tilted SEM stage. Two sets of nanowires were grown (samples A and B). The nanowires in sample A were not intentionally doped. However, capacitance-voltage (C-V) measurements indicate a background n-doping density of $\sim 1 \times 10^{17}$ cm^{-3} [144]. In sample B the NWs were Si-doped with a density of $\sim 2 \times 10^{18}$ cm^{-3}.

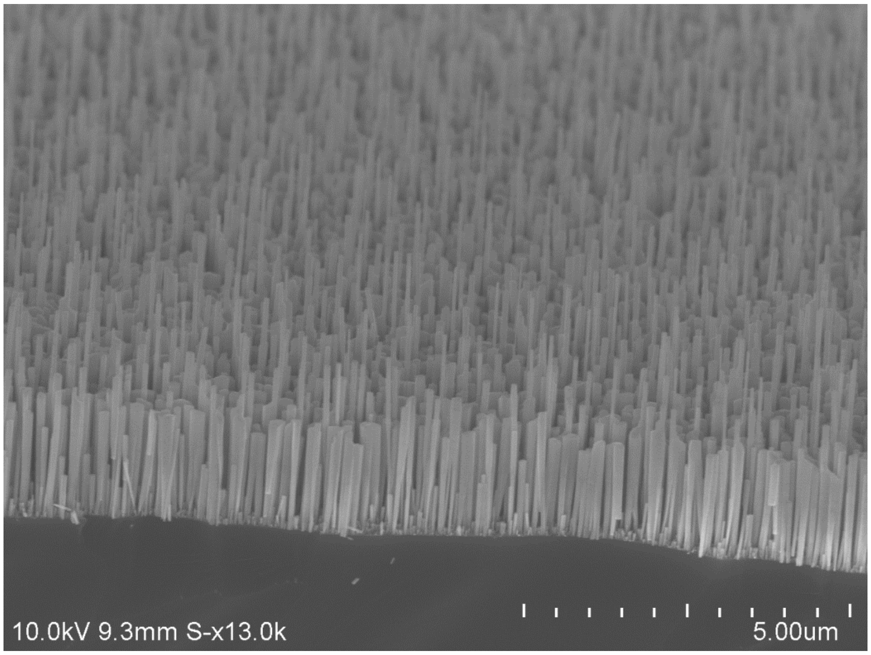

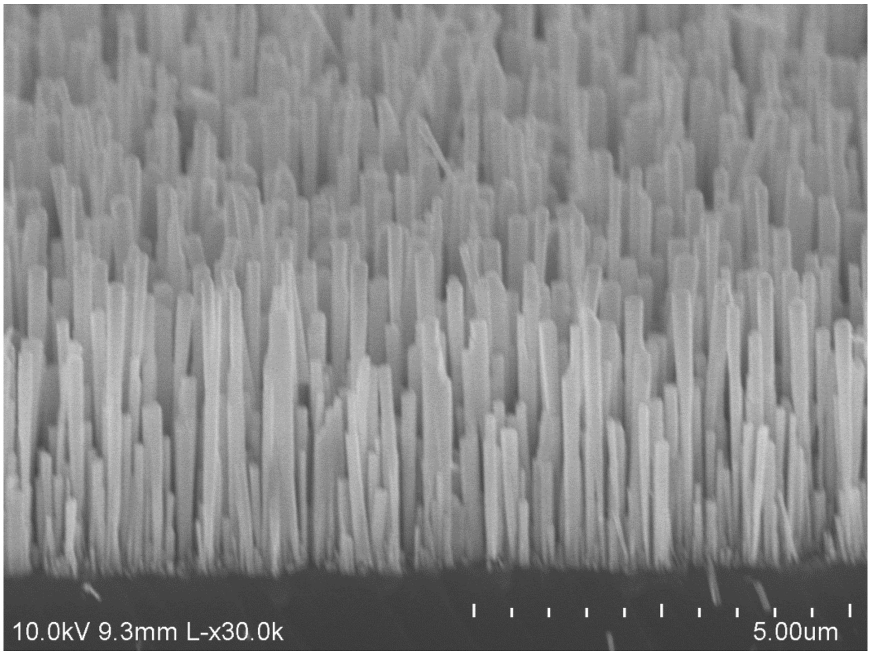

Figure 6.4 SEM images of grown nanowires on (001) Si, grown by plasma-assisted molecular beam epitaxy (PA-MBE).

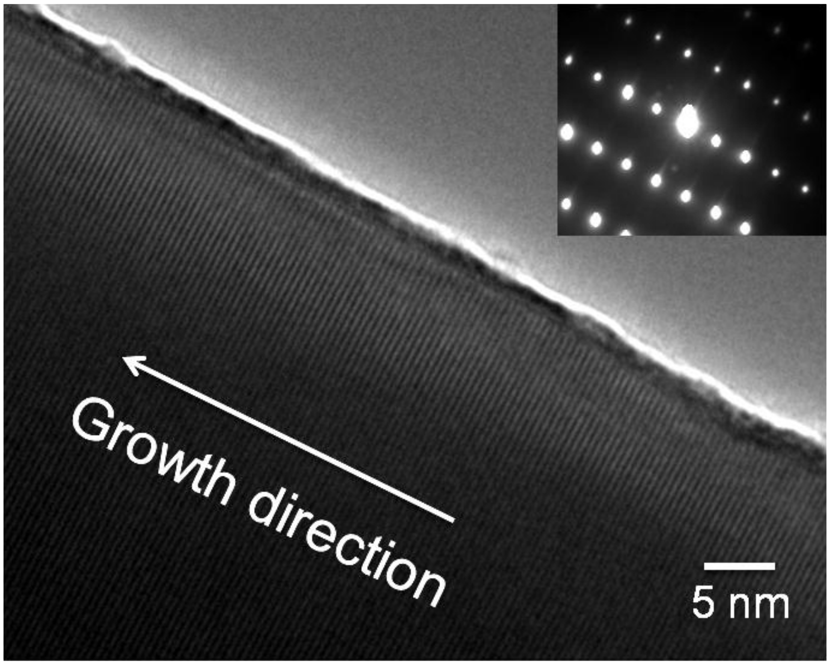

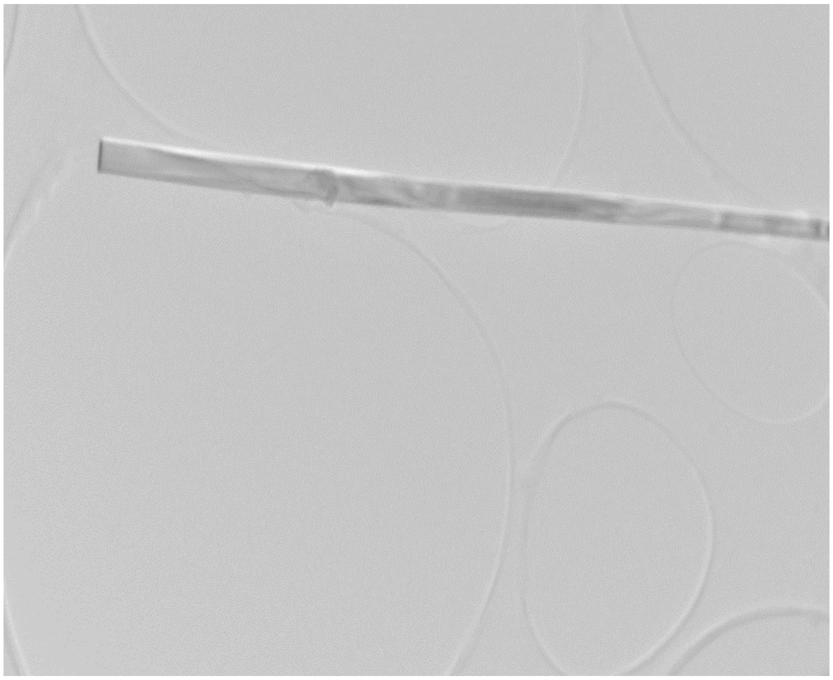

Figure 6.5 Low-resolution TEM image of a long single nanowire. The contrast difference is mainly due to the nanowire not being flat on the stage.

6.4 Spin Valve Fabrication

The nanowires are dispersed by drop casting a low density mixture of isopropyl alcohol and nanowires on a silicon wafer covered with 200 nm SiO_2 formed by thermal oxidation at the surface of the wafer. Single nanowires are identified with the help of a grid mask with alignment marks and SEM imaging.

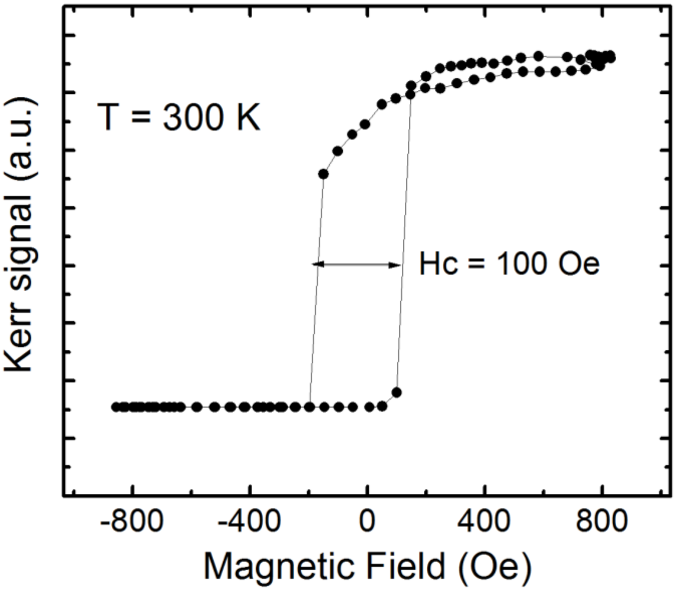

Figure 6.6 Ferromagnetic hysteresis measured by the magneto-optic Kerr effect (MOKE) on a bulk 70nm thick FeCo film e-beam evaporated on SiO_2. The magnetic field is swept in-plane, parallel to the film surface. The hysteresis show sharp magnetization switching characteristics with a coercivity value of approximately 100 Oe, verifying the ferromagnetism of the FeCo contacts.

Four contact regions are defined on a single nanowire by electron-beam lithography. Finally, 1 nm MgO tunnel barrier and 60 nm FeCo are deposited by e-beam evaporation to form the ferromagnetic tunnel contacts. The sample is then annealed at a temperature of 400 ºC for approximately 2 hours. This annealing step was found to be crucial in forming an appropriate tunnel barrier for spin injection. Due to the oxygen vacancies present in the MgO layer, nanoscale contacts are known to show a memristor-like behavior in the electrostatic characteristics of the device [145]. Indeed, we were able to observe memristive effects in our non-annealed devices. These devices showed no magnetoresistance response, and it has been reported that oxygen vacancies are detrimental to spin transport [146].

Figure 6.7 (left) Alignment marks used to identify exact position of a single nanowire dispersed on top of SiO_2. The minimum feature size is 1μm. (right) Optical micrography of dispersed nanowires.

Several ferromagnet/NW/ferromagnet (F/N/F) spin valves were fabricated with varying channel lengths ranging from 200 nm to 3.5 μm. A scanning electron microscope (SEM) of a completely fabricated device is shown in Fig. 6.9. Control devices with non-ferromagnetic Ti/Au detector contacts (F/N/N) were also fabricated. The magnetization characteristics of the FeCo films were investigated by magneto-optic Kerr effect (MOKE) measurements. The ferromagnetic hysteresis characteristics of a 70 nm FeCo film evaporated on SiO_2 are shown in Fig. 6.6. The applied magnetic field is swept in-plane, parallel to the film surface. The measured hysteresis exhibits sharp magnetization switching characteristics and a coercivity of ~100 Oe. The latter value is dependent on the thickness and lateral dimensions of the FeCo film.

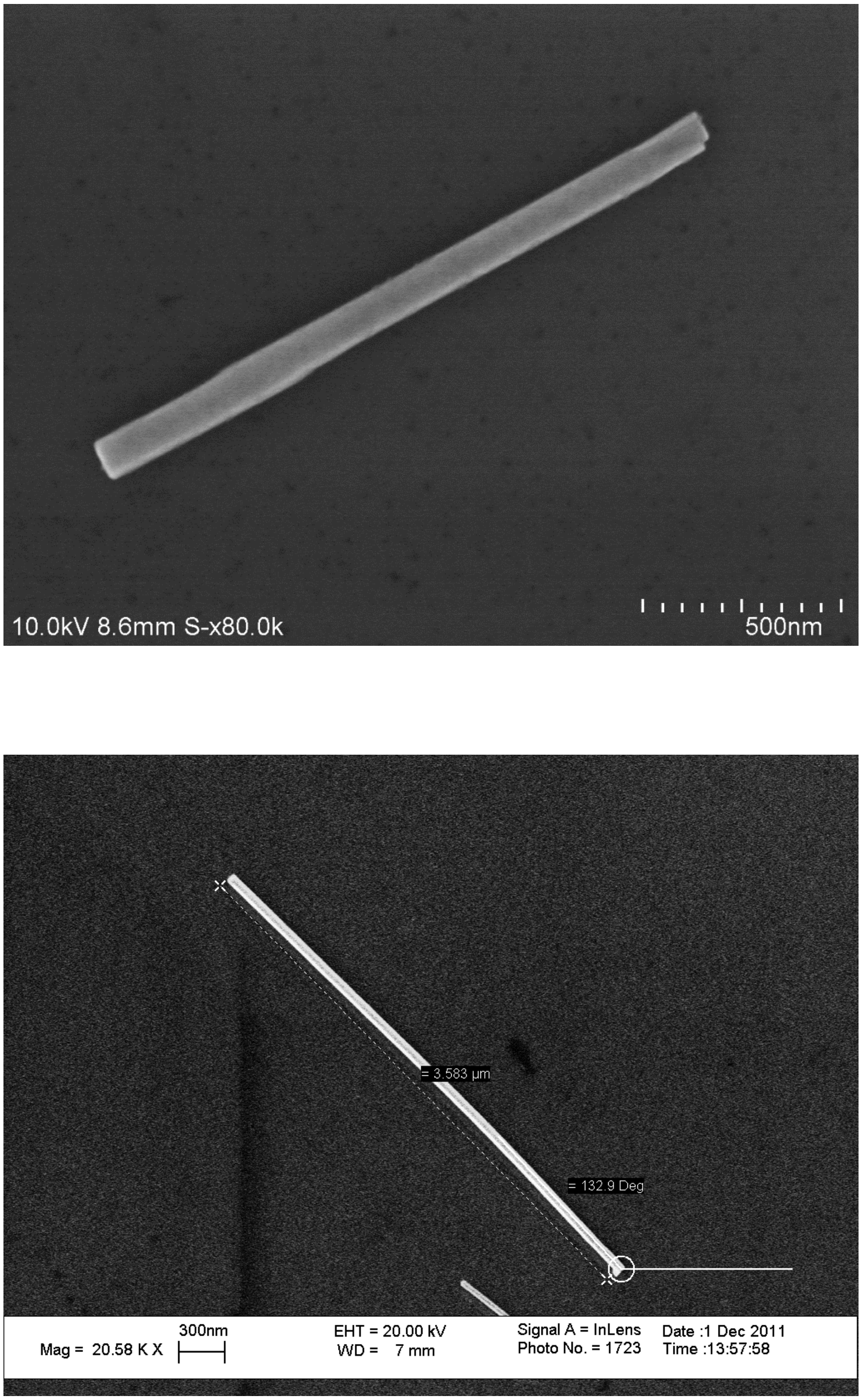

Figure 6.8 SEM images of a 2 and 4µm (top and bottom, respectively) single nanowire dispersed on thermally grown SiO_2.

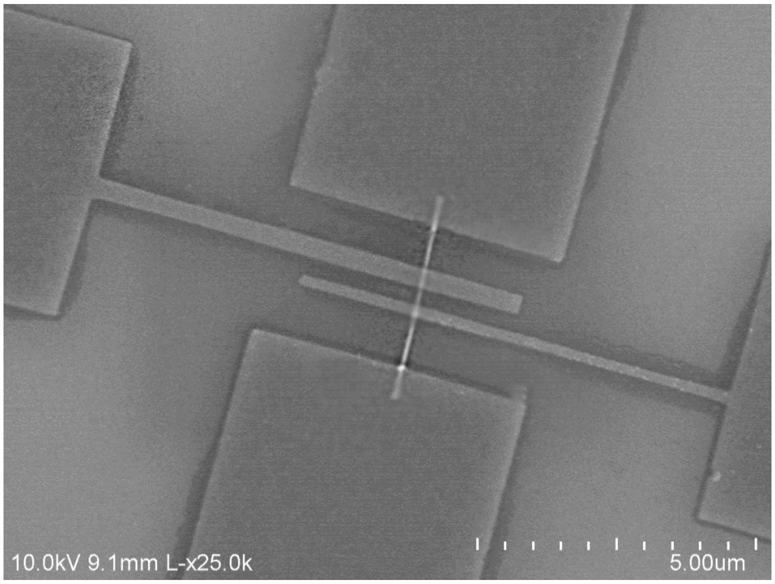

Figure 6.9 A top-down SEM view of the lateral spin valve fabricated on a ~4 μm long nanowire using e-beam lithography. The middle two contacts have different aspect ratios to induce different coercivity values. Multiple devices were fabricated and measured for both samples A and B.

6.5 Device characterization

This section covers several electrical and magnetic characterizations of the fabricated two- and four-terminal spin valves. I-V characteristics can elucidate several important properties of the ferromagnet/tunnel barrier/semiconductor (FM/TB/SC) interface, such as the quality of the tunnel barrier and if there are any stray currents passing through the SiO_2 insulating platform.

6.5.1 I-V characteristics

Figure 6.11(a) shows the typically measured two-terminal I-V characteristics of a single nanowire at different temperatures, measured in a Keithley 4200 IV probe station. Also shown are the I-V characteristics of the SiO_2 insulating layer. A non-linear variation of bias-dependent current through the NW is observed, which indicates tunneling electron transport across the FM/SC interface through the MgO tunnel barrier. However, this non-linearity cannot verify the quality of the tunnel barrier, such as the presence of pinholes.

The zero-bias resistance (ZBR), $R_0(T)/R_0(300K)$, exhibits weak insulator-like dependence on temperature, verifying spin injection into the NW via single step tunneling (Fig. 6.11(b)). The temperature dependence of ZBR is known to be the most reliable indicator of tunneling transport [147]. The SiO_2 layer, which does not exhibit any conductive breakdown up to 80V, provides a good insulating platform for the nanowire spin valve and our experiments.

The memristive I-V characteristic is shown below in Fig. 6.10. The black curve is the first virgin sweep of the device. The saturation of the current at higher voltages is due to the compliance limit set to prevent the device electrodes from burning. Other curves indicate successive voltage sweeps. The exact reason why such a significant hysteresis is present is not yet known. However, it is most likely due to the oxygen vacancies and other impurities present in the as-deposited MgO tunnel barrier, and this hysteresis effect can be reduce by annealing the sample on top of a hot plate for several hours.

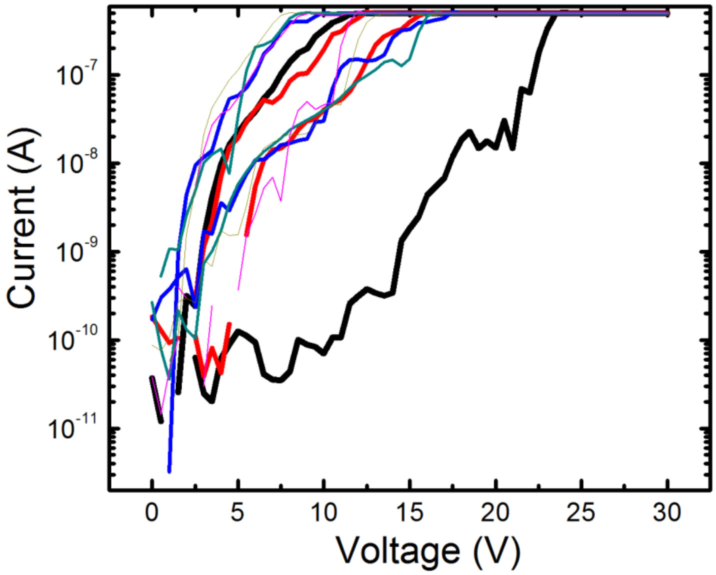

Figure 6.10 I-V characteristics of devices with non-annealed MgO contacts. The contacts show sizeable memresitive behavior. The solid black line corresponds to virgin sweep, with other solid lines corresponding to successive sweeps.

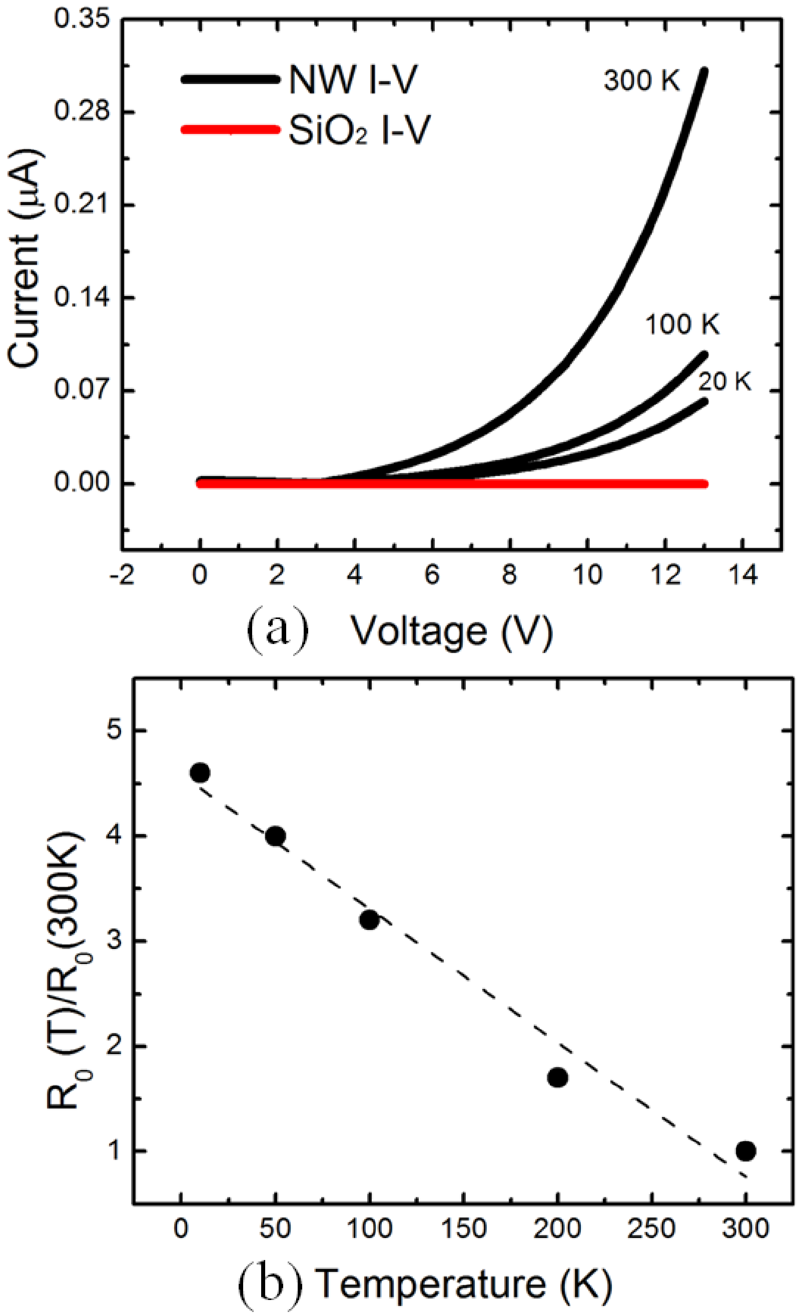

Figure 6.11 (a) Two-terminal I-V characteristics of a single NW at various temperatures (black line). Non-linear I-V characteristics indicate tunneling transport from the FeCo into the GaN NW through the MgO barrier. The current measured across the SiO_2 insulating platform (red line) shows no I-V up to an applied voltage of 40 V, precluding electrostatic interaction between the nanowire and the Si-substrate through the SiO_2 layer and providing a good insulated platform for our experiments. (b) Zero-bias resistance (ZBR) as a function of temperature. The weak temperature dependence (less than an order of magnitude) of the ZBR is a strong indication of the tunneling nature of the FeCo/MgO contacts.

6.5.2. Magnetoresistance characteristics

Magnetoresistance and spin accumulation measurements were made on the GaN nanowire devices with contacts in the conventional local and non-local spin valve configurations as schematically shown in Figs. 6.12 (a) and (b), respectively. The measurements were made, using a standard four-probe ac lock-in technique, as a function of channel length and temperature in the range of 150-300 K in a closed loop He cryostat. Samples of different channel lengths are loaded in the cryostat which is then mounted between the poles of an electromagnet such that the magnetic field is applied in-plane and orthogonal to the direction of spin transport. Temperature dependent magnetoresistance data from device A are shown in Fig. 6.13(a). The arrows indicate the relative orientation of the FeCo magnetization. The value of the magnetic field |H| for peak magnetoresistance is 150-200 Oe, corresponding to the coercivity difference of the FeCo electrodes. In contrast, there is no noticeable change of magnetoresistance in the control F/N/N devices. Non-local MR measurements are made to eliminate the response from possible spurious effects such as anisotropic magnetoresistance (AMR) and local Hall effects, which may resemble MR behavior arising from true spin injection [148, 149]. Results from non-local measurements with Sample A at T = 300 K are shown in Fig. 6.13(b). The value of |H| for peak spin accumulation coincides with those for peak MR. The peak accumulation corresponds to a voltage change ($\Delta V \sim 0.02$ mV). In contrast, the peak accumulation in the control F/N/N device is negligible. The variation of peak magnetoresistance with temperature in samples A and B, with channel lengths of 300 and 200 nm, respectively, are shown in Fig. 6.15(a). In general, the MR decreases linearly with increase of temperature and decreases with increase of doping in the nanowire. The

MR of the undoped NW spin valve is 10.5% at 300 K and 16% at 150 K. The decrease in MR with increasing temperature at a fixed bias is due to the decrease in the average spin relaxation time and hence the spin diffusion length, $\lambda_{sf} = (D\tau_{sf})^{1/2}$. The measured peak magnetoresistance at 300 K as a function of NW channel length for samples A and B are plotted in Fig. 6.15(b). The exponential decrease of magnetoresistance with NW channel length is also suggestive of diffusive spin transport and supports the temperature-dependent data.

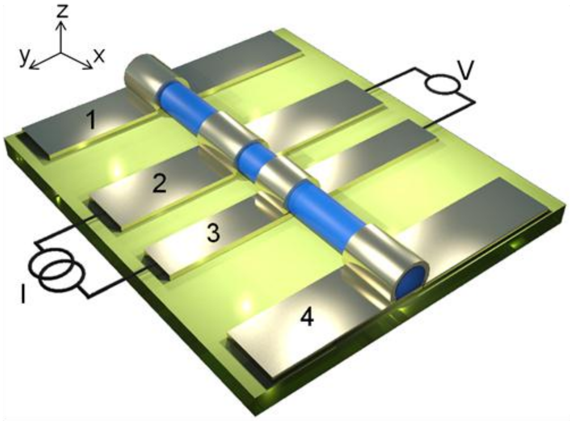

(a) Local measurement

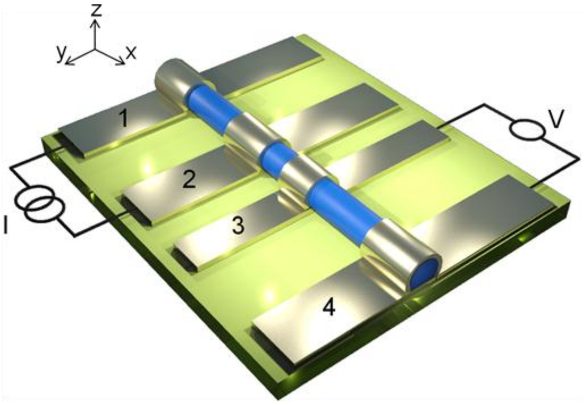

(b) Non-local measurement

Figure 6.12 A schematic illustration of the measurement scheme for (a) two-terminal (local) and (b) four-terminal (non-local) spin valve measurements.

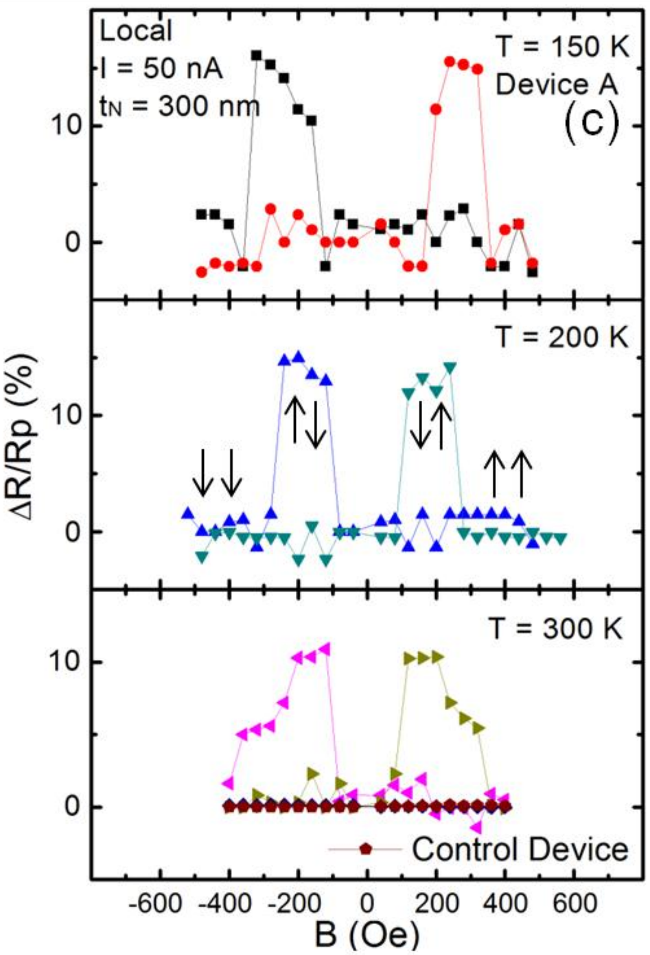

Figure 6.13 (c) Local and (d) non-local magnetoresistance measured on sample A for varying temperatures. A control device with a non-magnetic Ti/Au detector showed no magnetoresistance response, as expected. We note that the magnetic field in which the antiparallel peaks occur match for the local and non-local measurements.

6.5.3 Hanle characteristics

To further ascertain spin injection in the channel, Hanle precession measurements were made with sample A for two different nanowire channel lengths at T = 300 K. The Hanle effect is manifested as a Lorentzian-like change in the non-local voltage due to the precession (at a Larmor frequency $\omega_L = g\mu_B B_z/\hbar$, where g is the g-factor, μ_B is the Bohr magneton, and ħ is reduced Plank's constant) and suppression of spin that is subject to a transverse magnetic field (B_z). It is measured by first setting the magnetization of contacts 2 and 3 (Fig. 6.12 (b)) either in parallel or antiparallel state, then sweeping an out-of-plane magnetic field while measuring the non-local voltage (contacts 3 and 4). A constant current is flown through contacts 1 and 2.

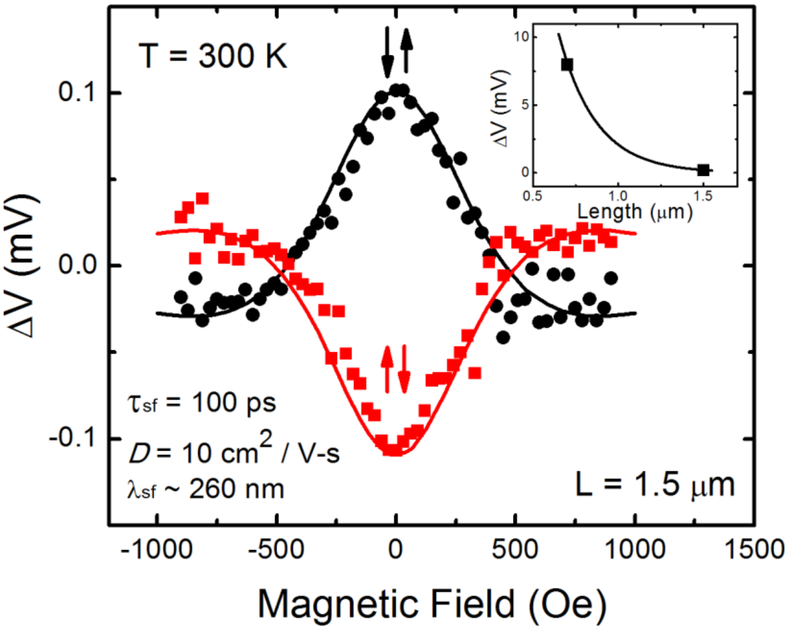

Figure 6.14 Four-terminal Hanle precession at T = 300 K for a device with channel length L = 1.5 μm. The precession and suppression of spin under a transverse magnetic field is clearly observed.

Clear suppression of spin in the channel was observed in the spin valves, as shown in Fig. 6.14, where the top and bottom branches correspond to parallel and antiparallel magnetization of contacts 2 and 3. For a longer channel length, the transit time is increased and the Hanle effect signal is more peaked in |H|, as is the case in our measurements. However, due to the relatively short length (~4 μm max length) of the epitaxially grown nanowires and thus a short channel, we were not able to observe a full 3π/2 precession. Typically, Hanle measurements are carried out with channel lengths of several microns in any material system. However, due to the limitation of the nanowire growth, it is difficult to grow very long nanowires with good thickness uniformity. A nanowire of approximately 10 μm or longer will be necessary to observe a full 3π/2 precession.

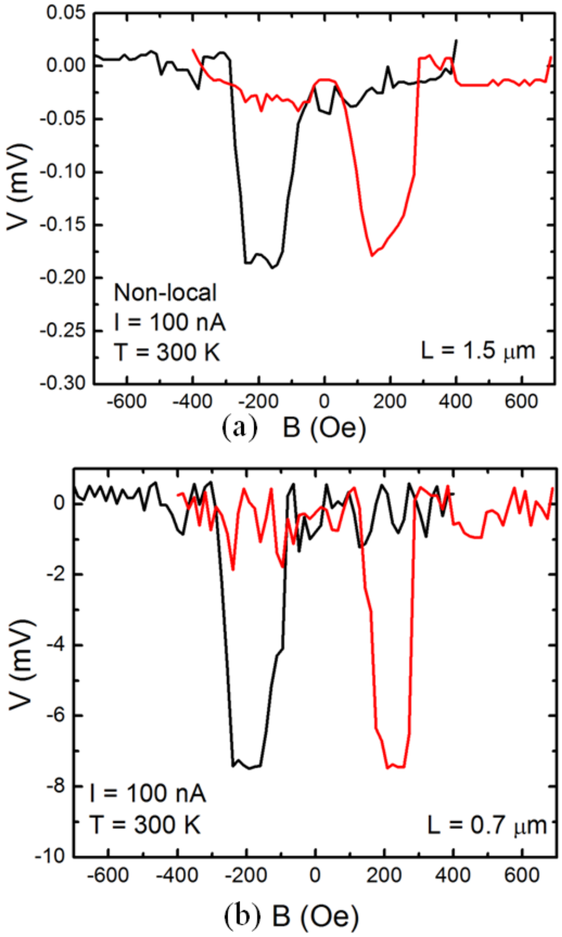

Figure 6.15 Four-terminal nonlocal characteristics at T = 300 K for two different channel lengths. No base voltage is observed.

6.6 Spin valve analysis

In this section we present theoretical analysis of the obtained experimental result using theory proposed by Fert and Jaffrès, and the widely accepted two-channel model for spin injection and transport via tunneling. It is possible to obtain nearly any spin-dependent parameter using these set of equations. The main analysis is done for two-terminal spin valve measurements (as opposed to non-local measurements) because the two-terminal configuration is most likely going to be the device geometry for practical spintronic devices.

6.6.1 Theory by Fert and Jaffrès

The length dependent two-terminal magnetoresistance was analyzed by the theory of Fert and Jaffrès [150], also recently used to describe spin injection and transport in Ge nanowires [151]. Accordingly,

$$\Delta R = \frac{2(\beta r_F + \gamma r_b^*)^2}{(r_b^* + r_F) + \frac{r_N}{2}\left[1 + \left(\frac{r_b^*}{r_N}\right)^2\right]\frac{l_N}{\lambda_{sf}^N}} \qquad \textbf{(6.2)}$$

and

$$R_P = 2(1-\beta^2)r_F + r_N \frac{l_N}{\lambda_{SF}^N} + 2(1-\gamma^2)r_b^* + 2\frac{(\beta-\gamma^2)r_F r_b^* + r_N(\beta^2 r_F + \gamma^2 r_b^*)\tanh\left(\frac{l_N}{2\lambda_{sf}^N}\right)}{(r_F + r_b^*) + r_N \tanh\left(\frac{l_N}{2\lambda_{sf}^N}\right)} \qquad \textbf{(6.3)}$$

The parameters used to calculate the percentage magnetoresistance $\Delta R/R_p$ are listed in Table 1. β and γ are the bulk spin polarization and a spin-dependent tunneling parameter, respectively. l_N is the NW channel length, r_F and r_N are the resistivity of the ferromagnet and NW multiplied by λ_{sf}, respectively, and r_b* is the interface resistance of the FeCo/MgO/GaN tunnel barrier contact. The solid lines in Fig. 6.15(a) are the calculated magnetoresistance values as a function of channel length, using λ_{sf}^N as a fitting parameter. The values of λ_{sf}^N at 300K are 300 nm and 250 nm for samples A and B, respectively. For a non-degenerate semiconductor, the spin diffusion length is defined by

$$\lambda_{sf}^{N} = \sqrt{\frac{k_B T \tau_{sf}}{2nq^2 \rho_N}} \qquad \textbf{(6.4)}$$

where n is the doping density and ρ_N is the resistivity of the NW. The spin lifetimes as a function of temperature in samples A and B, derived from the temperature-dependent MR data of Fig. 6.15(b), are depicted in Fig. 6.15(c).

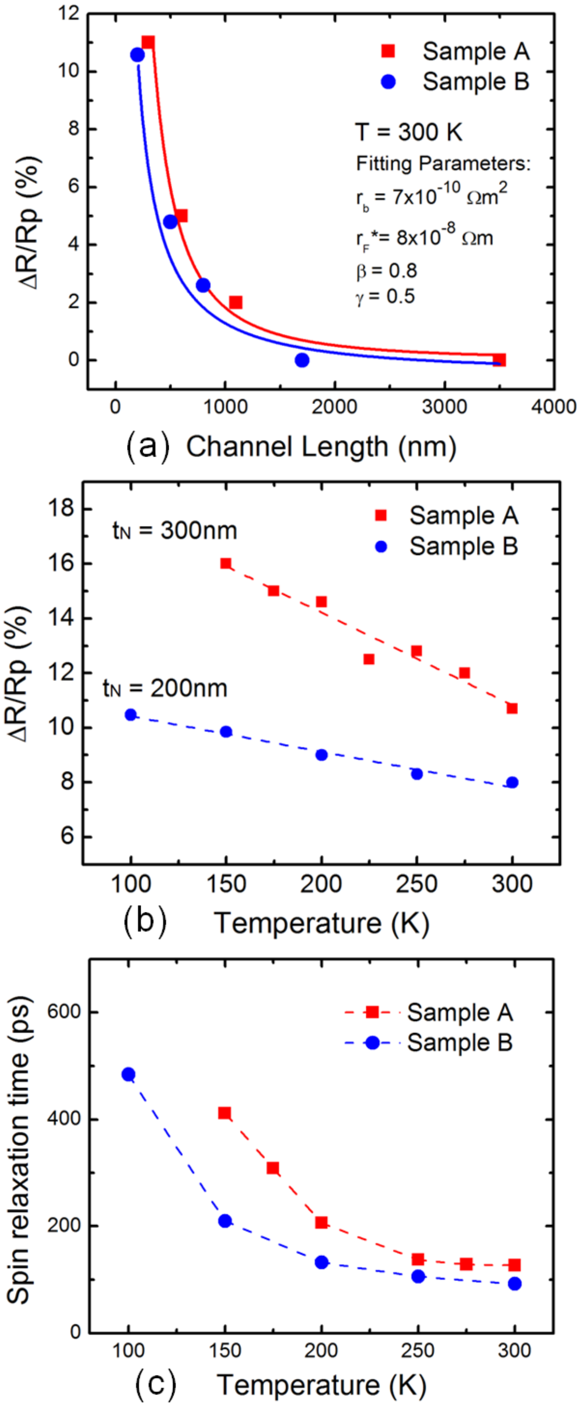

Figure 6.16 Magnetoresistance response as a function of (a) channel length and (b) temperature for samples A and B (red square and blue dots, respectively). The channel length dependent results are fitted with theory for two-terminal lateral semiconductor spin valves with spin diffusion length (l_{sf}) as the fitting parameter. The spin diffusion length in the GaN nanowire, extracted from the fit, comes out to be 300 nm and 250 nm for samples A and B, respectively; (c) Spin lifetime as a function of temperature for samples A and B, calculated from the magnetoresistance vs. temperature data.

Table 6.1 Parameter values for samples A and B. Mobility of each sample were estimated from Hall measurements done on epitaxially grown bulk GaN.

Parameter	Sample A	Sample B
τ_{sf} (nm)	120	90
r_N/λ_{sf} (Ωm)	$4.173\text{x}10^{-3}$	$3.24\text{x}10^{-4}$
r_F/λ_{sf} (Ωm)	$8\text{x}10^{-8}$	$8\text{x}10^{-8}$
r_b*(Ωm^2)	$0.8\text{x}10^{-9}$	$0.8\text{x}10^{-9}$
β	0.5	0.5
γ	0.4	0.4

6.6.2 Four-terminal Hanle and non-local analysis

To obtain an estimation of the transverse spin relaxation time, T_2, a model based on the Johnson-Silsbee theory [152] was used to fit the obtained Hanle data for a channel length of L = 1.5 μm (solid lines in Fig. 6.14), which is quantitatively given by [16]

$$\frac{V_{NL}}{I_{Inject}} \propto \pm\int_0^\infty \frac{1}{\sqrt{4\pi Dt}}\exp\left[-\frac{L^2}{4Dt}\right]\cos(\omega_L t)\exp\left[-\frac{t}{\tau_{sf}}\right]dt \qquad \textbf{(6.5)}$$

where D is the diffusion constant, τ_{sf} is the spin lifetime, L is the distance between the injector and detector electrodes, and + (-) sign indicates parallel (antiparallel) magnetization state of the FM electrodes. Here, D can be approximated by using the mobility values measured on a bulk GaN film grown in our lab with the same doping level as the nanowires. Invoking Einstein's relation $D = \mu k_B T / q$, we obtain a diffusion constant of D = 10 cm^2/V-s. Using a g-factor of 2 for GaN, we derive the spin lifetime τ_{sf} ≈ 100 ps, which translates to a spin diffusion length of λ_{sf} ≈ 260 nm at T = 300 K using the relation $\lambda_{sf} = (D\tau_{sf})^{1/2}$. Similar results were obtained for the 0.7 μm channel device.

The channel length dependent non-local measurement data can be fit independently to estimate λ_{sf} using the equation [153]

$$\frac{\Delta V}{I_{Inject}} = \frac{P^2 \rho \lambda_{sf}}{2A} \exp\left[\frac{-L}{\lambda_{sf}}\right] \tag{6.6}$$

where P is the polarization, ρ is the resistivity of the nanowire, *A* is the cross sectional area of the nanowire, and L is the distance between the injector/detector. Due to the good uniformity of the nanowire and the electrodes, a reasonable spin diffusion length can be estimated even with two data points. A good fit is made with values $P \approx 0.7\%$ and $\lambda_{sf} \approx$ 220 nm, as shown in the inset of Fig. 6.14. This value is in good agreement with the spin diffusion length derived from the analysis of the Hanle data, within experimental and fitting error. We also note that our spin lifetimes are in good agreement with values reported in ref. [123] and [124].

6.7 Spin Diffusion in Bulk GaN Measured With MnAs Spin Injector

In this section, we go on a slight tangent and discuss studies on spin injection into bulk GaN using MnAs as the spin injector using three-terminal Hanle precession measurements. The heterostructure and dimensions of the grown sample are shown in Fig. 6.17. The heterostructure consists of a 500 nm thick Si doped n-GaN bulk channel grown on a semi-insulating c-axis sapphire substrate with a 5 μm GaN template on top, a 1 nm thick AlAs tunnel barrier (TB) grown by molecular beam epitaxy (MBE) at a substrate temperature of 700 ºC, and a 35 nm thick ferromagnetic MnAs spin injector/detector grown at a low substrate temperature of 250 ºC. Three samples were grown, each with different doping densities (sample A: $4.2\text{x}10^{17}$ cm^{-3}, sample B: $1\text{x}10^{18}\text{e}^{-3}$, sample C: $7.8\text{x}10^{18}\text{cm}^{-3}$). Before growth, the native oxides were removed from the GaN template by dipping the substrate into aqueous HCl (1:1) for 15 minutes. The substrate was baked at 900º C prior to growth to remove impurities. The sample was fabricated into multiple three-terminal devices using standard optical lithography with each of the three contacts having a dimension of 200x150 μm^2. With reference to Fig. 6.17, contacts 1 and 3 are remote ohmic (Ti/Au) reference contacts and contact 2 is the ferromagnetic MnAs spin injector/detector. The distance between contacts 1 and 2 (and 2 and 3) is approximately 150 μm, which is much greater than the expected spin diffusion length in our GaN channel. The devices were wirebonded on a chip carrier and loaded into a cryostat between the poles of an electromagnet. The inset to Fig. 6.17 shows the measured magnetic hysteresis characteristics of a 35 nm MnAs film grown on GaN using the magneto-optic Kerr effect (MOKE) technique. The measurement indicates an in-plane easy axis of magnetization for the MnAs contact.

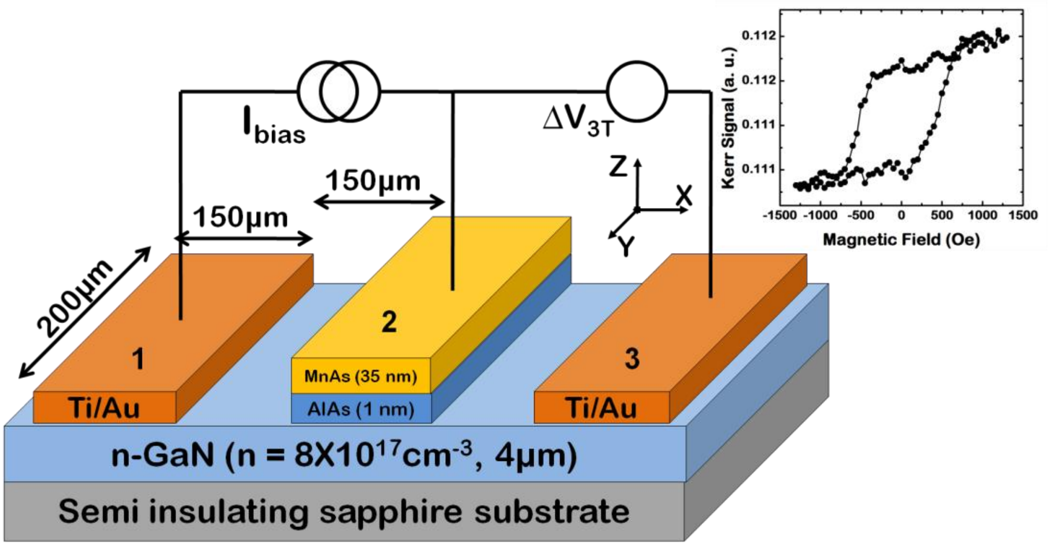

Figure 6.17 Schematic diagram of the heterostructure and dimensions of the fabricated device, along with the three-terminal Hanle measurement scheme. Inset shows the hysteresis characteristics of a 35 nm MnAs film grown on GaN.

To ensure that the MnAs/AlAs heterojunction provides a tunneling contact, the zero-bias resistance (ZBR) was measured as a function of temperature. The weak temperature dependence of the ZBR is regarded as an indication of single-step tunneling transport. The R_0(10 K)/R_0(300K) ratios did not exceed 3 for all three samples, verifying the tunneling nature of the MnAs/AlAs contact.

Three-terminal Hanle measurements were performed in a cryostat with the bias configuration shown in Fig. 6.17. This technique measures the spin accumulation and precession directly beneath the magnetic tunnel barrier contact interface. The measurements were carried out in a broad temperature range of 10 – 300 K and across several samples with different doping densities. A constant dc current is passed through contacts 1 and 2, while the voltage is measured across contacts 2 and 3 as a magnetic field perpendicular to the sample plane (B_z) is swept across the device. The MnAs contact is magnetized parallel to the plane of growth before the measurements. The spin accumulation due to injection causes a splitting of the spin-dependent electrochemical potential ($\Delta\mu = \mu_{up} - \mu_{down}$), which is detected as a voltage (ΔV_{3T}) across terminals 2 and 3. A perpendicular magnetic field (B_z) across the device precesses the accumulated spin at a frequency equal to the Larmor frequency, $\omega_L = g\mu_B B_z/\hbar$, resulting in precessional dephasing of the net spin accumulation in the channel, where g is the Lande g-factor ($g = 1.94$ for GaN) [123], μ_B is the Bohr magneton, and $\hbar$ is the reduced Planck's constant. However, since the three-terminal method primarily detects spin accumulation directly beneath the FM contact, localized interface states may cause spin to accumulate at the tunnel-barrier (TB)/semiconductor (SC) interface rather than the semiconducting channel, leading to erroneous overestimation on the spin lifetime and diffusion length (as pointed out by Tran et al. [37]). Therefore, it is necessary to provide evidence that the measured spin accumulation is in the channel rather than at the interface states. As shown later, analysis of the spin-resistance area product of our device, as well as the doping dependent spin lifetimes indicate that the spin accumulation is predominantly in the channel.

The three-terminal Hanle voltage, ΔV_{3T}, as a function of B_z is shown in Figs. 6.18(a) and (b) for different injection current across contacts 1 and 2, measured at room temperature. Fig. 6.18(a) corresponds to the case of spin injection, whereas Fig. 6.18(b) corresponds to spin extraction. The Lorentzian Hanle curve can be analyzed with the equation $V_{3T}(B_z) = \Delta V_{3T}(0) / [1+(\omega_L\tau_s)^2]$, where the spin relaxation time τ_s is used as a fitting parameter. $\Delta V_{3T}(0)$ is the voltage across contacts 2 and 3 at zero B_z.

An example Lorentzian fit is shown in Fig. 6.20(c) for sample A, yielding a spin lifetime of ~44, 27, and 21 ps at 300 K for samples A, B, and C, respectively. This value is in good agreement with the calculated value of ~35 ps for a sample with doping density of $n=2.2\times10^{17}cm^{-3}$ at room temperature. The small difference can be attributed to two factors. First, the three-terminal Hanle method gives a lower bound of spin lifetime due to increased interface scattering at the vicinity of the FM contact. Second, a lower doping level is expected to induce a longer spin lifetime due to the modification of the momentum scattering involved in spin relaxation time. This distinct change in spin lifetimes with respect to channel doping is in reasonable agreement with lifetimes measured by optical techniques

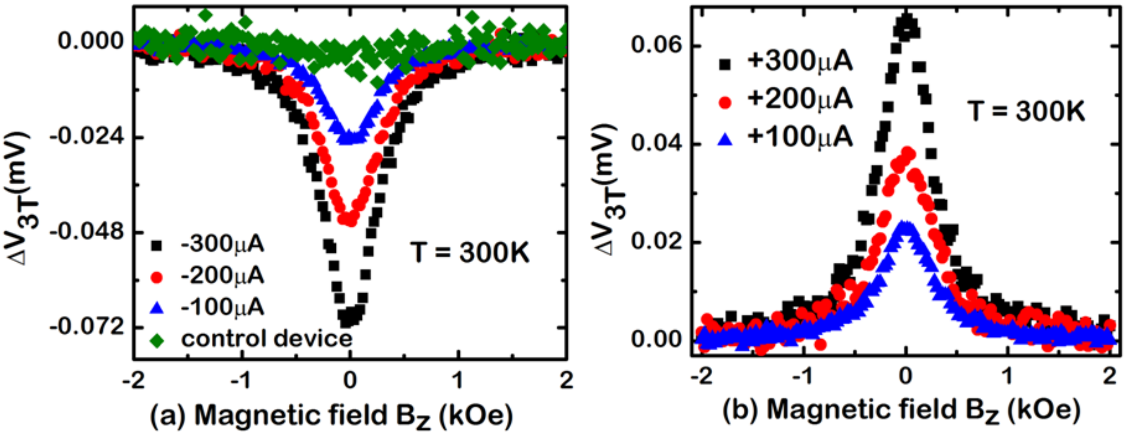

Figure 6.18 Bias dependent Hanle voltages (ΔV_{3T}) at room temperature for (a) negative bias (majority spin injection); and (b) positive bias (spin extraction) for sample A.

Figure 6.19 shows the spin diffusion length $L_{sd} = (\mu_e k_B T \tau_s/q)^{1/2}$ as a function of temperature calculated with the measured values of τ_s and μ_e. We derive a spin diffusion length of approximately 180, 140, and 80 nm at room temperature, for sample A, B and C, respectively, demonstrating that practical devices with MnAs as spin injectors into GaN may be realized with conventional lithography and fabrication techniques.

Spin current injected into a semiconductor can go through several processes that would relax the spin imbalance in the bulk. Of possible sources of spin relaxation, in wurtzite structures, Elliot-Yafet (EY) and D'yakonov-Perel' (DP) would play an important role. EY mechanism describes randomization of spin direction by scattering with impurities or phonons. This mechanism is proportional to momentum relaxation time. The functional form of EY mechanism for a given energy of spin in wurtzites is given by:

$$\frac{1}{\tau_\varepsilon^{EY}} \cong \left(\frac{\Delta_{SO}}{\Delta_{SO}+E_g}\right)^2 \left(1-\frac{m^*}{m}\right)^2 \left(\frac{\varepsilon}{E_g}\right)^2 \frac{1}{\tau_P} \qquad \textbf{(6.7)}$$

where Δ_{so} is spin-orbit coupling, E_g is semiconductor energy gap, m^*/m is the ratio of effective mass and free electron mass, and τ_p is the momentum scattering. In the case of GaN, the bandgap at room temperature (3.2 eV) is much larger than both the SOC energy and the kinetic energy (20-30 meV) (i.e. $k_B T, \Delta_{SOC} << E_g$). In the present experiment, the momentum relaxation time is of the order of $\tau_p = \frac{\mu m^*}{q} \approx 10^{-14} s$ which yields an EY relaxation time of the order of milliseconds, which cannot explain the measured spin relaxation time.

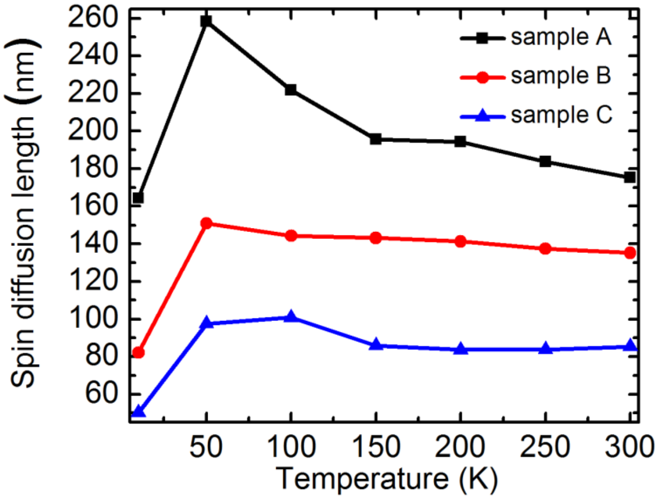

Figure 6.19 Spin diffusion length as a function of temperature for samples A, B, and C.

The DP mechanism describes spin randomization due to precession and scattering together. The direction of spin precession changes via momentum scattering. In wurtzite structures, both the Rashba and Dresselhaus spin-orbit coupling becomes important due to the intrinsic inversion asymmetry that is present. The spin scattering time of a given energy for this mechanism is given by:

$$\frac{1}{\tau_{\varepsilon}^{DP}} = \frac{4\tau_P}{3\hbar^2}[\alpha^2(\frac{2m^*\varepsilon}{\hbar^2}) + \frac{2}{5}\alpha\beta_3(b-4)(\frac{2m^*\varepsilon}{\hbar^2})^2 + \frac{7(4-b)^2+8(1+b)^2}{175}\gamma_3\beta_3^2(\frac{2m^*\varepsilon}{\hbar^2})^3] \quad \textbf{(6.8)}$$

where α is Rashba coupling including linear Dresselhaus component, β_3 is cubic Dresselhaus coefficient, *b* is the interference factor between Rashba and Dresselhaus components. For GaN, interference is negligibly small for the purposes of this analysis and the expected value of *b*=3.959 is approximated as *b*=4. The agreement with measured spin relaxation times is very good over the entire temperature range of measurement (Fig. 6.21).

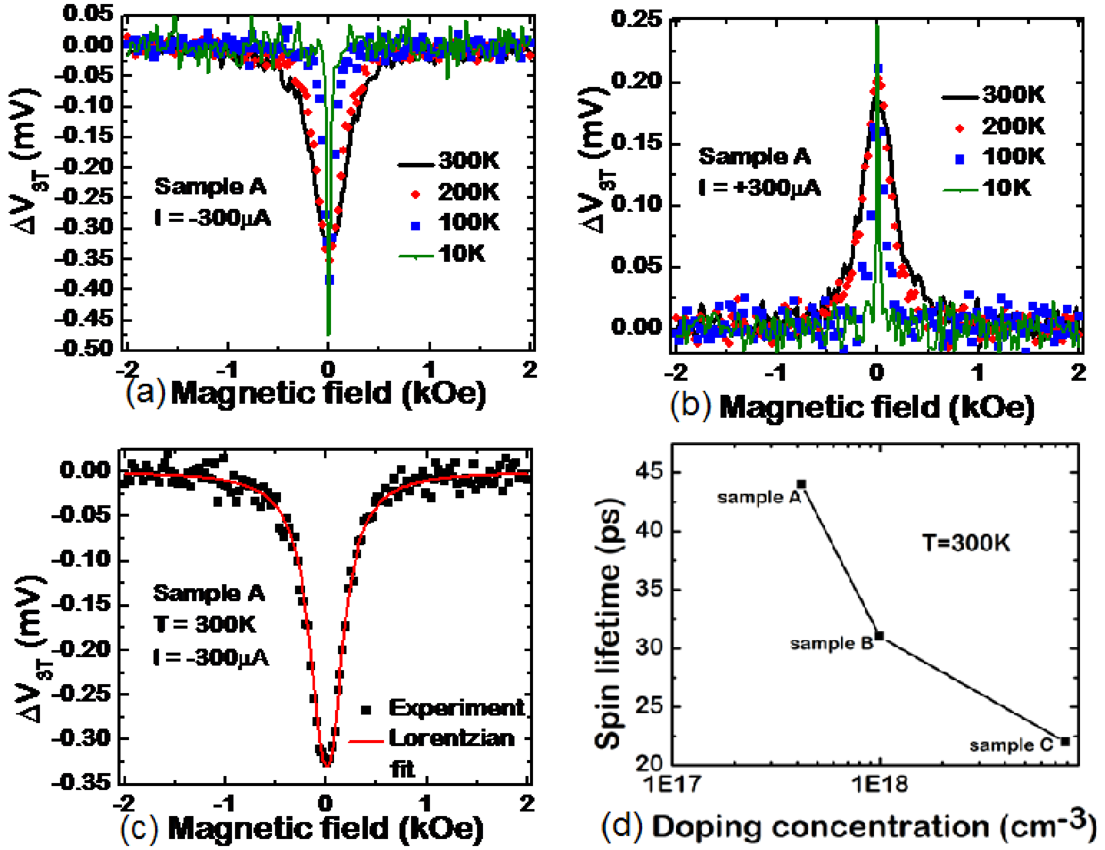

Figure 6.20 Temperature dependent Hanle signal for (a) spin injection and (b) spin extraction for sample A; (c) Lorentzian fit to the Hanle data for a bias current of 300 μA at room temperature; and (d) extracted spin lifetimes as a function of doping concentration (sample A, B, and C).

The thermal average of the spin relaxation, which is measured in the experimental technique presented in this letter, can be calculated from Eq. 6.7 and 6.8 as

$$\frac{1}{\tau_{\varepsilon}^{EY}} \cong \left(\frac{\Delta_{SO}}{\Delta_{SO}+E_g}\right)^2 \left(1-\frac{m^*}{m}\right)^2 \left(\frac{k_B T}{E_g}\right)^2 \frac{1}{\tau_P} \frac{I_{\upsilon+2.5}(\beta\mu) I_{1.5}(\beta\mu)}{I_{\upsilon+1.5}(\beta\mu) I_{0.5}(\beta\mu)} \qquad \textbf{(6.9)}$$

and

$$\frac{1}{\tau_{\varepsilon}^{DP}} = \frac{4\tau_P}{3\hbar^2}\left[\alpha^2 \left(\frac{2m^* k_B T}{\hbar^2}\right) \frac{I_{1.5}(\beta\mu)}{I_{0.5}(\beta\mu)} + \gamma_3 \beta_3^2 \left(\frac{2m^* k_B T}{\hbar^2}\right)^3 \frac{8 I_{\upsilon+3.5}(\beta\mu) I_{1.5}(\beta\mu)}{7 I_{\upsilon+1.5}(\beta\mu) I_{0.5}(\beta\mu)}\right] \qquad \textbf{(6.10)}$$

where $I_d(\beta\mu)$ is energy convolution of the scattering mechanism:

$$I_d(\beta\mu) = \beta^{d+1} \int_0^{\infty} x^d \frac{e^{-\beta x+\beta\mu}}{(1+e^{-\beta x+\beta\mu})^2} dx \qquad \textbf{(6.11)}$$

and υ depends on the type of source causing the scattering. Temperature dependence reduces to a well known quadratic dependence for EY mechanism and linear/cubic for DP mechanism in the high temperature limit, while saturates to a constant at low temperatures for both.

The amplitudes of the measured Hanle signal at 300K for |I|=100, 200 and 300 μA are $|V_{3T}(B_z=0)| \approx$ 0.025, 0.045 and 0.07mV, respectively, which correspond to spin resistance $R_S = |V_{3T}(B_z=0)| / I \approx$ 0.25, 0.225 and 0.233Ω. These values translate to spin resistance-area products $R_S.A= |V_{3T}(B_z=0)|\, A / I \approx$ 7.5, 6.7 and 7.0 kΩμm^2, respectively, for the 200x150μm^2 FM contact, which are in reasonable agreement with the theoretically predicted spin resistance-area product given by $R_S.A = \gamma^2 \rho L_{sd} \sim 2$ kΩμm^2. Here ρ is the GaN resistivity, L_{sd} is the spin diffusion length, and γ is the tunneling spin polarization of the FM MnAs contact. It is important to note that spin accumulation at interface states will cause the Rs·A value to be several orders of magnitude greater than that predicted by theory, as is the case in Tran *et al.*'s study, where they observed R_S·A

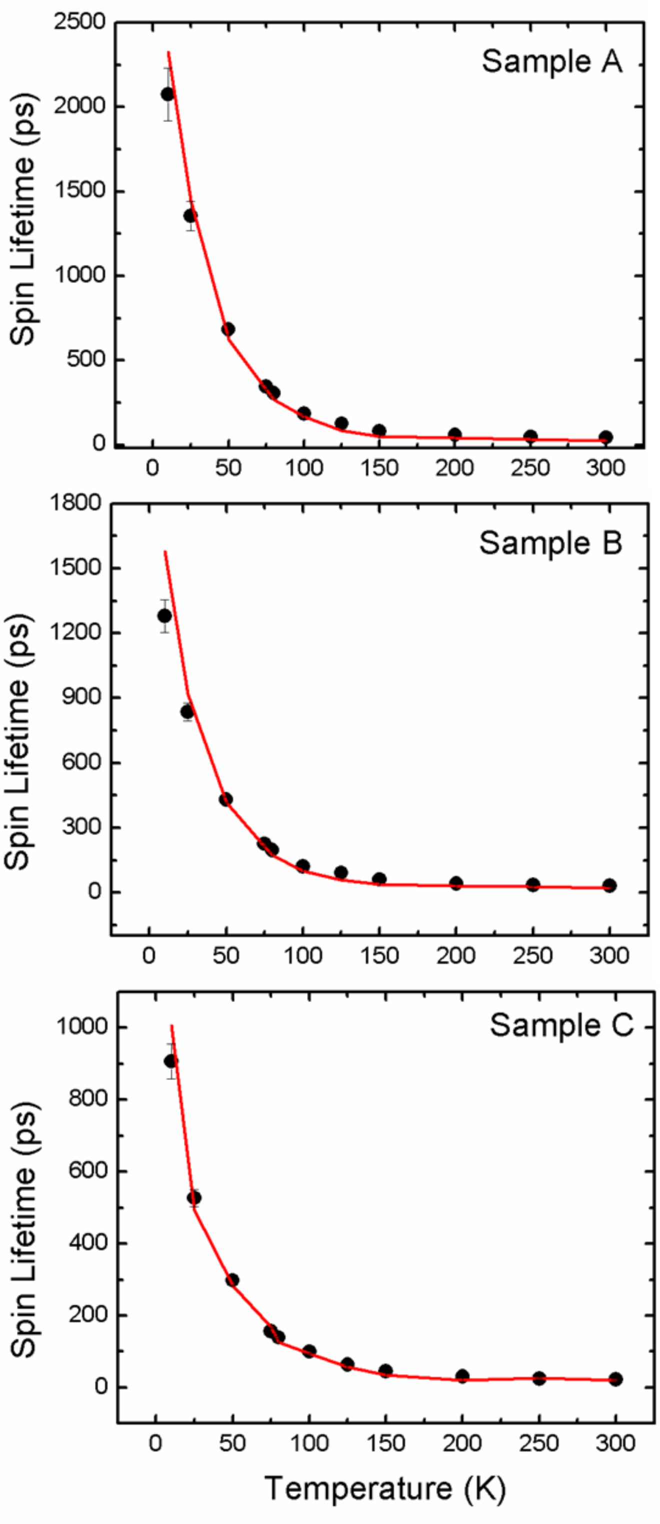

Figure 6.21 Theoretical fit to the spin lifetime for samples A, B, and C (top, middle, and bottom, respectively).

values three order of magnitude larger than that predicted by theory. This provides strong evidence that the measured spin accumulation is in the GaN channel and demonstrates that practical devices with MnAs as spin injectors into GaN may be realized with conventional lithography and fabrication techniques.

6.8 Comparison of Spin Lifetimes in Various GaN systems

At this point, it is instructive to compare our results with measurements done on other GaN systems, as it elucidates the possible effects of different spin relaxation mechanisms. At the time of writing, there are only a few measurements of spin lifetime conducted on epitaxially grown GaN, discussed briefly in the introduction of this chapter.

We compare the results of Beschoten *et al.* and Buβ *et al.* with our results. Both groups measured spin lifetime in bulk GaN using time-resolved Faraday-rotation and time-resolved Kerr-rotation, respectively. These measurements have been made, as pointed out in the introduction, on epitaxial GaN grown on mismatched substrates with a large defect density (10^{8}-10^{10} cm^{-2}) of threading dislocations and stacking faults. Their results indicate spin lifetimes of approximately 35-100 ps at room temperature. In comparison, nanowire-based spin valves show a spin lifetime of nearly 120 ps at room temperature. This superior performance of spin transport in nanowires can be attributed to spatial confinement effects and/or the reduction of the Elliot-Yafet relaxation mechanism. For now, a more rigorous experiments need to be done to verify exactly the contributions of each effect.

Spin relaxation in 3-dimensional n-doped GaN is usually attributed to either the Elliot-Yafet (EY-momentum scattering in the presence of impurity spin-orbit coupling) or the D’yakonov-Perel (DP-momentum scattering of spin-orbit coupled bands) spin relaxation mechanism. The EY relaxation scales with the square of the ratio of the SOC to the energy bandgap, as well as the ratio of the kinetic energy to the bandgap. In the case of GaN, the bandgap at room temperature (3.2 eV) is much larger than both the SOC energy and the kinetic energy (20-30 meV) (i.e. $k_B T, \Delta_{SOC} << E_g$). The EY mechanism describes randomization of spin orientation through momentum changes and the spin relaxation time in confined 2D structures is given by

$$\frac{1}{\tau_{EY}} = \left(\frac{\Delta_{SO}}{\Delta_{SO} + E_g} \right)^2 \left(1 - \frac{m_e^*}{m_e} \right)^2 \frac{E_c k_b T}{E_g^2} \frac{1}{\tau_p} \qquad \textbf{(6.7)}$$

In the DP spin scattering mechanism spin precession occurs in the effective magnetic field and the direction of precession is altered by momentum scattering. In wurtzite structures, intrinsic inversion asymmetry is present and Rashba and cubic Dresselhaus spin-orbit coupling become important. The spin lifetimes limited by DP scattering in two-dimensional wurtzite structures is given by:

$$\frac{1}{\tau_{DP}} = \frac{2\tau_p}{\hbar^2} \frac{I_1}{I_0} \left[\alpha^2 k_T^2 - 2\alpha\beta_3 k_T^4 \frac{I_{\nu+2}}{I_{\nu+1}} + \beta_3^2 k_T^6 \frac{I_{\nu+3}}{I_{\nu+1}} \right] \qquad \textbf{(6.8)}$$

where $I_\nu(\beta\mu)$, the energy convolution of the scattering mechanism is given by:

$$I_\nu = \beta^{\nu+1} \int_0^\infty x^\nu \frac{e^{\beta(\mu - x)}}{\left(1 + e^{\beta(\mu - x)}\right)^2} dx, k_T^2 = \frac{2m^*}{\hbar^2 \beta} \qquad \textbf{(6.9)}$$

and $\beta = 1/(k_B T)$ while the parameter ν depends on the relevant carrier scattering mechanism. The parameter ν is the power of the energy dependent scattering mechanism (E^ν), T_F is the Fermi temperature of the carriers, and γ_3 is a constant on the order of 1-10.

For a material where DP relaxation mechanism is dominating, the momentum scattering time becomes increasingly important. A more frequent momentum scattering rate will lead to a longer spin lifetime. Although Beschoten’s work stated a potential decoupling of momentum scattering rates and spin relaxation times, a recent report by our group on the spin relaxation in InGaN quantum disks [154] suggests otherwise. A quantum disk, by the virtue of their 2-dimensional quantum confinement (2D confinement), has much reduced momentum scattering rates compared to 3D bulk materials. For a DP dominated system, this will lead to shorter spin lifetimes. Indeed, a spin lifetime of ~100 ps was obtained for InGaN disks imbedded inside a GaN nanowire, with the lifetime decreasing with decreasing indium concentration. The spin lifetime vs. indium composition trend is also consistent with the explanation presented previously. A higher indium composition results in more scattering of the carriers inside the disk (due to increased defects associated with incorporation of indium during growth), leading to shorter momentum scattering times and longer spin lifetimes.

It is difficult to directly compare the results obtained from spin injection into a GaN nanowire using FeCo to the spin injection into bulk GaN using MnAs, due to the fact that a completely different tunnel barrier and ferromagnet, as well as measurement scheme, was used. However, if any conclusion can be made comparing these two sets of experiments, it is evident that defects in GaN systems does play a role in determining the spin relaxation process, which is directly associated with the EY relaxation mechanism. Previous studies state that the EY mechanism is nearly absent in GaN, but this may not be necessarily true. Further experiments must be done to clarify this property.

6.9 Summary

In summary, we have investigated spin injection, transport, and detection in single GaN nanowires free of growth defects by conducting measurements on spin valves made with FeCo/MgO tunnel contacts. The nanowires are grown epitaxially on (001) Si substrates by PA-MBE and the spin valves are fabricated by dispersing single nanowires on SiO_2/Si and subsequent deposition of MgO and FeCo. Spin injection is confirmed by non-local and Hanle measurements. Measurements have been made with spin valves having different nanowire channel lengths and as a function of temperature and nanowire doping density. The largest magnetoresistance measured at room temperature is 10.5%. The magnetoresistance decreases with increase in doping level in the nanowire, channel length, and temperature. Analysis of the temperature-dependent MR data confirms diffusive spin transport in the nanowires. The spin diffusion length and spin lifetime in undoped GaN nanowires are 300 nm and 120 ps, respectively, at room temperature.

Chapter VII

Conclusions and Suggestions for Future Work

7.1 Summary of Present Work

This thesis has presented several spintronic devices based on III-V semiconducting materials with emphasis on increasing the operating temperature, obtaining a larger magnetoresistance response, and electrical modulation of spin precession. While most studies on spin properties of electrons are carried out at cryogenic temperatures, the work described in this thesis is mostly at room temperature, inching towards practical spintronic applications opposed to physical phenomena study. Key results and conclusions are highlighted in the following sections.

7.1.1 Room temperature GaAs spin valve with submicron channel created by FIB

Spintronics has been a subject of intense research as it allows us to directly observe a purely quantum mechanical property of charged particles present inside various materials. For this field to truly have an impact, practical *devices* must be made with functionalities to aid information processing that can operate at temperatures that most consumer electronics are subject to today. One way to increase the operating temperature of spintronic devices is to reduce the length that the polarized current needs to travel. The focused ion beam technique was used to create a submicron-length channel, which increased the operating temperature up to 300 K from 125 K. The FIB’d spin valves show much sharper magnetoresistance switching behavior compared to wet etched spin valves, which is contributed to the sharp edge of the ferromagnetic injector/detector electrodes created by FIB. In contrast, wet etched spin valves have rough MnAs edges due to the etching characteristics of MnAs. Therefore, it is advantageous to utilize a physical etching process rather than chemical etching for devices using MnAs as electrodes. This is one of the first demonstrations of a room temperature GaAs spin valve by reducing the channel length down to submicron-length.

7.1.2 Two- and Three-terminal vertical MnAs/GaAs/MnAs vertical spin valve

A high temperature electrical spin injection and detection in degenerately p-doped GaAs in vertical spin valves using valence band electron tunneling was demonstrated. Spin relaxation in these devices is dominated by the Bir-Aronov-Pikus mechanism, which is relatively insensitive to temperature. The spin injection and detection efficiency are mostly determined by the ferromagnetic contact polarization and spin independent hopping transport at the ferromagnet/semiconductor interface. The maximum measured magnetoresistance at 10 K and 300 K is 40% and ~1%, respectively. Spin relaxation in these devices was found to be relatively insensitive to temperature (T) for T > 125K. The spin injection and detection efficiencies are mostly dominated by the ferromagnetic contact polarization and spin independent transport at the ferromagnet/semiconductor interface. VBET in a p-doped semiconductor embedded in a vertical structure can be an important process for the realization of high temperature semiconductor spintronic devices.

Gate control and amplification of magnetoresistance are demonstrated at room temperature in a fully epitaxial three-terminal GaAs-based device. In addition to the two ferromagnetic spin injector and detector electrodes of a MnAs/AlAs/GaAs:Mn/AlAs/MnAs vertical spin valve, a third non-magnetic gate electrode (Ti/Au) is placed directly on top of the heavily p-doped GaAs channel layer. The magnetoresistance of the device can be amplified to reach values as high as 500% at room temperature with the application of a bias to the gate terminal which modulates the spin selectivity of the tunnel barriers. The experimental results are modeled by solving spin drift-diffusion and tunneling equations self consistently. Such a device could be used to make spin-based memory devices that are monolithically integrated with conventional GaAs based microelectronics.

7.1.3 Magnetoresistance of lateral semiconductor spin valves as a function of extended mesas outside the spin-polarized current path

The magnetoresistance of two probe lateral semiconducting spin valves with respect to varying mesa size is studied. It is shown theoretically that extended regions outside the spin-current path can act as an additional source of spin-relaxation, decreasing the magnetoresistance response. From a simplified expression of magnetoresistance derived from spin-diffusion equations, we show that it is important to etch away these extended regions for devices with channel lengths much smaller than the spin-diffusion length in order to achieve maximum magnetoresistance. Preliminary experimental data are in good agreement with the theory established in this article, where a 50% increase in magnetoresistance was observed by etching away extended mesa regions outside the spin-polarized current path.

7.1.4 Electrical control of spin precession in an InAs 2DEG quantum well spin valve

The control of magnetoresistance of a lateral spin valve with bias applied to a gate placed outside the channel region is demonstrated. The spin valve channel consists of an

$InAs/In_{0.53}Ga_{0.47}As/In_{0.52}Al_{0.48}As$ two dimensional electron gas (2-DEG) lattice matched to (001) InP. The polarizer and analyzer contacts are made with 35 nm type B $MnAs/In_{0.52}Al_{0.48}As$ Schottky tunnel barriers. The magnetoresistance changes from 0.14% to 4% at 10 K in a device in which the spin transport is in the direction of magnetization of the polarizer and analyzer contacts. The effect is absent in a GaAs channel spin valve and other control devices indicating that the change in magnetoresistance is due to Rashba spin-orbit coupling.

7.1.5 Spin injection into a high quality defect-free GaN nanowire using MgO/FeCo

The first direct measurement of spin transport characteristics in a GaN spin valve, with a relatively defect-free *single* GaN nanowire as the channel and FeCo/MgO as the tunnel barrier spin contact is reported. Measurements have been made as a function of doping in the nanowire and temperature. A magnetoresistance of 10.5% is measured at 300 K in an unintentionally doped nanowire spin valve and values of spin diffusion length and spin lifetime of 300 nm and 120 ps, respectively, are derived. Appropriate control measurements have been made to verify spin injection, transport, and detection.

7.1.6 Spin injection into a high quality defect-free GaN nanowire using MgO/FeCo

Spin injection and precession in bulk wurtzite n-GaN is demonstrated with a ferromagnetic MnAs contact using the three-terminal Hanle measurement technique. Analysis of the spin resistance-area product ($R_S \cdot A$) indicates that the spin accumulation is primarily in the n-GaN channel rather than at interface states. Spin relaxation in GaN is interpreted in terms of the D’yakonov-Perel mechanism, yielding a spin lifetime of 27 ps and a spin diffusion length of 110 nm at room temperature. Our results indicate that epitaxial ferromagnetic MnAs is a suitable high temperature spin injector for GaN.

7.2 Suggestions for Future Work

7.2.1 Ferromagnetic GaMnN nanowire-based spintronic memory device

A fundamental understanding of low-dimensional ferromagnetic semiconductor nanostructures is crucial for developing novel nanoscale spintronic devices. GaMnN nanowires in particular are gathering increasing attention due to its applicability towards nanocircuitry. GaMnN is a dilute magnetic semiconductor (DMS) which exhibits carrier-mediated ferromagnetism at and above room temperature, originating from the exchange interaction between Mn ions and holes. They represent an important class of nanometer-scale building blocks for miniaturized spintronic devices and circuitry. Experimental characterization and demonstration of a non-volatile and high density spintronic memory based on GaMnN nanowires is proposed.

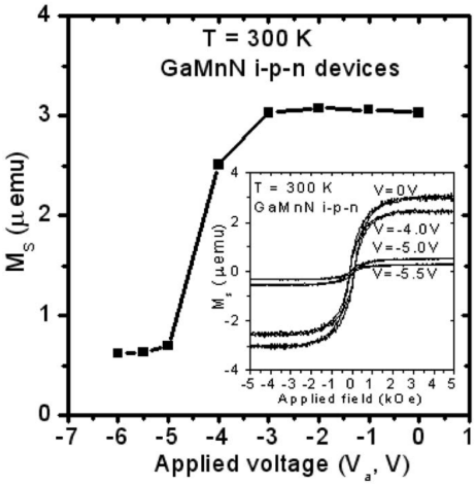

Figure 7.1 Change of magnetic moment (from ferromagnetic to paramagnetic) as a function of applied voltage to a p-n junction for GaMnN film.

Recently, an electrical control of the magnetic properties of GaMnN-DMS was demonstrated by Nepal *et al.* by situating the GaMnN-DMS directly on top of a p-type GaN layer [155]. The concentration of holes was controlled in the p-layer to switch the

GaMnN-DMS from a ferromagnet (high hole concentration) to a paramagnet (low hole concentration). Figure 7.1 shows the saturation magnetization (M_s) of a GaMnN film grown on top of a *p*-*n* junction at different reverse bias voltages across the junction (V_R) for a GaMnN film thickness of X_p=0.25 μm. For V_R > 3 V, the M_s is independent of applied voltage. The depletion width W_p at ~3 V is about 0.221 μm leaving almost 30 nm of *p*-GaN close to GaMnN/*p*-GaN interface.

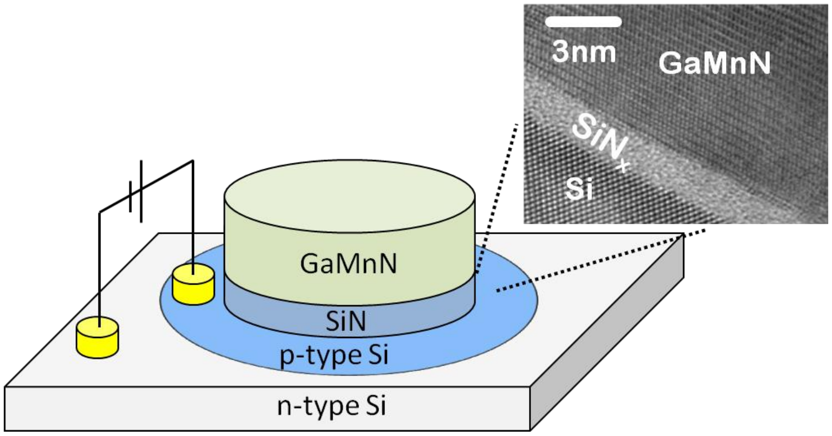

Figure 7.2 Schematic representation of a GaMnN DMS-based spintronic memory element. The hole concentration in the p-type Si region is controlled through a voltage bias between the p-n junction, which changes the magnetism property of the GaMnN nanowire from ferromagnetic to paramagnetic.

The penetration depth for the hole wave function into the *i*-GaMnN layer is believed to be less than 30 nm, which explains the constant value of M_s for V_R = 3 V and for forward bias. M_s starts to decrease at V_R =4 V. For V_R = 5 V the *p*-layer is fully depleted and the GaMnN film is almost paramagnetic. Thus, V_R increases the depletion width at the *p*-*n* junction by depleting the holes at the junction that interact with the localized Mn ion spins. At a high enough reverse bias, the p-GaN layer is fully depleted, and there are no itinerant holes to mediate ferromagnetism in the GaMnN layer, causing it to become paramagnetic. Hence, the ferromagnetism can be controlled at room temperature by biasing the structure. These binary magnetic states of GaMnN make it an attractive material for non-volatile memory applications. A schematic diagram of a nanostructure device utilizing GaMnN nanowires is shown below in Figure 7.2.

The proposed device consists of four regions: an n-type Si region, p-type Si well, GaMnN nanowire grown on top of the p-well, and a SiN insulator (naturally formed) between the Si substrate and GaMnN nanowire. When a negative voltage is applied to the p-n junction, the p-type layer is depleted of holes, causing the spin of the Mn atoms in the GaMnN nanowire to become disoriented due to the lack of carrier (hole) mediation; the saturation magnetization of GaMnN goes to zero as the negative voltage is increased, losing its ferromagnetism. When the negative voltage is removed, the concentration of holes in the p-type layer increases, reverting back the ferromagnetism of GaMnN. The SiN insulating layer plays a crucial role: it impedes the movement of holes once the negative voltage is taken off, allowing for stable binary magnetic states of the GaMnN nanowire. The SiN formed during GaMnN nanowire growth is also defect free, preventing hole transport through trap and impurity states. A tiny magnetic sensor embedded on each memory cell will read the magnetism present in the GaMnN nanowire for fast and low-power read operation. This memory is non-volatile in nature and will have zero off-state power dissipation. It will also operate at room temperature in the absence of any externally applied magnetic field. This novel nanostructured device will be one of the first to utilize magnetic nanowires for spintronic memory applications.

By nanopatterning the GaMnN nanowire growth using nanoimprint technology or e-beam patterning, a dense array of nanowires can be formed to create a structured memory circuitry, where each nanowire will act as a memory bit. A schematic illustration is shown in Figure 7.3. A magnetized nanowire can be normalized to signify an ON state, while a non-magnetized state can be normalized to signify an OFF state. By using a magnetism sensor with appropriate sensitivity, a high signal-to-noise ratio is expected.

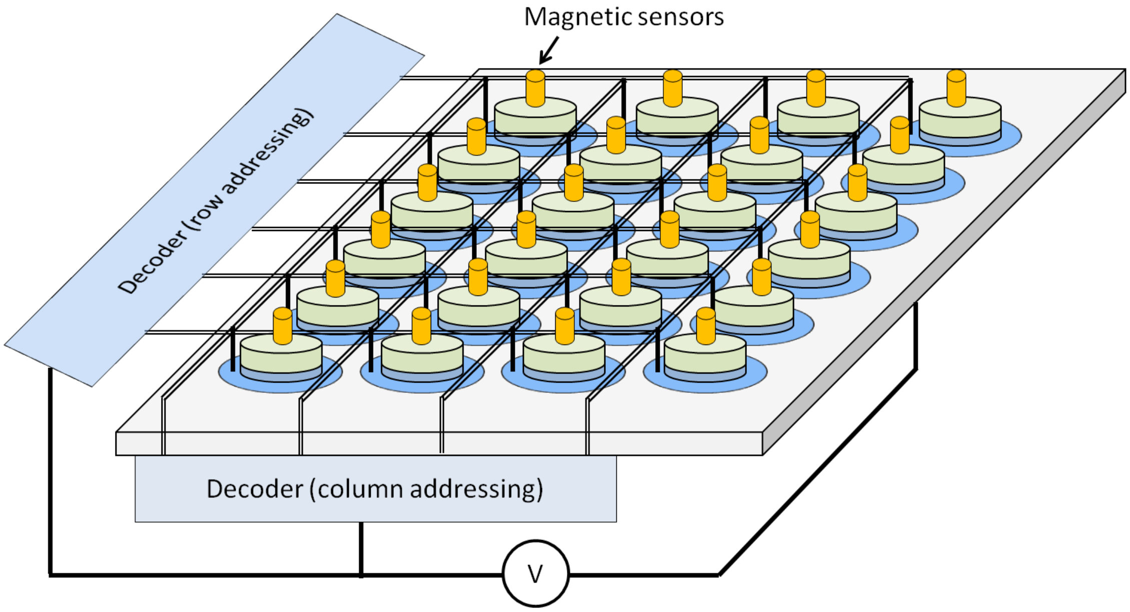

Figure 7.3 Illustration of GaMnN nanoscale memory array. The decoders address which bit to read/write information, and tiny magnetic sensors detect the magnetic state of each cell, which is then converted intto an output that can be read by any microprocessor.

Standard figure of merits for storage technology (programming time, addressing time, retention rate, power consumption, packing density, and signal-to-noise ratio) can be measured and compared to existing commercial technologies such as Flash RAM and DRAM to ensure that this technology has the potential to be competitive and viable.

7.2.2 Dilute magnetic semiconductor oxide based logic and memory device

Dilute magnetic semiconductor oxides (DMSOs) are another type of ferromagnets that can be utilized to design novel spintronic devices. It consists of an oxide material (such as TiO_2, HfO_2, ZnO, or ZrO_2) doped with magnetic metals (such as Mn, Ni, Co, Cr, or Fe). These materials show ferromagnetism at room temperature and its ferromagnetic properties may be tunable by controlling the concentration of defects (typically oxygen vacancies) present inside. Electrically tuning the ferromagnetism of a material directly translates to electrically tuning the spin detection/injection efficiencies if the DMSO material is used as electrical contacts, or may be utilized as a spin aligner if used as a channel material. Thus, without using spin-orbit coupling effects, which only manifests at low temperatures, one can have electrical control of spin-dependent effects at high temperatures. These materials can be typically made by sputter depositing.

Besides intriguing magnetic properties, the oxygen vacancies present in DMSOs yield to intrinsic memristive characteristics. A heterostructure to achieve this type of behavior is shown below.

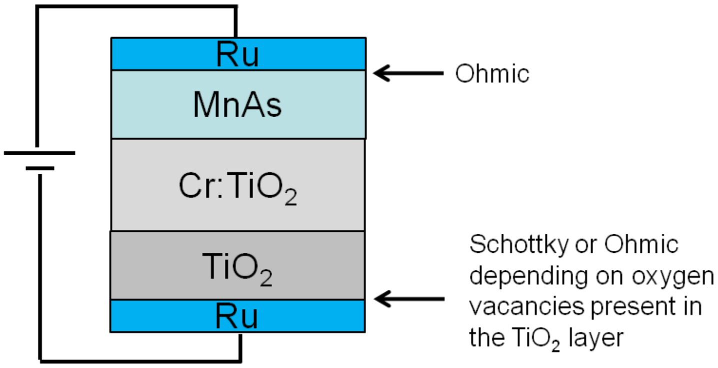

Figure 7.4 Illustration of a possible memristive DMSO cell.

The operation of DMSOs as a memristor is described in reference to Fig. 7.4. In general, one could simply use the fact that oxygen vacancies can be moved in and out of the layer; this property can be used to create a memristor element. For example, the interface between Ru and MnAs is ohmic (due to the low work function of MnAs), and the interface between TiO_2 and Ru is Schottky (thus, overall high resistance between the entire heterostructure). However, once oxygen vacancies are introduced into the TiO_2 layer, the interface between TiO_2 and Ru becomes Ohmic (overall low resistance). Thus this device has two stable states of low resistance and high resistance, which can be controlled by an externally applied voltage. The bi-stable state allows this type of device to be used as a memory cell.

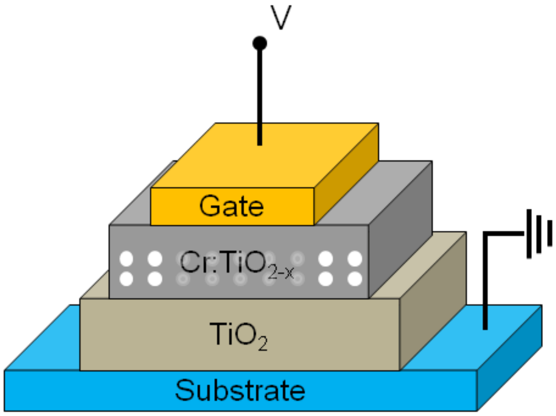

Figure 7.5 Structure for ionic transport of defects (oxygen vacancies) from a DMSO layer.

Dilute magnetic semiconductor oxides (DMSO) show ferromagnetism in the presence of oxygen vacancies in the material, as stated previosly. The oxygen vacancies can be moved in and out of the oxide into a TiO_2 layer via an electric field. The reason why oxygen vacancies produce ferromagnetism is still under debate. This control of ferromagnetism can be used to make a spin logic device, where two ferromagnetic electrodes pass spin polarized current through the DMSO. If the DMSO is ferromagnetic, the spins will transport through the DMSO from one FM to another. However, if the DMSO is depleted of oxygen vacancies and is no longer ferromagnetic, the spin current will be reduced between the two FM electrodes (not much experimental investigation has been done on such a device). Both the spin logic and memristor can be integrated into a hybrid charge-spin memristor logic circuit.

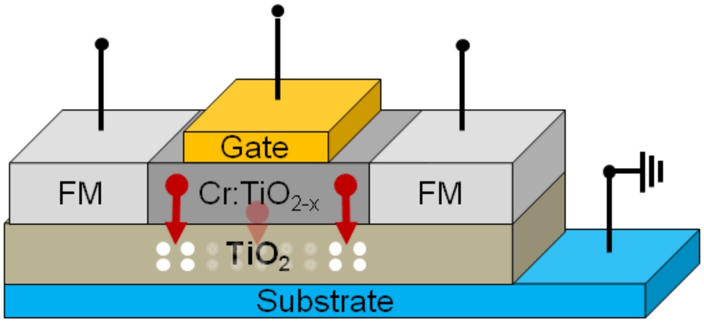

Figure 7.6 Structure for ionic transport of defects (oxygen vacancies) from a DMSO layer.

In spite of this unique property, there have been very limited understanding of the electronic/spintronic devices based on DMSOs. The proposed device will not only deliver a practical spin-charge coupled hybrid device, but will elucidate the fundamental characteristics of logic and memory devices based on DMSOs. If the oxygen vancancy concentration dependent ferromagnetism at room temperature can be established in these materials, then it can be used as efficient spin injecting or spin aligning electrode in magnetic tunnel junction devices such as STTRAM. The entire premise of this proposed device, however, depends whether the ferromagnetism can indeed be controlled by controlling the defect density.

Preliminary magnetic characterization on a TiO_2 layer using the magneto-optic Kerr effect (MOKE) measurement is shown below for a W/Cr:TiO_2/HfO/W stack. A 632 nm wavelength He-Ne laser was used as the probe beam (please refer to magnetic characterization of memory devices). The ferromagnetism of the top TiO_2 layer was probed as a function of applied bias across the heterostructure. A clear hysteresis characteristic is observable on a virgin layer as a function of applied magnetic field parallel to the sample surface (black curve), with the coercivity being approximately 800 Oe. The magnetism characteristics of the TiO_2 layer changes drastically with an applied

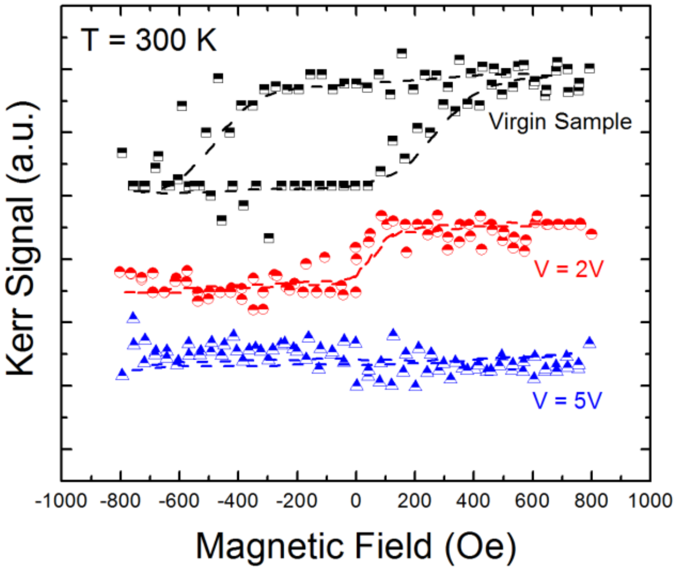

Figure 7.7 Modulation of ferromagnetism in a TiO_2 layer, measured by magneto-optical Kerr effect measurements.

---

bias across the heterostructure, as shown in Fig. 7.7. The coercivity decreases by a significant amount with an applied voltage of 2 V to the heterostructure (red curve), and a complete disappearance of any magnetic properties at an applied voltage of 5 V (blue curve). This preliminary result reinforces the feasibility of the proposed MOKE characterization method and verifies the underlying physics to successfully implement the DMSO devices. Further study needs to be done to quantify the correlation between the density of defects to the magnetic properties of the DMSO layer.

7.3 CONCLUSION

In this dissertation, several novel devices with high operating tempreatures and magnetoresistance response were designed and experimentally demonstrated. An overview of the most recent magnetoresistance values and spin lifetimes/diffusion lengths are shown in Table 7.1.

Table 7.1 Magnetoresistance and spin lifetime/diffusion lengths for various III-V semicondutors reported to date.

Material	*Geometry*	*Magnetoresistance* (%)	*Spin lifetime/diffusion length*
GaAs	Lateral	1% at T = 10 K, 0.1% at T = 300 K	24 ns (10 K)[133]
	Vertical	25% at T = 300 K	400 ps (300 K)[*]
GaN	Lateral/bulk	n/a	75 ps (300 K)[123,124]
	Lateral/NW	10% at T = 300 K	100 ps (300 K)[*]
	Quantum disk	n/a	80 ps (300 K)[154]
Ge	Lateral/bulk	n/a	1.08 ns (4 K), 100 ps (300 K)[157]
	Lateral/NW	0.8% at T = 4 K	100 μm+ (4 K)[151]
InAs	Lateral/2DEG	0.17% at T = 10 K	5 ps at T = 20 K[78]
Graphene	Lateral	n/a	600 ps (4 K), 300 ps (300 K)[156]
Si	Lateral	n/a	1 ns (300 K)[158]

APPENDICES

Appendix A

Magneto-optic Kerr effect (MOKE) measurements

A.1 Introduction

The Magneto-optic Kerr Effect (MOKE) technique is primarily used to measure magnetic properties of thin films. It measures the reflection of polarized light by a material sample subjected to a magnetic field. Usually, the change in the direction of the polarization and ellipticity (which ultimately leads to a change in the light intensity) indicates that the film under study has magnetic properties, such as ferromagnetism. There are several "geometries" for the MOKE technique: (1) Polar, (2) Longitudinal, and (3) Transverse. These configurations indicate the direction of magnetic field with respect to the plane of incidence. The polar geometry has the magnetic field parallel to the plane of incidence, normal to the sample surface. The longitudinal geometry has the magnetic field parallel to the plane of incidence and also parallel to the sample surface. Finally, the transverse geometry has the magnetic field directed normal to the plane of incidence and parallel to the sample surface. Each of the geometries is illustrated in Fig. A.1. The longitudinal and transverse MOKE setup is described here.

A.2 Components, Settings, and Connections

A typical MOKE setup and its block diagram are shown in Fig. A.2. The components consists of:

- Laser
- Two focusing lenses
- Photoelastic modulator (HINDS Instrument PEM-100)
- Polarizer/analyzer
- Optical power detector (Newport 1815-C)

The laser passes through the polarizer into a focusing lens (20 cm), which focuses the laser onto the sample of interest. The reflected laser from the sample is passed through another focusing lens (10 cm) into the PEM and the analyzer, and finally into the detector.

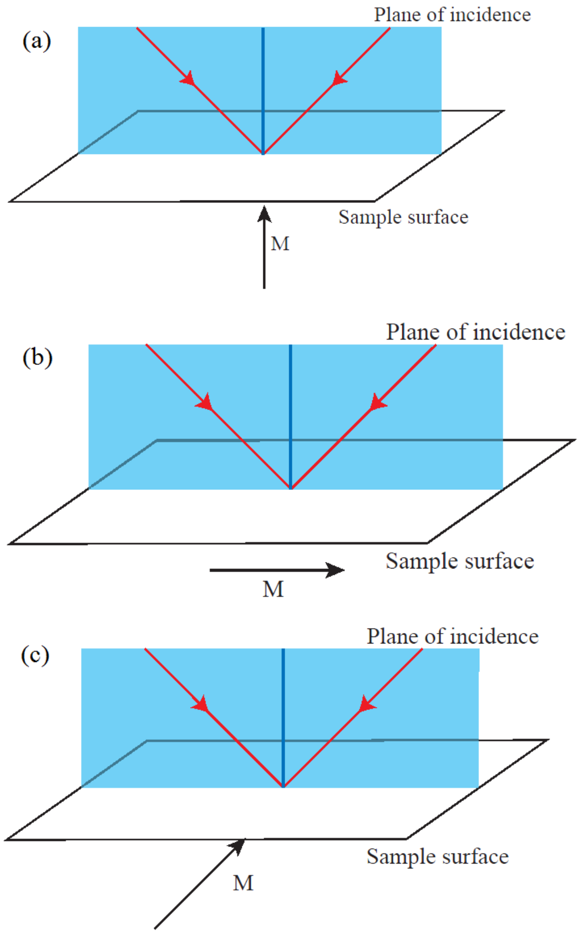

Figure A.1 Several geometries possible for MOKE measurement [source: HINDS Instruments].

It is best to tilt the PEM such that the incident reflected light is not normal to the PEM. This reduces the “modulated interference” effect that may be present when a PEM is used with lasers. Another way to circumvent this issue is to coat the PEM optical components with antireflective coating. The polarizer and analyzer are oriented 45 degrees with respect to each other. A typical value for the polarizer is 0 degrees and 45 degrees for the analyzer.

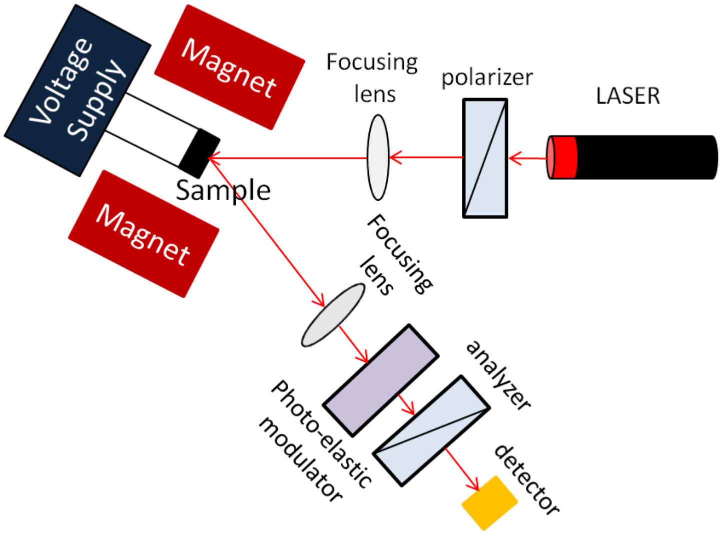

Figure A.2 Illustration of the magneto-optic Kerr effect (MOKE) measurement setup. Not shown is the lock-in amplifier, in which the detector signal is fed as an input and the photo-elastic modulator provides the reference signal.

A typical setting used for the PEM (Model: TEM 100) is given below:

- Frequency (1f): 50 Hz
- Wavelength: 523.5 or 632 nm (must match the wavelength of the laser used)
- Retardation angle: 108°

The optical power detector must be calibrated for the particular laser used. For the 632 nm wavelength laser, a calibration factor of 2.72 is used (1010 multiplier) without an attenuator.

It is best to tilt the PEM such that the incident reflected light is not normal to the PEM. This reduces the “modulated interference” effect that may be present when a PEM is used with lasers. Another way to circumvent this issue is to coat the PEM optical components with antireflective coating. The polarizer and analyzer are oriented 45 degrees with respect to each other. A typical value for the polarizer is 0 degrees and 45 degrees for the analyzer.

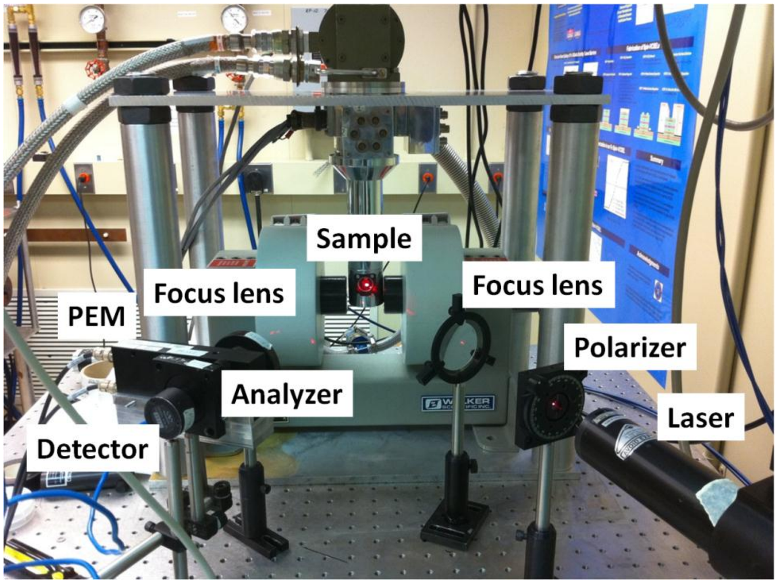

Figure A.3 Photograph of the MOKE setup. The cryostat is used for low temperature or temperature dependent measurements.

A.3 Low temperature MOKE measurements

Depending on the situation, a low temperature or temperature dependent MOKE measurement can be made. This is done by placing the cryostat between the poles of the electromagnet. The sample must be glued on the cryostage with cryogrease for good temperature conduction. For stable results, you must wait 5-10 minutes after each temperature change for the temperature of the sample to stabilize. Otherwise, the amplitude of your data may show a linear increase or decrease shift as the sample temperature tires to stabilize while the measurement program is running. The entire measurement is controlled by a computer and interfaced with standard IEEE GPIB communication method. The lock-in amplifier settings are: A/AC/Float, Normal, Sync filter on. The sensitivity and time constants are set depending on the intensity of laser reflection off the surface of the sample. The connections are shown in Fig. A.4.

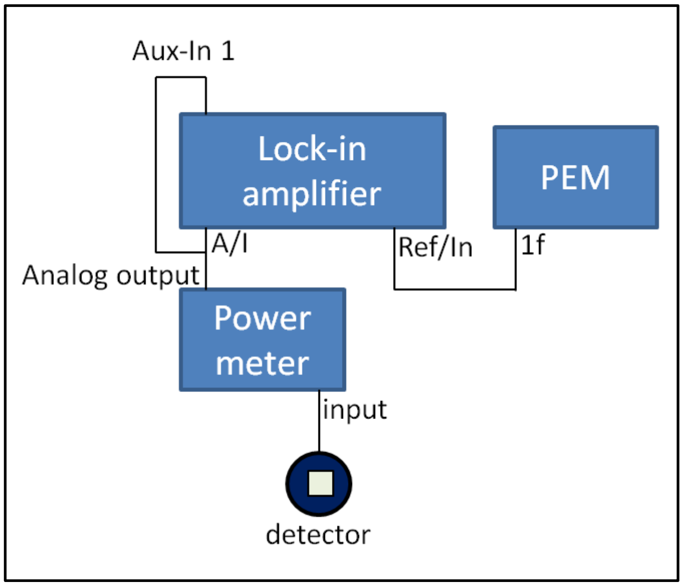

Figure A.4 Block diagram of the MOKE setup connections.

Appendix B

Prototype Vertical Spin Valve Memory Array

B.1 Introduction

The operation of the three-terminal vertical spin amplifier as a prototype three-bit memory cell is discussed in this section. As described in chapter 4.4, the output voltage when the FM contacts are in the parallel configuration at some critical gate bias $V_{critical}$ is very small (~10^{-5} V). This is the lowest output voltage this device can produce. The highest output voltage this device can produce is when the FM contacts are aligned in the anti-parallel configuration. Thus, we are able to utilize this fact to use this device as a memory cell. The OFF state is defined as when the FM contacts are in the parallel configuration, and the ON state is when the FM contacts are in the anti-parallel configuration. A micrograph of the fabricated memory array is shown in Fig. B.1. Three cells with the best characteristics were selected to be tested.

B.2 Memory Characteristics

Fig. B.2 (top figure) shows the ON/OFF states of the three memory cells with a critical gate bias of $V_{critical} = 0.3509112$ V. All three bits show an ON/OFF ratio of greater than 100, with the max ratio of 1000. We attribute this difference to the slight variation in fabrication, as even a small different in geometry could change the $V_{critical}$ value which can severely affect the OFF voltage level. The OFF state of every cell is set by applying a magnetic field of 0.4 Tesla, thus setting the magnetization of the MnAs contacts in the parallel configuration. To achieve an ON state, a short joule heating current is applied across the desired cell, heating the MnAs beyond its Curie temperature (T_c = 315 K) and demagnetizing the MnAs contacts. Demagnetization of the contacts was enough to cause a voltage to increase several orders of magnitude compared to the parallel state (10^{-3} V vs. 10^{-5} V). A more robust and elegant way would have been to apply a local magnetic field across each bit and achieve field-induced switching of the MnAs contacts.

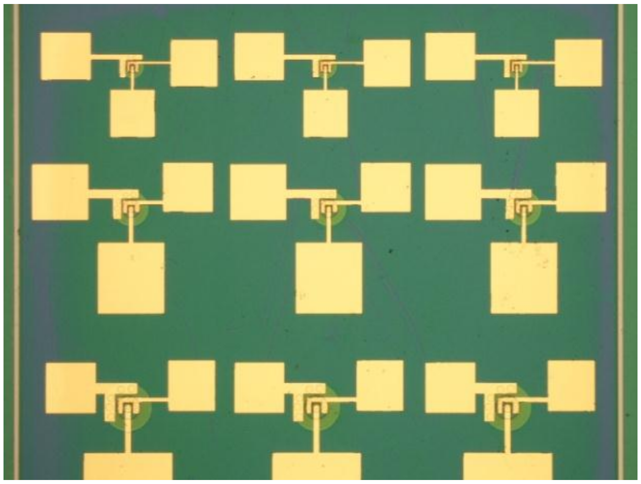

Figure B.1 Micrograph image of a fabricated three-terminal vertical spin amplifier memory array. Devices with varying dimensions are made, and the three devices with the best I-V response was chosen for measurement.

Fig. B.2 (bottom figure) shows a sequence of bits programmed for this one dimensional array. Because of the heat generated by the joule heating current, degradation of the memory array was severe and could only be reprogrammed 5-7 times before breaking down. From Fig. B.2 (bottom figure) it can be seen that after each reprogramming cycle, the OFF state voltage becomes larger until there is hardly any difference between ON and OFF state. We attribute this to parasitic capacitance at the

FM/TB/SC interfaces and degradation of the p-GaAs channel due to repeated heating. The exact reason for this behavior needs further investigation.

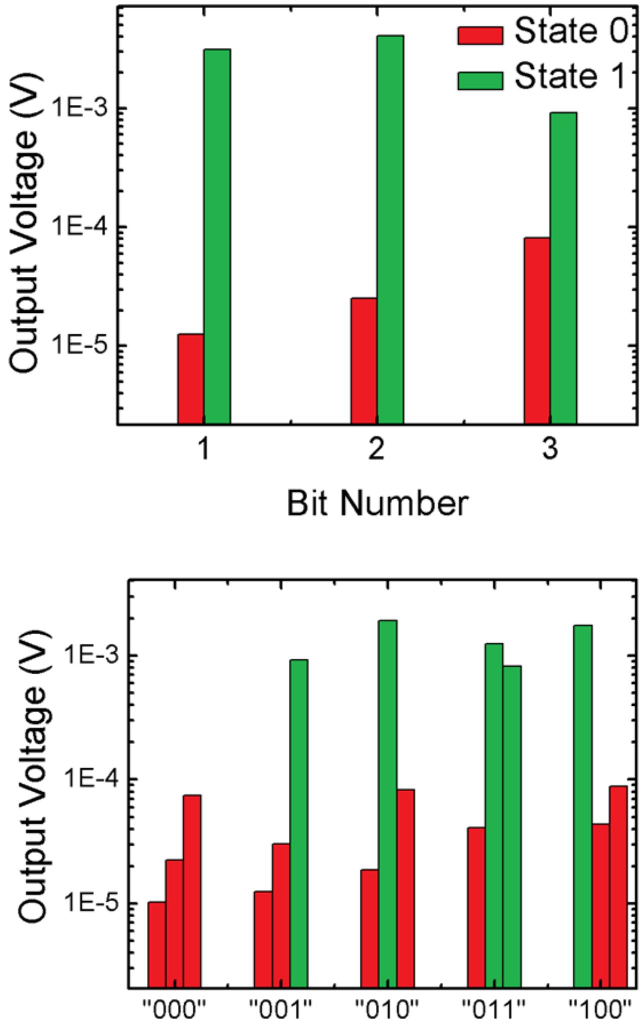

Figure B.2 (top) Voltage states of the three memory cells. (bottom) Sequence of programmed bits for the one-dimensional memory array. It can be seen that the cell characteristics degrade with each individual read/write operation.

B.3 Read/Write Procedure

The operation and (re)programming procedure is described below:

1) The gate of each bit is biased at the critical gate voltage ($V_g = V_{crit}$) such that V_P is ~10^{-5} V at all times.

2) All bits are set to state "0" when they are magnetized in the parallel configuration by an externally applied magnetic field.
3) Selected bits (by switch) are heated above the Curie temperature of MnAs (315 K) via a joule heating current, which demagnetizes the MnAs contacts. The demagnetized state induces a higher resistance than the parallel configuration state, leading to a higher output voltage ($V_{demag} \sim 10^{-3}$ V, state "1").
4) Desired bits are selected by the switch and read out.
5) Steps 2-4 are repeated for reprogramming.

Although the method of programming is crude, this is one of the first demonstrations of semiconductor based spin-memory array operating at room temperature.

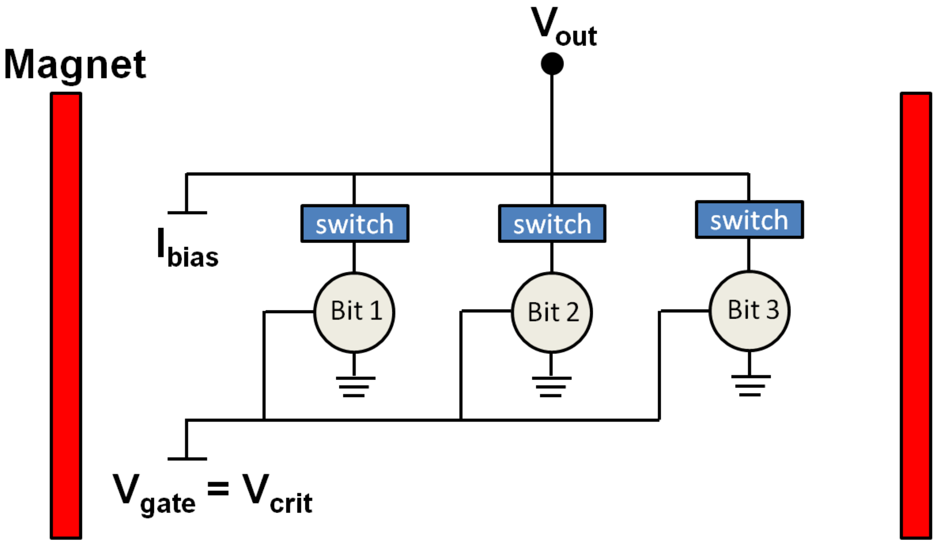

Figure B.3 Schematics of the three-bit memory array read/write operation circuitry. A joule heating current is applied to demagnetize the MnAs electrodes while an external magnetic field is used to reprogram the bits.

In conclusion, a semiconductor based spin-memory array operating at room temperature is demonstrated. A simple resistive model is used to explain the operating principle of a single memory cell, which has an average ON/OFF ratio of greater than 100, with a maximum ON/OFF ratio of 1000 at room temperature. The memory is non-volatile with a retention time of greater than 48 hours without noticeable change in on the ON/OFF ratio. This proof-of-concept prototype circuitry shows the viability of vertical spin valves for memory applications at room temperature.

Appendix C

Simulation of the Gate Potential in the 3-T Spin Amplifier

C.1 Introduction

This section pertains to chapter 4.4. The three-terminal vertical spin amplifier can be modeled by self-consistently solving 3D Poisson’s equation for electrostatics and 2D spin drift-diffusion for transport along with spin dependent tunneling at the ferromagnet/semiconductor interface (Tsu-Esaki model). What is of importance is how the gate electrode affects the channel electrostatically. The theoretical model presented in chapter 4.4 is most valid when the electric field due to the gate is evenly distributed throughout the channel region and not localized near the gate contact. To verify this, 3D TCAD tool Sentaurus was used to calculated the 3D Poisson and 2D spin drift-diffusion equation self consistently. The exact dimensions of the three-terminal vertical spin amplifier were used for the simulation (the figures C.1 and C.2 are not to scale, meaning that the scale factor of the x- and z-axis is different to make the structure more viewable. The absolute dimensions are exactly the same as the fabricated device).

The simulation indicates that the entire channel region is indeed affected by the gate electrode, as shown in Fig. C.1 and C.2, which show the electrostatic potential in the channel as a function of several gate voltage. Finding the exact magnitude was not the goal for this simulation, but rather to see the distribution of gate potential across the channel.

C.2 Sentaurus Simulation Codes

Sentaurus device editor code (*.scm):

```
(sde:clear)
(sdegeo:set-auto-region-naming OFF)

;Create Layers
(sdegeo:create-cylinder
   (position 0 0 0.0)
   (position 0 0 0.035) 100 "Metal" "Bot.Contact")

(sdegeo:create-cylinder
   (position 0 0 0.035)
   (position 0 0 0.036) 32.5 "GaAs" "bgaas")

(sdegeo:create-cylinder
   (position 0 0 0.036)
   (position 0 0 0.0375) 32.5 "AlAs" "B.Barrier")

(sdegeo:create-cylinder
   (position 0 0 0.0375)
   (position 0 0 0.0455) 32.5 "GaAs" "Channel")

(sdegeo:create-cylinder
   (position 0 0 0.0455)
   (position 0 0 0.0465) 7.5 "AlAs" "T.Barrier")

(sdegeo:create-cylinder
   (position 0 0 0.0465)
   (position 0 0 0.0475) 7.5 "GaAs" "tgaas")

;Create Gate
(sdegeo:set-default-boolean "BAB")
(sdegeo:create-cylinder
   (position 0 0 0.0455)
   (position 0 0 0.0457) 14.5 "Silicon" "Filler")

(sdegeo:create-cylinder
   (position 0 0 0.0455)
   (position 0 0 0.0457) 25 "Metal" "Gate.Contact")

(sdegeo:delete-region (find-region-id "Filler"))

;Contact declaration
(sdegeo:define-contact-set "drain"
  4.0 (color:rgb 1 0 0) "##")
(sdegeo:define-contact-set "gate"
  4.0 (color:rgb 0 1 0) "==")
```

```
(sdegeo:define-contact-set "source"
  4.0 (color:rgb 0 0 1) "<><>")

(sdegeo:set-current-contact-set "source")
(sdegeo:set-contact-boundary-faces (find-region-id "Bot.Contact"))

(sdegeo:set-current-contact-set "drain")
(sdegeo:set-contact-faces (find-face-id (position 0 0 0.0475) ))

(sdegeo:set-current-contact-set "gate")
(sdegeo:set-contact-boundary-faces (find-region-id "Gate.Contact"))

(sdegeo:delete-region (find-region-id "Gate.Contact"))
(sdegeo:delete-region (find-region-id "Bot.Contact"))

;Define doping level
(sdedr:define-constant-profile "Const.BG" "BoronActiveConcentration" 5e21)
(sdedr:define-constant-profile-region "PlaceCD.BG" "Const.BG" "Channel")

;Meshing strategies
(sdedr:define-refeval-window "RefEvalWin.Global" "Cuboid"
  (position -40 -40 0.0) (position 40 40 0.0456))

(sdedr:define-refinement-window "RefEvalWin.Channel" "Cuboid" (position -5 -5
0) (position 5 5 0.0456))

(sdedr:define-refinement-size "RefDef.Channel" 1 1 1 0.5 0.5 0.5)

(sdedr:define-refinement-placement "RefPlace.Channel" "RefDef.Channel"
"RefEvalWin.Channel")

;Saving structure
(sde:save-model "spinamp_sde")

;Meshing structure (meshing done both in the DF-ISE and TDR format to show
the command line)
(sde:build-mesh "mesh" "-P" "spinamp_msh")
(sde:build-mesh "mesh" "-P -F tdr" "spinamp_msh")
```

An example simulation condition code is given below. Note the ‘Physics’ section, where the temperature is set at T = 300 K and the electron and hole quantum effects due to the extremely thin channel region are considered (*.cmd):

```
File {
  * input files:
  Grid=   "spinamp_msh.tdr"
  * output files:
  Plot=   "spinamp_drain_des.dat"
  Current="spinamp_drain_des.plt"
  Output= "spinamp_drain_des.log"
}
```

```
Electrode {
  { Name="source"    Voltage=0.0 Barrier=0.8}
  { Name="drain"     Voltage=0.05 Barrier=0.8}
  { Name="gate"      Voltage=0.0}
}

Physics {
  Temperature = 300
  Mobility( DopingDep HighFieldsat Enormal )
  EffectiveIntrinsicDensity( OldSlotboom )
  eQuantumPotential hQuantumPotential

}

Plot {
  ConductionBandEnergy ValenceBandEnergy
  eDensity  hDensity  eCurrent  hCurrent
  Potential  SpaceCharge  ElectricField
  eMobility  hMobility
  Doping  DonorConcentration   AcceptorConcentration
  eQuasiFermi hQuasiFermi
  eQuantumPotential hQuantumPotential
}

Math {
  Extrapolate
  Derivatives
  NewDiscretization
  Iterations = 100
}

Solve {
  Poisson
  #-initial solution:
  Coupled { Poisson eQuantumPotential hQuantumPotential }
  #-ramp drain:
 Quasistationary (   InitialStep = 0.01
                     MaxStep=0.02
                     MinStep=1e-6
                     Goal {Name="gate" Voltage=0.32}

)
                  { Coupled { Poisson eQuantumPotential hQuantumPotential } }
}
```

C.3 Simulation Results

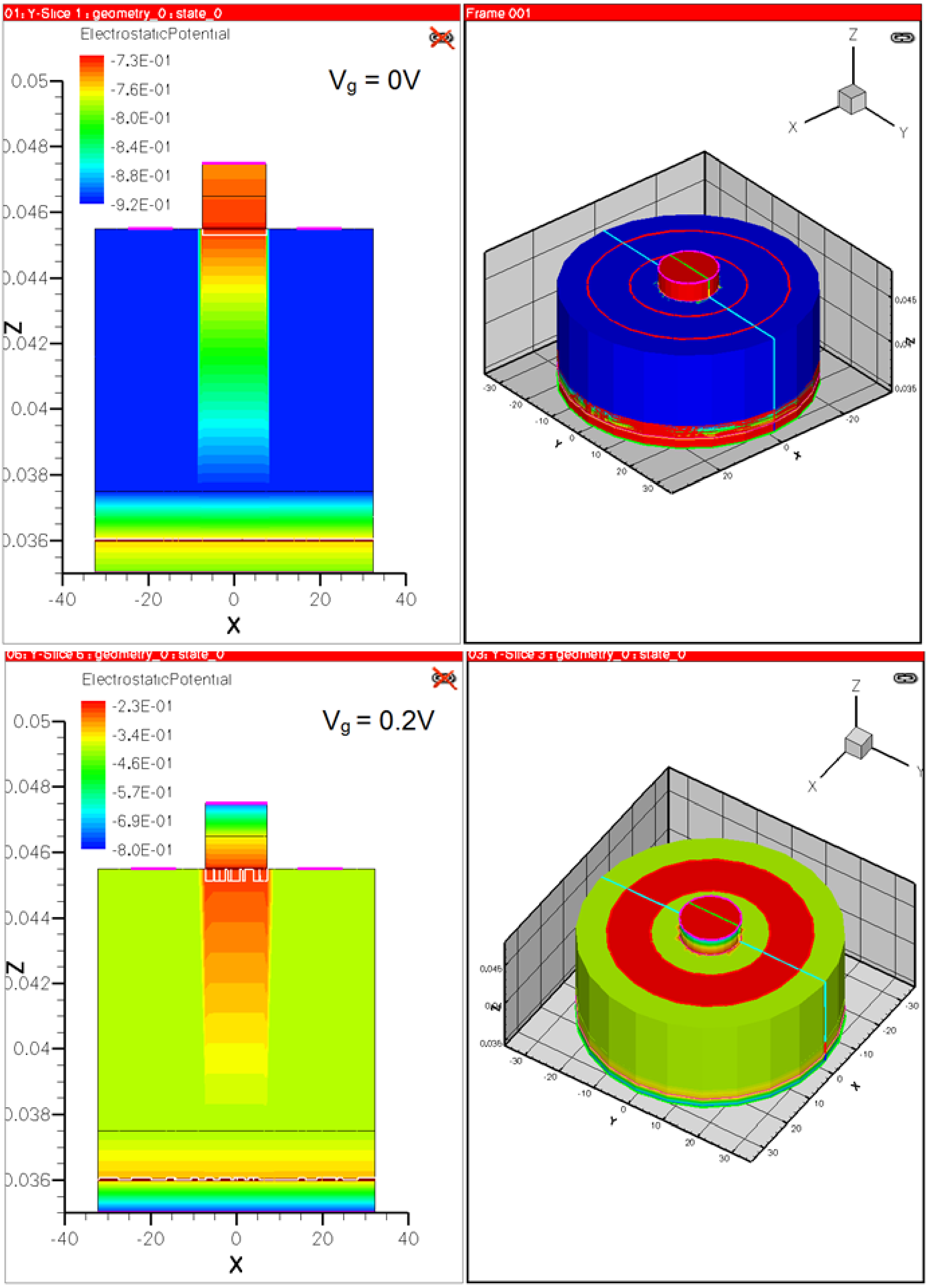

Figure C.1 Sentaurus simulation results of the three-terminal vertical spin amplifier for a gate bias of 0V (top) and 0.2 V (bottom).

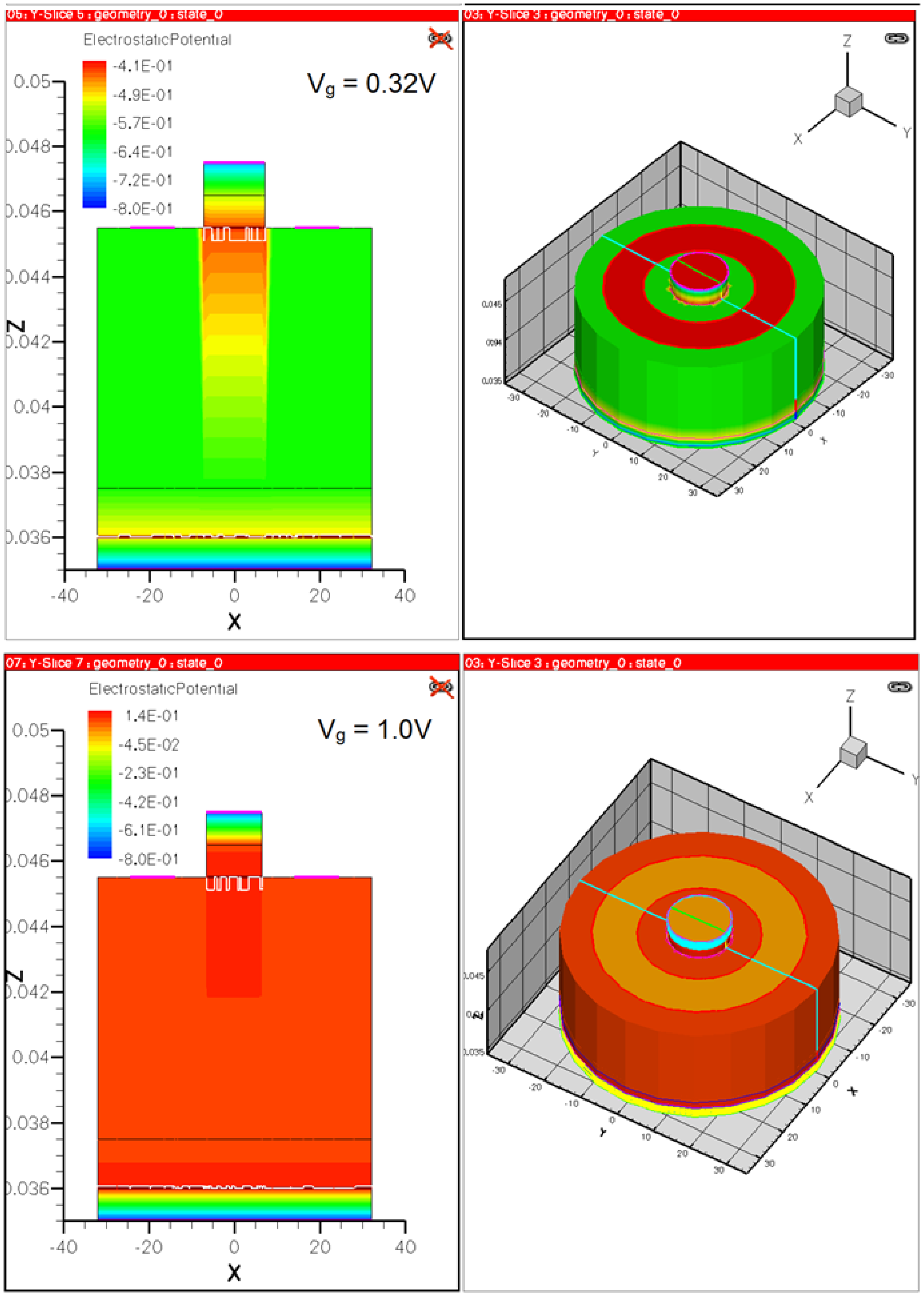

Figure C.2 Sentaurus simulation results of the three-terminal vertical spin amplifier for a gate bias of 0.32V (top) and 1.0 V (bottom).

Appendix D

Derivation of the Mesa-Size Dependent Magnetoresistance

This model was derived and developed by Abu Naser Zainuddin from Purdue University under Prof. Supriyo Datta. It is provided here for completness of the study presented in section 4.5.

To solve Equation 1 we assumed that at two edges of the channel $d\mu^+/dx = d\mu^-/dx = 0$, which implies that there is no spin-relaxation at the edges. Equation 1 can be pictorially represented by a distributed network of series and shunt resistance components (see Figure 4.21(c)). Kirchoff's current conservation law applied at each node of this distributed circuit will yield a set of equations that is identical to a discretized version of Equation 1. The components are given by, $[G_c] = [g_c^+\ 0;0\ g_c^-]$, $[R_{sc}] = [2r_{sc}\ 0;0\ 2r_{sc}]$ and $[G_{sf}] = [g_s\ -g_s;-g_s\ g_s]$. Here, g_s is the spin-relaxation conductance ($m^{-1}\Omega^{-1}$) connecting both spin channels, and is given by $1/(4r_{sc}\lambda_s^2)$.

The distributed network in Figure 4.21(c) can be replaced by an equivalent lumped (l) network, by approximating the extended contacts with point source contacts but keeping the total conductance the same. Such an approximation is valid when spin polarized electrons can easily penetrate underneath the contacts with negligible lowering of their chemical potential, which implies that the contact lengths are far smaller than the charge penetration depth [105] as well as the spin-diffusion length. As a result, in the lumped network, g_c^+ → $g_c^{+,-}$ ($m^{-1}\Omega^{-1}$) × L_c inside $[G_c]_l$, where L_c is the contact length. The series [R_{sc}] components can be replaced with a single $[R_{sc}]_l$ given by $[R_{sc}]_l = [r(1+a)\ r(1-a);r(1-a)\ r(1+a)]$, where L_i is the channel length inside the current path, $r = r_{sc}L_i$, and $a = (\lambda_s/L_i)\sinh(L_i/\lambda_s)$. The shunt spin-relaxation components are separated into two spin-relaxation components, one for channel regions in the current path $([G_{sf}^{i}]_l)$ and another for channel regions out of the current path $([G_{sf}^{o}]_l)$, given as, $([G_{sf}^{i,o}]_l) = [\ g_s^{i,o}\ -g_s^{i,o};\ -g_s^{i,o}\ g_s^{i,o}\ ]$ where $g_s^{i,o} = 1/(2r_{sc}\lambda_s)\tanh(L_{i,o}/2\lambda_s)$. We note that since there is no charge current flowing in the unetched regions, the spin components of the charge current would be equal in magnitude but opposite in direction and, thereby, resulting in a shunt spin-relaxing path g_s^o**.** By solving the lumped network for parallel (R_p) and anti-parallel (R_{ap}) resistances, we can write an expression for MR as (assuming $L_i << \lambda_s$),

$$R_p = \frac{2}{g_c}\left[\frac{y^2\{4x+(1-p^2)\}+2y(1+2x)+1}{1+y\{4x+(1-p^2)\}}\right]$$

$$R_{ap} = \frac{2}{g_c}\left[\frac{(1+4x)}{4x+(1-p^2)}+y\right]$$

$$MR = \frac{R_{ap}-R_p}{R_p} = \frac{p^2}{[1+4xy+y(1-p^2)][1+4xy+y(1-p^2)+4x]-p^2} \quad \text{(eq. 2)}$$

$$p = \frac{g_c^+ - g_c^-}{g_c}, g_c = g_c^+ + g_c^-, x = \frac{g_s^i + g_s^o}{g_c} = \frac{g_{sf}}{g_c}, y = \frac{1}{2}rg_c$$

The MR expression in Equation 2 has two parameters, x and y. In the simplest case where the spin-relaxation conductance (g_{sf}) in the channel and the resistance inside the current path (r) are negligible (i.e. x → 0 and y → 0), MR approaches the maximum value of $p^2/(1-p^2)$. Therefore, keeping both x and y as small as possible will lead to a higher MR response. But to stress on the effect of extended mesa we now focus on x and its role on MR assuming y is made sufficiently small by reducing the distance of current path, L_i. However we note that this could as well reduce x but it is not the only factor affecting x. A shorter L_i will reduce the x parameter inside the current path (i.e. $x^i=g_s^i/g_c$), but the component outside the current path ($x^o=g_s^o/g_c$) could still limit MR. So, x^0 should also be reduced. This can be done either by etching away the mesa (reducing g_s^o), or by increasing the interface conductance (increasing g_c) for a given mesa length L_o.

BIBLIOGRAPHY

[1] W. Gerlach and O. stern, Zeitschrift fur Physik A Hadrons and Nuclei 9, 353-355 1922.

[2] S. Goudsmit and G. E. Uhlenbeck, Physica 6, 273 1926.

[3] T. Taniyama, E. Wada, M. Itoh, and M. Yamaguchi, NPG Asia Materials 3, 65-73 2011.

[4] P. M. Tedrow and R. Meservey, Phys. Rev. Lett. 26, 192 (1971).

[5] M. Julliere, Phys. Lett. 54, 225 (1975).

[6] L. Berger, Phys. Rev. B 54, 9353 (1996).

[7] J. C. Slonczewski, J. Magn. Magn. Mater. 19, L1 (1996).

[8] R. Fiederling, M. Keim, G. Reuscher, W. Ossau, G. Schmidt, A. Waag, and L. W. Molenkamp, Nature 402, 787 (1999).

[9] Y. Ohno, D. K. Young, b. Beschoten, F. Matsukara, H. Ohno, and D. D. Awschalom, Nature 402, 790 (1999).

[10] M. Holub, J. Shin, D. Saha, and P. Bhattacharya, Phys. Rev. Lett. 98, 146603 2007.

[11] D. Basu, D. Saha, C. C. Wu, M. Holub, Z. Mi, and P. Bhattacharya, Appl. Phys. Lett. 92, 091119, 2008.

[12] D. Saha, D. Basu, and P. Bhattacharya, Phys. Rev. B. 82, 2010.

[13] A. G. Aronov, JEPT Lett. 24, 32 (1976).

[14] M. Johnson and R. H. Silsbee, Phys. Rev. Lett. 55, 1790 (1985).

[15] D. Saha, M. Holub, P. Bhattacharya, and Y. C. Liao, Appl. Phys. Lett. 89, 142504 (2006).

[16] X. Lou, C. Adelmann, S. A. Crooker, E. S. Garlid, J. Zhang, K. S. M. Reddy, S. D. Flexner, C. J. Palmstrom, and P. A. Crowell, Nature Phys. 3, 197 (2007).

[17] S. Datta and B. Das, Appl. Phys. Lett. 56, 665 (1990).

[18] H. C. Koo, J. H. Kwon, J. Eom, J. Chang, S. H. Han, and M. Johnson, Science 18, 1515 (2009).

[19] H. Kum, D. Basu, P. Bhattacharya, and W. Guo, Appl. Phys. Lett. 95, 212503 (2009).

[20] S. Bandyopadhyay, arXiv:0911.0210v1 2009.

[21] J. Fabian and I. Zutic, Phys. Rev. B 69, 115314 (2004).

[22] M. E. Flatte, Z. G. Yu, E. Johnston-Halperin, and D. D. Awschalom, Appl. Phys. Lett. 82, 26 (2003).

[23] A. Fert and S. Lee, Phys. Rev. B. 53, 6554 (1996).

[24] Fig. 2.1 and 2.2 taken from Ph.D. dissertation of A. T. Fillip.

[25] E. I. Rashba, Phys. Rev. B 62, R16267 (2000).

[26] R. Jansen, B.-C. Min, and S. P. Dash, Nat. Mat. 9, 133-138 (2010).

[27] C. H. Li, O.M.J. van't Erve, and B. T. Jonker, Nat. Comm. 2, 245 (2011).

[28] S. P. Dash, S. Sharma, R. S. Patel, M. P. de Jong, and R. Jansen, Nature 462, 26 (2009).

[29] E. Liu, J. Nah, K. M. Varahramyan,and E. Tutuc, Nano Lett. 10, 3297-3301 (2010).

[30] A. T. Hanbicki, S.-F. Cheng, R. Goswami, O.M.J. van't Erve, and B. T. Jonker, H14.00004, APS March Meeting (2012).

[31] D. Basu, H. Kum, P. Bhattacharya, and D. Saha, Appl. Phys. Lett. 97, 232505 (2010).

[32] A. Das, J. Heo, M. Jankowski, W. Guo, L. Zhang, H. Deng, and P. Bhattacharya, Phys. Rev. Lett. 107, 066405 (2011).

[33] B. Beschoten, E. Johnston-Halperin, D. K. Young, M. Poggio, J. E. Grimaldi, S. Keller, S. P. DenBaars, U. K. Mishra, E. L. Hu, and D. D. Awschalom, Phys. Rev. B 63, 121202(R) (2000).

[34] J. H. Buss, J. Rudolph, F. Natali, F. Semond, and D. Hagele, Phys. Rev. B 81, 155216 (2010).

[35] T. Maassen, J. Jasper van den Berg, N. IJbema, F. Fromm, T. Seyller, R. Yakmova, and B. J. van Wees, Nano Lett. DOI: 10.1021/nl2042497 (2012).

[36] W. Han and R. K. Kawakami, Phys. Rev. Lett. 107, 047207 (2011).

[37] M. Tran, H. Jaffres, C. Deranlot, J. M. George, A. Fert, A. Miard, and A. Lemaıtre, Phys. Rev. Lett. 102, 036601 (2009).

[38] I. Zutic, J. Fabian, S. Sarma, Reviews of Modern Physics 76, 323 (2004).

[39] Several contradicting reports have been published indicating absence or presence of ferromagnetism in GaMnN nanowires.

[40] Adaped from Ph.D. dissertation of Mike Holub.

[41] F. Heusler, Z. Angew. Chem. 17 260 (1904).

[42] S. Hilpert and T. Dieckmann, Ber. Dtsch. Chem. Ges. A, 44, 2378 (1911).

[43] Figure from an on-line presentation, or Wikiepdia. May no longer be available. Copyright belongs to the respective owner.

[44] L. Daweritz, F. Schippan, A. Trampert, M. Kastner, G. Behme, Z. M. Wang, M. Moreno, P. Schutzendube, K. H. Ploog, Jour. of Crystal Growth 227-228 (2001).

[45] R. I. Dzhioev, K. V. Kavokin, V. L. Korenev, M. V. Lazarev, B. Y. Meltser, M. N. Stepanova, B. P. Zakharchenya, D. Gammon, and D. S. Katzer, Phys. Rev. B 66, 245204 (2002).

[46] B. J. Jonsson-Akerman, R. Escudero, C. Leighton, S. Kim, I. K. Schuller, and D. A. Rabson, Appl. Phys. Lett. 77, 1870 (2000).

[47] W. F. Brinkman, R. C. Dynes, and J. M. Rowell, J. Appl. Phys. 41, 1915 (1970).

[48] S. Ohya, I. Muneta, P. N. Hai, and M. Tanaka, Phys. Rev. Lett. 104, 167204 (2010).

[49] D. Saha, L. Siddiqui, P. Bhattacharya, S. Datta, D. Basu, and M. Holub, Phys. Rev. Lett. 100, 196603 (2008).

[50] R. H. Fowler and L. Nordheim, Proceedings of the Royal Society of London 119, 173 (1928).

[51] H. J. M. Swagten from Handbook of Magnetic Materials, Edited by K. H. J. Buschow, Elsevier BV, Amsterdam, (2003).

[52] R. Mattana, J.-M. George, H. Jaffres, F. Nguyen Van Dau, A. Fert, B. Lepine, A. Guivarc’h, and G. Jezequel, Phys. Rev. Lett. 90, 166601 (2003).

[53] S. Yuasa, T. Nagahama, A. Fukushima, Y. Suzuki, and K. Ando, Nat. Mat. 3, 869 (2004).

[54] R. Tsu and L. Esaki, Appl. Phys. Lett. 22, 562 (1973).

[55] Z. G. Yu and M. E. Flatte, Phys. Rev. B 66, 201202 (2002).

[56] R. P. Panguluri, G. Tsoi, B. Nadgorny, S. H. Chun, N. Samarth, and I. I. Mazin, Phys. Rev. B, 68, 201307(R) (2003).

[57] Y. Xu, D. Ephron, and M. R. Beasley, Phys. Rev. B 52, 2843 (1995).

[58] G. L. Bir, A. G. Aronov, and G. E. Pikus, Zh. Eksp. Teor. Fiz. 69, 1382 (1975); Sov. Phys. JETP 42, 705 (1976).

[59] J. H. Jiang and M. W. Wu, Phys. Rev. B 79, 125206 (2009).

[60] S. Sugahara and M. Tanaka, Appl. Phys. Lett. 80, 11 (2002).

[61] C. Chappert, A. Fert and F. N. Van Dau, Nat. Mater. 6 (11), 813-823 (2007).

[62] B. T. Jonker et al., Nat. Phys. 3 (8), 542-546 (2007).

[63] N. W. Gray and A. Tiwari, Appl. Phys. Lett. 98 (10), 102112 (2011).

[64] X. Jiang et al., Phys. Rev. Lett. 94 (5), 056601 (2005).

[65] S. P. Dash et al., Nature 462 (7272), 491-494 (2009).

[66] Y. Ohno et al., Nature 402 (6763), 790-792 (1999).

[67] M. Holub, J. Shin, D. Saha and P. Bhattacharya, Phys. Rev. Lett. 98 (14) (2007).

[68] D. Saha, M. Holub, P. Bhattacharya and Y. C. Liao, Appl. Phys. Lett. 89 (14), 142504 (2006).

[69] X. Lou et al., Nat Phys 3 (3), 197-202 (2007).

[70] I. Appelbaum, B. Huang and D. J. Monsma, Nature 447 (7142), 295-298 (2007).

[71] H. Dery, L. Cywinski and L. J. Sham, Phys. Rev. B 73 (16), (2006).

[72] B. Behin-Aein, D. Datta, S. Salahuddin and S. Datta, Nat. Nanotechnol. 5 (4), 266-270 (2010).

[73] S. Mark et al., Phys. Rev. Lett. 106 (5), (2011).

[74] J. Fabian and I. Zutic, Phys. Rev. B 69 (11), (2004).

[75] N. Rangaraju, J. A. Peters and B. W. Wessels, Phys. Rev. Lett. 105 (11), (2010).

[76] J. Wunderlich et al., Science 330 (6012), 1801-1804 (2010).

[77] S. Datta and B. Das, Appl. Phys. Lett. 56 (7), 665-667 (1990).

[78] H. C. Koo et al., Science 325 (5947), 1515-1518 (2009).

[79] H. Kum, D. Basu, P. Bhattacharya and W. Guo, Appl. Phys. Lett. 95 (21), 212503 (2009).

[80] S. S. P. Parkin et al., Nat. Mater. 3 (12), 862-867 (2004).

[81] D. Basu, H. Kum, P. Bhattacharya and D. Saha, Appl. Phys. Lett. 97 (23), (2010).

[82] D. Saha, D. Basu, P. Bhattacharya, Appl. Phys. Lett. 93, 194104 (2008).

[83] R. Mattana et al., Phys. Rev. Lett. 90 (16), (2003).

[84] D. Basu, P. Bhattacharya, W. Guo and H. Kum, J. Phys. D Appl Phys 42 (9), (2009).

[85] S. Ohya, K. Takata and M. Tanaka, Nat. Phys. 7 (4), 342-347 (2011).

[86] H. Ohno et al., Appl. Phys. Lett. 69 (3), 363-365 (1996).

[87] T. Valet and A. Fert, Phys. Rev. B 48 (10), 7099 (1993).

[88] Z. G. Yu, Flatte, and M. E., Phys. Rev. B 66 (23), 235302 (2002).

[89] R. Tsu and L. Esaki, Appl. Phys. Lett. 22 (11), 562-564 (1973).

[90] G. Schmidt et al., Phys. Rev. B 62, 8 (2000).

[91] T. Valet, A. Fert, Phys. Rev. B 48, 10 (1993).

[92] Z. G. Yu and M. E. Flatte, Phys. Rev. B 66, 201202 (2002).

[93] A. M. Roy, D. E. Nikonov and K. C. Saraswat, J. Appl. Phys. 107, 064504 (2010).

[94] O. M. J van't Erve, C . Awo-Affouda, A. T. Hanbicki, C. H. Li, P. E. Thompson and B. T. Jonker, IEEE Trans. Elect. Dev., 56, 2343 (2009).

[95] D. Saha, D. Basu, M. Holub and P. Bhattacharya, Appl. Phys. Lett. 92, 022507 (2008).

[96] H. C. Koo, H. Yi, J. B Ko, J. Chang. S. H. Han. D. Jung, S. Huh and J. Eom, Appl. Phys. Lett., 90, 022101 (2007).

[97] N. Tombros, C. Jozsa, M. Popincuic, H. T. Jonkman and B. J. van Wees, Nature 448, 571 (2007).

[98] A. Fert, J.-M. George, H. Jaffr´es and R. Mattana, IEEE Trans. Electron Devices 54, 921 (2007).

[99] A. Fert and H. Jaffr´es, Phys. Rev. B, 64, 184420 (2001).

[100] H. Dery, L. Cywi`nski and L. J. Sham, Phys. Rev. B. 73, 041306, (2006).

[101] T. Valet and A. Fert, Phys. Rev. B, 48, 7099 (1993).

[102] Z. G. Yu. and M. E. Flatt´e, Phys. Rev. B, 66, 235302 (2002).

[103] M. Johnson and J. Beyers, Phys. Rev. B, 67, 125112 (2003).

[104] M. Johnson and R.H. Silsbee, Phys. Rev. Lett., 55, 1790 (1985)

[105] C. Lan, D. Zakharov and R. G. Reifenberger Appl. Phys. Lett., 92, 213112, (2008).

[106] X. Lou, C. Adelmann, S. A Crooker, E. S. Garlid, J, Zhang, K. S. M. Reddy, S. D. Flexner, C. J. Palmstrøm and P. A. Crowell, Nature Phys. 3, 197 (2007).

[107] D. Saha, M. Holub, and P. Bhattacharya, Appl. Phys. Lett. 91, 072513 (2007).

[108] S. Datta and B. Das, Appl. Phys. Lett. 56, 665 (1990).

[109] J. H. Kwon, H. C. Koo, J. Chang, S. H. Han, and J. Eom, Appl. Phys. Lett. 90, 112505 (2007).

[110] H. Koo, H. Yi, J. B. Ko, J. Chang, S. H. Han, D. Jung, S. G. Huh, and J. Eom, Appl. Phys. Lett. 90, 022101 (2007).

[111] Das et.al., PRB 39, 1411 (1989).

[112] D. Basu, P. Bhattacharya, W. Guo, and H. Kum, J. Phys. D: Appl. Phys. 42, 092001 (2009).

[113] Y. Y. Wang and M. W. Wu, Phys. Rev. B 72, 153301 (2005).

[114] N. S. Averkiev, L. E. Golub, and M. Willander, Semiconductors 36, 91-97 (2002).

[115] M. H. Liu and C. R. Chang, Phys. Rev. B 74, 195314 (2006).

[116] Mishra, U.K.; Parikh, P.; Wu, Y.-F. Proceedings of the IEEE 2002, 90, 1022- 1031.

[117] Schubert, E. F.; Kim, J. K. Science 2005, 308, 1274-1278.

[118] Butte, R.; Christmann G.; Feltin, E.; Carlin, J.-F.; Mosca, M.; Ilegems M.; Grandjean N. Phys. Rev. B 2006, 73, 033315.

[119] Christopoulos, S.; Baldassarri Hoger von Hogersthal, G.; Grundy, A. J. D.; Lagoudakis, P. G.; Kavokin, A. V.; Baumberg, J. J.; Christmann, G.; Butte, R.; Feltin, E.; Carlin, J.-F.; Grandjean, N. Phys. Rev. Lett. 2007, 98, 126405.

[120] Buss J. H.; Rudolph J.; Natali F.; Semond F.; Hagele D. Appl. Phys. Lett. 2009 95, 192107.

[121] Banerjee, A.; Doğan, F.; Heo, J.; Manchon, A.; Guo, W.; Bhattacharya, P. Nano Lett., 2011, 11, 5396.

[122] Krishnamurthy, S.; Schilfgaarde, M. V.; Newman, N. Appl. Phys. Lett. 2003, 83, 9.

[123] Beschoten, B.; Johnston-Halperin, E.; Young, D. K.; Poggio, M.; Grimaldi, J. E.; Keller, S.; DenBaars, S. P.; Mishra, U. K.; Hu, E. L.; Awschalom, D. D. Phys. Rev. B 2001, 63, 121202(R).

[124] Buss, J. H.; Rudolph, J.; Natali, F.; Semond, F.; Hagele, D. Phys. Rev. B 2010, 81, 155216.

[125] Bertness, A. K.; Roshko, A.; Sanford, A. N.; Barker, J. M.; Davydov, A. V. J. Crys. Growth 2006, 287, 522.

[126] Cerutti, L.; Ristic, J.; Fernandez-Garrido, S.; Calleja, E.; Trampert, A.; Ploog, K. H.; Lazic, S.; Calleja, J. M. Appl. Phys. Lett. 2006, 83, 213114.

[127] Kishino, K.; Kikuchi, A.; Sekiguchi, H.; Ishizawa, S. S. Proc. SPIE 2007, 6473, 64730T-1.

[128] Guo, W.; Zhang, M.; Banerjee, A.; Bhattacharya, P. Nano Lett. 2010, 10, 3355.

[129] Nguyen, H. P. T.; Zhang, S.; Cui, K.; Han, X.; Fathololoumi, S.; Couillard, M.; Botton, G. A.; Mi, Z. Nano Lett. 2011, 11, 1919.

[130] Kiselev, A. A.; Kim, K. W. Phys. Rev. B 2000, 61, 13115.

[131] Holleitner, A. W.; Sih, V.; Myers, R. C.; Gossard, A. C.; Awschalom, D. D. Phys. Rev. Lett. 2006, 97, 036805.

[132] Jaffres, H.; George, J.-M.; Fert, A. Phys. Rev. B 2010, 82, 140408(R).

[133] Zainuddin, A. N. M.; Kum, H.; Basu, D.; Srinivasan, S.; Siddiqui, L.; Bhattacharya, P.; Datta, S. J. Appl. Phys. 2010, 108, 123913.

[134] Heo, J.; Guo, W.; Bhattacharya, P. Appl. Phys. Lett. 2011, 98, 021110.

[135] Das, A.; Heo, J.; Jankowski, M.; Guo, W.; Zhang, L.; Deng, H.; Bhattacharya, P. Phys. Rev. Lett. 2011, 107, 066405.

[136] Lu, T.-C.; Chen, J.-R.; Lin, S.-C.; Huang, S.-W.; Wang, S.-C.; Yamamoto, Y. Nano Lett., 2011, 11, 2791.

[137] Guo, W.; Banerjee, A.; Zhang, M.; Bhattacharya, P. Appl. Phys. Lett. 2011, 98, 183116.

[138] Rashba, E. I. Phys. Rev. B. 2000, 62, 16267I.

[139] Schmidt, G.; Ferrand, D.; Molenkamp, L. W.; Filip, A. T.; van Wees, B. J. J. Phys. Rev. B 2000, 62, R4790.

[140] Parkin, S. S. P.; Kaiser, C.; Panchula, A.; Rice, P. M.; Hughes, B.; Samant, M.; Yang, S. Nat. Mater. 2004, 3, 862.

[141] Jiang, X.; Wang, R.; Shelby, R. M.; Macfarlane, R. M.; Bank, S. R.; Harris, J. S.; Parkin, S. S. P. Phys. Rev. Lett. 2005. 94, 056601.

[142] A. Kanno and Y. Masumoto, J. Luminescence 119-120, 178 (2006).

[143] J. H. Buss, J. Rudolph, T. Schupp, D. J. As, K. Lischka, and D. Hagele, Appl. Phys. Lett. 97, 062101 (2010).

[144] Guo, W.; Banerjee, A.; Bhattacharya, P.; Ooi, B. S. Appl. Phys. Lett. 2011, 98, 193102.

[145] Strukov, D. B. Snider, G. S.; Stewart, D. R.; Williams, R. S. Nature 2008, 453, 80-83.

[146] Miao, G. X.; Park, Y. J.; Moodera, J. S.; Seibt, M.; Eilers, G.; Munzenberg, M. Phys. Rev. Lett. 2008, 100, 246803.

[147] Jonsson-Akerman, B. J.; Escudero, R.; Leighton, C.; Kim, S.; Schuller, I. K.; Rabson, D. A. Appl. Phys. Lett. 2000, 77, 12.

[148] Johnson, M.; Silsbee, R. H. Phys. Rev. Lett. 1985, 55, 1790.

[149] Costache, M. V.; Zaffalon, M.; van Wees, B. J. Phys. Rev. B. 2006, 74, 012412.

[150] Fert A.; Jaffres, H. Phys. Rev. B. 2001, 64, 184420.

[151] Liu, E.; Nah, J.; Varahramyan, K. M.; Tutuc, E. Nano Lett. 2010, 10, 3297-3301.

[152] Johnson, M.; Silsbee R. H. Phys. Rev. B 1988, 37, 5312.

[153] Godfrey, R.; Johnson, M. Phys. Rev. Lett. 2006, 96, 136601.

[154] A. Banerjee, F. Dogan, J. Heo, A. Manchon, W. Guo, and P. Bhattacharya, Nano Lett. 11, 5396 (2011).

[155] N. Nepal, M. Oliver Luen, J. M. Zavada, S. M. Bedair, P. Frajtag, and N. A. El-Masry, Appl. Phys. Lett. 94, 132505 (2009).

[156] Wei Han, K. Pi, K. M. McCreary, Yan Li, Jared J. I. Wong, A. G. Swartz, and R. K. Kawakami, Phys. Rev. Lett. 105, 167202 (2010).

[157] Yi Zhou, Wei Han, Li-Te Chang, Faxian Xiu, Minsheng Wang, Michael Oehme, Inga A. Fischer, Joerg Schulze, Roland. K. Kawakami, and Kang L. Wang, Phys. Rev. B 84, 125323 (2011).

[158] Tomoyuki Sasaki, Tohru Oikawa, Toshio Suzuki, Masashi Shiraishi, Yoshishige Suzuki, and Katsumichi Tagami, Appl. Phys. Express 2, 053003 (2009).

[159] J. A. Katine, F. J. Albert, R. A. Buhrman, E. B. Myers, and D. C. Ralph, Phys. Rev. Lett. 84, 3149 (2000).